SOME VISCOSITY EFFECTS IN AXIAL FLOW COMPRESSORS

Thesis by

John T. Bowen

In Partial Fulfillment of the Requirements

For the Degree of

Doctor of Philosophy

California Institute of Technology

Pasadena, California

1949

Abstract

1. A thirty-six inch tip diameter axial flow air compressor, auxiliary apparatus and instrumentation have been constructed and have been successfully operated for securing accurate test data.

2. Special instruments for detailed flow measurements near bounding surfaces have been constructed and successfully used.

3. On the basis of data secured from the test installation, it has been established that flow energy losses which result from fluid friction on actual compressor blade surfaces are considerably greater than would be expected from measured or calculated two-dimensional results. Furthermore, the range of low-loss operation is significantly reduced.

4. Test results indicate that the outer and inner wall boundary regions, which are affected by fluid friction, may or may not become more extensive through several stages of an axial flow compressor, depending on the specific compressor design.

5. Measurements indicate that a considerable portion of overall compressor losses occur near the outer and inner extremes of the blade sets because of poor flow incidence conditions in the wall boundary regions.

Acknowledgements

The writer wishes to express his sincere gratitude to the many individuals and organizations whose efforts contributed to portions of the program outlined in this thesis.

In particular, the permanent members of the project staff, Mr. L. J. Downs, Mr. F. T. Linton, Miss G. Pauwels and Mr. T. Taniguchi, cooperated in test work and data reduction far beyond the normal requirements of their duties.

Mr. Rolf H. Sabersky has been a close friend and coworker throughout the research program and the period of graduate study. His selfless cooperation and encouragement have made the entire period a pleasant one.

Professor W. Duncan Rannie supervised the thesis research as well as the overall project. The writer is most grateful to Professor Rannie for his personal interest and invaluable participation in the project, and for many private sessions of instruction in the general field of Applied Mechanics.

CONTENTS

I Introduction

By the year 1946 the multi-stage axial flow air compressor had become a frequently used component in gas turbine systems. Single stage axial flow pumps and compressors had found numerous industrial applications. However, a great deal of the developmental effort on such devices had taken place under conditions which required that a practical working machine be produced in the shortest possible time, hence relatively few fundamental investigations of internal flow patterns had been made. It was apparent at that time that further significant improvement in the axial flow compressor required careful theoretical and experimental investigations, portions of which could appropriately be conducted in the Institute laboratories.

It was believed that a coordinated theoretical and experimental research program could contribute substantially to the improvement of overall compressor efficiency, to the extension of the useful performance range and could provide information which would aid compressor and pump engineers in designing machines to suit a wide variety of prescribed operating conditions. A great deal of the experimental work required by such a program could be done in the low-speed, low-Mach number regime of operation, particularly since considerable test accuracy could be achieved with a relatively inexpensive and convenient installation.

Such a program was undertaken by the Mechanical

Engineering Laboratory with the support of the Office of Naval Research, Department of the Navy. Professor W. D. Rannie supervised the entire program. Design and supervision of construction of the test installation was conducted as a joint project by Mr. R. H. Sabersky and the writer. The program could conveniently be divided into three portions: determination of overall compressor performance, investigation of the ideal, "perfect fluid" internal flow, and investigation of fluid viscosity ("real fluid") effects in the internal flow. The first program was conducted jointly; experimental and theoretical work for the second was conducted by Mr. Sabersky, and has been reported in Reference 5. Experimental and theoretical work on viscosity effects was conducted by the writer, and constitutes the subject of Sections III, IV and V of this report.

A convenient and adequate design theory for axial flow turbomachines, based on the equations of motion of an inviscid fluid, had already been developed by Professor Rannie. A substantial portion of the overall program was devoted to detailed experimental confirmation of the theory. However, little or no theoretical information was available on viscosity effects, and such experimental evidence as had been secured was largely uncoordinated.

The investigation of viscosity effects was therefore begun by locating those regions of the compressor flow stream were such effects are most important. Near the

surface of the compressor blades and near the outer and inner compressor walls, viscous effects appeared to be of decisive importance. Hence these regions were selected for initial theoretical and experimental investigation. It is believed that some significant results have been obtained, but many questions remain to be answered by further investigation.

Construction and operation of the test equipment and instrumentation are discussed in Section II. Section III provides a general introduction to viscosity effects in axial flow turbomachines. Sections IV and V present specific results and conclusions on viscous effects. Some detailed information, which may not be of general interest, has been included in Appendices I to V. All figures and tables are grouped in the final pages of the report.

II The Experimental Program

2:1 The Test Equipment

2:1.1 Design Criteria and Principal Dimension

In accordance with the purpose stated in the introduction (Sec. I), the test installation was to be constructed so as to be suitable for a large variety of different research experiments. To limit somewhat the scope of the problems to be investigated it was decided to restrict the present work to low speed flow. It was felt that a more thorough understanding of this field would contribute most to successful application of multistage compressors.

To satisfy the requirement of a flexible installation, the compressor was designed so that each blade (and each blade row) would be removable and also have an adjustable angle setting. For the same reason, instrumentation was provided to allow detailed measurements near the blade rows as well as overall performance measurements. The compressor was to be sufficiently large to permit the use of instruments of reasonable size without causing undue interference with the flow. The compressor speed was chosen high enough to produce pressure difference that could be measured with good accuracy. On the other hand it was to be low enough to avoid structural difficulties inherent in the design of an adjustable blade fastening arrangement, and to keep within the power limitations of

the available laboratory. The hub ratio was to be relatively low to simulate a design requirement of modern high performance compressors and to allow study of three-dimensional flow patterns.

There was to be a sufficient number of stages to permit duplication of conditions typical of the middle and last stages of a multistage compressor. In addition, one row of entrance (pre-rotation) vanes and two rows of rear (recovery) vanes were required. It was felt that the effects of axial spacing between blade rows had been established by other investigations, hence fixed axial positions could be adopted for all blade rows (Ref. 1). The blade aspect ratios and cascade solidities were to be typical of modern high performance compressors. Finally, the compressor structure was to be quite rigid, so that tip clearances and general alignment could be maintained.

With the above considerations, the following characteristics were adopted for the compressor:

1. Tip diameter of 36 inches (= 2 R)
2. Hub ratio of .60 (inner diameter 21.60 inches) $= \xi_i$
3. A maximum of three complete (rotor and stator) stages plus entrance vanes.
4. All blade angles adjustable by $1/2^{\circ}$ increments.
5. Maximum power consumption of about 100 H. P.
6. Speed range up to 2000 R. P. M. (315 f.p.s. tip speed).

7. Thirty rotor blades per row and thirty-two stator blades per row.

The compressor and test installation were constructed to these specifications and have been in operation for some months.

The compressor is driven by a cradled electric dynamometer, from which torque and speed measurements are derived and input power computed. The total flow volume is measured by a calibrated entrance duct which precedes the compressor. The flow is regulated by a throttle following the compressor. The average pressure rise is computed from detailed surveys taken immediately behind the last blade row in the compressor. These internal surveys are possible through a system of access ports. Thus, from dynamometer measurements and internal surveys, overall performance and efficiency are established.

2:1.2 The Compressor Installation

A general view of the compressor installation is given in Fig. 1. The air enters from the left through a screen and bell mouth (F-1). It passes through the calibrated cylindrical duct (F 3) and into the compressor (F 5). Leaving the compressor the air is deflected vertically upward through a vaned elbow (F 7) and passes out into the room through the throttle valve (D 7). The dynamometer (F 9) drives the compressor by means of a coupled shaft which passes through the elbow. The

dynamometer is supplied with direct current from a motor-generator set (A 7), which is controlled from the panel (E 6). The main operating desk (E 4) contains various recording and measuring apparatus. Directly in front of the desk is a 20 tube manometer bank (D 1). Compressor assembly is facilitated by a two ton electric hoist, which covers the working area.

The laboratory floor is 17 ft. below the ground surface. Both the compressor and dynamometer are mounted on foundation blocks insulated from the floor slab. The laboratory has adequate light and ventilation and the interior air temperature is between 65 and 90°F year around. Alternating current (60 cycle) power is avilable at 2300, 440, 220, and 110 volts. The motor-generator set supplies D. C. power at zero to 250 volts for the dynamometer and auxiliary equipment. Wet cell storage batteries are used to supply direct current for instrumentation. Water, steam and compressed air are available in the laboratory.

In addition to the space shown in Fig. 1, adjacent floor area is available for compressor maintenance and auxiliary test equipment. A nearby room at the same level is used for storage.

2:1.3 The Compressor Structure

Throughout this description of the axial flow compressor structure reference will be made to the cross-

section drawing, Fig. 2, and to illustrations of the compressor in several stages of assembly, Figs. 3 to 8 inclusive.

The outer case consists of two cast iron half-cylindrical shells bolted together along a horizontal plane through the central axis of rotation, (see Fig. 2 and 3). The rows of stator blades are mounted in these shells. Within the outer case a hollow steel shaft supports three cast iron drums, each capable of carrying one row of rotor blades (see Fig. 4 and 5). The hollow shaft is supported by two grease lubricated roller bearings, the outer races of which are pressed into the supporting strut assemblies (Fig. 2). These steel strut assemblies rest in close fitting channels at either end of the outer case (Fig. 6) and may be rotated about the central axis. The latter feature enables strut wakes to be positioned with respect to measuring instruments. Attached to each strut assembly is a cylindrical aluminum filler section of the same diameter as a rotor drum, extending to within 1/16 inch of the rotating assembly. (Figs. 2 and 4).

An essential feature of the test compressor is a set of six rectangular instrument ports on the upper half-cylinder (Figs. 2 and 7). Ports are located at $22\frac{1}{2}^{o}$ on either side of vertical and are axially placed in the second and third rotor planes, the first, second and third stator planes, and behind the third stator plane as shown in Fig. 2. A special instrument carriage (see Sec. 2:2.3)

can be held in any of the ports, and thus detailed surveys can be made behind any stage or partial stage.

In order to maintain uniform clearance between blade tips and the outer casing or rotor drums, it was necessary to require close machining of the compressor structural elements as well as the blades themselves. Careful inspection was made with these results:

The inner surface of the assembled case is cylindrical within .001 inch, its exact diameter is 36.000 in. at 68°F.

The rotor drums are 21.600 ± .001 inches in diameter.

The rotor drums are concentric with the inner surface of the case within .001 inch.

The counter bores, which position radially rotor and stator blades, are of uniform depth within .002 inch.

Other significant dimensions (blade hole location, port location, etc.) were held generally within .010 inch. The instrument carriage casting and port plugs were machined in the case and are therefore absolutely flush with the inner surface.

Discussion of blade tolerances and tip clearances will be reserved for Sec. 2:1.4.

It will be of interest to describe the sequence of operations in assembly and disassembly of the compressor and to give approximate time estimates for the operations. For this purpose the compressor is assumed to be completely assembled with three stages of blading plus entrance vanes

and rear vanes. It is desired to remove the present rotor and stator blades and entrance vanes, to replace them by another set, to re-align the rear vanes, and to reassemble the equipment.

a. Connecting ducting and the upper half of the outer case are removed, Fig. 3. (Time 3.0 man hr.)

b. The rotor and supporting strut assembly is removed from the case, Fig. 5, and the filler sections and rotor drums are disassembled sufficiently to permit removal of the rotor blades, Fig. 8. (Time 5.5 man hr.)

c. Blading is removed from the outer casing and the rotor drums.

Per row of rotor blades: Time 3.5 man hr.

Per row of stator blades or entrance vanes: Time 3.0 man hr.

To re-align rear vanes: Time 5.0 man hr.

d. The new rotor and stator blades and entrance vanes are put in place:

Per row of rotor blades: Time 7.0 man hr.

Per row of stator blades or entrance vanes: Time 6.5 man hr.

e. The rotor assembly is prepared for replacement in the outer case. (Time 4.0 man hr.)

f. The reassembly is completed. (Time 5.0 man hr.)

Total labor amounts to 92.0 man hr., or about 46 hr. assuming the usual crew of two experienced mechanics.

2:1.4 Blade Construction

A procedure for selection of blade design parameters and specification of individual blade cross-sections is given in Section 2:3. It is assumed here that tables of profile coordinates and orientations are available for the desired blade set. A typical set of data is given in Table 1, representing the coordinates for the center section of the "free vortex" stator. Depending on the twist (radial rate of change of section-orientation) and camber of the blade, from five to eight sections are specified as shown in Fig. 9. Orientation of each section is given by the angle between its chord line and that of the (center) reference section. In addition one point on each section is selected which is to be intersected by the central axis of the blade shank (Fig. 9). This point must be selected in some systematic manner in order to avoid surface "waviness" and is usually taken as the centroid of the cross section. Selection of the centroid minimizes centrifugal bending effects for rotor blades. In the case of compressor blades a theoretical airfoil thickness distribution generally yields a trailing edge which is too thin for practical fabrication or handling. Consequently, the thickness is modified over the rear 15% of the airfoil section to yield a trailing edge of .020 inch.

When the preceding properties have been determined, a ten times size drawing of each section is prepared on

a specially coated steel sheet similar to those used for aircraft master layouts. The section profile, chord line, centroid, appropriate reference lines and notations are scribed through the surface coating and are blackened with a copper sulphate solution. This process gives clear lines of good contrast (generally about .010 inch wide). A typical 10 x section drawing is shown in Fig. 10.

The section drawings are next photographed and from the resulting glass plate negatives full scale (1 x) metal templates are printed. Two sets of these templates are made, one slightly greater than full scale to allow for shrinkage in casting, and the other exactly full scale for finishing and final inspection. A full scale template print is also shown in Fig. 10.

Blade construction proceeds along the following lines: a master pattern or permanent mold is constructed, blades are cast, the blade shanks are machined, the surfaces are hand finished and the blades are then ready for inspection. The two sets of blading ("vortex" and "solid body") supplied to date for this project were constructed by the Aerolab Development Co., of Pasadena, California. Since the sub-contractor was selected on the basis of competitive bidding in every case, it appears that for lots of approximately 100 blades of each design, casting and hand finishing is successfully competitive with other processes which have been developed.

Both sand casting and permanent mold castings have

been successful. The metal used has been ALCOA 356, aluminum alloy without heat treatment. In one case a master pattern is first made, in the other a cast iron mold. Shrinkage must be considered and sufficient material allowed for subsequent finishing. The blade trailing edge is cast considerably over thickness to insure free flow of metal in casting.

After the shank is turned, the blade is mounted in the finishing fixture where it can be checked against accurate templates as finishing proceeds, Fig. 11. Each of the specified sections is periodically checked during the subsequent hand-filling and scraping process. The surface is "faired in" between sections. A skillful operator is ableto achieve remarkable accuracy in finishing, as will be subsequently described.

Detailed physical inspection of each blade is made in the template fixtures, Fig. 12. Each blade is x-ray photographed and inspected for internal and surface flaws. The shank dimensions of each blade are checked. In addition to routine inspection, one blade is selected at random from each order of rotor or stator blades. This blade is invested in a low melting temperature alloy, reference surfaces are established and the blade is cut at each of the originally specified sections. The sections are blued, reference lines are established and all burrs are removed from the blade sections itself. A prepared section is shown in Fig. 13. The sections

are photographed and printed to ten times full size on metal sheets. Previously, ten times size prints of the original section drawings have been produced on glass plates. By superposition of a glass plate on the corresponding sectioned blade photograph, it is possible to check the contour accuracy within .0005 inch, full scale, and to obtain an independent check on the entire process. A typical comparison is shown in Fig. 14.

Experience with four sets of blades (approximately 100 per set) has shown that the following accuracy is economically attainable with the preceding construction method:

Profile accuracy - first 25% upper surface - $\pm$ .003 inch

Profile accuracy - other regions - $\pm$ .005 inch

Chord length - $\pm$ .015 inch

Section orientation - $\pm$ 15 minutes of an arc

Location of section centroids - $\pm$ .015 inch

In order to attain angle adjustability for the rotor and stator blades and entrance vanes, the fastening system shown in Fig. 15 was adopted. Attached to the blade shank, and aligned within 5 minutes of an arc to the central reference section, is an indexing plate containing holes spaced at $4\frac{1}{2}$ degree intervals. Fixed to the rotor drum or case is a similar plate with holes spaced at 4 degree intervals. Thus by mating different pairs of holes, angle adjustment by $\frac{1}{2}$ degree increments is possible. The blade

and indexing arrangement are securely clamped in place by a bridge and lock-nut as shown in Fig. 16. Details of the blade shank are shown in Fig. 9.

The tips of both rotor and stator blades are machined to approximately 18.0 and 10.8 inch radii respectively (Fig. 9). This procedure insures accurate and uniform tip clearance over the entire tip chord length. The root sections are machined square to clear the adjacent wall by approximately .010 inch. Several counter-bored holes are provided in the outer case through which rotor blade tip clearance can be measured with a standard depth micrometer. Such measurements have shown the tip clearance to be uniform within $\pm$ .005 inch. The nominal clearance used thus far has been .029 inch for both rotor and stator tips. The clearance can be further decreased by placing shims under the blade shanks or be increased by re-machining the tips.

Special plugs are provided for filling the blade shank sockets when less than three full stages of blading are in use. The exposed surfaces are machined to the wall radii so as to leave smooth wall surfaces. Rotor and stator plugs are shown in Fig. 17.

2:1.5 The Dynamometer and Electrical System

During the design and procurement phase of the project, it was found impossible to obtain a commercial,

cradled dynamometer in the scheduled time. A preliminary investigation of torque-measuring devices had indicated that only a cradled dynamometer would reliably give the desired accuracy of torque measurement. Hence it was necessary to construct a dynamometer starting with a rebuilt 125 H. P. direct current motor. Concurrently with the other construction, a 100 KW motor generator set was procured and installed at the Institute's expense. Electrical specifications of both dynamometer and motor generator set are given in Table 2.

A general view of the dynamometer is shown in Fig. 18. The outer case of the motor is supported by two end pedestals containing counter rotating bearings which give effectively frictionless suspension. A detail view of one bearing is shown in Fig. 20 and a layout drawing in Fig. 19. The bearings are driven in opposite directions by auxiliary slow speed motors through chain and sprocket arrangements. In order to eliminate a periodic drag torque which excited oscillations in the measuring system, it was necessary to use precision bearings mounted to concentricities of the order of .0002 inch and to load centrally each bearing. Field and armature current is brought into the dynamometer from above (Fig. 18) through the mercury contacts shown in Fig. 21. These contacts exert no appreciable torque on the suspended system. A tachometer generator and a centrifugal overspeed switch are mounted at the rear of the dynamometer. The lead

wires from these auxiliaries are quite flexible and therefore introduce little error. The dynamometer is attached to the compressor drive shaft by a solid coupling which is easily disconnected for dynamometer calibration.

The torque reaction on the suspended motor case, and thus the compressor driving torque (plus windage) is measured by a Hagan Thrustorq (size 3.5) mounted as shown in Fig. 18. This instrument is further described in Sec. 2:2.2. The counterweights shown in Fig. 18 extend the torque measuring range. A hanger for calibrating weights is provided on the opposite side of the dynamometer.

A wiring diagram of the principal electrical components is shown in Fig. 23. In this diagram the wiring of meters, protective devices, etc. is not shown. One of the two 50 KW D. C. generators is operated at constant voltage (125 v.) and supplies field current to the dynamometer. Potential from the other generator is variable and may be added to or subtracted from that of the "constant voltage bus". Thus a range of zero to 250 volts DC is available for the dynamometer armature. In addition the dynamometer field current may be varied. By these means the full speed range from zero to 2000 RPM is attainable. The entire system is operated from the panels shown in Fig. 22. This sequence of operations is followed in starting the equipment:

a. The M. G. set is started.

b. The dynamometer field is excited.

c. Dynamometer armature voltage is reduced to zero.

d. The dynamometer armature contactor is closed.

e. Dynamometer armature voltage is increased and the dynamometer speed increases proportionately.

f. Further speed increase or adjustment is obtained by varying the dynamometer field current.

The equipment may be stopped by simply stopping the M. G. set or, with better control, by reversing the above sequence of operations.

2:1.6 Ducting and Throttle

A drawing of the screen, bell mouth and entrance duct is shown in Fig. 24. The screen was installed to prevent foreign objects from entering the compressor air stream. The bell mouth gradually accelerates the air, guiding it into the duct. The cylindrical duct is two diameters in length, with an interconnected set of four wall static pressure orifices located one diameter from the front. Calibration of the static orifices is discussed in Sec. 2:2.2. The duct is mounted on a castered carriage to facilitate its adjustment or removal. Interior surfaces of the bell mouth and duct are enameled and polished to give undisturbed flow.

Attached to each strut assembly (Fig. 2) is a wooden fairing whose purpose is to accelerate gradually the air from the cylindrical duct into the annual compressor cross-section. These fairings are ogival in shape (Fig. 24),

and have waxed and polished surfaces.

Between the compressor and the exit elbow a short cylindrical duct is installed. This duct may be parted on a diametral plane to facilitate disassembly of the compressor (see Fig. 1). A drawing of the elbow is shown in Fig. 25. Sheet metal turning vanes were installed to minimize losses and thus permit operation at maximum flow rate. The elbow is mounted on a carriage to permit its easy removal or adjustment (Fig. 1). It was provided that the elbow could be mounted horizontally for attachment of an auxiliary blower that would extend the flow range of the compressor. A transition section connects the elbow to the throttle valve. All joints in the ducting are gasketed to prevent excessive air leakage.

The throttle valve (Fig. 26) is provided for regulating the flow resistance and thus the compressor flow volume. It consists of two rectangular metal doors which roll in side beams, their position being controlled by a right and left hand threaded lead screw. The screw is driven by a variable speed motor. For normal adjustment of the throttle a door speed of one ft./min. has been found convenient. A revolution counter driven by the lead screw indicates the throttle position. This latter feature has proved very convenient for quickly obtaining the approximate flow rate. The doors are equipped with electrical limit switches and mechanical stops.

2:2 Instrumentation

2:2.1 Introduction

The test installation was designed to allow accurate determination of compressor speed, total through flow rate, driving torque, air density, static pressure rise, work input to the air stream, and complete details of the internal flow patterns. The first five quantities are determinable by external measurement, the last two only by means of instruments located within the test compressor. In the following sections methods of determining, respectively, the overall performance quantities, and details of the flow pattern, will be discussed. Special emphasis is placed on measurement of the internal flow pattern, since the results of such measurements constitute the subject of major portions of the subsequent discussion.

2:2.2 Overall Performance Measurement

a. Compressor Speed

Speed of rotation of the test compressor is determined by means of a commercial electric tachometer unit. A small two pole generator is attached directly to the dynamometer shaft (Fig. 20). The alternating current output of the generator drives electrically an indicating instrument located in the control desk (Fig. 27). The entire system is available commercially (Standard Electric

Time Co., Chrono-Tachometer Unit, Type S G). An indication of shaft speed, accurate to within±2 R. P. M., is available on a 6" dial type instrument. For more accurate speed determination, a synchronized clock-revolution counter is provided. The use of timing intervals which are multiples of 1/10 minute is convenient. Intervals of one minute were used during all test runs. The accuracy thus obtainable is±1/2 R. P. M. for the average speed. Accuracy of the system was checked by recording the tachometer generator output and that of a standard 1000 cycle tuning fork on an oscillograph. The speed determined in this manner was checked against that obtained by use of the indicating unit.

b. Torque

The compressor driving motor is cradled as described in Sec. 2:1.5 so as to form a conventional dynamometer system. The driving motor outer case actuates a self-balanced pneumatic diaphragm mounted at fixed distance from the suspension center (Fig. 18). The diaphragm unit is available commercially (Hagan Corp., "Thrustorq" Model 3.5). Balancing air pressure is measured on a mercury manometer. Accuracy is contingent upon minimizing drag torques which act on the cradled system. By providing highly accurate, counter rotating support bearings (Sec. 2:1.5) and low drag mercury electrical contacts,

an accuracy of ±.4 ft. lb. is obtained (determined by calibration data scatter).

A shaft coupling is provided so that the dynamometer can be disconnected from the compressor. It is then possible to calibrate the entire torque measuring system with standardized hanger weights. In order to secure satisfactory accuracy in the low-speed, low-torque operating condition, a "Thrustorq" unit was selected which has a range of 0 to 50 ft. lb. when actuated by the dynamometer. Since a total torque range of 0 to 300 ft. lb. was required, the range is extended in a stepwise fashion by the counter weights shown in Fig. 18. Complete torque calibration curves for the dynamometer are shown in Fig. 28. It will be noted that a linear torque-mercury column deflection relation is obtained.

c. Air Density

Wet and dry bulb temperature measurements are taken in the moving air stream immediately in front of the bell mouth screen (Fig. 24). Barometric height and temperature are obtained from a standard mercury barometer located approximately 25 ft. above the compressor center line. Temperatures are read to the nearest 1/10 degree Farenheit and barometric height to the nearest 1/100 inch. No convenient air density computation tables were available, hence the system of density determination given in

Appendix II was developed. By this system density determination, accurate to at least 1/4%, is achieved.

d. Flow rate

As described in Sec. 2:1.6, a set of static pressure orifices is located in the entrance duct. Using a 3/16" tip diameter Prandtl type pitot tube, series of velocity traverses were taken along two perpendicular duct diameters at various flow rates. Simultaneously, the duct static pressure and air density factors were measured. Then by integration of the survey data, total flow rate and average through flow velocity were obtained. There was prepared a master calibration curve of mean velocity, $\overline{Ca}$ (ft./sec.), through the compressor annulus vs. $\frac{h}{\rho}$, where h is the wall static pressure (below atmospheric) in inches of water and ρ the air density in slugs/ft.^{3}. A reproduction of this curve is shown in Fig. 29. A precision water manometer (Sec. 2:2.4) is used to determine the duct static pressure to within $\pm$.001 inch water and, if the air density is known, the average through flow velocity is readily obtained.

Despite the absence of straightening vanes or a settling chamber, flow in the entrance seems reasonably uniform and stable. Careful direction measurements in the duct have indicated that no large scale eddies are present. However, since at the normal operating conditions (750 R. P. M., design flow) the duct pressure is

only about .250 inch of water, the accuracy of mean velocity determination is probably not better than 1/2%. At higher compressor speeds and flow rates, the accuracy is much improved. Further discussion of this matter is given in Sec. 2:4.1.

e. Static Pressure

Static pressure orifices (.030" in diameter) are provided in the outer casing of the test compressor. An orifice is located in the plane of the axial clearance space between each blade row. Pressures measured at these locations can be correlated with internal measurements (See Sec. 2:4.2).

f. Work Input to the Air Stream

Work input or total pressure rise of the air stream is determined by surveying in detail total pressure and velocity in a chosen plane downstream of a particular blade row. Usually, a circumferential sector of 15° is explored (the stator blade spacing is 11.25°). In the subsequent data reduction, this sector is assumed to be typical of the entire annulus. For checking the validity of this assumption, holes are provided at two additional locations, equally spaced from the instrument ports (Sec. 2:2.3f), through which probes can be inserted. The data of Fig. 30 are typical of a number of such checks which have shown the assumption of circumferential uni-

formity to be valid. Further discussion of internal survey instruments is given in the following section.

2:2.3 Internal Measurements

For detailed measurements of the flow pattern inside the test compressor a number of small total pressure, static pressure and direction measuring probes have been used (Fig. 31). A special traversing carriage (Fig. 16) was constructed to hold and position these instruments. In order to check blade surface pressures small orifices were inserted in a stator blade. These instruments are described in detail in the following paragraphs.

a. Total Pressure Probe - Kiel Type

A total pressure probe of the design shown in Fig. 31 was used to determine total pressure (stagnation pressure) where the air flow direction was not well known. A calibration curve of pressure vs. air incidence angle is shown in Fig. 32. It is seen that this construction causes the pressure indication to be insensitive to incidence angle over a range of approximately $\pm 45^{\circ}$. Probes of several sizes in this design are available commercially (Whitney Instrument Co.).

b. Pitot Tube

The .058 inch diameter Prandtl type pitot tube shown in Fig. 31 was used for both total pressure and static

pressure measurement. It will be recalled that the accuracy of static pressure indication depends upon the exact location of the orifices and reasonable uniformity of the incident stream. Calibration curves of total pressure and static pressure vs. air incidence angle are shown in Fig. 33. It is seen that the total pressure indication is correct within $\pm 6^{\circ}$ incidence angle, while the static pressure is correct within 1% velocity pressure up to $\pm 7^{\circ}$ incidence angle. The air stream velocity pressure, $\frac{\rho}{2} v^2$, is equal to the difference of these two pressures.

c. Special Total Pressure Probes.

In order to measure accurately total pressures near boundaries or compressor blade surfaces, impact tubes of still smaller diameter were required. The two designs shown in Fig. 31 were constructed to fill this need. Pieces of .020" O. D. by .010" I. D. stainless steel tubing were bent to the required shape and cemented into the holder. One design was used near the inner compressor wall and for blade wake exploration; the other for measurement near the compressor outer wall. A calibration curve of pressure vs. air incidence angle for the inner wall probe is shown in Fig. 34. Total pressure indication is seen to be correct within $\pm 8^{\circ}$ incidence angle. If the static pressure field is known, it is clear that velocities near bounding surfaces can be determined with the aid of these instruments.

d. Cylindrical Direction Probe.

In flow regions remote from bounding walls and where the radial velocity component was negligible, the three-hole, cylindrical direction probe shown in Fig. 31 was used for determining flow direction. The instrument was used as a null indicator, i.e., it was rotated about the cylinder axis until the pressures at the two side orifices equalized. A calibration curve of pressure differential vs. yaw angle is shown in Fig. 35. When aligned in the flow direction, the center hole indicates total pressure. Using the electric pressure pickup subsequently described (See Sec. 2:2.4), angular changes as small as 1/10 degree were detectible. The instrument was procured commercially (Whitney Instrument Co.).

e. Claw Type Direction Probe.

Since it was frequently necessary to measure flow direction near the outer and inner compressor walls and in regions of large velocity gradient, the special claw type direction probe shown in Fig. 31 was constructed (the design was suggested by Ref. 3). As is true of the three-hole probe, the instrument measures direction only in a plane normal to its axis of rotation. However, radial velocities are relatively small in the test compressor when operating in other than the extreme "stalled" range, hence either probe gives a good measure of air flow direction if its axis is directed along a radius. A calibration curve

for the claw probe is shown in Fig. 36, although it was also used as a null indicator. Its sensitivity is seen to be equal to that of the cylindrical probe, however the fact that its pressure orifices are only .015 inch apart rather than .090 inch, results in its indication being reliable in a stream of much higher transverse velocity gradient.

Both direction probes are furnished with locating collars (Fig. 31) which fit accurately into the instrument carriage (See Sec. 2:2.3f). The relation of the collar flat to the compressor reference surfaces is accurately known. Pressure orifice locations give a rough indication of zero incidence angle, however more accurate knowledge of the absolute zero angle is necessary. This information is obtained and frequently checked by placing the particular probe, mounted in the instrument carriage, in a one inch diameter vertical test jet as shown in Fig. 37. A reference surface on the carriage is carefully leveled and the angle for null indication determined. The carriage is then placed and re-leveled on the opposite side of the jet, thus bringing the probe axis into its original horizontal plane but directed oppositely. The angle for null indication is again determined. It is seen that the mean of these two determinations gives the true zero incidence angle direction with respect to the carriage reference surface.

f. Instrument Carriage.

A special instrument carriage for radial and circumferential positioning of test probes in the compressor was provided. Detail design and construction were performed by the Boller and Chivens Instrument Co. The carriage is shown in two possible mountings by Figures 16 and 38.

In the first case (Fig. 16), the assembly fits into any one of the six rectangular instrument posts which were described in Sec. 2:1.3. The base casting is rigidly bolted to the compressor housing and conforms perfectly to the inner wall cylindrical surface since it was machined in place when the compressor was constructed. The traversing carriage moves in the base casting on a circular track, whose center coincides with the compressor axis. By this means, a probe which is held in the traversing carriage can be moved through a total circumferential angle of fifteen degrees. Circumferential position is indicated by the lower dial (Fig. 16) to the nearest .01 degree of arc.

Within the traversing carriage, one drive is available to position a probe radially in the compressor and another to rotate a probe about its own axis. Radial position and direction are indicated by the center and upper dials to the nearest .01 inch and .1 degree, respectively.

A slot is provided in the base casting to provide clearance for a probe as it is circumferentially traversed. An important feature of the carriage design is a flexible sliding tape (Fig. 39) which covers this slot on either side of the probe. The tape conforms closely to the inner cylin-

drical surface causing negligible disturbance to the flow.

Circumferential traverses are possible only before or behind a blade row with the arrangement described above. To provide for flow pattern measurement between and within blade rows when the compressor is being operated with several stages, a set of accurately located, 7/8 inch diameter holes were bored in the outer housing. The location of these holes is shown in Fig. 40. When the traversing carriage is mounted as shown in Fig. 38, radial and directional probe positioning is possible at one circumferential location upstream or downstream of each blade row. Since the radial holes are arranged in pairs, accurate alignment of the carriage for flow direction measurement is achieved by use of the mounting bar and dowel pin system shown.

The entire instrument carriage arrangement was constructed with considerable precision and tests have shown that the accuracy of positioning for each component is at least as good as its indicator dial least count.

g. Static Pressure Blade.

For use in the calculation of cascade losses, (See Sec. 4:2) it was desirable to determine, both by calculation and measurement, the pressure distribution on cascade airfoil sections. To aid in the latter objective, one "Free Vortex" design stator blade was provided with static pressure orifices as shown by Fig. 41. Eight .010 inch

diameter orifices were spaced along each blade surface at the center section (r = 14.40 in.). These orifices were internally connected to small stainless steel tubes which were brought out through the blade shank and attached to the selector shown in Fig. 42. Thus with the compressor maintained at a particular operating condition, static pressures at each of the sixteen locations could be measured in turn. Insertion of the system of orifices presented some problems, chiefly because an existing cast aluminum blade was used and drilling the relatively long, small diameter holes proved difficult. However, the finished blade was quite satisfactory and an accurate, undisturbed contour was maintained at the measurement section.

2:2.4 Pressure-Indicating Instruments

Many of the instruments described in the preceding sections require, ultimately, the accurate measurement of one or more static pressures. Three types of pressure indicators were used: a twenty tube vertical manometer bank, so-called micro-manometers, and a special strain gage pressure pickup which was used for accurate pressure indication with instruments having very small orifices.

a. The Manometer Bank

A vertical bank of twenty, six m.m. diameter, six

ft., manometer tubes was constructed (Fig. 27). Separate instruments could be connected to the upper end of each tube and the lower ends were attached to a common manifold. A movable reservoir connected to the manifold could be used to adjust the zero pressure reference level.

This manometer bank was used only for rough pressure indication in the tests described herein, because the compressor was usually operated at low speed, and accuracy obtainable with a vertical tube was insufficient. For higher speed tests this instrument would be essential.

b. Micro-Manometers

Two precision water manometers were procured for use with flow measuring instruments and as laboratory standards (Fig. 27). The type used is commercially available (Meriam Instrument Co., Micro-Manometer, Size 10). Each has a range of 0-10 inches water pressure. A fixed, inclined glass tube contains a scribed reference line to which the water meniscus is adjusted by vertical movement of the fluid reservoir. The reservoir is mounted on a precision lead screw whose position is indicated by a scale and micrometer dial calibrated in 1/1000 inch divisions. Pressure connections can be made either to the (closed) reservoir or to the free end of the manometer tube, thus allowing pressure differentials and pressures above or below atmospheric to be measured.

The fluid used was supplied by the manometer manu-

facturer. It is colored and has suitable surface tension for good meniscus formation. Its density was checked and found to be 1.000 $\pm$ .001 gm/cc over the laboratory temperature range, thus for the required accuracy temperature correction was not ordinarily necessary.

These manometers proved most satisfactory for entrance duct and compressor wall pressure measurements and could also be used with the Kiel type total head probe. However, reservoir and connecting tube air volumes were too great to permit their use with the pitot tube, yaw probes, or special total pressure probes.

c. Pressure Pickup

For use with the small orifice flow instruments, a commercial electric pressure pickup was procured (Statham Inst. Co., Model P-5, Size $\pm$ .2 p.s.i.). This instrument could be mounted near the test probe, thus minimizing connecting tube volume (Fig. 38). Internally it consists of a small, low volume, metal bellows which can be subjected to both internal and external pressures. Thus it can be used as a differential gage or can indicate pressures above or below atmospheric. The bellows, in extending a very small distance, actuates a set of electric strain gages. Resistance change of the gages is remotely determined by the bridge circuit shown in Fig. 43. The bridge is balanced to give zero deflection of a sensitive, light beam galvanometer. Several sensitivity ranges are avail-

able in the circuit for use with a variety of flow pressures. The entire system was calibrated (and frequently checked) using one of the micro-manometers as a standard. The overall system gives linear response as shown by Fig. 44. Operating in the 0-2 inch pressure range, the system accuracy is $\pm$ .002 inch of water.

Because of its speed of response, convenience, and reliability, this system proved highly satisfactory for use with the direction probes, pitot tube, special total pressure tubes, and pressure blade.

2:3 Design of the Compressor Blading

Blading for the test compressor was designed by use of the applicable perfect, incompressible fluid equations of motion, supplemented by certain empirical rules. The entire subject of compressor blade design, as well as calculation of perfect fluid flow patterns and compressor performance, is treated in considerable detail in References 4 and 5. However, a brief resume of the design calculations for the test compressor blading is given here for completeness. Verification of the design method by test data is given in Reference 5.

2:3.1 Basic Equations

The steady flow of a perfect, incompressible fluid in an annular duct is considered. The fluid is acted on by

alternate rows of fixed and rotating blades which impart energy to the fluid and raise its static pressure. Assume that there is sufficient axial spacing between blade rows so that equilibrium conditions are established. Assume further that in such a plane of equilibrium, there exists symmetry of all quantities about the axis of rotation, i.e., in effect, each blade row contains an infinite number of blades.

Consider first planes of equilibrium (1) and (2) upstream and downstream respectively of a rotating blade row. Then the Bernoulli equation may be written along a streamline as

$$p_1 + \frac{\rho}{2}(w_1^2 - r^2\omega_0^2) = p_2 + \frac{\rho}{2}(w_2^2 - r^2\omega_0^2) \qquad (1)$$

if the radial shift in streamline location is neglected and where p = static pressure

ρ = fluid density

w = fluid velocity relative to the rotor

r = radius from the central axis

ω_0 = angular velocity of the rotor

and if equilibrium plane (3) is downstream of the next stationary blade row,

$$p_2 + \frac{\rho}{2} c_2^2 = p_3 + \frac{\rho}{2} c_3^2 \qquad (2)$$

where c = fluid velocity relative to fixed axes.

Or if the fluid velocity is resolved into axial and

circumferential components C_a and C_u (from the boundary conditions, no radial component can exist in the equilibrium plane), Equation (2) becomes

$$p_2 + \frac{\rho}{2}(C_{a_2}^2 + C_{u_2}^2) = p_3 + \frac{\rho}{2}(C_{a_3}^2 + C_{u_3}^2) \tag{3}$$

From the velocity vector diagram it is seen that

$$W^2 = C_a^2 + (r\omega_0 - C_u)^2$$

$$= C_a^2 + r^2\omega_0^2 + C_u^2 - 2r\omega_0 C_u$$

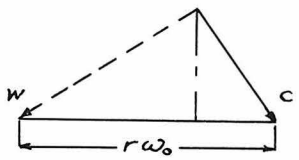

and thus Eq. (1) becomes

$$p_1 + \frac{\rho}{2}(C_{a_1}^2 + C_{u_1}^2 - 2r\omega_0 C_{u_1}) = p_2 + \frac{\rho}{2}(C_{a_2}^2 + C_{u_2}^2 - 2r\omega_0 C_{u_2}) \tag{4}$$

The equations for radial pressure equilibrium must also be satisfied, thus

$$\frac{dp_1}{dr} = \rho\frac{C_{u_1}^2}{r}$$

$$\frac{dp_2}{dr} = \rho\frac{C_{u_2}^2}{r} \tag{5}$$

$$\frac{dp_3}{dr} = \rho\frac{C_{u_3}^2}{r}$$

And, finally, the (incompressible) continuity equation is (assuming cylindrical bounding walls)

$$\int_{r_i}^{r_o} C_{a_1} r\,dr = \int_{r_i}^{r_o} C_{a_2} r\,dr = \int_{r_i}^{r_o} C_{a_3} r\,dr = \frac{Q_d}{2\pi} \tag{6}$$

where Q_d = design volume flow rate.

If it is further assumed that the flow pattern is to repeat throughout successive stages, i.e., flow geometry at (1) and (3) are identical, equations (3) and (4) yield

$$(p_3 - p_1) = \rho r\omega_0 (C_{u_2} - C_{u_1}) \tag{7}$$

Then differentiating Eq. (3) and substituting Eq. (5)

$$\frac{C_{u_2}^2}{r} + \frac{1}{2}\frac{d}{dr}(C_{a_2}^2 + C_{u_2}^2) = \frac{C_{u_1}^2}{r} + \frac{1}{2}\frac{d}{dr}(C_{a_1}^2 + C_{u_1}^2)$$

which may be rearranged as

$$\frac{d}{dr}(C_{a_2}^2) + \frac{1}{r^2}\frac{d}{dr}(r^2 C_{u_2}^2) = \frac{d}{dr}(C_{a_1}^2) + \frac{1}{r^2}\frac{d}{dr}(r^2 C_{u_1}^2) \tag{8}$$

The designer now has a choice of flow patterns subject only to the requirements of equations (6), (7), and (8). Examination of these equations reveals that (7) and (8) contain five unknown quantities, $(p_3 - p_1)$, C_{a_1}, C_{a_2}, C_{u_1}, C_{u_2}. Eq. (6) serves to determine the constants of integration. Thus with two equations and five unknowns, three additional conditions may be imposed.

One convenient and desirable condition is that $(p_3 - p_1)$ = const., independent of radius. Then defining

$$\psi_d = \frac{p_3 - p_1}{\frac{\rho}{2} u_0^2} \tag{9}$$

where $u_0 = r_0 \omega_0$ the rotor tip velocity, Eq. (7) becomes

$$\psi_d = 2\left(\frac{r}{r_0}\right)\frac{C_{u_2} - C_{u_1}}{u_0} = \overline{\psi}_d = const. \tag{10}$$

Since for the test compressor the entering air is of constant total pressure p_t, it follows that

$$\frac{dp_t}{dr} = 0 \tag{11}$$

Then as a consequence of the assumptions of repeating flow pattern and ψ = const., it follows that (11) must hold at each station.

Now since each side of Eq. (8) is merely a total pressure derivative, it follows from (11) that

$$\frac{d}{dr}(C_{a_2}^2) + \frac{1}{r^2}\frac{d}{dr}(r^2 C_{u_2}^2) = 0 \tag{12}$$

$$\frac{d}{dr}(C_{a_1}^2) + \frac{1}{r^2}\frac{d}{dr}(r^2 C_{u_1}^2) = 0 \tag{13}$$

There thus remain three equations and four unknowns, and one additional condition can be chosen. In other words, even with the design flow rate, design pressure rise and entrance condition specified, one additional condition can be imposed.

Examination of the equations will show that a condition which results in a considerable design simplification is

$$r C_{u_1} = \text{const.} \quad \text{or} \quad C_{u_1} = \frac{\alpha}{r} \tag{14}$$

the so-called "free vortex" velocity distribution. Then it follows from (13) that $C_{a_1} = \text{const.}$ and from (10) that

$$C_{u_2} = \frac{r_0 u_0}{2}\frac{\bar{\psi}_d}{r} + \frac{\alpha}{r} = \frac{\text{const.}}{r} \tag{15}$$

and from (12) $C_{a_2} = \text{const.}$ Finally it will be convenient to define

$$\phi = \frac{C_a}{u_0} \tag{16}$$

Hence $$\phi_1 = \phi_2 = \bar{\phi}_d = \text{const.} = \frac{Q_d}{u_0 \pi (r_0^2 - r_c^2)} \tag{17}$$

Thus if the design pressure and flow parameters $\bar{\psi}_d$ and $\bar{\phi}_d$ are specified and the compressor geometry is given, only choice of the constant (α) is required to fix the entire

vortex flow pattern at the design condition. Then the problem remains to choose a finite number of suitable blade sections that will produce the flow pattern.

It may be well to recall here the assumptions on which these design equations are based:

a. Perfect, incompressible fluid
b. Annular duct of constant cross-section
c. Equilibrium flow conditions
d. Complete axial symmetry
e. Repeating flow pattern in successive stages
f. Uniform stage pressure rise at the design condition
g. Uniform inlet total pressure
h. Free vortex distribution of circumferential velocity

At the design condition, a flow pattern results which has uniform axial velocity and uniform total pressure over each section. There are, of course, numerous other useful flow patterns, some of which are discussed in Ref. 5.

2:3.2 Test Compressor Blading

Because the design flow pattern described in the preceding section has frequently been used for gas turbine system compressors, and because of the simple velocity distribution at the design operating condition, a pattern of this class was selected for design of the first set of test compressor blading.

Choice of the constant, α , in Eq. (14) remains. For a modern high performance compressor this choice would be influenced by the possibility of compressibility effects and by permissible air turning angles in the actual compressor cascades. In order to obtain a design similar to that used in gas turbine system compressors, the value $\alpha = .145\, r_o u_o$ was adopted for the test compressor. Further discussion of this choice is given in Ref. 5.

The compressor hub to tip radius ratio had been fixed at $\frac{r_i}{r_o} = .60$. Again to simulate the design conditions of a typical modern compressor, the design flow and pressure rise coefficients were chosen as $\bar{\phi}_d = .450$ and $\bar{\psi}_d = .400$.

From these design parameters and the preceding equations, the design flow pattern becomes

$$\begin{aligned} C_{a_1} &= C_{a_2} = .450\, u_o \\ C_{u_1} &= .145\, u_o \left(\frac{r_o}{r}\right) \\ C_{u_2} &= .345\, u_o \left(\frac{r_o}{r}\right) \end{aligned} \tag{19}$$

It is clear that a knowledge of these velocity components as functions of the radius is sufficient to determine the air flow angles.

Thus the stator entrance angle at any radius is

$$\cot \gamma_2 = \frac{C_{u_2}}{C_a}$$

and the exit angle

$$\cot \gamma_1 = \frac{C_{u_1}}{C_a}$$

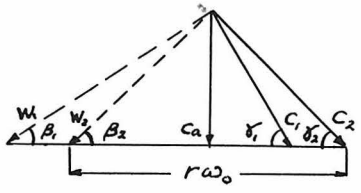

For the rotor (relative) entrance angle

$$\cot \beta_1 = \frac{r\omega_o - C_{u_1}}{C_a}$$

and the exit angle

$$\cot \beta_2 = \frac{r\omega_o - C_{u_2}}{C_a}$$

Complete design calculations for the test compressor flow pattern are given in Tables 3 and 4.

Actual compressor blade sections were next selected assuming that a cylindrical section taken through a given blade row has aerodynamic properties identical with those of an infinite cascade of untwisted airfoils of the same cross-section. Properties of two dimensional airfoil cascades can be predicted from theory, from experiment, or by empirical rules. Various methods are discussed in Ref. 5. For design of the test compressor blading, an essentially empirical method was used. Eight sections were computed for the rotor blades and five for the stator. It is clear from the preceding discussion that blading for each of the three stages is identical. Cascade notation is defined in Fig. 45.

The number of rotor and stator blades was selected as 30 and 32 respectively. Thus the gap or spacing, s, at each blade section was fixed. The airfoil chord length, c, was varied to give $1.45 \leq \frac{s}{c} \leq .87$ depending upon the required air turning angle. It was believed that imposing these limits would result in good cascade efficiency. Cascade test data (See Sec. 4:6) shows that, if the entering flow direction is tangent to the airfoil mean camber line at the leading edge, i.e., has zero incidence angle, losses are minimized. This condition was applied at each calculated section.

The air turning angle for a stator section is

$$\theta_S^* = \gamma_1 - \gamma_2$$

and for a rotor section

$$\theta_R^* = \beta_2 - \beta_1$$

Generally θ^* must be less than about 35° for good performance in the chosen $\frac{c}{s}$ range. (This requirement influences the choice of the constant α, as previously noted). If θ_c is the camber angle of the blade section, $\theta^* < \theta_c$, i.e., the flow is not turned by the full amount of camber. Thus θ_c must be exaggerated to secure the desired air turning. For cascades with circular arc camber lines, a relation between θ_c and θ^* has been established empirically by H. Constant (Ref. 6)

$$\theta^* = \theta_c (1 - .26\sqrt{s/c}) \qquad (20)$$

Thus by applying Eq. (20) and the zero incidence angle condition, an airfoil camber line can be derived at each blade section. These calculations for the vortex blading are summarized in Tables 3 and 4.

A thickness distribution similar to that of modern, low drag airfoils was adopted for the blade sections (See Fig. 46). A suitable maximum thickness was chosen and the resulting thickness function symmetrically disposed about the derived mean camber line. This process is outlined for one blade section in Table 1.

Thus, finally, the complete geometry of several blade cross-sections was derived and blade construction could proceed as outlined in Sec. 2:1.4. Entrance vanes were required to deflect the entering, axially flowing air into

the stator exit pattern of Eq. (19). These vanes form essentially a turbine cascade, since the static pressure must fall as circumferential velocity is added. Therefore, rather than employing Eq. 20 for blade section design, the thin airfoil cascade theory of Ref. 4 was used. Otherwise, the vane design method was identical to that used for rotor and stator blades.

Two rows of rear vanes were required to straighten the flow and minimize duct losses. All rear vanes were designed without twist and with 30° camber. In practice, the vanes were adjusted for what seem to be the best mean entrance conditions. All flow measurements were taken upstream of these vanes.

2:3.3 Real Fluid Effects

It was noted in the preceding sections that viscosity and compressibility effects were neglected in the design computation except indirectly in Eq. 20. Since all tests were conducted at low rotational speeds and flow Mach numbers, the fluid density was, indeed, practically constant, as shown in Sec. 2:5.4. However, as will be seen from the performance results of Sec. 2:5.1, fluid viscosity has considerable influence on the flow, even at the design condition.

Fluid friction on the blade surfaces and walls causes energy dissipation in the form of heat, which will be considered as an energy loss in interpreting the test results. Thus the compressor is not 100% efficient and the design

pressure rise is not reached at the design operating condition. Indeed, since losses were neglected in the design equations, the parameter $\bar{\psi}$ is properly considered as a design power input coefficient, rather than as a pressure rise coefficient.

Due to fluid friction on the bounding walls, axial velocities in the central portion of the annulus are somewhat higher than the mean axial velocity. Thus the true design condition comes at a lower value of $\bar{\phi}$ than that assumed in the calculations.

The above mentioned factors are commonly taken into account in the design of compressors for specific applications. It is hoped that the information of Sections IV and V may aid designers in this effort. However, since no exact operating characteristics were required of the test compressor, these viscosity effects could be ignored in designing the blades.

2:4 Reduction of Test Data

2:4.1 Overall Performance Data

a. Reference Velocity

The rotor tip velocity u_o is used as a velocity reference in computing dimensionless coefficients. It is computed from tachometer readings as

$$u_o = \frac{3\pi}{60} (R.P.M.) \quad ft./sec. \tag{21}$$

b. Mean Flow Rate

The mean flow rate coefficient is defined as

$$\bar{\phi} = \frac{Q}{\pi (r_o^2 - r_c^2) u_o} \tag{22}$$

or as

$$\bar{\phi} = \frac{\bar{C_a}}{u_o} = \frac{1}{u_o} \frac{\int_0^{2\pi} \int_{r_c}^{r_o} C_a \, r \, d\theta \, dr}{\pi (r_o^2 - r_c^2)} \tag{23}$$

where $\bar{C_a}$ = mean axial velocity

θ = circumferential angle

and the other symbols are as previously defined.

For routine data taking, Eq. 22 is utilized. As noted in Sec. 2:2.2, measurement of entrance duct wall pressure and air density are sufficient to determine the flow rate, Q, or mean axial velocity $\bar{C_a}$.

Equation 23 may also be used if internal survey data are taken between blade rows. The two methods of obtaining $\bar{\phi}$ have been compared by the data of Table 5. It is seen that the results check within a few percent even at low flow rates; thus either method is shown to be valid.

c. Power Input

From simultaneous torque and speed measurements (Sec. 2:2.2) the power input is

$$P = \omega_o T \quad - \text{ ft. lb./sec.}$$

where P = power input

ω_o = angular velocity - radians/sec.

T = dynamometer torque - ft. lb.

The power input coefficient is defined as

$$\bar{\psi} = \frac{P}{\frac{\rho}{2} u_o^2 Q} = \frac{\omega_o T}{\frac{\rho}{2} r_o^2 \omega_o^2 \pi (r_o^2 - r_i^2) r_o \omega_o \bar{\phi}}$$

$$= \frac{2T}{\rho \omega_o^2 \pi r_o^3 (r_o^2 - r_i^2) \bar{\phi}} \qquad (24)$$

Thus torque, speed, air density, and flow coefficient are needed to determine the power input coefficient. Compressor windage and bearing loss are small and no correction is made for these quantities.

d. Pressure Rise

The local total pressure coefficient at any point in the compressor is

$$\psi' = \frac{p_t - p_a}{\frac{\rho}{2} u_o^2} \qquad (25)$$

where p_t = measured total (stagnation) pressure

p_a = atmospheric pressure

and the other symbols are as previously defined. Then the mean total pressure rise coefficient is

$$\bar{\psi}' = \frac{\int_0^{2\pi} \int_{r_i}^{r_o} \psi' \phi \, r \, d\theta \, dr}{\bar{\phi} \pi (r_o^2 - r_i^2)} \qquad (26)$$

The local total pressure is measured by one of the probes described in Sec. 2:2.3. The flow direction is determined at every point. Using the direction data, a pitot tube survey is made to determine the local velocity, c. Then at every

point,

$$\phi = \left(\frac{c}{u_o}\right) \sin\gamma = \left(\frac{c_a}{u_o}\right) \tag{27}$$

Surveys are performed over a typical sector (11.25 degrees circumferential angle) between blade rows as previously noted. The integration of Eq. 26 is performed either graphically or numerically using generally 7 radial and 15 circumferential intervals.

Friction losses in the entrance duct are known from evaluation of Eq. 26 upstream of the entrance vanes at various flow rates. The correction $\Delta\bar{\psi}'$ is shown in Fig. 47. This correction is applied in efficiency calculations.

It should be noted that since Eq. 26 is usually evaluated immediately downstream of a stator blade row, blade wake mixing losses are not deducted.

e. Efficiency

The compressor efficiency is defined as

$$\eta = \frac{\text{Airstream energy increase}}{\text{Work input}}$$

hence

$$\eta = \frac{\bar{\psi}' + \Delta\bar{\psi}'}{\bar{\psi}} \tag{28}$$

where the symbols are as defined by Eq. 24, 26 and Fig. 45.

According to the previous definitions, it is seen that the efficiency defined by Eq. 28 is weighted with respect to local flow rate and corrected for entrance duct loss, but is not corrected for compressibility, mixing loss, or

compressor bearing and windage losses.

2:4.2 Special Data

a. Total Pressure

The local total pressure is measured with either a Kiel probe, pitot tube, or special total pressure probe. Manometer or electrical pressure pickup readings are reduced using appropriate calibration data. The total pressure coefficient ψ' is computed from Eq. 25.

b. Direction

Flow direction is measured with the claw probe or three hole direction probe. Measured angles are corrected to the calibrated reference direction.

c. Velocity

The pitot tube is aligned in the flow direction using previously determined angle data. Total pressure and static pressure may be read separately, or their difference, the velocity pressure, may be read. In either event, two readings are sufficient to determine all three quantities. Manometer or gage calibration data are applied to yield pressure in suitable units. The local static pressure coefficient is

$$\psi_s = \frac{p - p_a}{\frac{\rho}{2} u_o^2} \tag{29}$$

and with the previously defined total head coefficient, ψ',

$$\frac{c}{u_o} = \sqrt{\psi' - \psi_s} \tag{30}$$

The axial velocity coefficient is then

$$\phi = \frac{C_a}{U_o} = \left(\frac{C}{U_o}\right) \sin \gamma \qquad (31)$$

and a circumferential velocity coefficient is defined as

$$\lambda = \frac{C_u}{U_o} = \left(\frac{C}{U_o}\right) \cos \gamma \qquad (32)$$

Where the flow direction angle, γ (with respect to the plane of rotation), is known from previous direction measurements.

d. Static Pressure

In some cases local static pressure in the compressor air stream could be measured with the pitot tube. However, for measurements between blade rows and near bounding walls there was insufficient space to allow the use of even the smallest available pitot tube. However it was possible to measure the outer boundary static pressure between any two blade rows (Sec. 2:2.3). There was sufficient clearance to allow radial surveys of total pressure and flow direction. It is then possible to deduce the radial static pressure distribution.

Assume that the flow is in radial equilibrium and that the static pressure is a function of radius only in the region considered. (These assumptions are justified by test data in Sec. 5:3.1). Then from radial equilibrium

$$\frac{dp}{dr} = \rho \frac{C_u^2}{r} \qquad (33)$$

the total pressure is

$$p_t = p + \frac{\rho}{2} C^2$$

and the circumferential velocity is

$$C_u = c \cos\gamma$$

Substituting these expressions in (33)

$$\frac{dp}{dr} + \frac{2\cos^2\gamma}{r} p = \frac{2\cos^2\gamma}{r} p_t \qquad (34)$$

Since p_t and γ are assumed to be functions of radius only, Eq. 34 is a first order linear equation which is easily integrated.

The result is

$$p = \frac{p_o\, e^{\int_{r_c}^{r_o} 2\cos^2\gamma \frac{dr}{r}} - \int_r^{r_o} 2\cos^2\gamma\, p_t\, e^{\int_{r_c}^{r} 2\cos^2\gamma \frac{dr}{r}} \frac{dr}{r}}{e^{\int_{r_c}^{r} 2\cos^2\gamma \frac{dr}{r}}}$$

where $p = p(r)$ = the static pressure at any radius

p_o = the static pressure at the outer radius r_o and the other symbols are as previously defined. Or using the dimensionless coefficients defined by Eq. 25 and 29:

$$\psi_s = \frac{\psi_{so}\, e^{\int_{r_c}^{r_o} 2\cos^2\gamma \frac{dr}{r}} - 2\int_r^{r_o} \psi' \cos^2\gamma\, e^{\int_{r_c}^{r} 2\cos^2\gamma \frac{dr}{r}} \frac{dr}{r}}{e^{\int_{r_c}^{r} 2\cos^2\gamma \frac{dr}{r}}} \qquad (35)$$

Using this equation, local static pressure and velocity have been determined for a number of locations (See Sec. 5:3.1).

2:5 Overall Performance

As previously pointed out (Sec. 2:1.1), the test installation was designed and constructed in a flexible arrangement to make possible the pursuit of various research programs. Neither of the two initial programs had, as a primary objective, the study of overall compressor performance. Consequently, since the data required for such a study are laborious to take and to reduce, only a few performance tests were made. These tests have, however, proved useful for checking the design theory and for correlation with internal loss measurements.

2:5.1 Single Stage Performance

Input power and pressure rise measurements were obtained at several flow rates for a single stage (including entrance vanes) of vortex blading operated at 750 R. P. M. These data are presented in the form $\bar{\psi}$ and $\bar{\psi}'$ vs. $\bar{\phi}$ in Fig. 48. Symbols used here and data reduction methods are as stated in Sec. 2:4.1 and Appendix I.

It will be recalled that for this blade set, the design parameters were $\bar{\psi}_d = .40$, $\bar{\phi}_d = .45$. Figure 48 shows that $\bar{\psi} = \bar{\psi}_d = .40$ for $\bar{\phi} = .43$, i.e. approximately $4\frac{1}{2}\%$ below the design flow rate. This result is as expected according to the discussion of Sec. 2:3.3. Thus a $4\frac{1}{2}\%$ effective area reduction occurred as a result of boundary layer growth. With this adjustment, the design condition is well predicted.

It is seen that the maximum efficiency, $\eta = 89\%$ is obtained at $\bar{\phi} = .42$. The Reynolds number, R_e, for $\bar{\phi} = .42$ at 750 R. P. M. is 67,000 where

$$R_e = \frac{u_o c \bar{\phi}}{\nu} \qquad (36)$$

and c = mean blade chord

ν = kinematic viscosity

This value is rather low, and the low efficiency is probably accounted for by relative larger losses at low R_e. The data of Ref. 7 are illuminating in this respect. From a series of efficiency measurements on a set of test compressors, the curve of maximum obtainable efficiency which is reproduced in Fig. 49 was deduced. This curve represents an envelope of measured efficiencey data. In order to check the effect of Reynolds number on maximum efficiency of the test compressor, one set of tests was performed at 1500 R. P. M. or $R_e = 134,000$. The efficiency obtained was 93%. Inspection of Fig. 49 reveals that an equivalent increase is predicted. Furthermore, the data of Sec. 2:5.3 give additional evidence of this Reynolds number effect.

Returning to the performance data of Fig. 48, several common phenomena of axial flow compressor performance can be seen. At higher than design flow rate the pressure rise falls rapidly. This performance result is predictable from the perfect fluid theory of compressor performance (Ref. 4). A performance curve calculated for the compressor, using this theory, is reproduced in Fig. 48. Due probably

to poor flow incidence angles relative to the blading, the compressor efficiency also falls in this range. However the range from slightly below design flow rate to maximum flow rate is the stable and generally most useful operating range for an axial flow compressor.

For flow rates lower than design, the power input coefficient, $\bar{\psi}$, rises at first linearally as predicted by perfect fluid theory, and then somewhat less rapidly. (Note that $\bar{\psi}$ represents work input per unit mass of fluid). The pressure rise coefficient, $\bar{\psi}'$, rises to somewhat above its design value but then decreases rapidly. Efficiency decreases steadily from the design value. The rapid decrease of pressure rise and efficiency, which are often referred to as "compressor stalling", are largely due to poor cascade efficiency and limited air turning capacity at large positive air incidence angles (See Sec. 4:6).

The operating range below the design condition is perhaps less useful than that above. It is clear that in the range where $\frac{d\bar{\psi}'}{d\bar{\phi}}$ becomes positive, unstable operation may be encountered in some applications of such a compressor. Furthermore, the efficiency falls more rapidly in this range than above the design condition. Below $\bar{\phi} = .370$, audible flow pulsations were observed in the test compressor. Near $\bar{\phi} = .330$, the flow became quite unstable and measurements were difficult to obtain. It is believed that this extreme instability was associated with intermittent flow separation over portions of the compressor blades.

2:5.2 Three Stage Performance

Power and pressure rise were also measured for three complete stages of vortex blading operated at 750 R. P. M. In order to reduce the time required for data taking, pressure rise behind the third stator row was measured at only the center radius. The correct weighing was then obtained by using the data of Fig. 47, which were deduced from previous single stage measurements. Other flow measurements (Sec. 5:3.1) confirm the belief that this procedure correctly indicates flow trends and gives $\bar{\psi}'$ accurate within perhaps ± 1%. The test results are presented in Fig. 50.

Again it is seen that the design point was correctly predicted when the effective area reduction of approximately 4½% is considered. The efficiency seems to be somewhat lower than for a single stage. Perhaps more significant is that the "stall" condition comes at considerably higher $\bar{\phi}$. This fact can be detected in Fig. 50 by rapid decrease in efficiency and rounding off of the $\bar{\psi}'$ curve. The effect has been frequently observed and is one factor which seriously limits the usefulness of single stage data for predicting multi-stage axial flow compressor performance. Probably both viscous phenomena and mutual interference between blade rows are operative, but no complete explanation for this effect is known to the writer.

It is seen from Figs. 48 and 50, that data at higher flow rates were obtained for three stage operation. This is because a greater pressure rise was available to overcome

duct losses.

2:5.3 Speed-Power Data

Throughout the previous discussion, the dimensionless work and flow coefficients $\bar{\psi}$ and $\bar{\phi}$ have been used to describe compressor performance. Since most of the tests reported herein were conducted at a single compressor rotative speed (750 R. P. M.), these coefficients may be regarded merely as a convenience. However in other investigations (Ref. 1 and 8), both coefficients have been used to correlate data obtained at widely varying rotative speeds. It has been shown that for different speeds, if $\bar{\phi}$ is maintained constant, a constant $\bar{\psi}$ will result, providing compressibility effects are small.

In order to confirm this result for the test compressor, three stage tests were conducted at the design throttle setting for speeds between 500 and 1500 R. P. M. Power input and flow rate were measured, as was the pressure rise at one point behind the third rotor row. Due to change of the throttle resistance coefficient, $\bar{\phi}$ varied slightly with speed, hence $\bar{\psi}$ was corrected to $\bar{\phi} = .450 = \text{const.}$ by the relation

$$\bar{\psi} = \bar{\psi}_{meas.} - \left(\frac{d\bar{\psi}}{d\bar{\phi}}\right)(\bar{\phi} - .450)$$

From Fig. 50, it is seen that $\frac{d\bar{\psi}}{d\bar{\phi}} = -4.8$ near the design condition. The measured efficiency was weighted to give $\eta = 86\%$ at 750 R. P. M. since this value had been previously obtained by more careful tests (Fig. 50). The results are

shown in Fig. 51, from which it is clear that $\bar{\psi}$ is constant (within the limits of error) for $\bar{\phi}$ constant. The effect of Reynolds number (or speed) on pressure rise and efficiency is also shown. It will be recalled from Sec. 2:5.1, that on the basis of previous investigations, an increase of peak efficiency of approximately 4% was expected between 750 and 1500 R. P. M. Fig. 51 shows an efficiency increase of 3% for this range which justifies the expectation.

2:5.4 Density Change

It has been assumed throughout the report that changes in air density in passing through thecompressor are negligible. This section is intended to verify the assumption.

The lowest static pressure in the compressor occurs at the inner radius behind the entrance vanes; the highest at the outer radius behind the third stator row. For $\bar{\phi} = .45$, the measured pressures at these locations were $\psi_s = -.295$ and $\psi_s = +.750$, respectively.

Then for $u_o = 118$ ft./sec. (750 R. P. M.), barometric height (corrected) of 29.25 in. Hg, and $\rho = .00225$ slug/ft.^{3} (which are typical operating conditions),

$$\frac{p_s}{p_a} = 1.006 \doteq \frac{\rho}{\rho_a}$$ at the highest pressure location

$$\frac{p_s}{p_a} = .998 \doteq \frac{\rho}{\rho_a}$$ at the lowest pressure location

Hence the maximum density change is of the order of 1/2%, which is within the accuracy of the reduced flow data.

For multi-stage operation at higher rotative speeds, density changes should be considered.

III Real Fluid Phenomena

3:1 Introduction

In considering the overall performance of the test compressor (See Sec. 2:5), it became clear that, while performance in a region near the design point could be approximately predicted by assuming the working fluid to be inviscid, several phenomena could be explained only as viscous fluid effects. Among these phenomena were the apparent "area contraction" of the flow stream, losses at the design condition, the rapid increase of losses at flow rates both greater and less than design, and "stalling"of the compressor. Since relatively little information on these phenomena is at present available, investigations were undertaken to provide some of the fundamental information required for explaining and predicting them.

Consideration of the energy distribution over annular cross-sections of the test compressor will be revealing. Since the air stream is essentially isothermal, the total pressure, $p_t = p + \frac{\rho}{2} c^2$ will provide an adequate index of specific energy in the fluid. In Fig. 52 are shown contour plots of total pressure distribution over typical sections downstream of rotor and stator blade rows. The contours represent lines of constant specific energy in terms of the local pressure coefficient $\psi' = \frac{\Delta p_t}{\frac{\rho}{2} u_o^2}$ It is seen that regions of large energy defect exist near the outer and inner boundaries (the wall boundary regions), and also directly downstream of a stator blade trailing edge

(the blade wake). Behind a rotor blade, only the wall boundary regions are detected, because there total head measured in a stationary reference system represents an average value. If measurements are made by an instrument moving with the rotor, a wake pattern is detected. Measurements in the rotating system have been made by Weske (Ref. 9).

Summation of energy defect (weighted with respect to the axial velocity component) behind the first stator row indicates that about 61% is associated with the bounding walls, and 39% with the blade wakes. It should be noted, that losses in the entrance duct are included in the bounding wall defect, whereas the wake defect is attributable only to the stator row.

In this section additional data and analysis for wall boundary regions and blade wakes are presented. In addition, some methods of predicting these effects by techniques of fluid mechanics are illustrated. Throughout, the boundary layer concept is adopted, hence it may be well to review briefly the development of this concept.

3:2 The Boundary Layer Concept

A review of some aspects of the boundary layer* theory,

---

* The abbreviation b. l. will be used for "boundary layer" where convenient.

as developed by Prandtl and his successors, is given here for the reader's convenience. Among the comprehensive treatises on this subject are those of Ref. 10 and Ref. 11. Reference 12 provides a modern b. l. bibliography.

A convenient model in hydrodynamics is the incompressible, "perfect" fluid, i.e., a fluid which is homogeneous, inviscid, and of constant density. For such a fluid, the equations of hydrodynamics take an especially simple form, and flows computed from them correspond remarkably well to reality for moderate velocities. If, as in many practical problems, the flow in question had originally uniform velocity, the simple Bernoulli equation relates pressure and velocity at any point in the perfect fluid.

However, for most flows, it has been observed that the fluid velocity near an immersed solid boundary is equal to the velocity of the bounding solid, i.e., that there is "no slip" between a fluid and an immersed body. Furthermore, if the Reynolds number is sufficiently high, it is found that the influence of the solid is appreciable only in a thin layer adjacent to its boundary, the so-called "boundary layer". Outside the b. l. region, flow conditions are well represented by the perfect fluid, while within the region a more complicated model is required.

If flows are observed which have uniform, constant velocity outside a wall, b. l., and zero velocity at the boundary, two common types of velocity distribution are encountered; these are illustrated in Fig. 53. The first is

the "laminar" layer characterized by a moderate velocity gradient at the boundary and by steady, nonfluctuating flow parallel to the boundary. The second is the "turbulent" layer which has a larger velocity gradient at the boundary, and, as is experimentally verified, only a mean parallel flow, superposed on which are smaller fluctuating velocities in all directions. Even in the second case, a thin laminar layer must exist very close to the wall - the "laminar sub-layer".

There are several useful definitions of boundary layer extent or thickness. Perhaps the simplest, but one which is distinctly arbitrary, is to define the thickness, δ, as that distance normal to the fixed boundary at which the velocity becomes a certain fraction of its free stream value. A common definition is $y = \delta$ for $v = .995V$. There are two definitions which become useful in analytical treatment, the "displacement thickness",

$$\delta^* = \int_0^\infty \left(1 - \frac{v}{V}\right) dy \tag{37}$$

and the "momentum thickness",

$$\vartheta = \int_0^\infty \frac{v}{V}\left(1 - \frac{v}{V}\right) dy \tag{38}$$

It will be observed that each of these has a definite value for a profile of the type shown in Fig. 53. The ratio $H = \frac{\delta^*}{\vartheta}$ has been found useful (Ref. 13) as a shape parameter for b. l. profiles.

If a uniform flow impinges on an immersed, streamlined body, such as an airfoil section, it will be observed that a laminar b. l. will form from the leading edge and become thicker downstream. This laminar layer may exist over the entire upper and lower surfaces or there may occur on either or both surfaces a transition to a turbulent layer. The turbulent layer then becomes thicker (at an increased rate) toward the trailing edge. Prediction of the occurrence and location of transition is essential to calculation of the ultimate b. l. thickness. At present, however, such prediction is based largely on empirical rules which are reliable only under restricted circumstances. Further discussion of this problem for the case of compressor blading will be found in Sec. 4:3.2.

In the presence of rising pressure in the direction of flow, the phenomenon of flow "separation" may occur. This condition is illustrated in Fig. 54. An adverse pressure gradient exists on the upper surface of an airfoil, and at large angles of attack separation occurs. Separation results in major distortion of the flow field with a consequent alteration of the airfoil pressure distribution which produces "form" or pressure drag. This is the flow phenomenon associated with airfoil "stalling".

Surface shear or skin friction for a laminar boundary layer is given by the Newtonian friction law, $\tau_o = \mu \left(\frac{\partial v}{\partial y}\right)_o$ where τ_o is wall shear stress, μ the fluid viscosity, and $\left(\frac{\partial v}{\partial y}\right)_o$ the velocity gradient at the wall. For a turbulent

layer, the wall shear is known only empirically in forms equivalent to $\tau_0 = f(R_\delta, V, H)$ where $R_\delta = \frac{\delta V}{\nu}$, the b. l. Reynolds' number. If a surface integration of wall shear and normal pressure is performed over an airfoil, its lift and drag forces are obtained. However, the lift can be closely approximated by other means, and the profile drag can be obtained more easily from a knowledge of the b. l. shapes and thickness at the trailing edge.

It is clear that in an axial compressor, airfoil boundary layers represent regions of velocity defect and therefore of pressure energy defect or loss. The magnitude of these losses can be estimated (Sec. 4:4) from b. l. calculation, except possibly when separation occurs. It will be seen that both energy defect and drag may be used as criteria of profile loss. In the compressor problem, an additional "loss" must be considered, namely that due to the mixing process which occurs in the blade wakes. The b. l. fluid in passing off the blade surfaces forms the defective regions shown in Fig. 52. But if the same measurements were taken several chord lengths further downstream, only the wall boundary regions would remain distinct, the blade wakes having become mixed with the main flow. In the mixing process, momentum is conserved, but pressure energy is dissipated by fluid friction.

Two principal procedures are available for analytical treatment of b. l. growth in a non-uniform pressure field. The first involves direct solution of the hydrodynamic

equations for a viscous fluid. The second begins with the "Kármán integral relation" which can be derived either by use of the hydrodynamic equations, or by direct momentum balance. This second approach has found wider engineering application and will be utilized in this report. It will be seen that the application of this method depends upon assumption of a suitable wall shear relation and the nature of the boundary layer profile.

3:3 Compressor Boundary Regions

In Fig. 55 there is shown an axial velocity profile measured behind the test compressor first rotor, near the outer compressor wall. A summary of its principal characteristics is given below in terms of b. l. notation.

$$\delta_{.995} \doteq .750''$$

$$\delta^* = .102''$$

$$\vartheta = .074''$$

$$H = \frac{\delta^*}{\vartheta} = 1.38$$

In addition, a plot of the relation $\frac{v}{V} = \left(\frac{y}{\delta}\right)^{\frac{1}{n}}$ is shown for comparison. The values of n and δ were selected to give ϑ and δ^* the same values as those measured. Fluid which forms this boundary region has passed successively through the (fixed) entrance vane cascade and the rotor cascade, where work has been done on the fluid. The flow pattern is quite complex, indeed more complex than is indicated by Fig. 55,

since the tangential velocity component must also vanish at the wall. However, additional experimental data (Sec. 5:1) seem to justify analytical treatment of the complex boundary region in the manner of b. l. theory. For turbulent boundary layers on airfoils the shape parameter H has values of the order of 1.5 (Ref. 13) and the velocity distribution is well represented by a 1/5 power law. The fact that parameters of similar magnitude are measured for a compressor wall "boundary layer" is taken as additional evidence for treatment in this manner. In any event, only the ultimate results obtained by regarding the wall regions as boundary layers can justify the method. Hence, for the present, boundary layer methods will be applied to the outer and inner boundary regions without further comment.

The compressor blade wake profiles of Fig. 56 illustrate phenomena which are significant in the determination of cascade loss. These profiles were obtained from circumferential surveys in a plane approximately .42 chord lengths downstream of the blade section trailing edge. The first shows a narrow, well defined wake region which results from moderate, attached profile boundary layers. The total pressure loss is therefore low. The second profile shows a broad, poorly defined wake region which probably results from flow separation on one surface. The total pressure loss is comparatively high in this case.

IV Cascade Boundary Layers and Loss

In the preceding section, a general survey of real fluid phenomena in an axial flow compressor was given. In this section, the subject of compressor cascade boundary layer growth and loss is treated in some detail. Boundary layer growth is calculated for a particular cascade. This calculation necessarily involves a knowledge of the velocity distribution on airfoil surfaces, which knowledge is obtained by calculation and by measurement. A method is developed for computing total pressure loss from wake measurements in the test compressor. Comparison is made between the various methods of loss determination.

4:1 Principal Definitions.

A number of quantities are defined which provide criteria by which the performance of a cascade of airfoils may be judged. These quantities include turning angle, loss coefficient, lift coefficient, and drag coefficient. Utilization of these quantities will be restricted to a two-dimensional incompressible flow. Fig. 45 illustrates these and additional definitions.

The Turning Angle, θ^*, is defined as the angle between the flow direction at distances sufficiently upstream and downstream of the cascade, so that uniform flow conditions exist. It is clear that experimental measurements, which must often be obtained near the cascade, require special interpretation before the turning angle can be

satisfactorily computed.

The Loss Coefficient, $\Omega = \frac{\bar{\omega}}{\frac{1}{2}\rho V_1^2}$, where $\bar{\omega}$ is the mean loss of total pressure in passing through the cascade, and V_1 is the velocity far upstream of the cascade. The loss, $\bar{\omega}$, may be computed between any two planes upstream and downstream of the cascade but will depend in magnitude on location of the downstream station. Thus if the downstream station is taken at the trailing edge plane, $\bar{\omega}$ will include only total pressure loss which is due to dissipation in the airfoil boundary layers, while if a station further downstream is chosen, a certain proportion of wake mixing loss will be included. Strictly then, only two downstream locations are useful, the trailing edge plane, for which $\bar{\omega} = \bar{\omega}_p$, the profile loss; and a plane far downstream where mixing is substantially complete, for which $\bar{\omega} = \bar{\omega}_p + \bar{\omega}_\mu$

The Lift Coefficient. It can be shown (Ref. 20) that for potential flow through a cascade, the resulting force on an individual airfoil section is normal to the vector mean of the (uniform) velocities at plus and minus infinity, Fig. 45. Then for a flow with losses, the lift, L, is taken as that component of the total force which is normal to the vector mean velocity, $\bar{V}_m$. The lift coefficient becomes

$$C_L = \frac{L}{\frac{\rho}{2} |\bar{V}_m|^2 c}$$

Again, the strict specification of C_L depends upon determination of uniform flows remote from the cascade.

The Drag Coefficient. According to the preceding discussion, the profile drag, D_p, is that component of the total airfoil force which is parallel to the mean velocity. Then

$$C_{Dp} = \frac{D_p}{\frac{\rho}{2} |V_m|^2 c}$$

For strictly two-dimensional, incompressible flow through a cascade, where the uniform upstream and downstream conditions are presumed to be known, relationships between turning angle and lift, and loss and drag have been derived (Ref. 6).

The pressure rise is

$$\Delta p = p_2 - p_1 = \frac{\rho}{2} (v_1^2 - v_2^2) - \bar{\omega}$$

The axial component of blade force is

$$F_a' = s \Delta p$$

The tangential force component is given by the momentum flux equation

$$F_u' = s \rho v_a (v_{u_1} - v_{u_2})$$

The mean velocity is

$$v_m = v_a \csc \gamma_m$$

where v_a is assumed to be constant and

$$\cot \gamma_m = \frac{\cot \gamma_1 + \cot \gamma_2}{2}$$

Then the following relations result

$$C_L = 2 \left(\frac{s}{c}\right) (\cot \gamma_1 - \cot \gamma_2) \sin \gamma_m - C_D \cot \gamma_m \qquad (39)$$

$$C_D = \left(\frac{s}{c}\right)\frac{\overline{\omega}}{\frac{\rho_2}{\rho_1}V_1^2}\,\frac{\sin^3\gamma_m}{\sin^2\gamma_1} = \left(\frac{s}{c}\right)\Omega\,\frac{\sin^3\gamma_m}{\sin^2\gamma_1} \qquad (40)$$

It should be noted that the C_D given by Eq. (40) is not strictly as previously defined. This is because $\overline{\omega}$ necessarily includes mixing losses (since Station 2 must be far downstream), whereas no additional drag force results from the mixing process.

4:2 Velocity Distribution in an Airfoil Cascade

For boundary layer and loss calculations, it is necessary to know the velocity distribution about a cascade airfoil in the region just outside the surface boundary layer. This result may be approximated by perfect fluid calculations or by measurement of surface static pressures, from which velocities can be calculated. Both methods have been utilized and are outlined in the following sections.

4:2.1 Calculation of Cascade Velocity Distribution

It is assumed that a three-dimensional compressor cascade can be represented by an infinite, two-dimensional cascade of airfoils whose profiles are identical with the compressor blade section at a particular radius. This means, in particular, that the effects of radial velocities on the cascade performance are neglected. Surface velocities in the two-dimensional cascade can be calculated by the

methods of potential theory if the working fluid is assumed, for this purpose only, to be inviscid. Actually, the velocities calculated in this manner will be slightly smaller than those which would be measured in the cascade, since the surface boundary layers effectively contract the flow area.

The subject of potential flow through an infinite cascade of airfoils has been extensively treated in the literature, for example in References 14 to 19. For the general direct problem, (given the cascade geometry and incident flow, to find the velocity distribution) two methods have been successful. The first seeks to find a set of conformal transformations leading from the cascade to a perfect circle. For a cascade of airfoils of arbitrary shape, finding such transformations involves successive approximations (Refs. 15 and 18). Suitable transformations have been found, the cascade plane velocities are obtained by the usual methods. The second approach obtains first the potential flow about a single airfoil of the cascade and then, by a series of rather more physical approximations, corrects this flow for the effect of the other cascade airfoils. A method of the second type, that of Ref. 14 is used in this report.

The center section (r = 14.40 in.) of the free vortex stator cascade is considered. The equivalent two-dimensional cascade is shown in Fig. 57. In order to simplify the calculations, the actual airfoil profiles are replaced by

thin circular arc airfoils geometrically identical to the profile mean camber line. For a particular section lift coefficient, the thin airfoil velocities will be somewhat smaller than those corresponding to the thick profile, but the velocity distribution and velocity gradients should be nearly the same. Calculations for one flow condition are carried out in Appendix IV. The following results are obtained (See Fig. 45 for notation):

Entrance angle, $\gamma_1 = 46^\circ 0'$

Exit angle, $\gamma_2 = 68^\circ 26'$

Turning angle, $\theta^* = \gamma_2 - \gamma_1 = 22^\circ 26'$

Section lift coefficient, $C_L = 1.026$

The calculated surface velocity distribution is shown in Fig. 61. It is seen that for this flow condition, a sharp velocity peak occurs near the convex surface leading edge. The velocity decreases rapidly toward the trailing edge, hence the pressure gradient is such as to cause rapid boundary layer growth.

Since the potential theory of airfoil cascades was not of primary interest and because the measurement of blade surface pressures proved feasible, no further discussion of velocity calculation is given.

4:2.2 Experimental Determination of Cascade Velocity Distribution

a. Surface Pressure Measurement

To provide information for obtaining velocity distribution,

surface pressure measurements were made at sixteen points along the center section (r = 14.40 in.) of a free vortex stator blade. The construction of the blade and the methods of measurement and data reduction are discussed in Sec. 2:2.3 and 2:4.2 respectively.

With the pressure blade located in the first stator row, the compressor was operated at a flow condition ($\bar{\phi}$) which yielded the desired air incidence angle at the test section. The results of a particular test are shown in Fig. 62. The static pressure coefficient, ψ_s , is plotted along the airfoil chord line for each surface. The enclosed area thus represents the net force acting normal to the chord line. If the same pressure data are plotted along an axis normal to the chord line, the resulting net area represents the force parallel to the chord line. Thus the net force due to normal surface pressures can be obtained:

$$f_y = \oint \psi_s \, d\left(\frac{x}{c}\right)$$
$$f_x = \oint \psi_s \, d\left(\frac{y}{c}\right) \qquad (41)$$

where f_y = section force coefficient normal to the chord line

f_x = section force coefficient parallel to the chord line and the coordinates are oriented as shown in Fig. 62.

It will be recalled that cascade lift and drag forces were defined (Sec. 4:1) as being perpendicular and parallel, respectively, to the mean velocity vector. Then it is easily shown that

$$C_L = \left(\frac{u_o}{V_m}\right)^2 \left[f_y \cos(\gamma - \gamma_m) - f_x \sin(\gamma - \gamma_m) \right]$$

$$C_D = \left(\frac{u_o}{V_m}\right)^2 \left[f_y \cos(\gamma - \gamma_m) + f_x \sin(\gamma - \gamma_m) \right]$$

But if the axial component of the mean velocity is assumed to remain constant (no radial flow),

$$V_m = \frac{V_a}{\sin \gamma_m}$$

thus,

$$\frac{u_o}{V_m} = \frac{u_o}{V_a} \sin \gamma_m = \frac{\sin \gamma_m}{\phi_m}$$

where ϕ_m = average axial velocity coefficient at the radius in question.

Hence

$$C_L = \frac{\sin^2 \gamma_m}{\phi_m^2} \left[f_y \cos(\gamma - \gamma_m) - f_x \sin(\gamma - \gamma_m) \right]$$

$$C_D = \frac{\sin^2 \gamma_m}{\phi_m^2} \left[f_y \cos(\gamma - \gamma_m) + f_x \sin(\gamma - \gamma_m) \right] \qquad (42)$$

with the force coefficients as defined by Eq. 41.

By means of velocity and direction surveys before and behind the first stator blade row at the mid-section, the entrance (γ_1) and exit (γ_2) flow angles and ϕ_m were determined. Since the flow angles were measured near to blade rows, they probably represent the true mean flow directions

not closer than $\pm$ 1.0°. The mean velocity direction was calculated from the relation (See Fig. 45)

$$\cot \gamma_m = \frac{\cot \gamma_1 + \cot \gamma_2}{2} \tag{43}$$

The flow angles and ϕ_m are plotted in Fig. 63 against $\bar{\phi}$, which is used as the flow condition parameter.

Lift and drag coefficients for ten sets of static pressure data are computed in Table 6 using Eq. 42 and the data of Fig. 63. The computed drag coefficients are used as a check on the data reduction method. Since in every case the value of C_D is of the proper order of magnitude, it is concluded that the mean flow direction has been correctly deduced.

It is clear that by use of the previously derived relation between C_L and entering and exit flow angles (Eq. 39), the angle data of Fig. 63 can be used directly to compute a lift coefficient, C_L', quite independently of the surface pressure data. The relation used is

$$C_L' = 2\left(\frac{s}{c}\right)(\cot \gamma_1 - \cot \gamma_2) \sin \gamma_m \tag{44}$$

the effect of C_D being neglected in this approximation. These calculations are also given in Table 6. The agreement between C_L and C_L' is quite good except possibly at very high $\bar{\phi}$ where radial velocities may become significant. Thus two checks on the validity of both the pressure blade data and the flow data of Fig. 63 indicate that sufficient accuracy is obtained for the present purposes.

b. Surface Velocity Calculation

The velocity just outside the profile boundary layer is calculated by assuming that the static pressure gradient normal to the surface is zero. This is a common assumption in boundary layer calculations and is valid if the boundary layer thickness is small compared to the surface curvature, which is the case over the surface regions considered.

Since flow outside the boundary layer is iso-energetic, the Bernoulli equation is applied along a streamline

$$p + \frac{\rho}{2} V^2 = p_{t_1}$$

where p = the surface static pressure

V = velocity just outside the b. l.

p_{t_1} = the (uniform) total pressure of the entering flow

Or writing the equation in dimensionless form

$$\frac{V}{u_o} = \sqrt{\psi_1' - \psi_s} \tag{45}$$

If the average axial velocity component is assumed constant

$$\frac{V}{V_m} = \frac{V}{u_o}\,\frac{u_o}{V_m} = \frac{V}{u_o}\,\frac{\sin\gamma_m}{\phi_m}$$

Hence

$$\frac{V}{V_m} = \frac{\sin\gamma_m}{\phi_m}\sqrt{\psi_1' - \psi_s} \tag{46}$$

The total pressure coefficient, ψ_1', was measured just upstream of the test section and is given by Fig. 63 along with ϕ_m and γ_m.

Using Eq. 46 and the data of Fig. 63, surface velocities were calculated from the ten sets of pressure measurements.

Values of V/V_s were taken from "faired" curves. The velocity data are shown plotted along the section chord line in Figs. 64 to 73. Since with only sixteen measurement points it was not always possible to locate exactly the points of zero velocity (stagnation point) or maximum velocity, each was assumed to occur at the leading edge ($\frac{x}{c} = o$) in doubtful cases. Because no measurement could be made over the rear 10% of the profile, the trailing edge velocity was obtained by extrapolation.

The velocity data are of some interest in themselves, apart from this usefulness for boundary layer calculations, since they represent a rather complete history of a compressor cascade's performance under actual operating conditions. With flow incidence angles, i^* , ranging from $+ 4.6^\circ$ to $- 11.9^\circ$, section lift coefficients, C_L between 1.08 and .28 were obtained. It is seen that at a large negative incidence angle (Fig. 73), moderate velocity peaks form on both surfaces. At a positive incidence angle (Fig. 65) no peak occurs on the concave surface, but on the upper surface an extreme peak forms near the leading edge which causes large adverse pressure gradients over the entire surface. This condition induces rapid boundary layer growth, as is shown in the next section.

4:3 Cascade Boundary Layer Growth

4:3.1 Basic Equations

The calculations of this section are carried out using essentially the standard aerodynamic methods which have been developed largely for single airfoil profile drag computations and which were briefly outlined in Sec. 3:2. Therefore, no attempt is made to justify completely the methods, rather the equations are given and reference is made to original sources.

The equations used are based on the Kármán integral relation which is derived in Ref. 11 and 12 and is reproduced here for the case of steady, incompressible, two-dimensional flow along an essentially straight boundary with the pressure gradient $\frac{\partial p}{\partial y}=0$ in the b. l.:

$$\frac{\partial}{\partial x}\int_0^\delta u^2\,dy - V\frac{\partial}{\partial x}\int_0^\delta u\,dy = V\frac{\partial V}{\partial x}\delta - \frac{\tau_0}{\rho}$$

or in a form which is independent of the upper limit

$$\frac{\partial V}{\partial x}\int_0^\infty (V-u)\,dy + \frac{\partial}{\partial x}\int_0^\infty (V-u)\,u\,dy = \frac{\tau_0}{\rho} \qquad (47)$$

Using the previously (Sec. 3:2) defined displacement and momentum thicknesses

$$\frac{d\vartheta}{dx} + \frac{dV}{dx}\frac{\vartheta}{V}\left(2+\frac{\delta^*}{\vartheta}\right) = \frac{\tau_0}{\rho V^2} \qquad (48)$$

It will be observed that in obtaining this form of the momentum equation, no specific assumptions have been made as to the nature of the b. l. velocity profile or the friction law, hence it may be applied to both laminar and turbulent b. l.'s.

For treatment of laminar boundary layers the method of Ref. 23 is used. A flat plate, "Blasius" type velocity

profile is assumed as shown in Fig. 53 and the condition $\tau_o = \mu \left(\frac{\partial v}{\partial y}\right)_o$ is used. Then the following relation results*:

$$\frac{(R_\vartheta)_1^2}{R_c} = .442 \left(\frac{V_m}{V_1}\right)^{7.17} \int_0^{\left(\frac{x}{c}\right)_1} \left(\frac{V}{V_m}\right)^{8.17} d\left(\frac{x}{c}\right) \tag{49}$$

where $R_\vartheta = \frac{\vartheta V}{\nu}$

$R_c = \frac{c V_m}{\nu}$

and $( )_1$ represents a quantity at the upper limit of integration. The assumption of profile similarity is valid only where the pressure gradient is favorable, i.e. where the surface velocity is either constant or increasing in the flow direction, and where laminar separation does not occur. A more general treatment of the laminar case is available in Refs. 24 and 25.

Turbulent boundary layers are treated by the method of Ref. 26 or Ref. 27. It is assumed that the boundary layer shape parameter, $H = \frac{\delta^*}{\vartheta}$, has a constant value along the surface. An empirical friction law of the form

$$\frac{\tau_o}{\rho V^2} = \frac{k}{R_\vartheta^n} \tag{50}$$

is used where

$$R_\vartheta = \frac{\vartheta V}{\nu}$$

---

* Zero b. l. thickness is assumed at the l. e. This assumption is not strictly justified by exact solution of the b. l. equations (Ref. 24 and 25), but more elaborate calculations seemed unjustifiable.

and V = velocity just outside the b. l. at any point.

Then Eq. 48 becomes integrable and the result is

$$\left(\frac{\theta_2}{c}\right) = \frac{1}{\left(\frac{V_2}{V_m}\right)^{H+2}}\left\{\frac{(n+1)\,k}{R_c^{\,n}}\int_{\left(\frac{x}{c}\right)_1}^{\left(\frac{x}{c}\right)_2}\left(\frac{V}{V_m}\right)^{(H+1)(n+1)+1} d\left(\frac{x}{c}\right) + \left(\frac{\theta_1}{c}\right)^{n+1}\left(\frac{V_1}{V_m}\right)^{(H+2)(n+1)}\right\}^{\frac{1}{n+1}} \qquad (51)$$

where V_m = the mean of entering and exit cascade velocities

$R_c = \frac{V_m c}{\nu}$

k, n are defined by Eq. 50

and the subscripts $(\,)_1$, and $(\,)_2$ represent quantities at the lower and upper limits of integration respectively.

Since the assumption H = const. is basic to the derivation of Eq. 51, it is clear that this equation can be accurately used only in regions where the boundary layer velocity profile does not change radically. This means that turbulent flow separation cannot be predicted and that if separation occurs, the boundary layer region will become considerably thicker than indicated by Eq. 51. There seems to be no reason why the more general method of turbulent boundary layer calculation (Ref. 13), which indicates incipient flow separation, could not be used, however the computational labor involved is excessive for the present purposes.

4:3.2 The Stator Cascade

The velocity data of Figs. 64 to 73 were used to

calculate convex and concave surface boundary layer growth for the vortex stator blade center section ($r = 14.40$ in.) for compressor operation at 750 R. P. M. Eq. 49 was used for either surface to compute the laminar b. l. momentum thickness from $\left(\frac{x}{c}\right) = 0$, the leading edge to $\left(\frac{x}{c}\right) = \left(\frac{x}{c}\right)_1$, the assumed location of transition to a turbulent layer. Eq. 51 was used to compute the turbulent layer growth from $\left(\frac{x}{c}\right)_1$ to $\left(\frac{x}{c}\right)_2$, the trailing edge. The shape parameter was taken as H = 1.5 = const. (Ref. 27). A friction law of the form of Eq. 50 was used with $k = .0180$ and $n = .30$. These values were selected to best approximate experimental data obtained from pipe and flat plate turbulent b. l. measurements (Ref. 27) at very low Reynolds number, R_ϑ. Actually this procedure is not strictly justifiable, since turbulent b. l. are usually not observed with values of R_ϑ as low as were encountered in these calculations. This point is discussed further in this section.

With these assumptions, Eq. 49 becomes

$$\left(\frac{\vartheta_1}{c}\right)^2 = \frac{.422}{R_c}\left(\frac{V_m}{V_1}\right)^{9.17} \int_0^{\left(\frac{x}{c}\right)_1} \left(\frac{V}{V_m}\right)^{8.17} d\left(\frac{x}{c}\right) \qquad (52)$$

and Eq. 51 becomes

$$\left(\frac{\vartheta_2}{c}\right) = \left(\frac{V_m}{V_1}\right)^{3.5} \left\{ \frac{.0234}{R_c^{.30}} \int_{\left(\frac{x}{c}\right)_1}^{1.0} \left(\frac{V}{V_m}\right)^{4.25} d\left(\frac{x}{c}\right) + \left(\frac{\vartheta_1}{c}\right)^{1.3} \left(\frac{V_1}{V_m}\right)^{4.55} \right\}^{.769} \qquad (53)$$

Even for the standard airfoil problem, prediction of the occurrence and location of laminar to turbulent boundary layer transition is difficult and is, at present, based largely on empirical rules. According to Ref. 11, in a neutral pressure gradient, transition occurs for $(R_{\theta})_t \geq 250$, depending on the turbulence level. This reference applies to airfoils in flight and wind tunnel models, where the approach velocity is steady with perhaps some turbulent fluctuations. It has also been established (Ref. 28) that a laminar b. l. is quite unstable in the presence of strong adverse pressure gradients (static pressure increasing in the flow direction) and that either laminar separation or transition is induced under such conditions.

The preceding considerations apply under essentially steady state conditions. A compressor stator row, however, operates in a quasi-steady flow, since relatively large periodic velocity fluctuations are produced by upstream rotor blade wakes. Similar, but perhaps less severe, conditions prevail on those portions of an airplane wing which operate in propeller wakes. Flight tests reported in Ref. 29 indicate that transition in the wake region occurs considerably nearer the l. e. on both surfaces than on other portions of a wing. It seems likely that a similar phenomenon may occur in compressor cascades.

Based on the foregoing considerations, transition was assumed to occur in the stator cascade either at the location of a velocity maximum or where a strong favorable pressure

gradient terminated. The selected transition points are indicated on the velocity curves. Boundary layer calculations for the 10 sets of experimental velocity data and the one calculated condition are shown in Table 7.

In addition, Fig. 74 illustrates the progressive b. l. growth over both surfaces for the calculated velocity distribution. It is seen that at this lift condition, the predicted growth is very rapid on the convex surface and that the final momentum thickness is considerably greater than on the concave surface. Thus for $C_L = 1.026$, $i^* = +.2^\circ$ and $\vartheta^* = 22.5^\circ$

$$\left.\begin{aligned} \vartheta_u &= .047 \text{ in.} \\ \delta_u^* &= .070 \text{ in} \end{aligned}\right\} \quad \text{upper (convex) surface}$$

$$\left.\begin{aligned} \vartheta_l &= .008 \text{ in.} \\ \delta_l^* &= .012 \text{ in.} \end{aligned}\right\} \quad \text{lower (concave) surface}$$

In the next section, computation of cascade loss from such results is considered.

4:4 Cascade Loss

4:4.1 Calculation Procedure

A system is next developed for deducing the profile total pressure defect from calculated trailing edge b. l. results. The method depends upon selection of an appropriate velocity profile in the b. l. and can, therefore, be applied only to cases where the flow is attached at the trailing edge.

The following information is available from previous calculations: the t. e. momentum thicknesses for convex (upper) and concave (lower) airfoils surfaces, ϑ_u and ϑ_ℓ , the corresponding b. l. shape parameters H_u and H_ℓ ; and the potential flow velocity at the t. e., V_o , which is the same for both surfaces. The situation is illustrated by Fig. 75.

Then the mean total head defect per cascade airfoil is

$$\omega_p = \frac{\int_0^s (p_t)_o (V_a)_o \, dy - \int_0^s p_t V_a \, dy}{\int_0^s V_a \, dy} \qquad (54)$$

where $(\,)_o$ indicates the potential flow conditions and the line integrations are taken along the path shown in Fig. 75.

But $(p_t)_o = p_o + \frac{\rho}{2} V_o^2$ = constant even though p_o and V_o are not individually constant. Also from the continuity equation

$$\int_0^s V_a \, dy = \int_0^s (V_a)_o \, dy = s \overline{V_a}$$

hence

$$\int_0^s (p_t)_o \rho (V_a)_o \, dy = \int_0^s (p_t)_o \rho V_a \, dy$$

and

$$\overline{\omega}_p = \frac{\int_0^s (p_{to} - p_t) V_a \, dy}{s \overline{V_a}}$$

but $p_{to} = p_t$ except in the b. l. regions , therefore,

$$\overline{\omega}_p \int_0^{\delta_u} (p_{to} - p_t) V_a \, dy + \int_0^{\delta_\ell} (p_{to} - p_t) V_a \, dy \Big/ s \overline{V_a}$$

Now $V_a\,dy = v\,dz$ where z is measured normal to either surface and $p_t = p_0 + \frac{\rho}{2} v^2$, since $\frac{\partial p}{\partial z} = 0$ in the b. l., as previously assumed.

Then

$$\overline{\omega_p} = \frac{\int_0^{\delta_u} \frac{\rho}{2} (V_0^2 - v^2)\, v\, dz + \int_0^{\delta_\ell} \frac{\rho}{2} (V_0^2 - v^2)\, v\, dz}{s\, \overline{V_a}}$$

or

$$\frac{\overline{\omega_p}}{\frac{\rho}{2} V_0^2} = \frac{\int_0^{\delta_u} \left(1 - \frac{v^2}{V_0^2}\right) \frac{v}{V_0}\, dz + \int_0^{\delta_\ell} \left(1 - \frac{v^2}{V_0^2}\right) \frac{v}{V_0}\, dz}{s \left(\frac{\overline{V_a}}{V_0}\right)}$$

it is seen that these definite integrals are similar in form to those defining momentum and displacement thickness. To permit their evaluation in terms of ϑ and H it is assumed that the b. l. velocity profile at the t. e. is given by

$$\frac{v}{V_0} = \left(\frac{z}{\delta}\right)^{\frac{1}{n}}$$

Then

$$\delta^* = \int_0^{\delta} \left(1 - \frac{v}{V_0}\right) dz = \frac{\delta}{n+1}$$

$$\vartheta = \int_0^{\delta} \left(1 - \frac{v}{V_0}\right) \frac{v}{V_0}\, dz = \frac{n\,\delta}{(n+1)(n+2)}$$

and $$H = \frac{\delta^*}{\vartheta} = \frac{n+2}{n}$$

from which $$n = \frac{2}{H-1}$$

and $$\delta = \frac{(n+1)(n+2)}{n}\,\vartheta$$

Also

$$\int_0^{\delta} \left(1 - \frac{v^2}{V_0^2}\right) \frac{v}{V_0}\, dz = \frac{2n\delta}{(n+1)(n+3)}$$

Hence

$$\frac{\bar{\omega}_p}{\frac{\rho}{2} V_0^2} = \frac{2\left[\frac{n_u+2}{n_u+3}\vartheta_u + \frac{n_\ell+2}{n_\ell+3}\vartheta_\ell\right]}{\delta\left(\frac{\bar{V}_a}{V_0}\right)}$$

$$= \frac{2\left[\frac{2H_u}{3H_u-1}\left(\frac{\vartheta_u}{\delta}\right) + \frac{2H_\ell}{3H_\ell-1}\left(\frac{\vartheta_\ell}{\delta}\right)\right]}{\left(\frac{\bar{V}_a}{V_0}\right)}$$

or finally

$$\Omega_p = \frac{\bar{\omega}_p}{\frac{\rho}{2} V_1^2} = 2\left(\frac{V_0}{V_1}\right)^2 \left(\frac{V_0}{\bar{V}_a}\right)\left[\frac{2H_u}{3H_u-1}\left(\frac{\vartheta_u}{\delta}\right) + \frac{2H_\ell}{3H_\ell-1}\left(\frac{\vartheta_\ell}{\delta}\right)\right] \quad (55)$$

The accuracy of the above expression will depend upon how well the actual b. l. profile can be represented by a power function $\frac{v}{V_0} = \left(\frac{z}{\delta}\right)^{1/n}$. For turbulent equilibrium flow in pipes, at moderate Reynolds numbers, such an expression with n = 7 has been found valid (Ref. 28). From the data of Ref. 13 actual turbulent b. l. profiles should be well represented for $1.29 \leq H \leq 1.90$. It might be noted that a change of H from 1.4 to 1.5 causes approximately a 3% change in the factor $\frac{2H}{3H-1}$.

For the calculation of Ω_p, Eq. 55 shows that V_0^3 enters as a multiplicative factor. It will be recalled (Sec. 4:2.2) that this velocity is actually obtained by extrapolation of the surface velocity data and thus may not be known with great accuracy. However, reference

to Eq. 53, which was used to obtain values of ϑ, shows that for this quantity, $V_0^{-3.5} \equiv V_2^{-3.5}$ is a multiplicative factor. Hence only $V_0^{-.5}$ influences the loss calculation, and moderate accuracy in the determination of V_0 is acceptable.

4:4.2 The Stator Cascade

Equation 55 was used to compute total pressure loss from the boundary layer data of Table 7.

If it is again assumed that the mean axial velocity $\overline{V_a}$ is constant through the cascade,

$$\overline{V_a} = V_m \sin \gamma_m = V_1 \sin \gamma_1 = \text{const.}$$

and

$$\left(\frac{V_0}{V_1}\right)^2 \left(\frac{V_0}{V_a}\right) = \left(\frac{V_0}{V_m}\right)^3 \left(\frac{V_m}{V_1}\right)^2 \frac{V_m}{V_a} = \left(\frac{V_0}{V_m}\right)^3 \frac{\sin^2 \gamma_1}{\sin^3 \gamma_m}$$

With the numerical values

$$H_u = H_\ell = 1.5$$

and

$$\frac{s}{c} = 1.088$$

Eq. 55 becomes

$$\Omega_p = 1.578 \left(\frac{V_0}{V_m}\right)^3 \frac{\sin^2 \gamma_1}{\sin^3 \gamma_m} \left(\frac{\vartheta_u}{c} + \frac{\vartheta_\ell}{c}\right) \qquad (56)$$

The values of $\frac{V_0}{V_m} \equiv \frac{V_2}{V_m}$ are obtained from the velocity data, Figs. 64 to 73. The angles γ_1 and γ_2 are given in Fig. 63.

The loss calculations are summarized in Table 8. In Fig. 76 values of Ω_p are plotted against i^*, the flow

incidence angle, where

$$i^* = 46.2^\circ - \delta, \qquad (57)$$

for the stator cascade. Discussion of the results is reserved for Sec. 4:6.

4:5 Measured Cascade Loss

Wake profile measurements were made at the stator mid-section $(r = 14.40)$ downstream of the first and third stator rows. From the measurements, the total pressure loss coefficient is computed.

4:5.1 Data Reduction

In principle, compressor cascade total pressure loss can be determined under given conditions by making total pressure velocity and direction surveys before and behind the chosen blade section and computing the weighted average total pressure defect. However, with available instrumentation, simultaneous measurement of all six quantities is not possible and the errors of measurement and flow reproducibility, which arise from separate tests, make reasonably accurate results difficult to obtain by this method. This difficulty is particularly true of profile loss, since the mean loss may be small (perhaps 3% of the velocity head). A method which depends, for its accuracy, largely on a single downstream survey is developed to circumvent the difficulty.

Total pressure, velocity and flow direction are measured

along a given circumference downstream of the cascade. The dimensionless axial velocity and total pressure parameters, ϕ and ψ' are plotted as shown in Fig. 77. From the faired ψ' curve, the maximum value, ψ^* is obtained. It is assumed that ψ^*, which is characteristic of the frictionless flow region, is equal to ψ' entering the cascade. Then

$$\Delta\bar{\psi}' = \frac{\overline{\Delta P_t}}{\frac{\rho}{2} u_0^2} = \psi^* - \bar{\psi}_2'$$

or

$$\Delta\bar{\psi}' = \frac{\int_0^{\theta_3} \phi_2 (\psi^* - \psi_2') \, d\theta}{\int_0^{\theta_3} \phi_2 \, d\theta} \qquad (\theta_3 = \text{cascade pitch angle}) \tag{58}$$

hence

$$\Omega = \Delta\bar{\psi}' \left(\frac{u_0}{V_1}\right)^2 = \frac{\Delta\bar{\psi}' \sin^2\gamma_1}{\phi_m^2} \tag{59}$$

assuming ϕ_m = const. through the cascade.

4:5.2 The Stator Cascade

Equations 58 and 59 were used to compute the loss coefficient, Ω, for the wake survey data shown in Figs. 77 to 90. A study of these data reveals many of the loss and boundary layer phenomena discussed in previous sections. The wakes are seen to be relatively narrow and well defined for $-3.6 \leq i^* \leq -6.5$ $(13.1 \leq \theta^* \; 15.4)$ and considerably broader for more extreme conditions. The profiles of Figs. 78 and 83 indicate that flow separation has probably taken place at these large turning angles.

The chosen value of ψ^* is indicated for each profile. As a check on the selection of ψ^* values, total pressure measurements were made upstream of the third stator row ($r = 14.40$ in.) . The comparison is shown in Fig. 91. It is seen that the ψ^* values agree quite well with the curve except possibly in the extreme stall condition.

Measurements for the third stator row indicated that values of γ_1 and ϕ_m required in Eq. 59 could, with sufficient accuracy, be taken from the first stator data of Fig. 63. This is possible because the flow pattern, particularly at the center radius, repeats almost perfectly through the three stages (See Sec. 5:3.1).

The loss coefficient calculations are summarized in Table 9 and Ω is plotted against i^* in Fig. 76.

In addition, stator blade wake measurements which were taken at several different radii have been reduced in the same manner and are shown in Fig. 92. These results reveal a considerable increase in cascade loss near the bounding walls.

These results are discussed in the next sections.

4:6 Discussion of Results

Cascade loss coefficients which were obtained from boundary layer calculations and from actual measurement in the test compressor are compared in Fig. 76. There is also shown, for an essentially identical cascade, loss data which was obtained in a two-dimensional cascade

tunnel.* Figure 76 shows turning angle data from the same sources.

It is seen that the turning angle data agree well, within perhaps two degrees over the unstalled range. This agreement is consistent with that obtained from other tests (Refs. 4 and 5). In general, measured or calculated two-dimensional cascade data can be applied to compressor blading providing the flow is essentially two-dimensional in the sense that the mean axial velocity at a given radius remains constant through the blade row.

From Fig. 76 it is seen that values of Ω obtained from boundary layer calculations are in good agreement with the cascade tunnel data. Actually the calculated values are somewhat higher than those measured; this may be due to the effort which was made in the b. l. calculations to simulate actual compressor conditions rather than those which prevail in a cascade tunnel. Early transition was assumed in the calculations, whereas laminar b. l.'s may have existed over large portions of the cascade tunnel blading. The cascade tunnel test data indicate that low losses are obtained for $-8^\circ \leq i^* \leq 7^\circ$ or a total range of 15 degrees. Losses increase abruptly outside of this range, particularly for positive incidence angles. Examination of Fig. 76 shows that the limiting air turning angle is approached at

---

* The data were taken from a classified document. They are believed to be quite accurate.

$i^* = 7°$ and that cascade "stalling" may be said to occur.

The calculated loss curve exhibits the same general characteristics. Low loss is predicted over a wide range of incidence angles, but due to the assumption of constant b. l. profile (H = const., see Sec. 4:3) separation or rapidly increasing loss is not indicated. If this restriction were removed, better agreement with cascade tunnel tests would certainly result. A method of compressor cascade loss calculation based on diffuser test data, which has been proposed by Howell (Ref. 6), appears to avoid the restriction and to indicate the stalling limit.

Loss measurements obtained from the test compressor (Fig. 76) are considerably higher than the results of either of the other methods. The minimum compressor measurement is $\Omega = .035$ as compared with $\Omega = .013$ from cascade tunnel tests and $\Omega = .019$ from b. l. calculations. Equally significant is the fact that the range of incidence angles for low loss is reduced to six degrees $(-8° \leq i^* - 2°)$ as compared with 15 degrees from cascade tunnel tests. There are a number of factors which may affect these comparisons.

a. Survey Plane Location

From Figs. 77 to 90 it will be observed that most of total pressure surveys were taken along a circumference approximately .05 inch or .02 chord length downstream of the section trailing edge. Other data denoted, in Fig. 76, by $\bar{\Delta}$, were taken farther downstream.

According to the discussion of Sec. 3:2, total

pressure loss is increased by the wake mixing process. Using the mixing loss calculation method of Ref. 30, a 15% increase might be expected. However, no effect of survey plane location is observed in the data.

b. Airfoil Contour Deviation

Departures of an airfoil section from design are not considered in the loss calculation. However manufacturing errors, roughness, and surface deposits may be present in the actual blading. As previously noted (Sec. 2:1.4), profile errors do not exceed $\pm$ .005", or approximately $\pm$ 2% of the maximum thickness. Random errors of this magnitude probably do not affect the profile loss appreciably. Blade surface roughness does not exceed 40 R. M. S. microinches which should be well within the laminar sub-layer, hence the surfaces may be considered smooth.*

Dirt deposits of considerable thickness occur after prolonged operation in the laboratory atmosphere. After several hundred hours, deposits up to 1/16 inch in thickness were formed near rotor and stator leading edges. Obviously such contour deviations cause local velocity dis-

---

* For a 1/7 root turbulent profile, the laminar sub-layer thickness is approximately $y/\delta = 68/R_\delta^{7/8}$ (Ref. 28). From Sec. 4:2.1, at the upper surface transition point, $\vartheta = 2.2 \times 10^{-4}$ in., $R_\vartheta = 12.9$. For a turbulent profile with H = 1.4, $\delta = 10\vartheta$, then $\delta = 2.2 \times 10^{-3}$ in., $R_\delta = 129$ or $y = (2.2 \times 10^{-3} \times 68)/(129)^{7/8} = 2.1 \times 10^{-3}$ in. Thus a sub-layer of at least .001 inch is to be expected over the airfoil surface.

turbances which might well change boundary layer conditions, hence the measurements were taken with carefully cleaned blades.

c. Wake Measurements

In Ref. 2 some experimental data are presented on the accuracy of total pressure measurement in a stream with large transverse total pressure gradient. It is concluded that depending upon the probe diameter in comparison to the gradient, an error results which gives wake widths smaller and jet widths greater than actually exist. The effect should be small with the .020 in. diameter probe which was used, however the true losses are, if anything, slightly larger than the measured values.

d. Reynolds Number

In Reference 6, it is shown that the permissible air turning angle for a compressor cascade, i.e., the maximum turning angle for moderate loss, is affected by the flow Reynolds number, R, where $R = \frac{cV}{\nu}$. Below an effective Reynolds number, $R_{eff.}$, of about 100,000, the maximum turning angle is severely restricted; above approximately 300,000 optimum turning capacity is attained. It is stated, that due to turbulent fluctuations, the effective Reynolds number in a cascade testing tunnel is increased by a factor as high as 3.0. Presumably the factor is as great or greater for a compressor. The value of $R_{eff.}$ for the two dimensional test data of Fig. 76 was estimated to be 350,000; the value for the test compressor was between 200,000 and 300,000. Thus both sets of data were near the upper critical limit, and

the Reynolds number effect is probably small.

e. Radial Velocities

Radial velocities in the compressor may arise from two causes. As has been shown in Ref. 5, the "perfect fluid" flow pattern through a compressor may involve radial velocities of considerable magnitude. The test compressor blading, which has a "free vortex" flow pattern, induces no radial velocities at the design condition ($\bar{\phi} = .45$), but for other conditions the flow pattern is three-dimensional. It follows from the continuity condition that the average axial velocity through each cascade section is not constant, i.e., that the stream tubes change in radius. Thus additional diffusion or contraction occurs which is not present in two-dimensional tests and which may considerably affect losses as well as turning angles. However, it will be seen from Sec. 5:3.1, that for the test compressor mid-radius the mean axial velocity is nearly constant, even off the design condition, and therefore that appreciable "perfect fluid" radial velocities are not present at the test section.

It is clear that, whereas the main flow may be without radial velocities, the fluid in the blade boundary layers cannot, in general, be in equilibrium in the radial static pressure field. Thus, so-called "secondary" radial flow must exist near the surfaces of both rotor and stator blades. Measurements made by Weske (Ref. 9) have shown directly the presence of such flows on rotor blades. Precisely what

effect "secondary" flow may have on cascade boundary layer development and loss is not clear, but the phenomenon mayaccount for part of the difference between two-dimensional and three-dimensional cascade loss.

f. Non-steady Flow

It has been previously pointed out that, due to wakes from upstream, moving blade rows, the flow entering a compressor cascade is not steady but in reality has a strong periodic component. For example, consider the stator cascade operating at the design condition, Fig. 93. The design incidence angle of the entering flow is $i^* = 0^\circ$. However, if the relative exit velocity from the preceding rotor is reduced to 75% of its "perfect fluid" value, the stator incidence angle becomes $+ 13.2^\circ$. It is clear from the data of Figs. 77 to 90 that a velocity defect at least this great is to be expected in the stator blade entrance plane and thus that the entering velocity fluctuates both in magnitude and direction. At a test compressor speed of 750 R. P. M., the fluctuations occur 375 times per second. It should be noted that for <u>either</u> rotor or stator compressor cascades, wakes from the immediately upstream blade row contain such a velocity component which has a larger, positive incidence angle (or angle of attack).

These considerations suggest several possible explanations for large compressor cascade losses. Periodic fluctuations in the absolute magnitude of entering

velocity and total head may result in effectively higher surface friction and thus induce generally higher cascade loss and promote earlier transition and flow separation. The fluctuations of entering velocity direction, which are always toward higher incidence angles, may promote the cascade "stalling" at apparently low incidence angles which was observed for the stator cascade, Fig. 76. Clearly there is insufficient evidence to permit any definite conclusions, but it is believed that these phenomena do deserve further investigation.

Finally it should be noted that some confirmation of the measurements obtained from the test compressor is available in the literature. Weske (Ref. 9) has also found that the range of permissible cascade incidence angles for low loss is much lower, approximately six degrees, in a compressor, than is expected from cascade tunnel tests.

British compressor designers (Ref. 1) have proposed a rule, based apparently on overall compressor performance data, which corrects cascade drag coefficients, obtained from two-dimensional tunnel tests, for use in an actual compressor; namely

$$C_D = C_{Dp} + .018\, C_L^2 + .020 \left(\frac{s}{h}\right)$$

where C_D = drag coefficient in the compressor

C_{Dp} = drag coefficient from tunnel tests

C_L = section lift coefficient

s = cascade spacing

h = blade height

Applying this rule to the stator cascade, (r = 14.40 in.) at the design condition with $C_{D_p} = .025$, $C_L = .70$

$$C_D = .025 + .009 + .007 = .041$$

Thus the cascade tunnel drag coefficient is increased by 64% in the actual compressor. Since both C_D and Ω are proportional to the blade boundary layer thickness, Ω would presumably be increased in proportion. A somewhat greater increase is indicated by Fig. 76. It is stated that this empirical rule has been found useful for predicting overall compressor efficiency.

4:7 Conclusions

Based on the foregoing results and discussion, the following conclusions are proposed.

a. The minimum total pressure loss and the approximate incidence angle range for low loss can be predicted, by standard aerodynamic calculations, for a two-dimensional compressor cascade which is operated under steady, uniform flow conditions. Either measured or calculated surface velocities may be used in such calculations.

b. Total pressure loss in an actual compressor cascade may be considerably greater (the order of twice as great) than is either measured or calculated for the equivalent two-dimensional cascade operating under steady, uniform flow conditions. Furthermore, the apparent flow

incidence angle range for low losses is considerably less.

c. It is suggested that two phenomena which may be responsible for these differences require further investigation. These phenomena are radial, "secondary" flow near compressor blade surfaces and periodic fluctuation in entrance velocity direction and magnitude.

V. The Wall Boundary Region

5:1 Introduction

The nature of the flow near the outer and inner bounding walls of the compressor annulus was previously illustrated in Sec. III. It is the purpose of the following section to give additional experimental and theoretical information on these regions.

Axial and circumferential velocity components measured downstream of a rotor blade row are shown in Fig. 94. It will be recalled that the axial velocity component must vanish at both boundaries and that the tangential component vanishes at the outer (fixed) boundary but approaches the hub peripheral velocity at the inner (rotating boundary). Thus while the flow direction in the central region of the annulus is determined only by the blading design, near either wall, pronounced deviations from design direction occur. From Fig. 94 it is seen that the flow through at least 1.5 inches or 20% of the blade height shows appreciable deviations from the perfect fluid pattern which are attributable largely to viscosity effects.

It is convenient to specify the boundary region extent before or behind a particular blade row by the boundary layer displacement and momentum thicknesses which are computed from the axial velocity distribution. Analytically these thickness parameters are

$$\delta^* = \int_0^{\delta} \left(1 - \frac{\phi}{\phi^*}\right) dy \tag{60}$$

$$\vartheta = \int_0^{\delta} \left(1 - \frac{\phi}{\phi^*}\right) \frac{\phi}{\phi^*} dy \tag{61}$$

where

ϕ = local axial velocity coefficient

ϕ^* = local axial velocity coefficient at the boundary layer limit, δ

y = distance normal to the boundary

Since the boundary layer thickness is small compared to the annulus radii, the effect of curvature is neglected in these definitions.

The experimentally determined radial velocity distributions, to which Eqs. 60 and 61 will be applied, are secured along radii which lie outside the wake area of the nearest upstream blade. In Fig. 95 axial velocity contours measured downstream of a stator blade row are shown. The blade wake areas are easily seen as regions of velocity depression. It is clear that the extent of the boundary layer is quite uniform outside the blade wake area and thus that the circumferential location of a survey radius will not greatly influence the calculated boundary layer parameters.

It should be noted that the boundary layer displacement thickness, δ^*, indicates the contribution of the

boundary in question to the effective "flow area contraction" which was detected from the overall compressor performance data (Sec. 2:5.1).

5:2 Analytical Treatment

In Appendix V, some preliminary attempts are made at analytical treatment of wall boundary layer growth in turbomachines and cascade tunnels. Essentially the conventional boundary layer approach is adopted, the immersed blade rows being replaced by equivalent body forces which act on the fluid. Momentum relations are set up, and the illustrative example of an untwisted stationary cascade intersecting a plane wall is treated. Such a problem might occur in tests of airfoil cascades in a two-dimensional tunnel. From the solution obtained it appears that accelerated wall b. l. growth should occur for flow through a compressor cascade. However, to date no test data have been obtained which are suitable for checking this result.

The analytical treatment of this problem has proved difficult, although some encouraging results have been obtained. It is believed that further effort along these lines may prove useful as a guide to experimental treatment.

5:3 Wall Boundary Layer Growth in the Compressor

5:3.1 Measurements and Data Reduction

Radial surveys of flow direction and total pressure were performed in the three-stage test compressor before and behind each blade row, eight locations in all.

The claw type direction probe was used for direction measurement, since it could be operated quite close to either boundary. The special .020 in. diameter probes were used for total pressure measurements near the walls, and check points were obtained elsewhere using the Kiel type probe. All probes were positioned by the instrument carriage in its radial survey mounting (Sec. 2:2.3 and Fig. 38). Circumferential location of the survey radii corresponded to the positions of the radial survey ports which are shown in Fig. 40. In all cases the radial survey paths were located outside stator blade wake areas.

Using measured total pressure and flow direction data and outer wall static pressures, radial static pressure distribution was determined for each of the eight locations by the method of Sec. 2:4.2. Using these static pressures, axial and circumferential velocity components could be calculated from the survey data. In general, the character of the velocity component and direction data was similar to that shown by Fig. 94.

A complete set of radial surveys was obtained at each of three flow conditions, corresponding to approximately $\bar{\phi}$ = .448, .392, .485, i.e., near the design condition,

below and above. The measured axial velocity distributions are shown by Figs. 96 to 101 in the form of ϕ vs. radius. A check on the validity of the data reduction process was obtained by computing the weighted mean axial velocity coefficient for each profile which could be compared with the corresponding $\bar{\phi}$ from overall measurements. These comparisons are shown on the figures. Actually, perfect agreement is not to be expected, since the radial survey measurements do not include the flow deficiency which is due to cascade wakes. However, it is seen that in all but four cases, the two determinations agree within three percent, which is interpreted as validation of the measurements and of the static pressure computation method of Sec. 2:4.2. Discrepancies in the four cases probably resulted from inaccurate outer wall static pressure determination. In any event, a small error in the general velocity level does not appreciably affect the calculated boundary layer thicknesses.

For each of the measured axial velocity profiles, the boundary layer thicknesses, δ^* and ϑ, were determined from Eqs. 60 and 61 at each boundary. A reasonable choice of the "free stream velocity" coefficient ϕ^* was possible for most of the measured profiles, but in several cases the generally large velocity gradient over the blade height made such a choice impossible. The boundary layer shape parameter, $H = \frac{\delta^*}{\vartheta}$, was also computed. Boundary layer characteristics of the velocity profiles are summarized

in Figs. 102 and 103.

5:3.2 Discussion of Results

Examination of the axial velocity profiles shown in Figs. 96 to 101 reveals that, in general, a flow pattern is closely repeated throughout the three stages. Near the design condition, at $\bar{\phi} = .448$, the axial velocity is essentially uniform over the central portion of the annulus at all locations. At higher and lower flow rates, the axial velocity becomes higher near the inner or the outer boundary respectively. These results are predicted by perfect fluid theory (Ref. 4). From the axial velocity magnitude in the center of the annulus, a general tendency for boundary layer growth in the flow direction is detectible, but the tendency is by no means extreme. Indeed, an approximately equivalent growth rate would be expected in the annular duct if no blading were present.

The outer wall boundary profiles are generally similar to that of a flat plate turbulent, boundary layer. As previously noted, the inner wall profiles show certain deviations which are due to the rotor hub peripheral velocity. At the lowest flow rate, $\bar{\phi} = .392$, a pronounced, progressive decrease of axial velocity near the inner boundary is observed. This condition is probably caused by severe cascade losses in the hub sections of the rotor blades. It is seen from Table 3 that these sections were designed for very high turning angles and thus might be expected to

"stall" earliest. Furthermore, in the next section it will be shown that the wall b. l. causes very poor cascade entrance conditions near the inner boundary which also promote early "stalling".

Characteristics of the wall boundary layers are shown in Figs. 102 and 103. The conclusion reached from examination of the annulus velocity profiles is confirmed by the displacement thickness data. There is a slight tendency for δ^* to increase through successive stages, but a large share of the increase seems to occur through the entrance vanes. Within the compressor blade rows the thickness seems to vary more or less at random. From the δ^* values of Fig. 103, a systematic increase of inner wall thickness in passing through the rotor rows appears, which is perhaps also chargeable to high cascade loss in the rotor root sections.

The b. l. shape parameter, H, fluctuates between 1.2 and 1.7 with an average value of perhaps 1.3. The value for the common 1/7 root turbulent profile is 1.29. This parameter is helpful for indicating a general constancy of b. l. shape, but its significance should not be overrated for the rather complex, three-dimensional profiles in question.

From the wall and cascade boundary layer data, an estimate of the effective "area contraction" can now be made. Consider the operating condition nearest to design, $\bar{\phi} = .448$. From Figs. 102 and 103, the average wall dis-

placement thickness are:

$$\delta^*_{av.} = .082 \text{ in. - outer wall}$$

$$\delta^*_{av.} = .094 \text{ in. - inner wall}$$

Then the effective area reduction from this source is

$$\frac{2\pi (r_o \delta_o^* + r_i \delta_i^*)}{\pi (r_o^2 - r_i^2)} = 2.4\ \%$$

From the data of Sec. 4:5, an approximate average value for the cascade wake displacement thickness is

$$\frac{\delta^*}{s} = .025$$

Hence the total effective area reduction would be approximately 2.4 + 2.5 = 4.9%. From the three stage performance data the area reduction is $\frac{.45 - .43}{.45} = 4.5\%$. Since the decrease of cascade wake displacement thickness which results from mixing is not included, the agreement of the two values may be considered satisfactory.

In the previous discussion the effect of blade tip clearances has not been considered. Perhaps the best estimate of the overall effect of tip clearance leakage, which is currently available in the literature, is the "volumetric efficiency" formula of Fickert (Ref. 31):

$$\eta_v = \frac{1}{1 + 4\mu \left[\frac{\varepsilon / 2r_o}{1 - \left(\frac{r_i}{r_o}\right)^2} \right] \sigma^{-1/2}}$$

where η_v = the multiplicative efficiency factor which accounts for air stream energy loss due to leakage

ε = mean tip clearance

μ = an orifice coefficient , $\sigma = \frac{\bar{\phi}^2}{\bar{\psi}}$

Using, for the test compressor, $\mathcal{E}$=.029" (Sec. 2:1.4), μ=.80 (the maximum value considered), and with $\sigma \doteq .50$ at the design condition,

$$\eta_v = .993$$

Thus a very small effect on overall performance is predicted.

No information concerning the local effect of tip clearance on the wall b. l. growth or the tip section performance is available. However, the detail surveys have shown no large effects which are chargeable to this source, and since theoverall effect is believed to be small, the phenomenon is not further considered.

It has been suggested that wall boundary layer growth in an axial flow compressor might be accelerated by the general adverse static pressure gradient in the flow direction and also by b. l. instability induced by the radial static pressure gradient. It is believed that additional experimental and theoretical investigation of these phenomena is required before their importance can be evaluated. However, from the present test compressor measurements, there seems to be no reason to assume that these phenomena exert major influences on the boundary layer flow.

5:4 Interaction of Wall and Cascade Boundary Layers

It is clear from the preceding discussion and the flow data of Figs. 96 to 101, that, although the wall boundary regions may not grow rapidly, if they are of appreciable extent they must profoundly alter flow conditions through the extreme blade cascade sections.

In Fig. 104 velocity diagrams are shown for a rotor and a stator blade section near the outer boundary ($r = 17.98$ in.). These diagrams are typical of a number which have been constructed from angle and velocity measurements in the compressor. They are compared with the corresponding blade design diagrams. It is seen that due chiefly to the axial velocity reduction, which greatly changes the entrance velocity relative to the rotor, the incidence angles for both rotor and stator are quite large, and high cascade losses undoubtedly result. Nevertheless, considerable air turning occurs, i.e., work is done on the boundary layer fluid but probably very inefficiently. Clearly these effects are cumulative, and the flow becomes successively less favorable until some kind of equilibrium pattern is established.

Similar conditions prevail at the inner boundary: the axial velocity is low, relative incidence angles are abnormally large, and high losses result.

Further evidence of these effects is shown in Fig. 92. For one flow condition, the loss coefficient and flow directions are shown at several radii. It will be recalled that the loss coefficient, Ω , represents the mean total

pressure deficiency referred to the maximum local total pressure in the wake region (See Sec. 4:5.1). Thus the wall boundary layer total pressure defect does not directly influence Ω , but only indirectly in producing unfavorable cascade entrance conditions.

Cascade losses in the central portion of the stream correspond approximately to the optimum values obtained from previous measurements (Sec. 4:5.2). It is seen that low losses are associated with small incidence angles ($+2^\circ < i^* < -2^\circ$) and moderate turning angles. Near each wall the losses increase to values typical of "stalled" cascades, as would be expected from the large incidence angles. It may be concluded that if compressor blading is designed to conform with a flow pattern which does not include real fluid effects, high cascade losses must occur near the bounding walls.

There seems to be no reason why some attempt should not be made in compressor blade design to minimize such losses. A higher rate of twist and perhaps greater camber and greater section thickness for the wall sections would certainly decrease the cascade losses and perhaps even decrease the wall boundary layers, by doing more work on the b. l. fluid.

5:5 Conclusions

Based on the foregoing results and discussion, the following conclusions are proposed.

a. Wall boundary layer growth in the test compressor is moderate, being approximately equivalent to that expected in an equivalent annular duct without blading. Hence, there is no reason to assume that rapid wall b. l. growth must occur in an axial flow compressor of moderately low hub to tip ratio. Such growth may or may not occur, depending largely upon the blade design.

b. The apparent "area contraction" of a compressor flow stream can be satisfactorily accounted for by wall and cascade boundary layer thicknesses.

c. Very high cascade losses and probably incipient cascade stalling occur near outer and inner walls due chiefly to the reduced axial velocity in the wall boundary layers.

d. It is suggested that attempts be made to design blading which conforms to the boundary flow near the outer and inner compressor walls.

References

1. Howell, A. R., Fluid Dynamics of Axial Compressors, in British Gas Turbine Jet Unit, War Emergency Issue No. 12, Institution of Mechanical Engineers, London.

2. Markowski, S. J. and Moffatt, F. M., Instrumentation for Development of Aircraft Power Plant Components Involving Fluid Flow, Reprint, Society of Automotive Engineers, 1947.

3. Eckert, B., Experiences with Flow-Direction Instruments, N. A. C. A. T. M. 969 (1941).

4. Bowen, J. T., Sabersky, R. H., and Rannie, W. D., Theoretical and Experimental Investigations of Axial Flow Compressors, Mechanical Engineering Laboratory, California Institute of Technology, Pasadena, (1949).

5. Sabersky, R. H., Experimental and Theoretical Investigations on the General Flow Patterns of Axial Flow Compressors, Doctoral Thesis, California Institute of Technology, (1949).

6. Howell, A. R., The Present Basis of Axial Flow Compressor Design, Part I, Aero Research Council, R. & M. 2095 (1942).

7. Eckert, B., The Influence of Physical Dimensions and Flow Conditions on Compressor Characteristics, Part A, BuShips 338, The Navy Department (1946).

8. Eckert, B., Calculation and Design of Flow Machines in Aircraft Power Plants, BuShips 338, The Navy Department (1946).

9. Weske, John R., An Investigation of the Aerodynamic Characteristics of a Rotating Axial-Flow Blade Grid, N. A. C. A. T. N. 1128 (1947).

10. Prandtl, L., Durand (Ed.), Aerodynamic Theory, Section III-G.

11. Goldstein, S., Modern Developments in Fluid Dynamics, Vol. I and II, Oxford (1938).

12. Tetervin, Neal, A Review of Boundary-Layer Literature, N. A. C. A. T. N. 1384 (1947).

13. von Doenhoff, Albert E., and Tetervin, Neal, Determination of General Relations for the Behavior of

Turbulent Boundary Layers, N. A. C. A. Report 772 (1943).

14. Katzoff, S., Finn, R. S., and Laurence, J., Interference Method for Obtaining the Potential Flow Past an Arbitrary Cascade of Airfoils, N. A. C. A. T. N. 1252 (1947).

15. Mutterperl, William, The Conformal Transformation of an Airfoil into a Straight Line and its Application to the Inverse Problem of Airfoil Theory, N. A. C. A. W. R. L-113.

Mutterperl, William, A Solution of the Direct and Inverse Potential Problems for Arbitrary Cascades of Airfoils, N. A. C. A. W. R. L-81.

16. Lighthill, M. J., A Mathematical Method of Cascade Design, R. & M. 2104 (1945).

17. Weinig, F., The Flow Around Turbine and Compressor Blades (Translation), BuShips, Navy Department (1946).

18. Garrick, I. E., On Plane Potential Flow Past a Lattice of Arbitrary Airfoils, N. A. C. A. T. R. 778 (1944).

19. Goldstein, Arthur W. and Jerison, Meyer, Isolated and Cascade Airfoils with Prescribed Velocity Distribution, N. A. C. A. T. N. 1038 (1947).

20. Keller, Curt and Marks, Lionel S., Axial Flow Fans, McGraw-Hill (1937).

21. Theodorsen, T., and Garrick, I. E., General Potential Theory of Arbitrary Wing Sections, N. A. C. A. Report 452 (1933).

22. Betz, A., Diagrams for Calculation of Airfoil Lattices, N. A. C. A. T. M. 1022 (1942).

23. Jacobs, E. N., and von Doenhoff, A. E., Formulas for Use in Boundary Layer Calculations on Low Drag Wings, N. A. C. A. W. R. L-319.

24. Falkner, V. M., A Further Investigation of Solutions of the Boundary Layer Equations, R. & M. 1884 (1937).

25. Falkner, V. M., Simplified Calculation of the Laminar Boundary Layer, R. & M. 1895 (1941).

26. Squire, H. B. and Young, A. D., The Calculation of the Profile Drag of Airfoils, R. & M. 1838 (1938).

27. Tetervin, Neal, A Method for the Rapid Estimation of Turbulent Boundary Thicknesses for Calculating Profile Drag, N. A. C. A. W. R. L-16.

28. Prandtl, L., and Tietjens, O. G., Applied Hydro and Aeromechanics, McGraw-Hill (1934).

29. Young, A. D. and Morris, D. E., Note on Flight Tests on the Effect of Slipstream on Boundary Layer Flow, R. & M. 1957 (1939).

30. Traupel, W., New General Theory of Multistage Axial Flow Turbomachines (Translation), Navy Department (1946).

31. Fickert, The Influence of the Radial Clearance of the Rotor on the Compressor Efficiency, Part C, BuShips 338, The Navy Department (1946).

32. Scott, H. H., The Noise Primer, General Radio Co., Cambridge, Mass. (1943).

Notes:

N. A. C. A. denotes the National Advisory Committee for Aeronautics, Washington, D. C. The following classes of reports are published by this organization: Report, Technical Note (T. N.), Technical Memorandum (T. M.), and Wartime Report (W. R.).

R. & M. denotes Aeronautical Research Council Reports and Memoranda, Ministry of Supply, London.

Navy Department The Bureau of Ships, Navy Department sponsered the preparation of a series of reports on Gas Turbine developments in Germany. These reports are available through Code 338, BuShips.

APPENDIX I: REPORT NOTATION

The symbols defined below are generally used throughout the report. Special symbols, subscripts, etc., are defined in the body of the report where needed.

Symbol	Definition
c	Absolute velocity (in a fixed coordinate system)
c_a	Absolute axial velocity component
c_u	Absolute tangential velocity component
c_r	Absolute radial velocity component
w	Velocity relative to a rotating coordinate system
w_a	Relative axial velocity component
w_u	Relative tangential velocity component
w_m	Relative mean velocity
v, u	Velocities
V, U	Reference velocities
q_v	Dynamic pressure
Φ	Velocity potential
Ψ	Stream function
F	Complex potential
ω_a	Axial vorticity component
ω_u	Tangential vorticity component
ω_o	Angular velocity
u_o	Tip velocity
ϕ, φ	Dimensionless axial velocity = c_a/u_o

λ	Dimensionless tangential velocity = c_u/u_o
p	Static pressure
p_t	Total (stagnation) pressure
ρ	Fluid density
μ	Fluid absolute viscosity
ν	Fluid kinematic viscosity
t	Temperature
T	Absolute temperature
r	Radius from center of rotation
R	Tip radius
$\mathcal{F}$	Dimensionless radius = r/R
$\mathcal{F}_i$	Hub ratio, i.e. ratio of hub to tip radii
x, r, θ	A cylindrical coordinate system
x, y, z	A Cartesian coordinate system
q, z, ζ	Complex numbers
h_o	Blade length
c	Airfoil chord length
s	Cascade pitch
γ	Direction of absolute velocity from plane of rotation
β	Direction of relative velocity from plane of rotation
θ_c	Cascade camber angle
θ^*	Air turning angle
α	Angle of attack to chord line

i^*	Air incidence angle
$\bar{\phi}$	Average axial velocity component
ψ	Local work coefficient
ψ'	Local total pressure rise coefficient
$\bar{\psi}$	Total work coefficient
$\bar{\psi}'$	Average total pressure rise coefficient
η	Compression efficiency
Γ	Circulation per unit length of airfoil
L	Lift force per unit length of airfoil
D_p	Profile drag per unit length of airfoil
C_l	Lift coefficient per unit length of airfoil
C_{Dp}	Profile drag coefficient per unit length of airfoil
f, F	Force components
C_p	Static pressure coefficient
P	Reaction ratio
σ'	Cavitation coefficient
δ	Boundary layer thickness
δ^*	Boundary layer displacement thickness
θ	Boundary layer momentum thickness
H	Boundary layer shape parameter = δ^*/θ
τ	Fluid shear stress
$R_{(x)}$	Reynolds number, $\frac{vx}{\nu}$, based on the dimension x
$\bar{\omega}$	Average total head defect per cascade airfoil
Ω	Total head defect coefficient

n, K, κ, a, α	Numerical constants defined in particular problems
$\Delta(\ )$	Change of quantity in parentheses
v_m	Mean cascade velocity
ϕ_m	The average axial velocity coefficient at a particular radius
γ_m	Mean velocity direction
ψ_s	Static pressure coefficient $= \frac{p - p_a}{\frac{1}{2}\rho u_o^2}$
b.l.	Boundary layer
l.e.	Leading edge
t.e.	Trailing edge

APPENDIX II

CALCULATION OF AIR DENSITY

Procedure

First the density of dry air at the dry bulb temperature and corrected barometric pressure is obtained. From wet and dry bulb data a correction is applied to the dry air density to yield the true atmosphere density. (Tables and References for this appendix follow the appendix immediately).

Notation

t = Dry bulb temperature - ^{o}F

t' = Wet bulb temperature - ^{o}F

H' = Barometer reading - in. Hg.

ΔH_t = Barometer correction for temperature - in. Hg.

ΔH_g = Barometer correction for gravity - in. Hg.

ΔH_l = Barometer correction for location - in. Hg.

H = Corrected barometric height - in. Hg.

H_v = Actual pressure of water vapor - in. Hg.

ρ = Atmosphere density - slug/ft.^{3}

ρ' = Density of dry air at dry bulb temperature - slug/ft.^{3}

k_ρ = Humidity correction factor

$\Delta\rho$ = Density correction = $k_\rho \rho$ - slug/ft.^{3}

Barometric Corrections

The barometer reading is corrected for thermal expansion of scale and mercury by the values given in Table A (Ref. A) (Note sign convention).

Standard elevation and latitude corrections to the earth's gravitational field are -.003 in. Hg. (750' elevation) and -.029 in. Hg. (34° 8' N) (Ref. B). These values summed up yield $\Delta H_g = -.032$ in. Hg.

The barometer is located approximately 25 ft. above the laboratory floor. For barometric pressure 29.30 and air temperature 70° F, the pressure at the laboratory floor is .026 in. Hg. greater, according to the isothermal atmosphere formula $\frac{H_1}{H_2} = e^{\frac{Mg}{RT}\Delta y}$. Since the correction is small, it will be assumed constant for the laboratory pressure and temperature range. Hence $H_1 = +.026$ in. Hg. Finally, the corrected barometric pressure is $H = H' - \Delta H_t + \Delta H_g + \Delta H_1$

Dry Air Density

The dry air density is given by Table B. This table was computed from the perfect gas equation

$$\rho = .041212 \frac{H}{t + 459.70} \text{ slug/ft.}^3$$

The following values of the physical constants were used in deriving the above equation.

$R_{universal} = 8.3136 \times 10^7 \frac{erg.}{deg.\ mol.}$ (Ref. C)

Mol. wt. air = 28.967 (Ref. C)

which yields

$R_{air} = 53.340 \frac{ft.\ lb.}{lb.\ F.}$

$g = 32.174 \frac{ft.}{sec.^2}$ (Ref. F)

Atmospheric Density

The mixture of air and water vapor is assumed to follow perfect gas laws.

Then $\frac{p_a}{\rho_a} = \frac{R}{m_a} T$; $\frac{p_v}{\rho_v} = \frac{R}{\rho_v} T$

m_a = Mol. wt. of air

m_v = Mol. wt. of water

$$\rho = \rho_a + \rho_v = \frac{1}{RT}(p_a m_a + p_v m_v)$$

$$\rho' = \frac{1}{RT}(p_a + p_v) m_a$$

Hence $$\frac{\rho}{\rho'} = \frac{p_a m_a + p_v m_v}{(p_a + p_v) m_a}$$

Let $p = p_a + p_v$ the total pressure

Then $$\frac{\rho}{\rho'} = 1 - (1 - \frac{m_v}{m_a}) \frac{p_v}{p}$$

Which is the formula used in the International Critical Tables, from which the value of $\frac{m_v}{m_a}$ is .6217 (Ref. G).

Hence finally $\frac{\rho}{\rho'} = 1 - .3783 \frac{H_v}{H}$ where H_v = pressure of water

vapor at dry bulb temperature.

The value of H_v can be obtained by finding the saturation pressure, H_v sat. (Ref H), at the dry bulb temperature and the relative humidity, r, from empirical wet-dry bulb tables (Ref. I). Then $H_v = r\, H_v$ sat.

$$\text{Thus } \frac{\rho}{\rho'} = 1 - .3783 \frac{r\ (H_v \text{ sat.})}{h} = 1 - k_\rho$$

$$\text{or } \rho = \rho' - \rho' k_\rho = \rho' - \Delta\rho$$

The above computations have been summarized in Table C for a barometric pressure of 29.30. The relative humidity is assumed to be independent of barometric pressure over the operating range (Ref. J). Since the factor, k_ρ, is small its value at 29.30 in. Hg. can be used over the range of barometric pressures encountered.

Summary - Computation Procedure

1. Compute corrected barometric pressure
   $H = H' - \Delta H_t - .006$ in. Hg.
   ΔH_t is read from Table A
2. Obtain dry air density, ρ', from Table B, using H and the dry bulb temperature, t. Interpolate to nearest .01 in. and $\frac{1}{2}^\circ$ F.
3. Obtain k_ρ from Table C using t and (t - t') to the nearest one $^\circ$ F.

4. Compute the atmospheric density correction

$$\Delta\rho = k_\rho \rho' \quad \text{slug/ft.}^3$$

5. Compute the atmospheric density

$$\rho = \rho' - \Delta\rho \quad \text{slug/ft.}^3$$

References

A. Handbook of Chemistry and Physics - 13th Edition - p. 1911

B. Handbook of Chemistry and Physics - p. 1918 - 1919

C. Handbook of Chemistry and Physics - p. 2412

D. Psychrometric Tables and Charts - Zimmerman and Lavine Industrial Research Service - 1945 - p. 1

E. Marks' Handbook - 4th Edition - p. 84

F. Handbook of Chemistry and Physics - p. 2391

G. International Critical Tables

H. Psychrometric Tables and Charts - Table 1

I. Psychrometric Tables and Charts - Table 31

J. Handbook of Chemistry and Physics - Note on p. 1922

TABLE A

BAROMETRIC TEMPERATURE CORRECTION

TEMP. (°F)	OBSERVED HEIGHT ("HG) 29.0	29.1	29.2	29.3	29.4	29.5
50	+.056	+.056	+.056	+.057	+.057	+.057
51	59	59	59	59	59	60
52	61	61	62	62	63	63
53	64	64	65	65	65	66
54	67	67	67	68	68	68
55	70	70	70	70	70	71
56	72	72	72	73	73	73
57	75	75	75	75	76	76
58	77	77	78	78	79	79
59	80	80	80	81	81	82
60	.082	.082	.083	.083	.084	.084
61	85	85	86	86	86	87
62	88	88	88	89	89	89
63	91	91	91	91	92	92
64	93	93	94	94	95	95
65	96	96	96	97	97	98
66	98	98	99	99	100	100
67	101	101	101	102	102	103
68	103	103	104	104	105	105
69	106	106	107	107	108	108
70	.109	.109	.110	.110	.111	.111
71	112	112	112	113	113	114
72	114	114	115	115	116	116
73	117	117	117	118	118	119
74	119	119	120	120	121	121

TEMP. (°F)	OBSERVED HEIGHT ("HG) 29.0	29.1	29.2	29.3	29.4	29.5
75	122	122	123	123	124	124
76	124	125	125	126	126	127
77	127	127	128	128	129	130
78	129	130	130	131	131	132
79	132	132	133	133	134	135
80	.135	.135	.136	.136	.137	.137
81	138	138	139	139	140	140
82	140	141	141	142	142	143
83	143	143	144	144	145	145
84	145	146	146	147	147	148
85	148	148	149	149	150	151
86	150	151	151	152	152	153
87	153	153	154	155	155	156
88	155	156	157	157	158	159
89	158	159	159	160	161	162
90	161	162	162	163	163	164
91	164	164	165	165	166	167
92	166	167	167	168	168	169
93	169	169	170	171	171	172
94	171	172	173	173	174	175
95	174	174	175	176	177	178
96	176	177	178	178	179	180
97	179	179	180	181	182	183
98	181	182	183	183	184	185
99	184	185	185	186	187	188
100	187	188	188	189	189	190

DRY AIR DENSITY

TABLE: B
(SHEET 1)

BAROMETRIC PRESSURE ("HG)	TEMPERATURE - °F										
	50	51	52	53	54	55	56	57	58	59	60
28.90	.002337	.002332	.002328	.002323	.002319	.002314	.002310	.002305	.002301	.002296	.002292
.92	38	34	29	25	20	16	11	07	02	98	93
.94	40	35	31	26	22	17	13	08	04	99	95
.96	42	37	32	28	23	19	14	10	05	2301	97
.98	43	39	34	30	25	20	16	11	07	03	98
29.00	.002345	.002340	.002336	.002331	.002327	.002322	.002318	.002313	.002309	.002304	.002300
.02	46	42	37	33	28	24	19	15	10	06	01
.04	48	43	39	34	30	25	21	16	12	07	03
.06	50	45	41	36	31	27	22	18	13	09	04
.08	51	47	42	38	33	28	24	19	15	11	05
29.10	.002353	.002348	.002344	.002339	.002335	.002330	.002326	.002321	.002317	.002312	.002308
.12	55	50	45	41	36	32	27	23	18	14	09
.14	56	52	47	42	38	33	29	24	20	15	11
.16	58	53	49	44	39	35	30	26	21	17	12
.18	59	55	50	46	41	36	32	27	23	18	14
29.20	.002361	.002356	.002352	.002347	.002343	.002338	.002334	.002329	.002325	.002320	.002316
.22	63	58	53	49	44	40	35	31	26	22	17
.24	64	60	55	50	46	41	37	32	28	23	19
.26	66	61	57	52	47	43	38	34	29	25	20
.28	67	63	58	54	49	44	40	35	31	26	22
29.30	.002369	.002364	.002360	.002355	.002351	.002346	.002342	.002337	.002333	.002328	.002324
.32	71	66	61	57	52	48	43	39	34	30	25
.34	72	68	63	58	54	49	45	40	36	31	27
.36	74	69	65	60	55	51	46	42	37	33	28
.38	76	71	66	62	57	53	48	43	39	34	30
29.40	.002377	.002373	.002368	.002363	.002359	.002354	.002350	.002345	.002340	.002336	.002331
.42	79	74	70	65	60	56	51	47	42	38	33
.44	80	76	71	67	62	57	53	48	44	39	35
.46	82	77	73	68	64	59	54	50	45	41	36
.48	84	79	74	70	65	61	56	51	47	42	38
29.50	.002385	.002381	.002376	.002371	.002367	.002362	.002358	.002353	.002348	.002344	.002339

DRY AIR DENSITY

TABLE: B (CONT)
(SHEET 2)

BAROMETRIC PRESSURE ("HG)	TEMPERATURE - °F										
	60	61	62	63	64	65	66	67	68	69	70
28.90	.002292	.002287	.002283	.002279	.002274	.002270	.002266	.002261	.002257	.002253	.002249
.92	93	89	85	80	76	72	67	63	59	54	50
.94	95	91	86	82	78	73	69	64	60	56	52
.96	97	92	88	83	79	75	70	66	62	57	53
.98	98	94	89	85	81	76	72	68	63	59	55
29.00	.002300	.002295	.002291	.002267	.002282	.002278	.002273	.002269	.002265	.002261	.002256
.02	01	97	93	88	84	79	75	71	66	62	58
.04	03	98	94	90	85	81	77	72	68	64	59
.06	04	2300	96	91	87	83	78	74	70	65	61
.08	06	02	97	93	88	84	80	75	71	67	63
29.10	.002308	.002303	.002299	.002294	.002290	.002286	.002281	.002277	.002273	.002268	.002264
.12	09	05	2300	96	92	87	83	79	74	70	66
.14	11	06	02	98	93	89	84	80	76	72	67
.16	12	08	04	99	95	90	86	82	77	73	69
.18	14	10	05	2301	96	92	88	83	79	75	70
29.20	.002316	.002311	.002307	.002302	.002298	.002294	.002289	.002285	.002280	.002276	.002272
.22	17	13	08	04	99	95	91	86	82	78	73
.24	19	14	10	05	2301	97	92	88	84	79	75
.26	20	16	11	07	03	98	94	90	85	81	77
.28	22	17	13	09	04	2300	95	91	87	82	78
29.30	.002324	.002319	.002315	.002310	.002306	.002301	.002297	.002293	.002288	.002284	.002280
.32	25	21	16	12	07	03	99	94	90	86	81
.34	27	22	18	13	09	05	2300	96	91	87	83
.36	28	24	19	15	11	06	02	97	93	89	84
.38	30	25	21	17	12	08	03	99	95	90	86
29.40	.002331	.002327	.002323	.002318	.002314	.002310	.002305	.002300	.002296	.002292	.002287
.42	33	29	24	20	15	11	06	02	98	93	89
.44	35	30	26	21	17	12	08	04	99	95	91
.46	36	32	27	23	18	14	10	05	2301	96	92
.48	38	33	29	24	20	16	11	07	02	98	94
29.50	.002339	.002335	.002330	.002326	.002322	.002317	.002313	.002308	.002304	.002300	.002295

DRY AIR DENSITY

TABLE: B (CONT)
(SHEET 3)

BAROMETRIC PRESSURE ("HG)	TEMPERATURE - °F										
	70	71	72	73	74	75	76	77	78	79	80
28.90	.002249	.002244	.002240	.002236	.002232	.002228	.002223	.002219	.002215	.002211	.002207
.92	50	46	42	37	33	29	25	21	17	13	08
.94	52	47	43	39	35	31	26	22	18	14	10
.96	53	49	45	41	36	32	28	24	20	16	11
.98	55	51	46	42	38	34	30	25	21	17	13
29.00	.002256	.002252	.002248	.002244	.002239	.002235	.002231	.002227	.002223	.002219	.002215
.02	58	54	49	45	41	37	33	28	24	20	16
.04	59	55	51	47	43	38	34	30	26	22	18
.06	61	57	52	48	44	40	36	32	27	23	19
.08	63	58	54	50	46	41	37	33	29	25	21
29.10	.002264	.002260	.002256	.002251	.002247	.002242	.002239	.002235	.002230	.002226	.002222
.12	66	61	57	53	49	44	40	36	32	28	24
.14	67	63	59	54	50	46	42	38	33	29	25
.16	69	64	60	56	52	48	43	39	35	31	27
.18	70	66	62	58	53	49	45	41	37	32	28
29.20	.002272	.002268	.002263	.002259	.002255	.002251	.002246	.002242	.002238	.002234	.002230
.22	73	69	65	61	56	52	48	44	40	35	31
.24	75	71	66	62	58	54	50	45	41	37	33
.26	77	72	68	64	59	55	51	47	43	39	34
.28	78	74	70	65	61	57	53	48	44	40	36
29.30	.002280	.002275	.002271	.002267	.002263	.002258	.002254	.002250	.002246	.002242	.002237
.32	81	77	73	68	64	60	56	51	47	43	39
.34	83	78	74	70	66	61	57	53	49	45	40
.36	84	80	76	71	67	63	59	55	50	46	42
.38	86	82	77	73	69	65	60	56	52	48	44
29.40	.002287	.002283	.002278	.002275	.002270	.002266	.002262	.002258	.002253	.002249	.002245
.42	89	85	80	76	72	68	63	59	55	51	47
.44	91	86	82	78	73	69	65	61	56	52	48
.46	92	88	83	79	75	71	66	62	58	54	50
.48	94	89	85	81	76	72	68	64	60	55	51
29.50	.002295	.002291	.002287	.002282	.002278	.002274	.002270	.002265	.002261	.002257	.002253

DRY AIR DENSITY

TABLE: B (CONT)
(SHEET 4)

BAROMETRIC PRESSURE ("HG)	TEMPERATURE - °F										
	80	81	82	83	84	85	86	87	88	89	90
28.90	.002207	.002202	.002199	.002195	.002191	.002187	.002183	.002179	.002175	.002171	.002167
.92	08	04	2200	96	92	88	84	80	76	72	68
.94	10	06	02	98	94	90	87	82	78	74	70
.96	11	07	03	99	95	91	87	83	79	75	71
.98	13	08	05	2201	97	93	89	85	81	77	73
29.00	.002215	.002210	.002206	.002202	.002198	.002194	.002190	.002186	.002182	.002178	.002174
.02	16	12	08	04	2200	96	92	88	84	80	76
.04	18	13	09	05	01	97	93	89	85	81	77
.06	19	15	11	07	03	99	95	91	87	83	79
.08	21	17	12	08	04	2200	96	92	88	84	80
29.10	.002222	.002218	.002214	.002210	.002206	.002202	.002198	.002194	.002190	.002186	.002182
.12	24	20	15	11	07	03	99	95	91	87	83
.14	25	21	17	13	09	05	2201	97	93	88	85
.16	27	23	19	14	10	06	02	98	94	90	86
.18	28	24	20	16	12	08	04	2200	96	92	88
29.20	.002230	.002226	.002222	.002218	.002213	.002209	.002205	.002201	.002197	.002193	.002190
.22	31	27	23	19	15	11	07	03	99	95	91
.24	33	29	25	21	16	12	08	04	2200	96	92
.26	34	30	26	22	18	14	10	06	02	98	94
.28	36	32	28	24	20	15	11	07	03	99	95
29.30	.002237	.002233	.002229	.002225	.002221	.002217	.002213	.002209	.002205	.002201	.002197
.32	39	35	31	27	22	18	14	10	06	02	98
.34	40	36	32	28	24	20	16	12	08	04	2200
.36	42	38	34	30	26	21	17	13	09	05	01
.38	44	40	35	31	27	23	19	15	11	07	03
29.40	.002245	.002241	.002237	.002233	.002229	.002224	.002220	.002216	.002212	.002208	.002204
.42	47	42	38	34	30	26	22	18	14	10	06
.44	48	44	40	36	32	27	23	20	15	11	07
.46	50	45	41	37	33	29	25	21	17	13	09
.48	51	47	43	39	35	31	26	22	18	14	10
29.50	.002253	.002249	.002244	.002240	.002236	.002232	.002228	.002224	.002220	.002216	.002212

DRY AIR DENSITY

TABLE: B (CONT)
(SHEET 5)

BAROMETRIC PRESSURE ("HG)	TEMPERATURE - °F										
	90	91	92	93	94	95	96	97	98	99	100
28.90	.002167	.002163	.002159	.002155	.002151	.002147	.002143	.002139	.002136	.002132	.002128
.92	68	64	60	56	53	49	45	41	37	33	29
.94	70	66	62	58	54	50	46	42	39	35	31
.96	71	67	63	59	56	52	48	44	40	36	32
.98	73	69	65	61	57	53	49	45	42	38	34
29.00	.002174	.002170	.002166	.002162	.002159	.002155	.002151	.002147	.002143	.002140	.002135
.02	76	72	68	64	60	56	52	48	45	41	37
.04	77	73	69	65	62	58	54	50	46	42	39
.06	79	75	71	67	63	59	55	51	47	44	40
.08	80	76	72	68	64	61	57	53	49	45	41
29.10	.002182	.002178	.002174	.002170	.002166	.002162	.002158	.002154	.002150	.002147	.002143
.12	83	79	75	71	67	64	60	56	52	48	44
.14	85	81	77	73	69	65	61	57	53	50	46
.16	86	82	78	74	70	67	63	59	55	51	47
.18	88	84	80	76	72	68	64	60	56	52	49
29.20	.002190	.002185	.002181	.002177	.002173	.002169	.002166	.002162	.002158	.002154	.002150
.22	91	87	83	79	75	71	67	63	59	55	52
.24	92	88	84	80	76	72	69	65	61	57	53
.26	94	90	86	82	78	74	70	66	62	58	55
.28	95	91	87	83	79	75	72	68	64	60	56
29.30	.002197	.002193	.002189	.002185	.002181	.002177	.002173	.002169	.002165	.002161	.002157
.32	98	94	90	86	82	78	74	71	67	63	59
.34	2200	96	92	88	84	80	76	72	68	64	60
.36	01	97	93	89	85	81	77	74	70	66	62
.38	03	99	95	91	87	83	79	75	71	67	63
29.40	.002204	.002200	.002196	.002192	.002188	.002184	.002180	.002177	.002173	.002169	.002165
.42	06	02	98	94	90	86	82	78	74	70	66
.44	07	03	99	95	91	87	83	79	76	72	68
.46	09	05	2201	97	93	89	85	81	77	73	69
.48	10	06	02	98	94	90	86	82	79	75	71
29.50	.002212	.002208	.002204	.002200	.002196	.002192	.002188	.002184	.002180	.002176	.002172

DRY AIR DENSITY

TABLE: B (CONT)
(SHEET 6)

BAROMETRIC PRESSURE ("HG)	TEMPERATURE - °F										
	100	101	102	103	104	105	106	107	108	109	110
28.90	.002128	.002124	.002120	.002117	.002113	.002109	.002105	.002102	.002099	.002094	.002091
.92	29	26	22	18	14	11	07	03	99	96	92
.94	31	27	23	20	16	12	08	05	2101	97	94
.96	32	29	25	21	17	14	10	06	02	99	95
.98	34	30	26	23	19	15	11	08	04	2100	96
29.00	.002135	.002132	.002128	.002124	.002120	.002116	.002113	.002109	.002105	.002102	.002098
.02	37	33	30	25	22	18	14	10	07	03	99
.04	38	35	31	27	23	19	16	12	08	04	2101
.06	40	36	32	28	25	21	17	13	10	06	02
.08	41	37	34	30	26	22	19	15	11	07	04
29.10	.002143	.002139	.002135	.002131	.002128	.002124	.002120	.002116	.002113	.002109	.002105
.12	44	40	37	33	29	25	21	18	14	10	07
.14	46	42	38	34	30	27	23	19	15	12	08
.16	47	43	40	36	32	28	24	21	17	13	09
.18	49	45	41	37	33	30	26	22	18	15	11
29.20	.002150	.002146	.002142	.002139	.002135	.002131	.002127	.002124	.002119	.002116	.002112
.22	52	48	44	40	36	33	29	25	21	18	14
.24	53	50	45	42	38	34	30	26	23	19	15
.26	55	51	47	43	39	35	32	28	24	20	17
.28	56	52	48	45	41	37	33	29	26	22	18
29.30	.002157	.002154	.002150	.002146	.002142	.002138	.002135	.002131	.002127	.002123	.002120
.32	59	55	51	47	44	40	36	32	29	25	21
.34	60	57	53	49	45	41	38	34	30	26	33
.36	62	58	54	50	47	43	39	35	31	28	24
.38	63	60	56	52	48	44	40	37	33	28	25
29.40	.002165	.002161	.002157	.002153	.002149	.002146	.002142	.002138	.002134	.002131	.002127
.42	66	62	59	55	51	47	43	40	36	32	28
.44	68	64	60	56	52	49	45	41	37	33	30
.46	69	65	62	58	54	50	46	42	39	35	31
.48	71	67	63	59	55	52	48	44	40	36	33
29.50	.002172	.002168	.002164	.002161	.002157	.002153	.002149	.002145	.002142	.002138	.002134

TABLE: C

HUMIDITY CORRECTION FACTOR

DRY BULB TEMP. (°F)	TEMPERATURE DIFFERENCE (°F)												
	1	2	3	4	5	6	7	8	9	10	11	12	13
50	.0044	.0041	.0037	.0035	.0031	.0029	.0026	.0023	.0020	.0018	.0015	.0013	.0010
51	46	42	39	36	33	30	27	24	22	19	17	14	11
52	47	44	41	38	35	32	29	26	23	20	18	15	12
53	49	45	42	39	36	33	30	27	25	21	19	16	14
54	51	48	44	41	38	35	32	29	26	23	20	17	15
55	.0053	.0049	.0046	.0043	.0039	.0037	.0033	.0030	.0028	.0024	.0021	.0019	.0016
56	55	51	48	44	41	38	35	32	29	26	23	20	17
57	57	53	50	47	43	40	37	33	30	27	24	21	19
58	59	55	52	48	45	41	38	35	32	29	26	23	20
59	61	58	54	51	47	44	40	37	34	31	27	25	21
60	.0063	.0060	.0056	.0053	.0049	.0046	.0042	.0039	.0036	.0032	.0029	.0026	.0023
61	66	62	59	54	51	47	44	40	38	34	31	28	24
62	68	64	61	57	53	50	46	43	39	36	33	30	26
63	71	67	63	59	55	52	48	45	41	37	34	31	28
64	74	70	65	61	57	54	50	47	43	40	36	33	29
65	.0076	.0072	.0068	.0064	.0060	.0056	.0053	.0049	.0045	.0042	.0039	.0035	.0031
66	79	75	71	67	62	59	55	51	47	44	40	37	33
67	82	77	73	69	65	61	57	53	50	46	42	39	35
68	85	80	76	71	68	63	60	55	52	48	45	41	37
69	88	83	78	75	70	66	62	58	54	51	47	43	40
70	.0091	.0086	.0082	.0077	.0073	.0069	.0065	.0061	.0056	.0052	.0049	.0046	.0042
71	94	89	85	80	76	71	67	63	59	55	51	47	44
72	97	93	88	84	79	75	70	66	62	58	54	50	46
73	100	96	91	87	82	77	73	69	64	60	56	53	49
74	104	99	94	90	85	81	75	71	67	63	59	55	51
75	.0108	.0103	.0097	.0093	.0088	.0084	.0079	.0075	.0070	.0066	.0061	.0058	.0053
76	112	106	102	96	91	86	82	77	72	69	64	60	56
77	116	110	105	100	95	89	86	81	76	71	68	63	58
78	120	114	109	104	99	94	89	84	79	75	70	66	61
79	124	117	112	107	102	97	92	88	83	77	74	68	64
80	.0128	.0121	.0116	.0111	.0105	.0100	.0096	.0091	.0085	.0081	.0076	.0072	.0067
82	137	131	125	119	114	108	102	98	92	87	82	78	73
84	146	140	133	127	121	115	111	105	100	94	89	85	79
86	155	149	142	136	131	125	118	113	107	102	97	92	86
88	165	159	152	146	140	133	128	121	115	110	105	98	93
90	.0176	.0169	.0163	.0156	.0149	.0143	.0136	.0130	.0125	.0119	.0112	.0106	.0101
92	188	180	174	166	160	152	147	141	133	127	121	115	109
94	200	193	185	177	170	164	156	150	143	137	131	125	118
96	212	206	197	190	181	175	168	161	153	146	139	135	128
98	225	218	209	202	193	186	179	171	164	157	150	143	136
100	.0240	.0232	.0222	.0215	.0207	.0200	.0192	.0182	.0175	.0170	.0162	.0155	.0147
102	254	246	238	228	220	212	204	196	188	180	172	167	159
104	273	262	253	245	233	225	217	208	200	194	186	177	169
106	289	277	268	260	251	242	233	224	215	206	197	191	182
108	307	294	285	275	266	256	247	237	228	221	212	202	196
110	.0325	.0312	.0302	.0292	.0282	.0271	.0261	.0251	.0245	.0235	.0225	.0218	.0208

TABLE: C (CONT)

HUMIDITY CORRECTION FACTOR

DRY BULB TEMP. (°F)	TEMPERATURE DIFFERENCE (°F)											
	14	15	16	17	18	19	20	21	22	23	24	25
50	.0007	.0005	.0002									
51	08	06	03	.0001								
52	10	07	05	02								
53	10	08	05	03	.0001							
54	12	09	07	04	02							
55	.0013	.0011	.0008	.0005	.0003							
56	15	12	09	06	04	.0001						
57	16	13	10	08	05	02						
58	17	14	11	09	06	04	.0001					
59	19	16	13	10	07	05	02					
60	.0020	.0018	.0014	.0011	.0009	.0006	.0003	.0001				
61	22	19	15	13	10	07	05	02				
62	23	20	17	14	12	09	06	03	.0001			
63	25	22	19	16	13	10	07	04	01			
64	26	23	20	17	14	12	09	05	03			
65	.0028	.0025	.0022	.0019	.0016	.0013	.0010	.0007	.0004	.0002		
66	30	27	25	21	17	14	12	08	06	02		
67	32	28	26	22	19	16	13	10	07	04	.0002	
68	34	30	28	24	20	18	14	12	09	05	03	
69	36	32	30	26	22	19	17	13	10	07	05	.0001
70	.0038	.0034	.0031	.0028	.0024	.0021	.0018	.0014	.0011	.0009	.0006	.0003
71	40	37	33	30	27	23	20	17	13	10	07	04
72	43	39	35	32	29	25	21	18	15	12	09	06
73	44	41	37	34	31	26	23	20	17	14	11	07
74	47	43	39	36	32	28	25	22	19	16	12	09
75	.0050	.0045	.0042	.0038	.0034	.0030	.0027	.0024	.0020	.0017	.0014	.0010
76	51	48	44	40	36	33	29	26	22	19	15	13
77	54	51	47	42	39	35	31	28	24	21	17	14
78	57	54	49	45	41	37	34	30	26	22	20	16
79	59	55	52	48	44	40	36	32	28	25	22	18
80	.0063	.0059	.0055	.0051	.0047	.0043	.0039	.0035	.0031	.0027	.0024	.0020
82	68	64	60	55	51	47	43	40	36	31	28	24
84	74	70	65	61	56	53	49	44	39	36	32	29
86	81	76	71	68	63	58	53	50	45	42	37	34
88	88	83	79	74	69	64	60	55	52	47	43	38
90	.0095	.0090	.0086	.0081	.0075	.0072	.0066	.0062	.0057	.0053	.0048	.0044
92	104	98	94	88	82	78	72	68	63	59	55	49
94	112	106	102	96	89	85	79	75	69	64	60	56
96	122	115	111	104	97	93	86	82	77	71	66	62
98	129	124	117	113	106	101	94	89	85	80	75	68
100	.0140	.0135	.0127	.0122	.0115	.0110	.0102	.0097	.0092	.0087	.0082	.0075
102	151	146	138	130	125	119	111	106	101	95	90	85
104	163	155	149	141	135	129	121	115	110	104	98	93
106	173	167	158	152	146	137	131	125	119	113	107	101
108	187	180	171	164	155	149	142	136	130	123	117	111
110	.0201	.0191	.0184	.0174	.0168	.0161	.0154	.0147	.0141	.0134	.0127	.0121

APPENDIX III

NOISE LEVEL

Noise produced by high speed axial flow compressors has often been a considerable annoyance, and suitable measures are frequently taken to isolate or diminish the disturbance. It was believed that the test compressor, operating below 2000 R.P.M., might be noisy, but that the problem would not be acute. In any case, the size and other usage of the laboratory made impractical any attempt at a large scale sound insulation. Experience has indicated that the compressor noise is, indeed, bothersome, but not unbearable.

With the compressor operating at 1500 R.P.M., single stage (free vortex blading), a number of measurements were made of general noise level and frequency distribution at various locations in the laboratory and nearby rooms. The noise level was measured with a General Radio Sound Level Meter, Type 759-B; the frequency distribution using, in addition, a General Radio Sound Analyzer, Type 760-A. The methods of measurement used were essentially those of Ref. 32.

The following noise level readings were obtained:

Edge of throttle valve	-	102 db.
Edge of bell mouth	-	95 db.

Operating desk	-	92 db.
Second balcony of laboratory	-	80 db.
Hallway on ground level	-	63 db.
Second and third floor offices	-	50 db.

For comparison, Ref. 2, lists the following:

Heavy city street traffic	-	95 db.
Average office	-	50 db.

The compressor noise is not of a completely random nature, certain distinct frequency components being distinguishable even by ear. The strong, higher frequency components appear to be especially annoying and fatiguing after exposure of $\frac{1}{2}$ hour or longer. A frequency spectrum measured at the operating desk is shown in Fig. 105. High amplitudes were detected at 770, 1550 and 3100 cycles per second which seem to be accounted for by the compressor itself. The lower frequency peaks may be due to the motor generator set or other auxiliaries. Frequencies above 7500 C.P.S. could not be measured with equipment available.

Assuming a sound pulse to be produced by a rotor blade passing a fixed point, the frequency would be $\frac{RPM}{60}$ x number of blades = $\frac{1500}{60}$ x 30 = 750 C.P.S. Or if the stator blade frequency is computed we have $\frac{1500}{60}$ x 32 = 800 C.P.S. The higher frequency peaks might be considered as second and fourth harmonics of these fundamentals. The precise mechanism of sound production in a compressor is

not known; the above calculations are intended only to suggest a correlation between the compressor speed and measured frequency peaks.

Some attempts were made to reduce the noise by placing sound absorbing baffles near the compressor outlet and inlet, where the noise level seemed highest. No appreciable improvement was detected by the measuring equipment, but there seemed to be some beneficial psychological effect on the operators. Since much of the test work can be done at 750 R.P.M., where the noise level is much lower, the noise problem is not an acute one.

Appendix IV

Cascade Velocity Calculation

The cascade to be treated is the section of the stator row of the free vortex blading at the mid-radius ($\xi = .80$, $r = 14.40$ in.) whose properties are given in Table 1. A drawing of the cascade together with a summary of its properties is shown in Fig. 57. One airfoil of this cascade is first considered. In order to obtain the best approximation to its total lift in cascade, the angle of attack for the single airfoil is taken as that of the vector mean of inlet and outlet velocities in cascade, given by the blade design calculations. The chosen angle of attack is $\alpha_m = 5°26'$, as shown in Fig. 57.

Calculation of single airfoil velocity distribution is, in itself, a rather involved process for an arbitrary shape. Perhaps the best known method is that due to Theodorsen (Ref. 21). An exact calculation is now in progress using this method. However in order to become familiar with the cascade correction method, calculations were first made replacing the cascade of thick airfoils by one of thin circular arc sections whose single airfoil properties are readily obtained.*

Flow about the circular arc airfoil is obtained by

---

* It should be noted that the transformation method is available for a cascade of thin airfoils (Ref. 4 and 17) and might have been used to attain the end result of these calculations.

means of the Joukowsky transformation. The process is shown geometrically in Fig. 59 for which the transformations are:

$$z = \zeta + \frac{t^2}{\zeta} \tag{62}$$

$$\zeta = q e^{-i\phi_t} + im \tag{63}$$

where $f = 2m$ and $\phi_t = \tan^{-1}\frac{m}{t}$

Correspondence between the z and q planes is given by these relations and is illustrated, for the 12 points computed, by Fig. 58. Knowing the flow potential about a circle,

$$F(q) = V_m\left[q e^{-i(\alpha+\phi_t)} + \frac{a^2}{q} e^{i(\alpha+\phi_t)}\right] + i\frac{\Gamma}{2\pi}\left[\ln\frac{q}{a} - i(\alpha+\phi_t)\right] \tag{64}$$

$$= \phi + i\psi$$

and applying the Kutta condition (rear stagnation point is located at the airfoil t. e.), which yields

$$\Gamma = 4\pi a V_m \sin(\alpha+\phi_t)$$

the velocity potential on the airfoil surface becomes

$$\frac{\phi}{c V_m} = 2\left(\frac{a}{c}\right)\left[\cos(\phi-\alpha-\phi_t) - (\phi-\alpha-\phi_t)\sin(\alpha+\phi_t)\right] \tag{65}$$

and the surface velocity is

$$\left|\frac{V}{V_m}\right| = \frac{2\left\{\sin(\phi-\alpha-\phi_t) + \sin(\alpha+\phi_t)\right\}\left\{\frac{1}{2}\left(1+\frac{m^2}{a^2}\right) + \frac{m}{a}\sin(\phi-\phi_t)\right\}}{\sqrt{\left[1+\frac{m}{a}\sin(\phi-\phi_t)\right]^2 - \left[\frac{t}{a}\cos(\phi-\phi_t)\right]^2}} \tag{66}$$

The computed isolated airfoil potentials and velocities are plotted in Figs. 60 and 61 respectively. It will be noted that the total circulation, Γ, is given by

$$\Gamma = (\Delta\phi)_{t.e.} = \left|\phi_{upper} - \phi_{lower}\right|$$

For the isolated airfoil,

$$C_L = \frac{2\Gamma}{V_m c} = 1.424$$

The cascade correction method of Ref. 14 is briefly outlined and results for the several steps given. Details of each step can be obtained by reference to the original note. The isolated airfoil in the chosen flow field is represented by a set of singularities located arbitrarily along the camber line. In the case of the circular arc, five vortices are used as shown in Fig. 60. The total vorticity must be equal to the total (isolated) airfoil circulation and the relative strengths are determined from the velocity potential distribution. Thus the strength of the first vortex, α', is chosen equal to the difference $\left|\phi_{upper} - \phi_{lower}\right|$ at a point midway between the first and second vortex locations. Vortex strengths for the isolated airfoil are given in Fig. 60. The isolated airfoil velocity potential, ϕ_f, is known on the airfoil surface and the stream potential, ψ_f, is taken as zero, since the surface is a stream line.

The other airfoils of the cascade are next introduced to the flow field. Each is represented by a set of five vortices of the strength previously determined. The disturbance potentials, ϕ_d and ψ_d, corresponding to the additional vortices are computed at the selected airfoil surface points. These computations are readily made by using a geometric potential plot, similar to that originally

proposed by Betz (Ref. 22).

In order to restore the chosen airfoil surface to its condition of zero stream potential, in the presence of the other cascade airfoil, a compensating stream potential ψ_c is introduced such that $\psi_c = -\psi_a$ on the airfoil surface. Then the conjugate (velocity) potential ϕ_c is determined by Fourier analysis in the circle plane.

Finally, the total circulation must be altered in order to maintain the Kutta condition at the t. e. Thus the additional circulation is

$$\Gamma_a = 2\pi \left(\frac{d\phi_c}{d\phi} \right)_{t.e.}$$

The final circulation and potential distribution might be obtained by simply summing the preceding values. However, a closer approximation to the cascade influence can be obtained by assuming the cascade airfoils all have the final circulation, Γ_t, but that the relative vortex strengths are the same as for the isolated airfoil, then

$$\Gamma_t = \Gamma_f + \frac{\Gamma_t}{\Gamma_f} \Gamma_a$$

or

$$\frac{\Gamma_t}{cV_m} = \frac{\Gamma_f / cV_m}{1 - \Gamma_a / \Gamma_f} \qquad (67)$$

and

$$(C_L)_t = \frac{(C_L)_f}{1 - \Gamma_a / \Gamma_f}$$

For the circular arc airfoil, it will be recalled that $(C_L)_f = 1.424$ and with

$$\frac{\Gamma_a}{\Gamma_f} = -.395 \quad , \quad (C_L)_t = 1.020$$

The corrected potential distribution is

$$\frac{\Phi_c}{cV_m} = \frac{\Phi_f}{cV_m} + \frac{\Phi_d + \Phi_c}{cV_m}\,\frac{\Gamma_c}{\Gamma_f} + \frac{\Gamma_f - \Gamma_c}{cV_m}\,\frac{\phi}{2\pi} \qquad (68)$$

which is plotted in Fig. 60 as the first approximation to the cascade effect.

It is clearthat the derived circulation and potential distribution can be used in representing the cascade airfoils by new singularities and, with the preceding method a second approximation can be obtained. This procedure appears to be convergent and may be repeated until changes in ϕ distribution are small. In many cases, satisfactory convergence is obtained after one or two approximations.

For the circular arc cascade, a second approximation yields $C_L = 1.026$ and potentials and velocities shown in Figs. 60 and 61. This approximation was assumed to be sufficiently accurate. It should be noted that, whereas for this simple case the isolated airfoil velocities can be analytically computed, the cascade correction velocities must be obtained by graphical differentiation of the correction potential. This step probably introduces the greatest errors.

In order to eliminate infinite velocity at the circular arc leading edge, the first 10% of the airfoil is replaced by a thickened profile having the same total loading but a velocity distribution similar to that of the actual stator blade section. The modified velocity is shown in Fig. 61.

For comparison with compressor data, it is useful to compute the entering and exit flow angles which correspond

to the calculated lift coefficient and chosen angle of attack.

For the chosen section, the blade setting angle is $\gamma = 61^\circ\ 12'$ (Table 4). Then with $\alpha_m = 5^\circ\ 26'$, $\gamma_m = \gamma - \alpha_m = 55^\circ\ 26'$. Since, by definition, $\Gamma = s\,\Delta C_u$ and $L = \rho V_m \Gamma = \frac{\rho}{2} V_m^2\, c\, C_L$ it follows that

$$\Delta C_u = \left(\frac{c}{s}\right) \frac{C_L}{2} V_m$$

Then for Ca = constant

$$\cot \gamma_1 = \frac{V_m \cos \gamma_m + \Delta C_u/2}{V_m \sin \gamma_m} = \cot \gamma_m + \left(\frac{c}{s}\right) \frac{C_L}{4 \sin \gamma_m}$$

$$\cot \gamma_2 = \frac{V_m \cos \gamma_m - \Delta C_u/2}{V_m \sin \gamma_m} = \cot \gamma_m - \left(\frac{c}{s}\right) \frac{C_L}{4 \sin \gamma_m}$$

For $C_L = 1.026$, $\gamma_m = 55^\circ\ 26'$ and $\frac{s}{c} = 1.0879$, $\gamma_1 = 46^\circ\ 0'$, $\gamma_2 = 68^\circ\ 26'$

And $\theta^* = \gamma_2 - \gamma_1 = 22^\circ\ 26'$ which is the calculated air turning angle.

Appendix V

Wall Boundary Layer Calculation

Illustrations of the application of the Kármán integral method to the calculation of cascade wall b. l. effects are given. The two-dimensional case is considered, i.e., a plane boundary is assumed (rather than the cylindrical boundary of an actual compressor) and the flow direction is everywhere parallel to the wall. It is further assumed that the flow pattern repeats after one cascade spacing.

The momentum integrals can be written in the manner of Ref. 11 for an element of axial length Δx, shown in Fig. 106.

In the X (axial) direction:

$$\frac{\partial}{\partial x}\int_0^{\delta}\int_0^{s} \rho u^2\, dy\, dz \cdot \Delta x - \iint_{\text{Top Surface}} \rho U^2\, dS = -\frac{\partial}{\partial x}\int_0^{\delta}\int_0^{s} p\, dy\, dz \cdot \Delta x + \int_0^{\delta}\int_0^{s} \rho f_x\, dy\, dz \cdot \Delta x - \int_0^{s} \tau_x\, dy \cdot \Delta x \tag{69}$$

In the Y (tangential) direction:

$$\frac{\partial}{\partial x}\int_0^{\delta}\int_0^{s} \rho u v\, dy\, dz \cdot \Delta x - \iint_{\text{Top Surface}} \rho U V\, dS = \int_0^{\delta}\int_0^{s} \rho f_y\, dy\, dz \cdot \Delta x - \int_0^{s} \tau_y\, dy \cdot \Delta x \tag{70}$$

with the notation defined by Fig. 106. The shear stresses τ_x and τ_y represent the effect of the bounding wall, while the body forces f_x and f_y arise from normal pressures and shear stresses on the surface of the immersed cascade airfoil. It has not been possible

to find any considerable simplification of Equations 69 and 70 in the general case, however, by restricting the problem somewhat, an illustration of their application is obtained.

The case treated is a cylindrical (untwisted) cascade of airfoils which intersects a fixed wall. The following assumptions are made:

a. The blades are untwisted.

b. The flow direction is known everywhere (infinite number of blades) and does not change with distance normal to the wall.

c. Shear forces on the immersed blade surfaces are neglected.

d. A (turbulent) boundary layer of known thickness exists upstream of the cascade and the flow has a constant axial component, i.e. U = const.

e. The static pressure is determined by flow outside the b. l. and does not change with distance normal to the wall.

f. Similarity prevails in the b. l. profile, i.e., H = const.

g. Steady, incompressible flow.

The notation is that of Fig. 106

For this case Eqs. 69 and 70 reduce to

$$\frac{d}{dx}\int_0^\delta u^2\,dz - U\frac{d}{dx}\int_0^\delta u\,dz = -\frac{\delta}{\rho}\frac{dp}{dx} - \frac{\tau_x}{\rho} + \int_0^\delta f_x\,dz$$

and

$$\frac{d}{dx}\left[\cot\gamma\int_0^\delta u^2\,dz\right] - U\cot\gamma\,\frac{d}{dx}\int_0^\delta u\,dz = -\frac{\tau_y}{\rho} + \int_0^\delta f_y\,dz$$

where $\delta = \delta(x)$ only. Then writing $u = U-(U-u)$ and integrating

$$-\frac{dU}{dx}\int_0^\delta (U-u)\,dz - \frac{d}{dx}\int_0^\delta u(U-u)\,dz = -U\delta\frac{dU}{dx} - \frac{\delta}{\rho}\frac{dp}{dx} - \frac{\tau_x}{\rho} + \int_0^\delta f_x\,dz$$

and

$$-\frac{d(U\cot\gamma)}{dx}\int_0^\delta (U-u)\,dz - \frac{d}{dx}\left[\cot\gamma\int_0^\delta u(U-u)\,dz\right] = -U\delta\frac{d}{dx}(U\cot\gamma) - \frac{\tau_y}{\rho} + \int_0^\delta f_y\,dz$$

Since here f represents the (normal) body force from the blade action

$$f_x = -f\sin\gamma \qquad \text{and} \qquad f_y = f\cos\gamma$$

and if the wall shear stress is τ_0, then

$$\tau_x = \tau_0\sin\gamma \qquad \tau_y = \tau_0\cos\gamma$$

Furthermore, the Bernoulli equation applies outside the b. l., hence

$$p = \text{const.} - \frac{\rho}{2}U^2\cot^2\gamma \qquad \text{since} \qquad \frac{dU}{dx} = 0$$

Introducing these relations, multiplying the resulting equations by $\sin x$ and $\cos x$ respectively and adding, the force integrals are eliminated

$$-U\cos\gamma\,\frac{d}{dx}(\cot\gamma)\int_0^\delta (U-u)\,dz - \sin\gamma\,\frac{d}{dx}\int_0^\delta u(U-u)\,dz$$

$$-\cos\gamma\,\frac{d}{dx}\left[\cot\gamma\int_0^\delta u(U-u)\,dz\right] = -\frac{\tau_0}{\rho}$$

but in this form, since $u \to U$ as $z \to \delta$, we may let $\delta \to \infty$ and defining

$$U\delta^* = \int_0^\infty (U-u)\,dz \qquad U^2\vartheta = \int_0^\infty u(U-u)\,dz$$

a differential equation in the b. l. parameters is obtained

$$\frac{d\vartheta}{dx} + \vartheta\left(1+\frac{\delta^*}{\vartheta}\right)\frac{1}{W}\frac{dW}{dx} = \frac{1}{\sin\gamma}\,\frac{\tau_0}{\rho W^2} \tag{71}$$

where

$$W^2 = U^2 + V^2 = U^2(1+\cot^2\gamma)$$

This equation is easily integrated by the method of Ref. 27. It is assumed that $H = \frac{\delta^*}{\vartheta}$ = const. and that the (turbulent) b. l. wall shear is given in the form

$$\frac{\tau_0}{\rho W^2} = \frac{k}{R_\vartheta^{\,n}}$$

where

$$R_\vartheta = \frac{\vartheta W}{\nu}$$

Then integrating between the l. e. (1) and t. e. (2) planes

$$\frac{\vartheta_2}{c} = (\sin\gamma_2)^{H+1}\left[\frac{k(n+1)}{R_c^{\,n}}\int_1^2 (\sin\gamma)^{(n-1)-(n+1)(H+1)}\,d\left(\frac{x}{c}\right) + \left(\frac{\vartheta_1}{c}\right)^{n+1}(\sin\gamma_1)^{-(n+1)(H+1)}\right]^{\frac{1}{n+1}} \tag{72}$$

where $R_c = \frac{cU}{\nu}$ and $\gamma = \gamma(x)$ is presumed to be a known function.

As an illustration of orders of magnitude, consider a compressor cascade under the following conditions:

$\gamma_1 = 70^\circ$, $\gamma_2 = 90^\circ$, $c = .25$ ft., $\frac{\vartheta_1}{c} = .005$, $U = 50\,\frac{ft.}{sec.}$

$\nu = 1.6 \times 10^{-4}$ ft.^{2}/sec., $R_c = 78{,}000$, $k = .017$,

$n \doteq .29$ (Ref. 27), $H = 1.40$

Then $(n-1) - (n+1)(H+1) = -3.81$,

$$\frac{K(n+1)}{R_c^n} = 8.37 \times 10^{-4} \quad , \quad \frac{\left(\frac{\vartheta_1}{c}\right)^{n+1}}{(\sin\gamma_1)^{(n+1)(H+1)}} = 1.57 \times 10^{-3}$$

Now

$$(\sin\gamma_1)^{-3.81} = 1.27 \quad , \quad (\sin\gamma_2)^{-3.81} = 1.00 \quad , \quad \Delta\left(\frac{x}{c}\right) \doteq .94 \quad \text{say,}$$

then $$\int_1^2 (\sin\gamma_1)^{-3.81} \, d\left(\frac{x}{c}\right) = 1.2 \text{ approximately.}$$

Hence

$$\left(\frac{\vartheta_2}{c}\right) = (\sin\gamma_2)^{H+1}\left[\frac{K(n+1)}{R_c^n}\int_1^2 (\sin\gamma)^{(n-1)-(n+1)(H+1)} \, d\left(\frac{x}{c}\right) + \left(\frac{\vartheta_1}{c}\right)^{n+1}(\sin\gamma_1)^{-(n+1)(H+1)}\right]^{\frac{1}{n+1}}$$

$$= \left[1 \times 10^{-3} + 1.57 \times 10^{-3}\right]^{\frac{1}{1.29}} = 9.8 \times 10^{-3}$$

or

$$\frac{\vartheta_2}{\vartheta_1} = 1.96$$

Unfortunately no adequate test data on wall b. l. in a two-dimensional cascade are available for comparison with the results of Eq. 72. However, it is clear that, although the action of an adverse pressure gradient through a stationary compressor cascade in increasing the rate of wall b. l. growth is indicated (Ref. 6), numerical results might be in considerable error, since interaction between blade and wall b. l.'s is not taken into account. For the same reason, and in addition, because of tip leakage, blade twist and secondary (radial) flow, application of the more general b. l. equations to actual compressor stages is difficult.

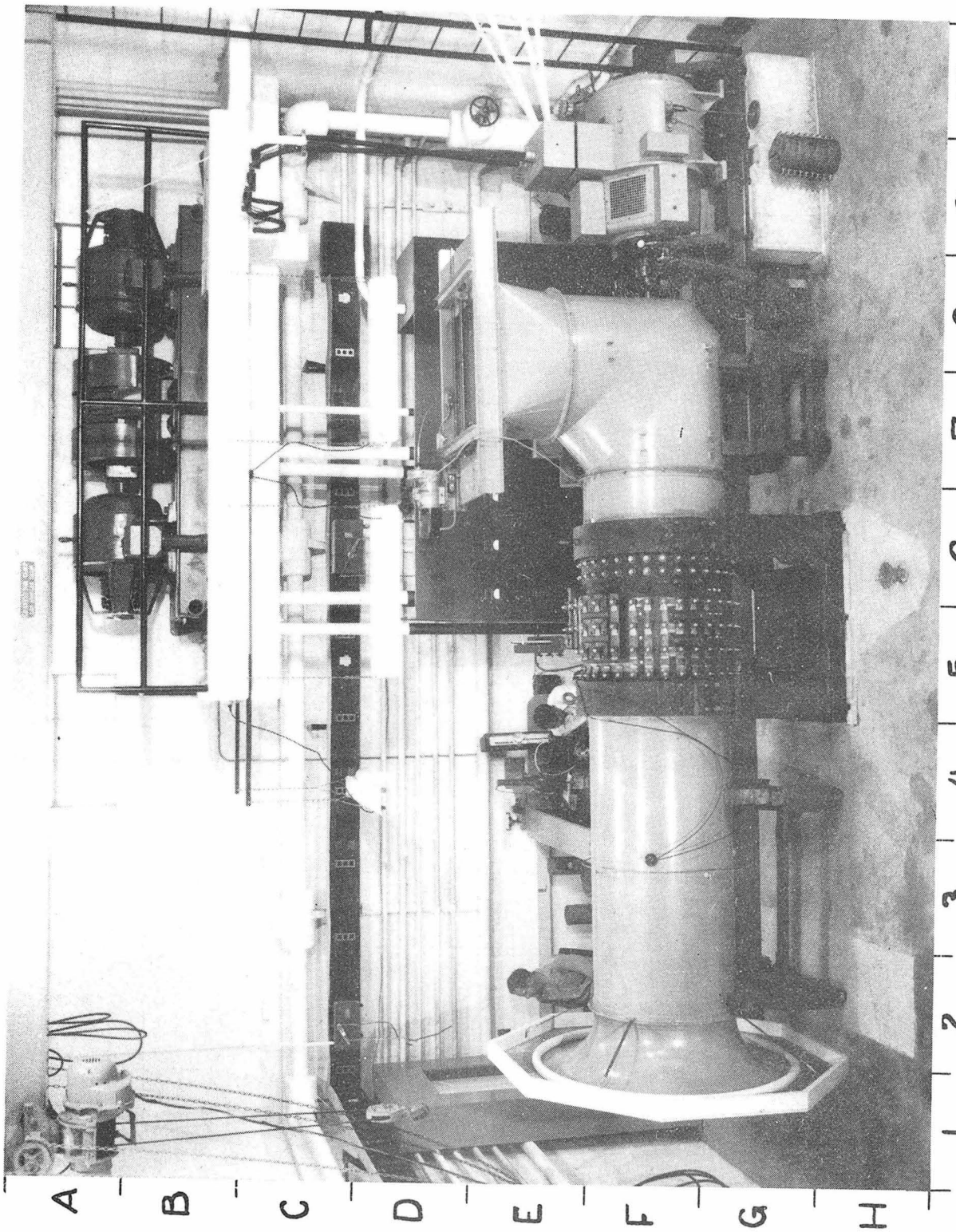

FIG. 1 GENERAL VIEW OF TEST INSTALLATION (SEE SEC. 2.1.2)

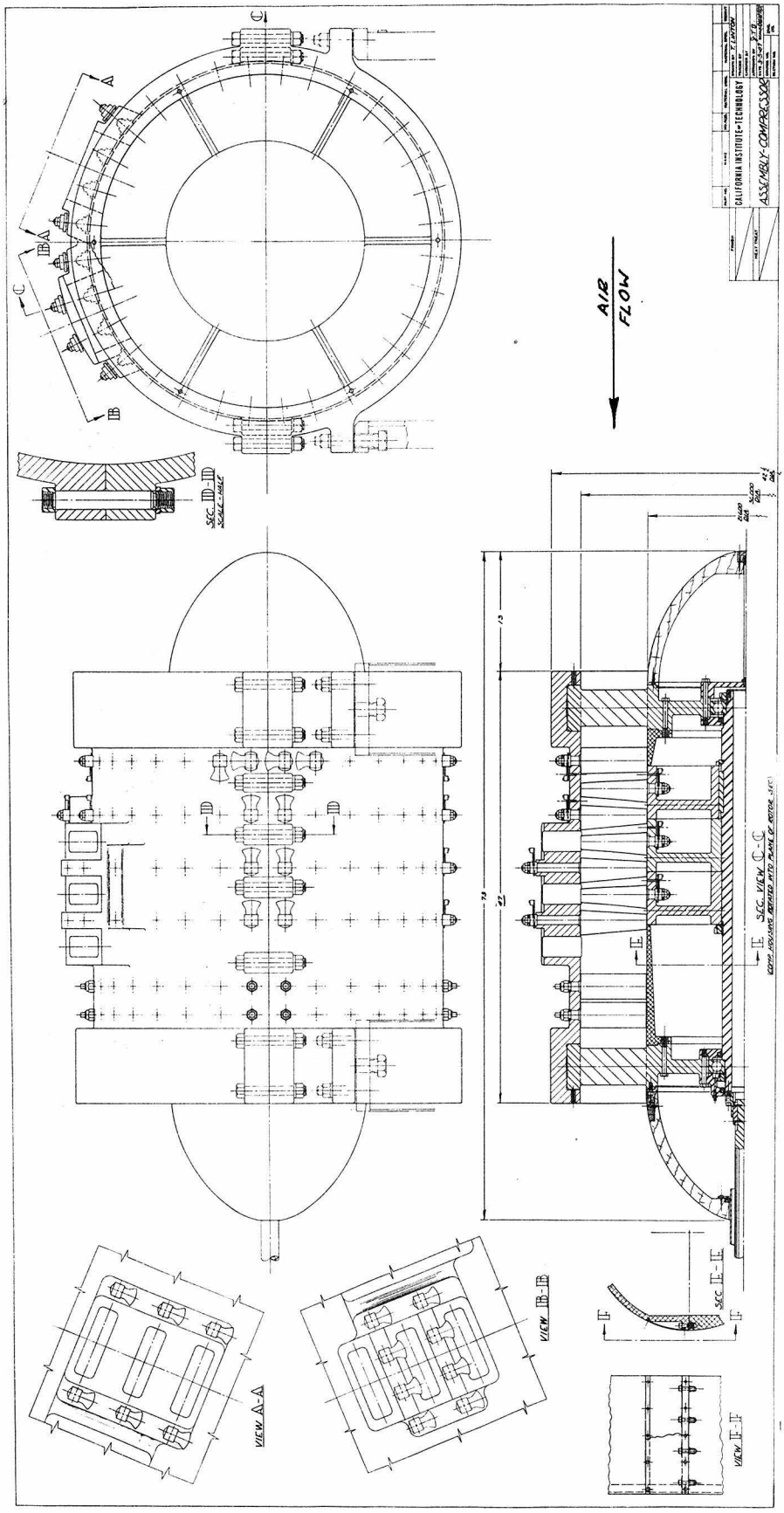
AIR FLOW
CALIFORNIA INSTITUTE of TECHNOLOGY
ASSEMBLY-COMPRESSOR
SEC. D-D
SCALE: HALF
VIEW A-A
VIEW B-B
SEC. E-E
VIEW E-F
SEC. C-C

Fig. 2

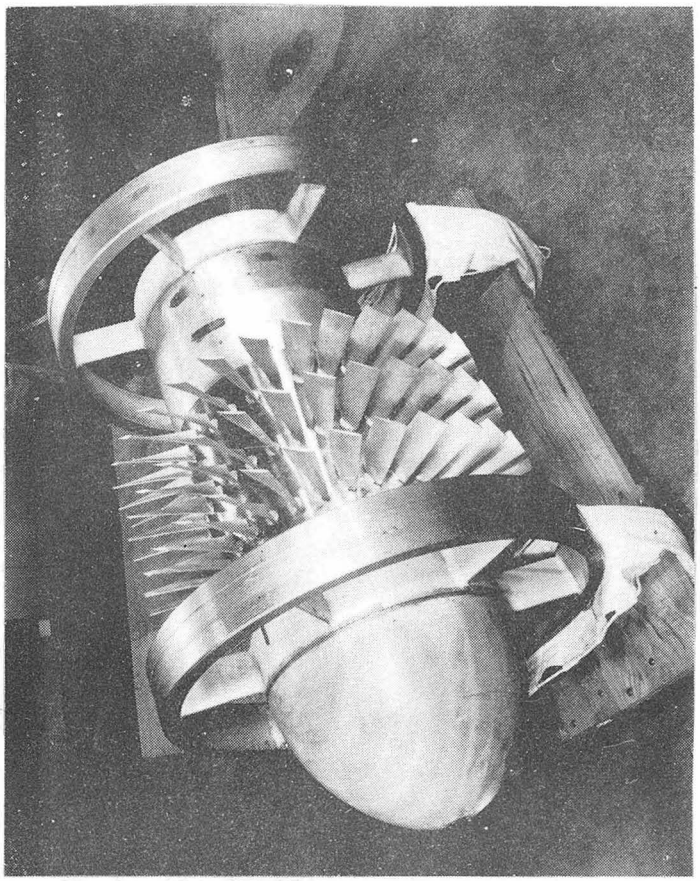

FIG. 4 ROTOR ASSEMBLY

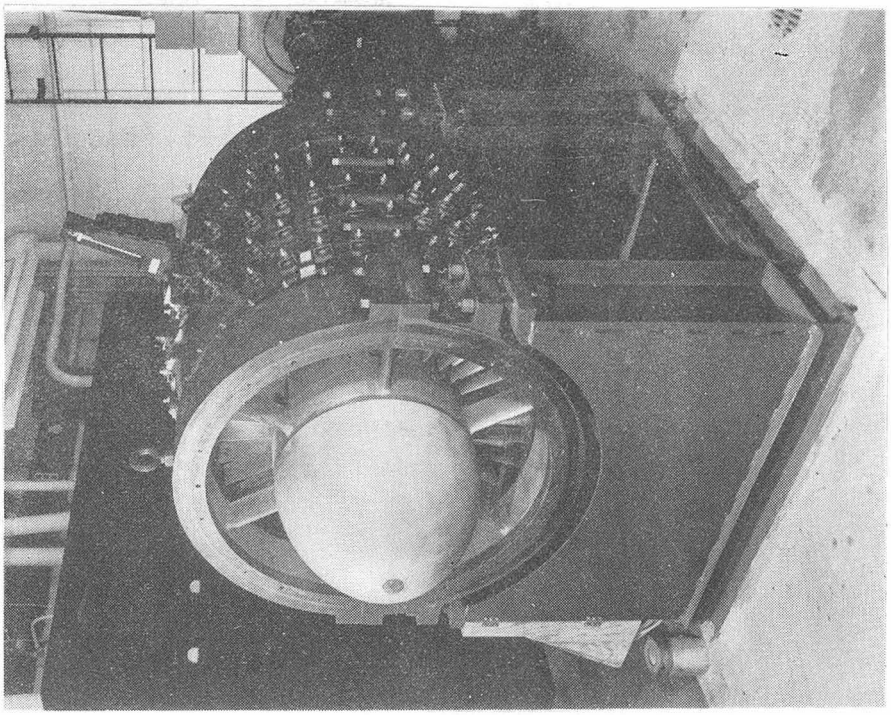

FIG. 3 ASSEMBLED TEST COMPRESSOR

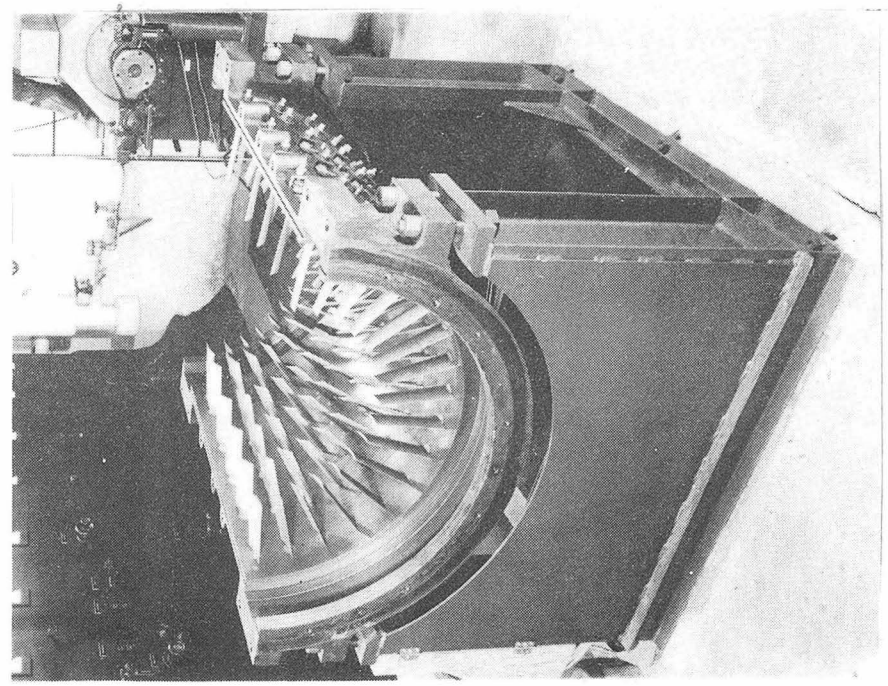

Fig. 6 LOWER HALF OF COMPRESSOR CASE

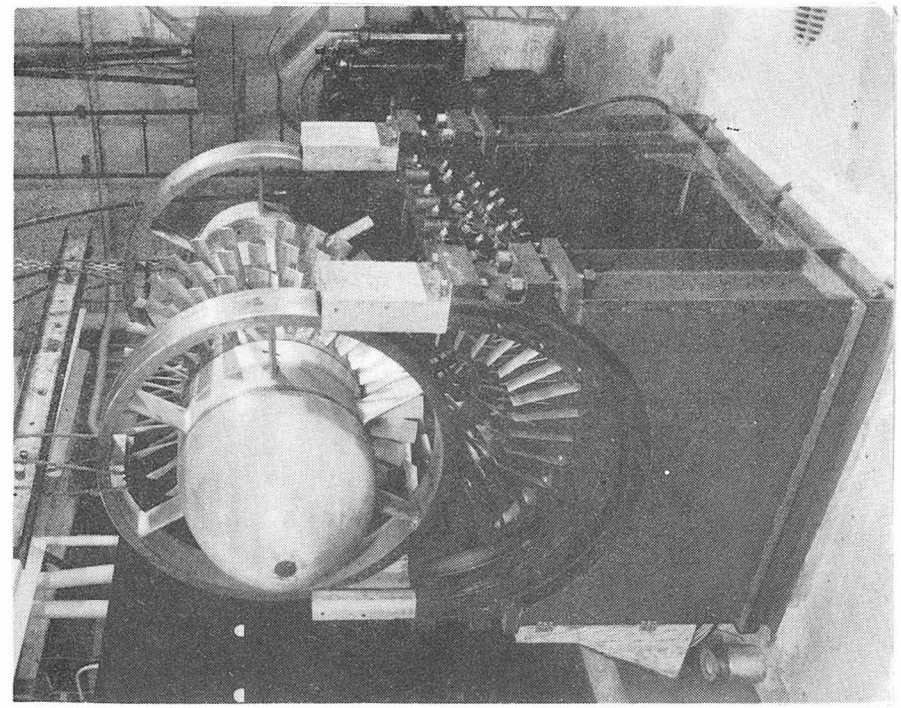

Fig. 5 ROTOR ASSEMBLY BEING PLACED IN CASE

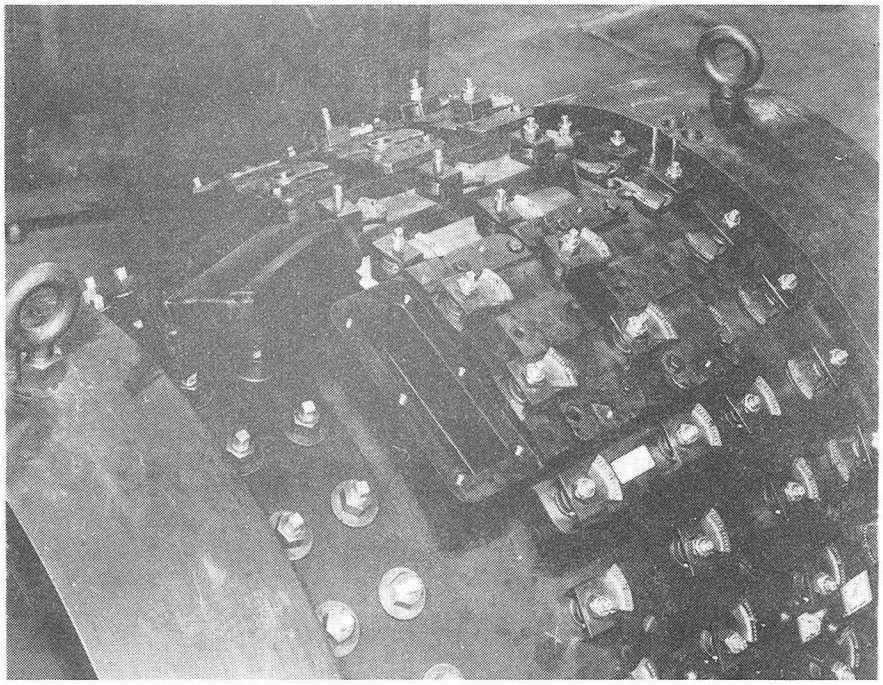

FIG. 7 DETAIL OF INSTRUMENT PARTS AND STATOR BLADE FASTENINGS

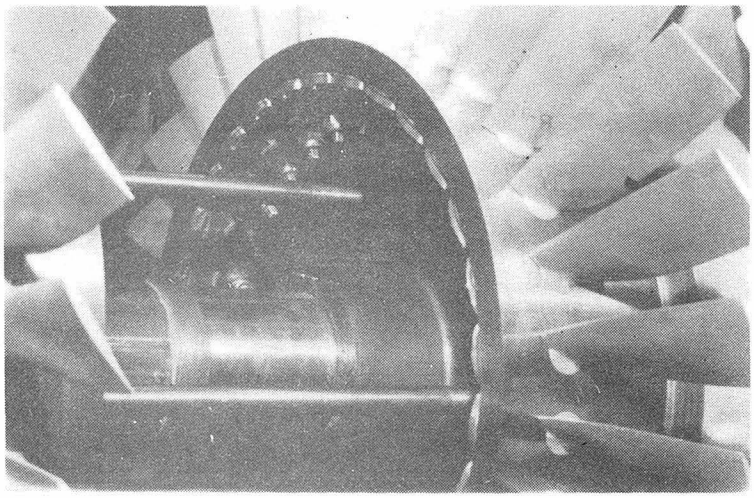

FIG. 8 DETAIL OF ROTOR AND ROTOR BLADE FASTENING

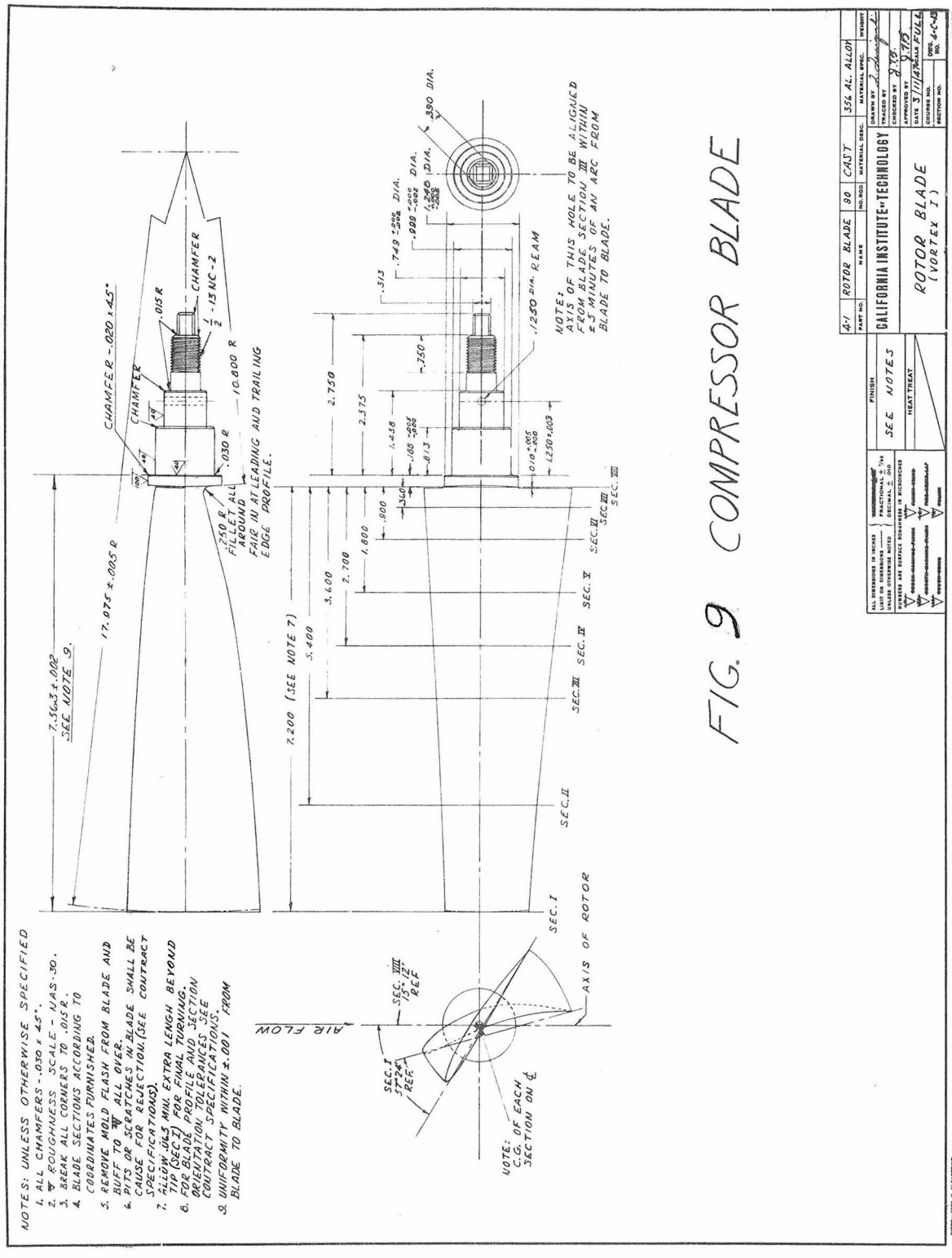

FIG. 9 COMPRESSOR BLADE

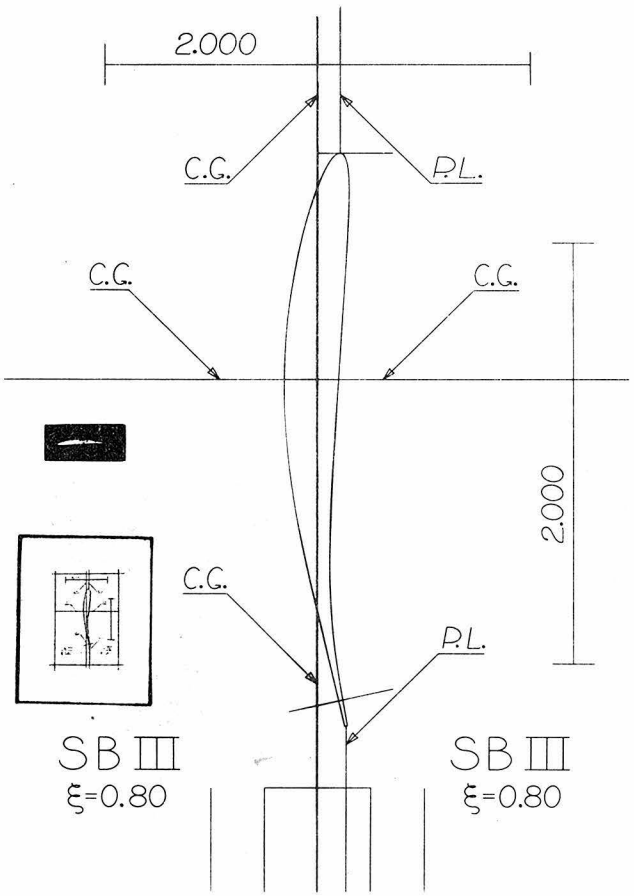

FIG. 10 MASTER BLADE DRAWING

THE PHOTOGRAPH SHOWS A 10X DRAWING OF A BLADE SECTION. A FULL SIZE PRINT OF THIS SECTION ON TEMPLET STOCK IS SHOWN IN THE UPPER LEFT CORNER AND AN ACTUALLY CROSSECTIONED BLADE IS SHOWN NEXT TO IT.

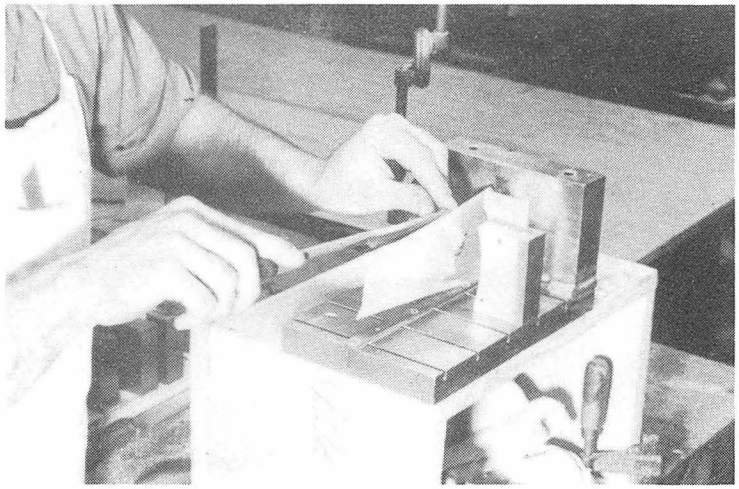

FIG. 11 BLADE BEING FINISHED.

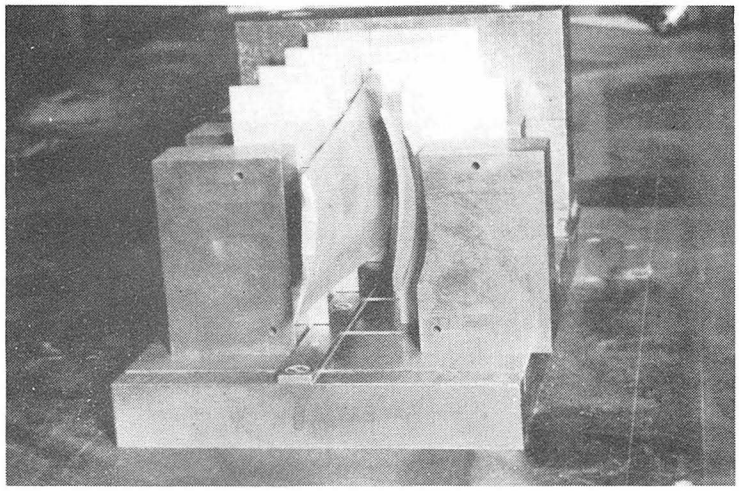

FIG. 12 BLADE BEING FINISHED WITH SECTION TEMPLATES.

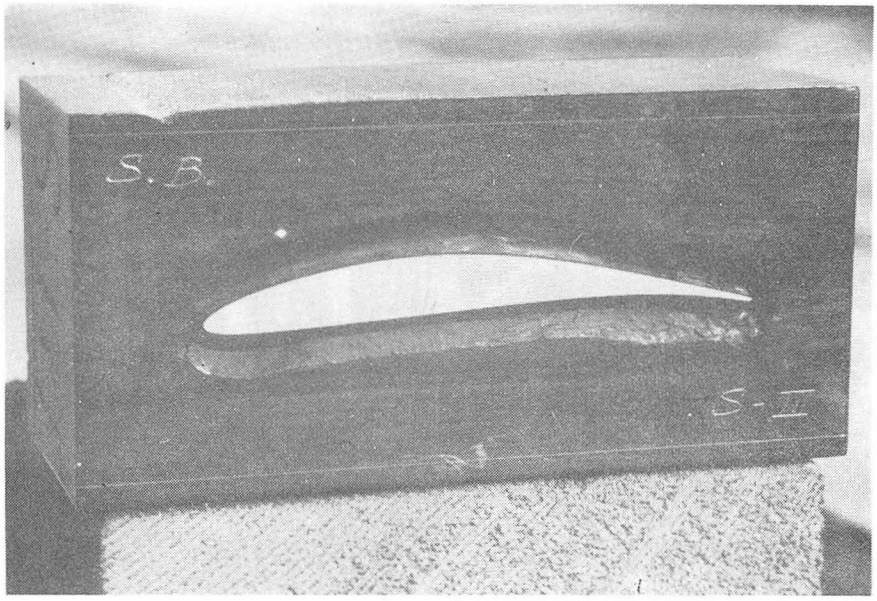

FIG. 13 A BLADE CROSS-SECTION

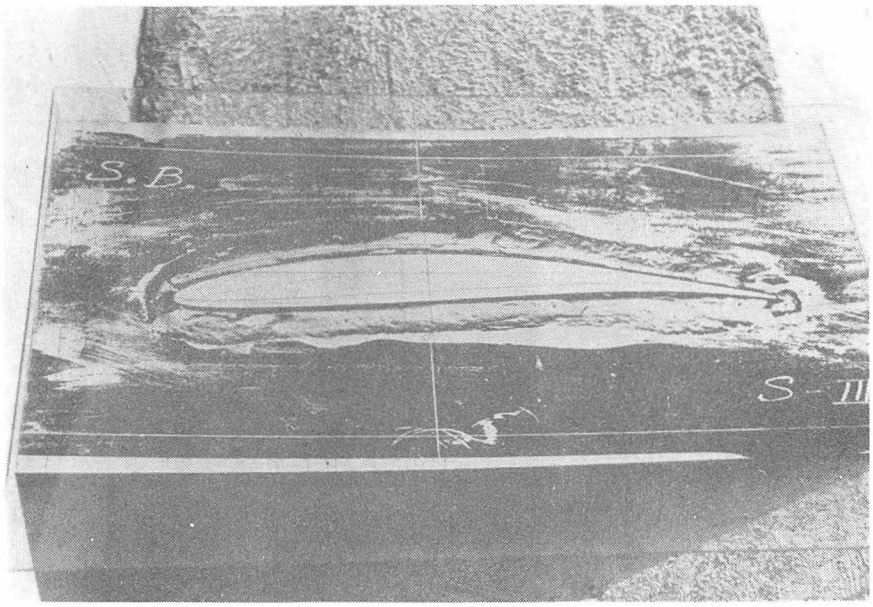

FIG. 14 SECTION COMPARISON TEST

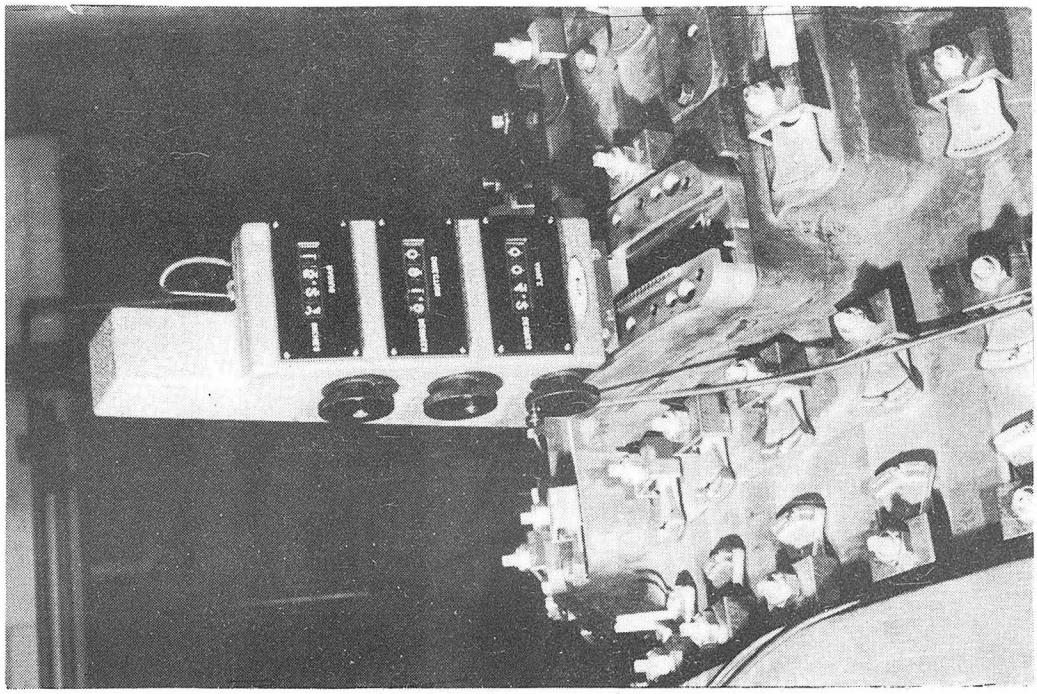

FIG. 16 INSTRUMENT CARRIAGE INSTALLED IN PORT

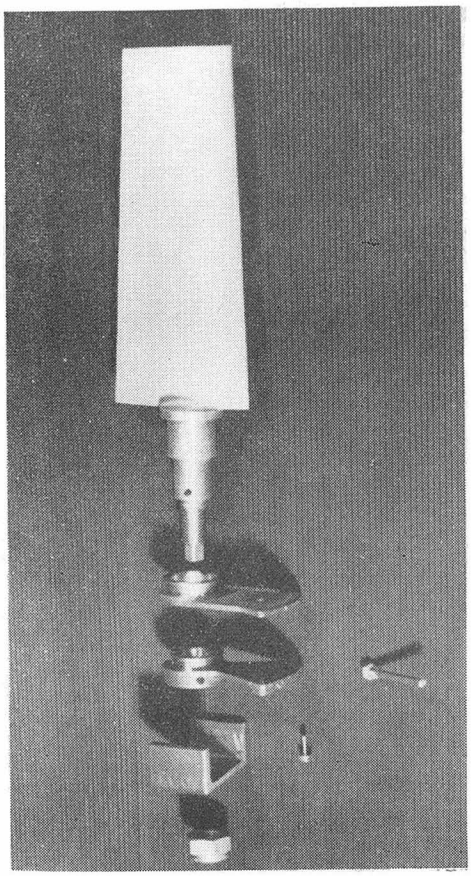

FIG. 15 DETAIL OF BLADE FASTENING MECHANISM

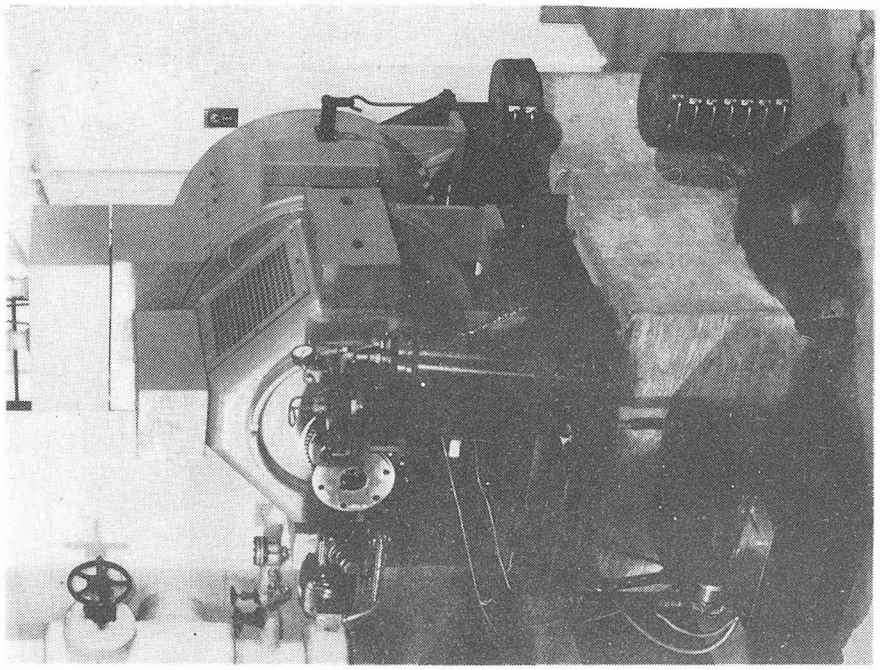

FIG. 18 THE DYNAMOMETER WITH DRIVE REMOVED

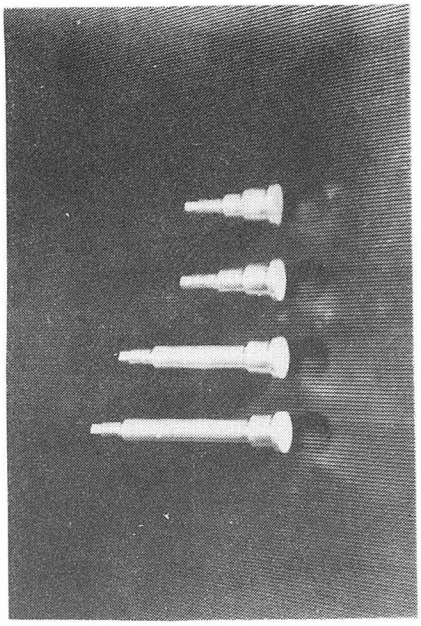

FIG. 17 ROTOR AND STATOR BLADE BLANK PLUGS

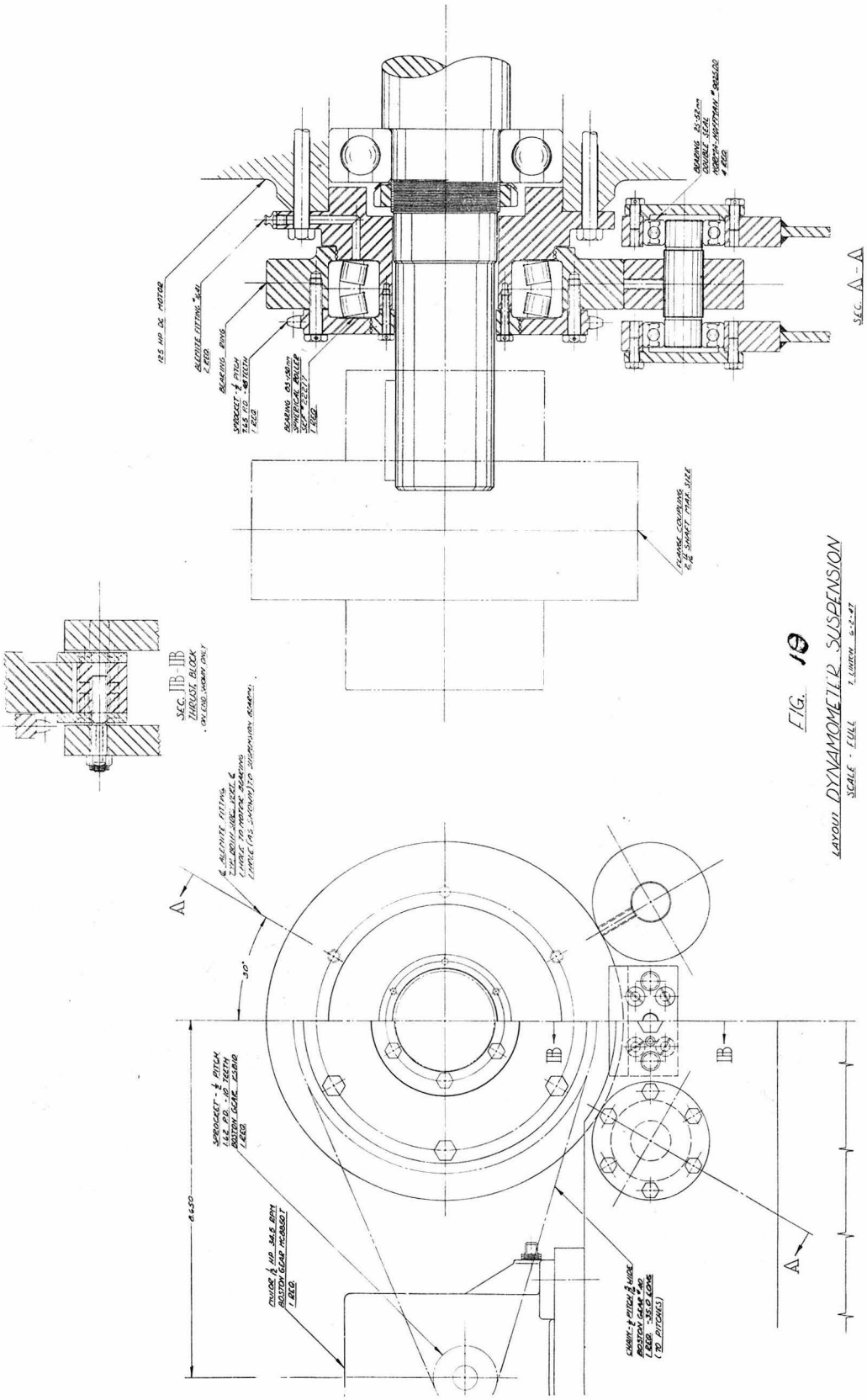
SEC. A-A
SEC. JB-JB
THRUST BLOCK
ON LOAD WORM ONLY
LAYOUT DYNAMOMETER SUSPENSION
SCALE - FULL

FIG. 19

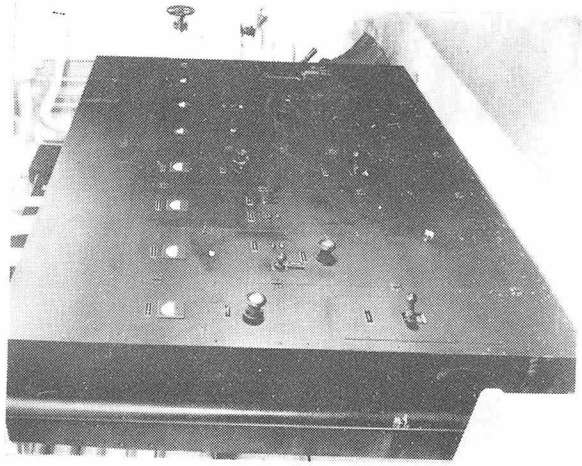

FIG. 22 DYNAMOMETER CONTROL

FIG. 20 DYNAMOMETER SUPPORT BEARINGS

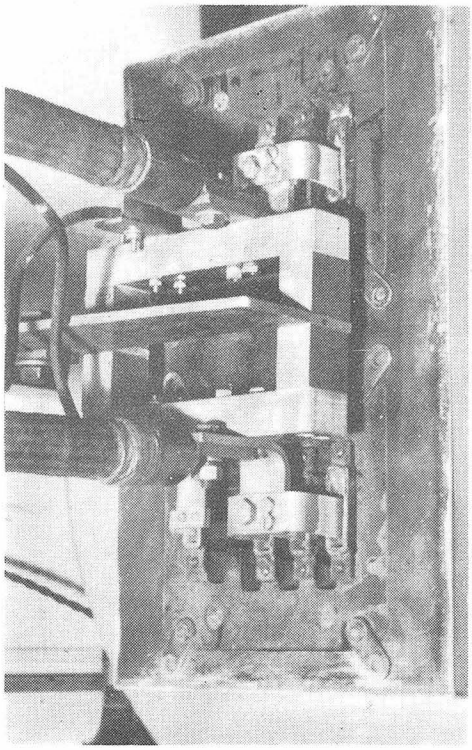

FIG. 21 DYNAMOMETER MERCURY CONTACT

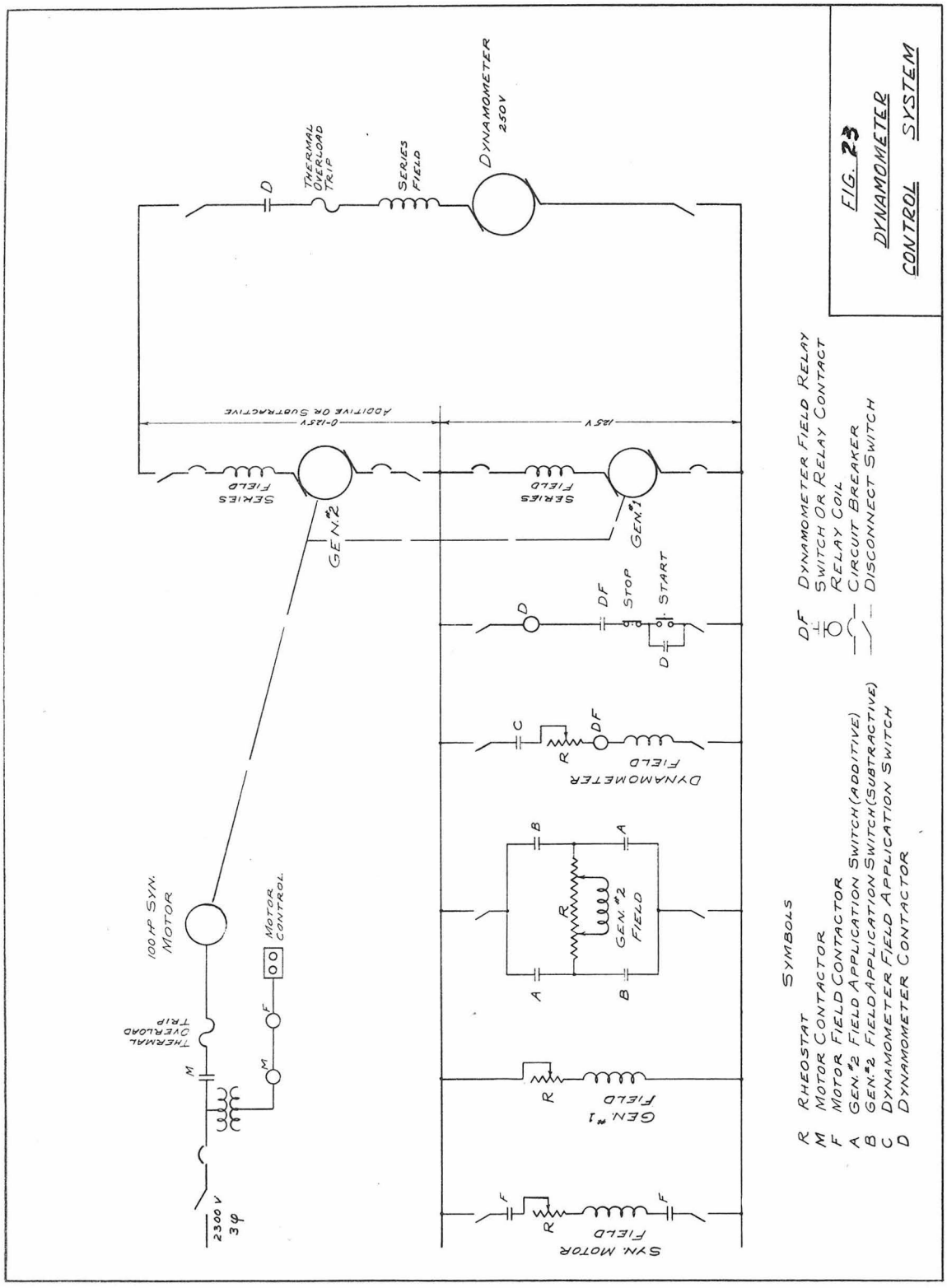

FIG. 23
DYNAMOMETER CONTROL SYSTEM

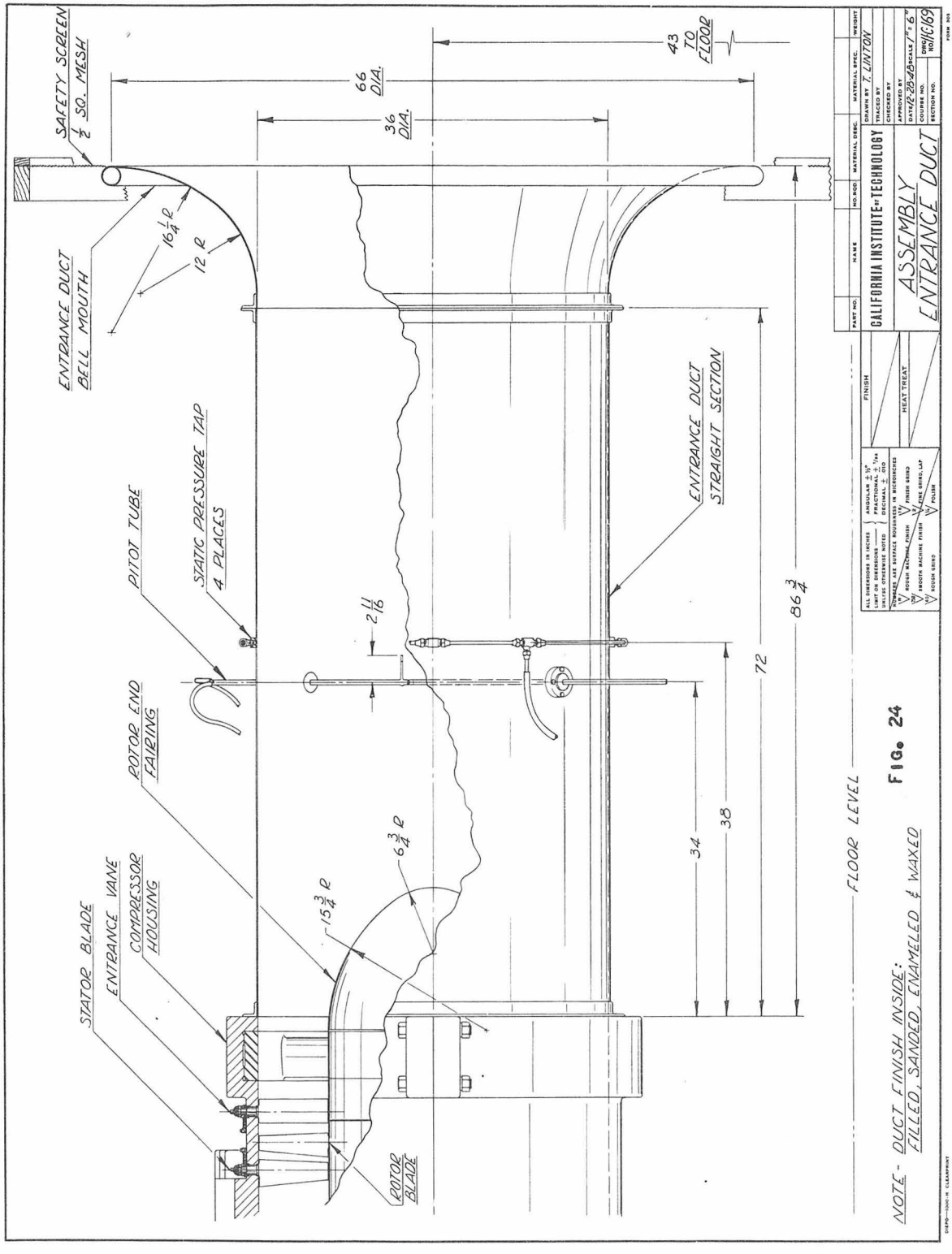

Fig. 24

NOTE - DUCT FINISH INSIDE:
FILLED, SANDED, ENAMELED & WAXED

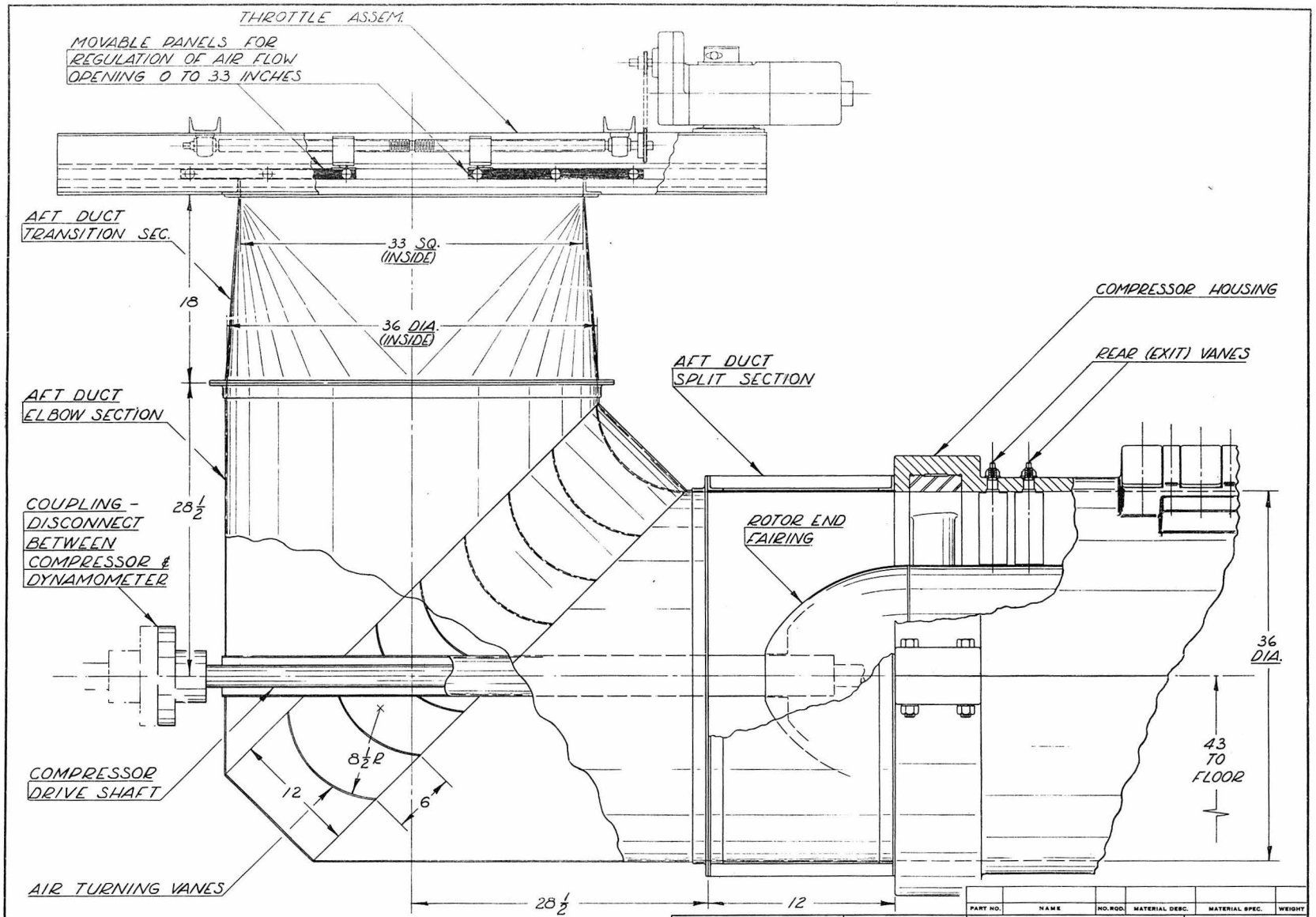

FIG. 25

PART NO.	NAME	NO. REQ.	MATERIAL DESC.	MATERIAL SPEC.	WEIGHT

ALL DIMENSIONS IN INCHES
LIMIT ON DIMENSIONS — UNLESS OTHERWISE NOTED
ANGULAR ± ½°
FRACTIONAL ± 1/32
DECIMAL ± .010

NUMBERS ARE SURFACE ROUGHNESS IN MICROINCHES
125 ROUGH MACHINE FINISH
63 SMOOTH MACHINE FINISH
32 ROUGH GRIND
16 FINISH GRIND
8 FINE GRIND, LAP
4 POLISH

FINISH
HEAT TREAT

CALIFORNIA INSTITUTE OF TECHNOLOGY

DRAWN BY T. LINTON
TRACED BY
CHECKED BY
APPROVED BY
DATE 1-18-49 SCALE 1" = 6"
COURSE NO. DWG NO. 1-G-170
SECTION NO.

ASSEMBLY AFT DUCTS

DIEPO—1000-H CLEARPRINT

FORM 303

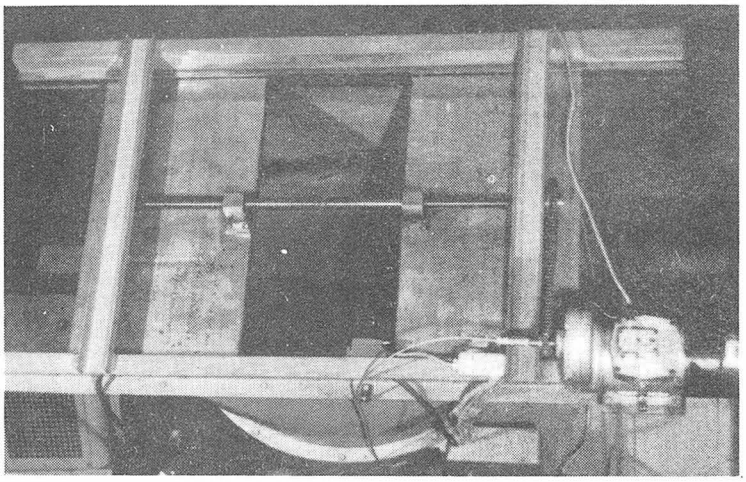

FIG. 26 THE THROTTLE VALVE

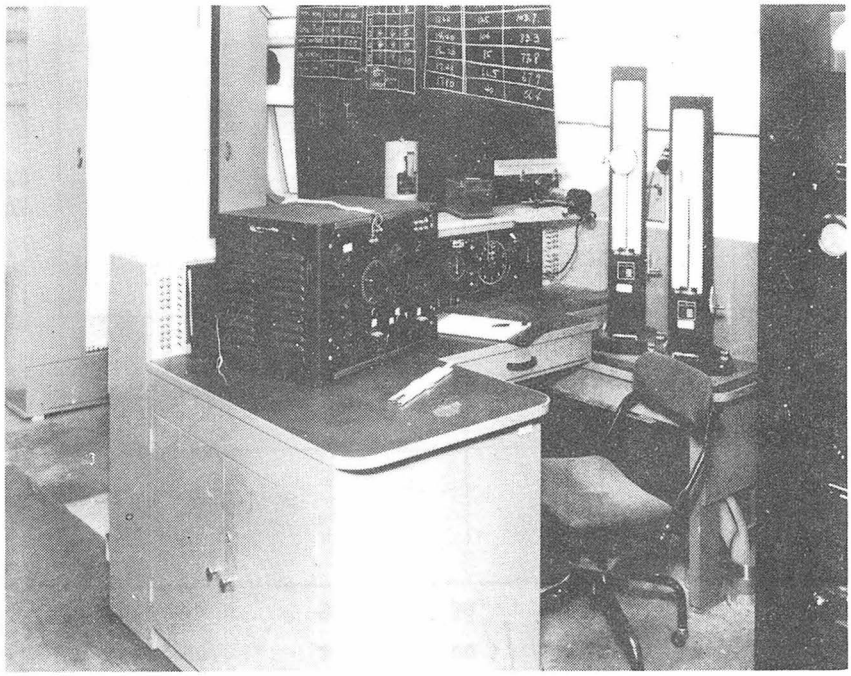

FIG. 27 THE OPERATING DESK

IN THE CENTER OF THE DESK THE TACHOMETER DIALS ARE SHOWN. THE CENTER DIAL IS FOR INSTANTANEOUS INDICATION. THE RIGHT HAND DIAL IS A CLOCK AND THE LEFT HAND DIAL A REVOLUTION COUNTER. THE TWO ARE COUPLED. ON THE DESK, TO THE RIGHT, TWO MERIAM MICRO MANOMETERS ARE SHOWN AND THE INSTRUMENT CASE TO THE LEFT CONTAINS THE BRIDGE FOR THE STATHAM PRESSURE GAGE. THE LEADS FROM THE GAGE ARE SEEN ON THE TOP OF THE BOX. IN THE BACKGROUND THE 20-TUBE MANOMETER IS SHOWN.

Fig. 28

DYNAMOMETER TORQUE CALIBRATION CURVE

FOR AXIAL-FLOW COMPRESSOR

C. I. T.

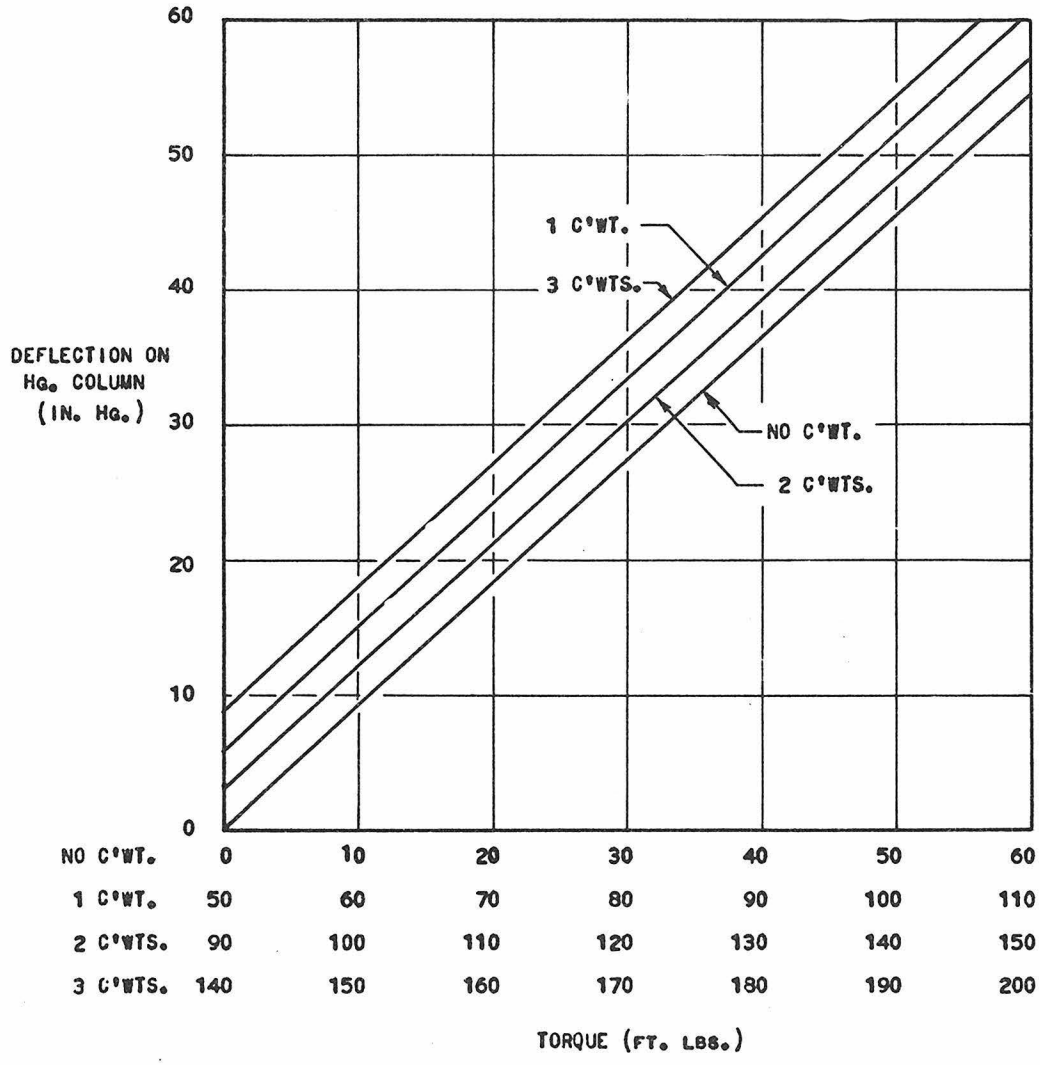

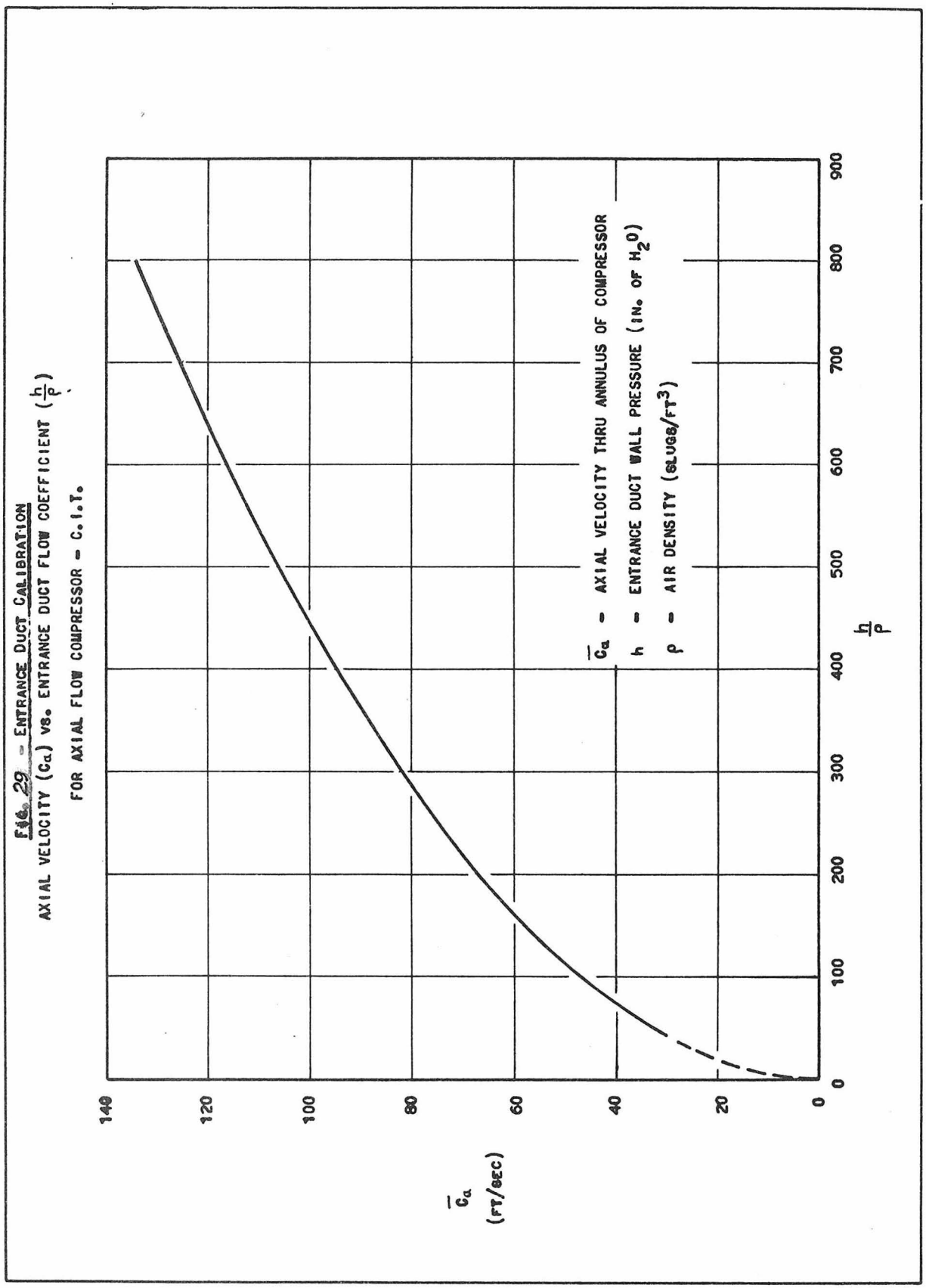

Fig. 29 - ENTRANCE DUCT CALIBRATION
AXIAL VELOCITY (C_a) vs. ENTRANCE DUCT FLOW COEFFICIENT ($\frac{h}{\rho}$)
FOR AXIAL FLOW COMPRESSOR - C.I.T.

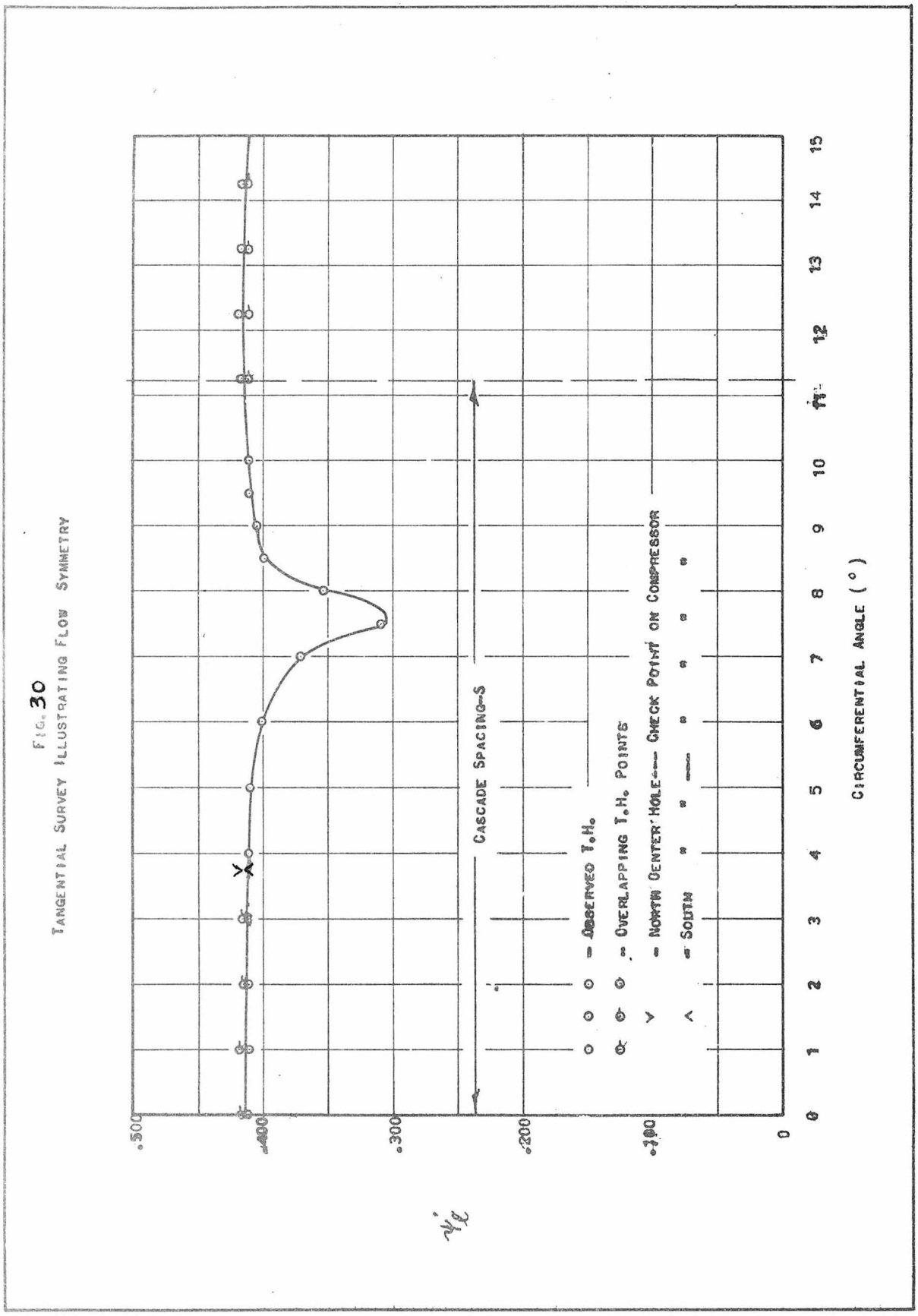

FIG. 30
TANGENTIAL SURVEY ILLUSTRATING FLOW SYMMETRY

FIG. 31

MEASURING PROBES

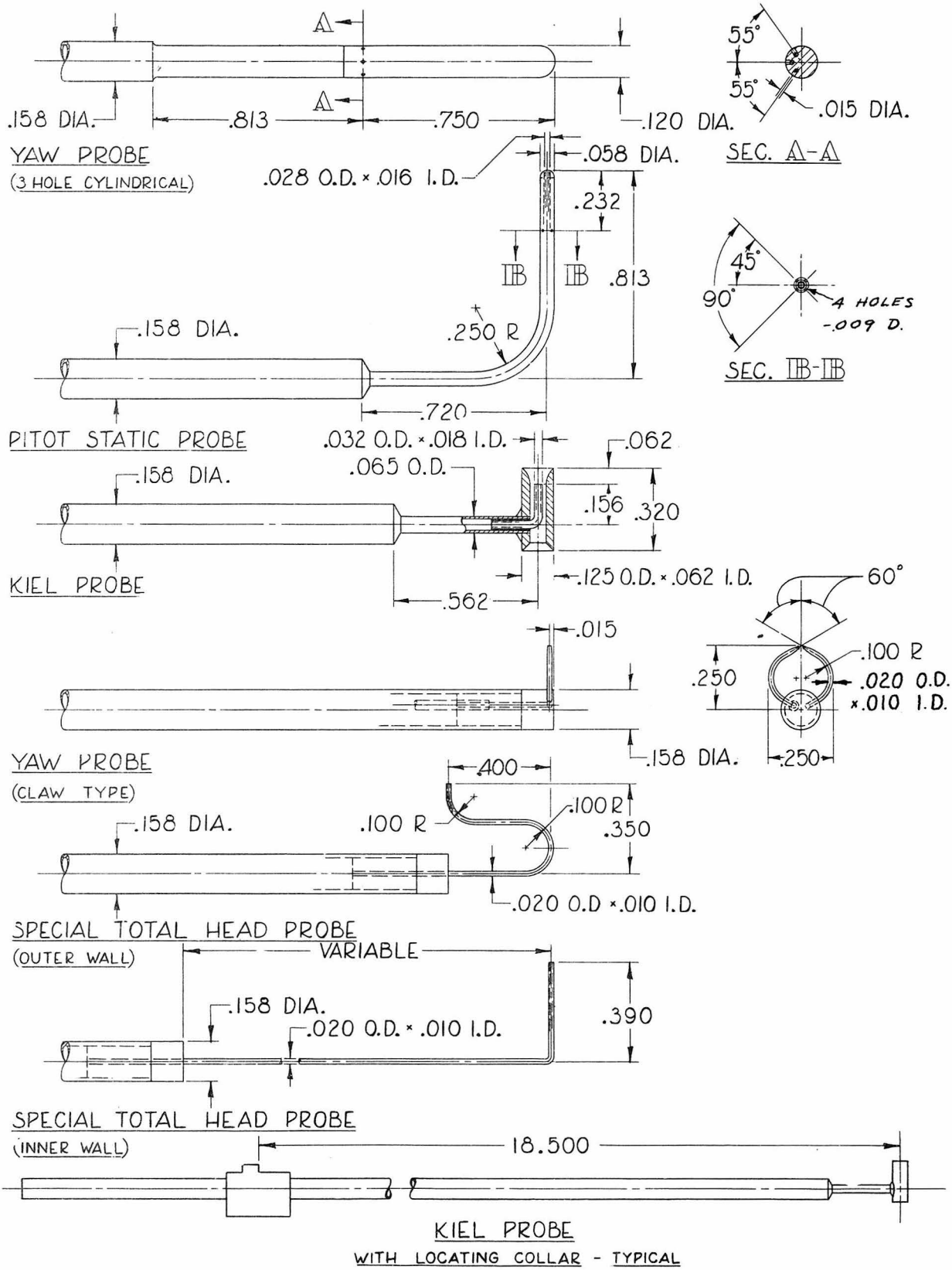

FIG. 32

KIEL TYPE TOTAL PRESSURE PROBE

- DIRECTION SENSITIVITY -

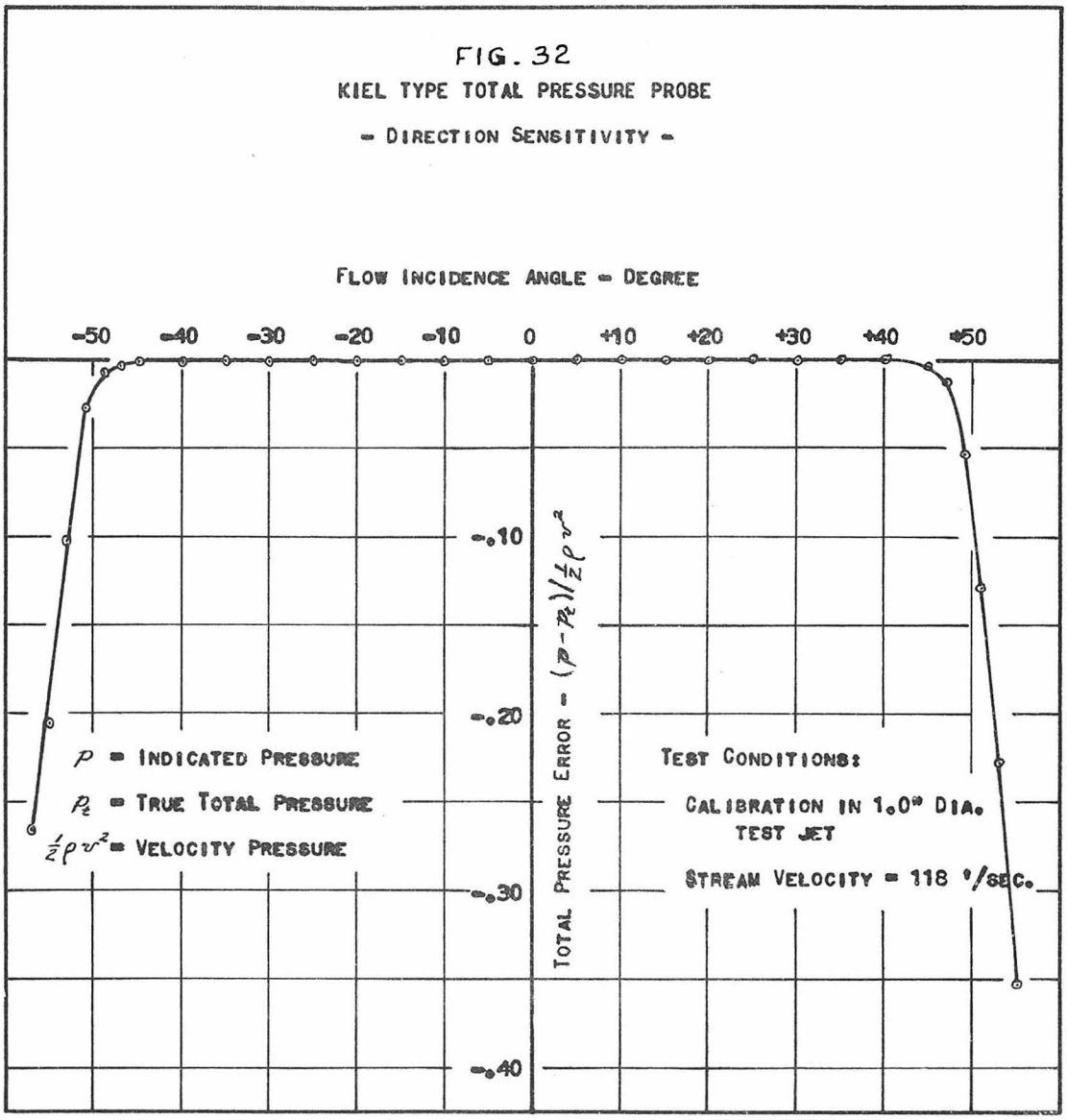

FIG. 33

PITOT TUBE - DIRECTION SENSITIVITY

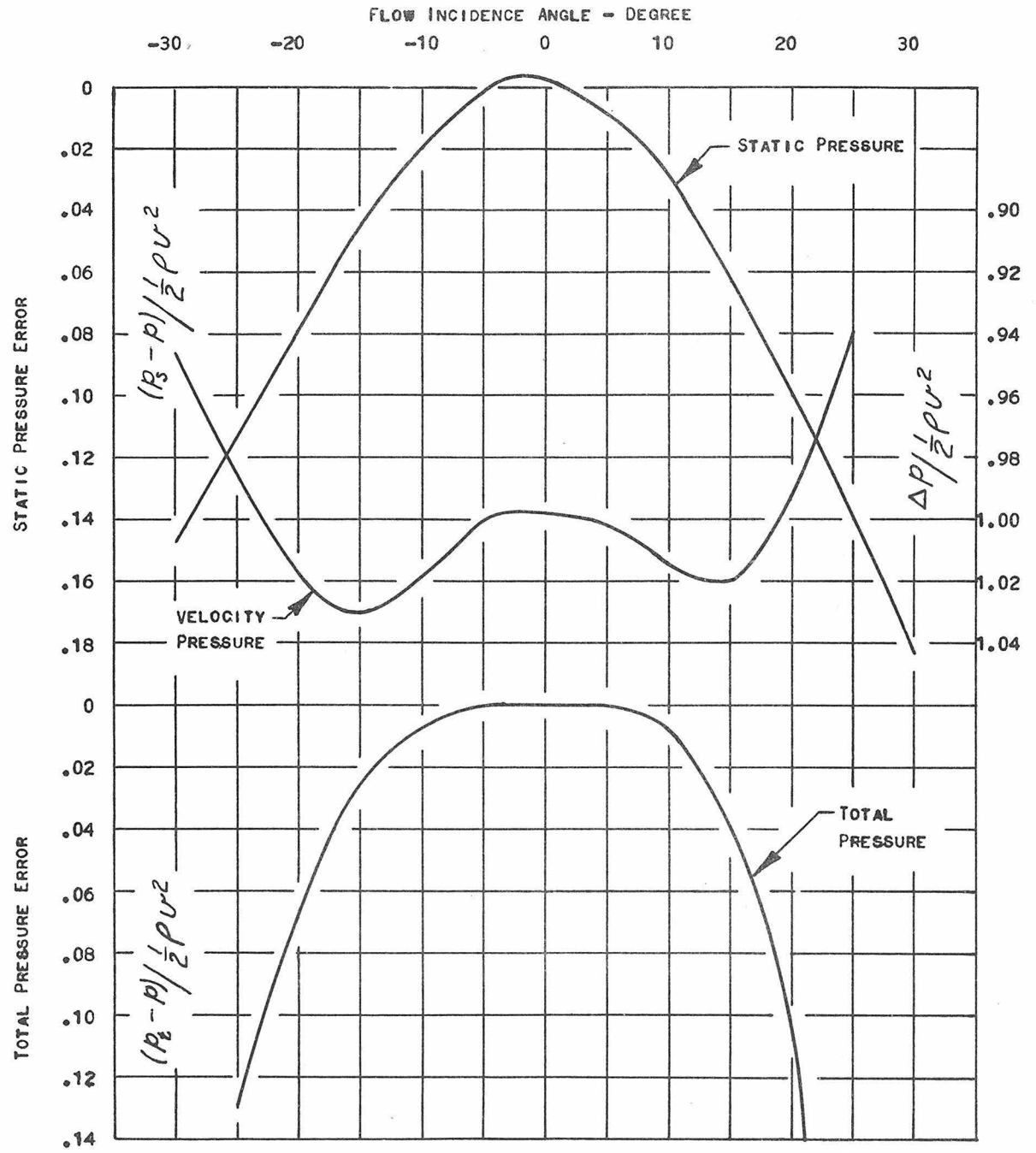

p = INDICATED PRESSURE

Δp = INDICATED DIFFERENTIAL

p_t = TRUE TOTAL PRESSURE

p_s = TRUE STATIC PRESSURE

$\frac{1}{2}\rho v^2$ = TRUE VELOCITY PRESSURE

DATA REPRODUCED FROM REF. 2

FIG. 34

SPECIAL TOTAL PRESSURE PROBE

▲ DIRECTION SENSITIVITY▲

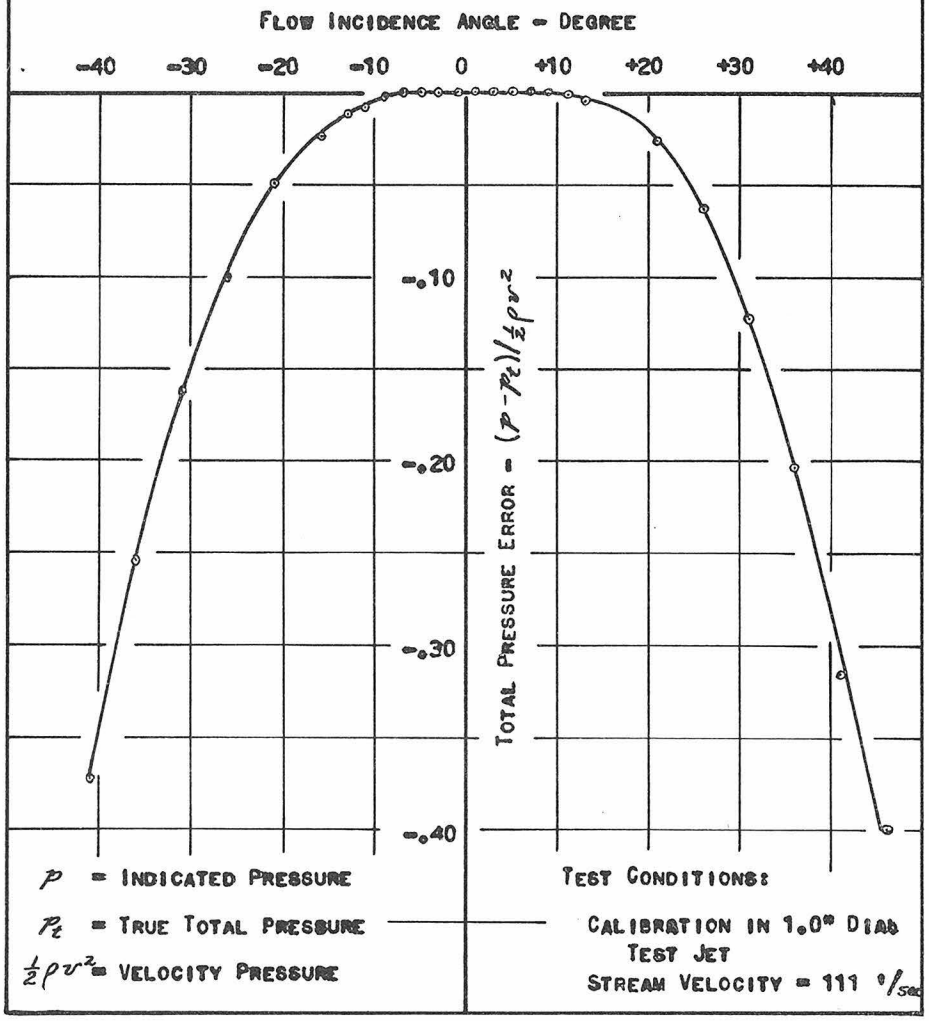

FIG. 35

CYLINDRICAL YAW PROBE

-DIRECTION SENSITIVITY-

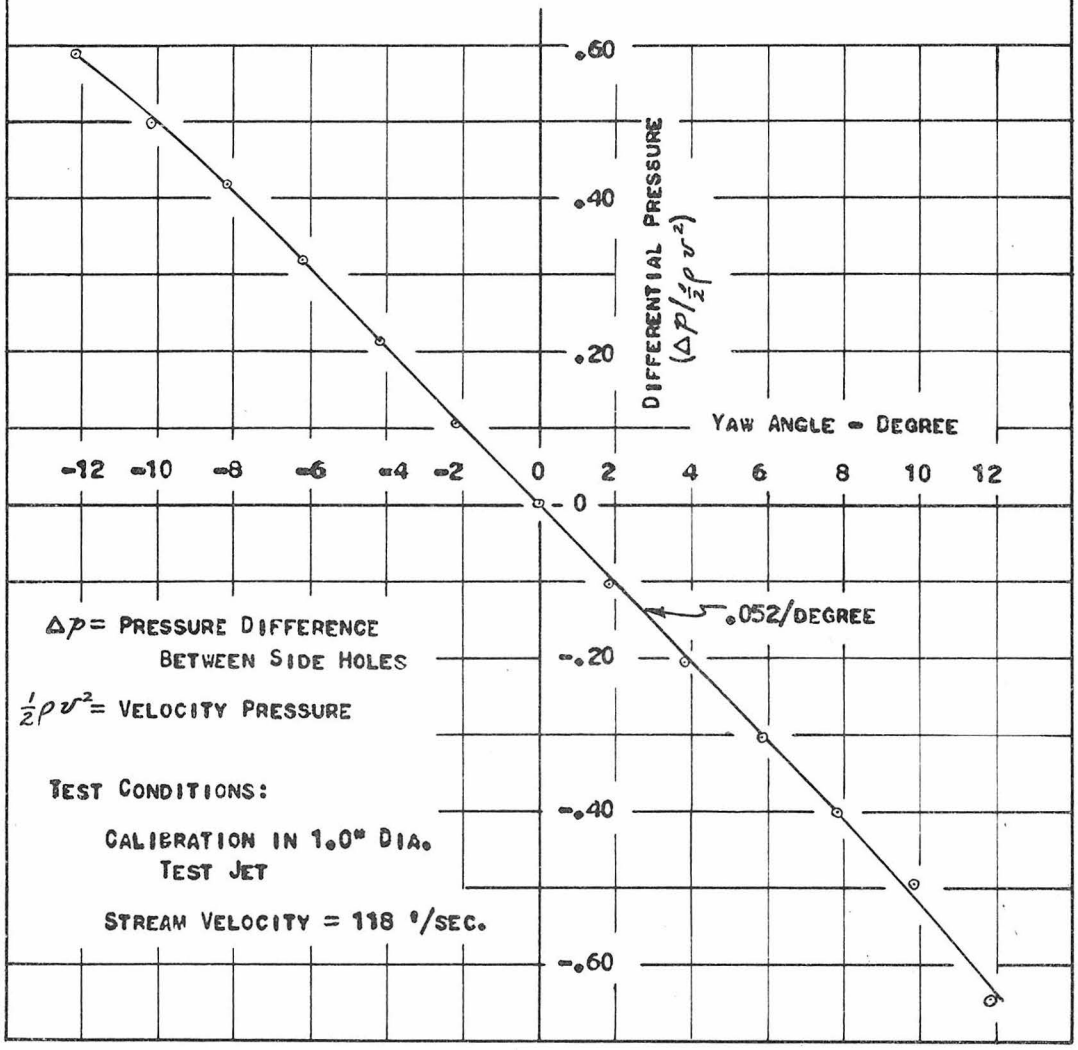

FIG. 36

CLAW TYPE YAW PROBE

-DIRECTION SENSITIVITY-

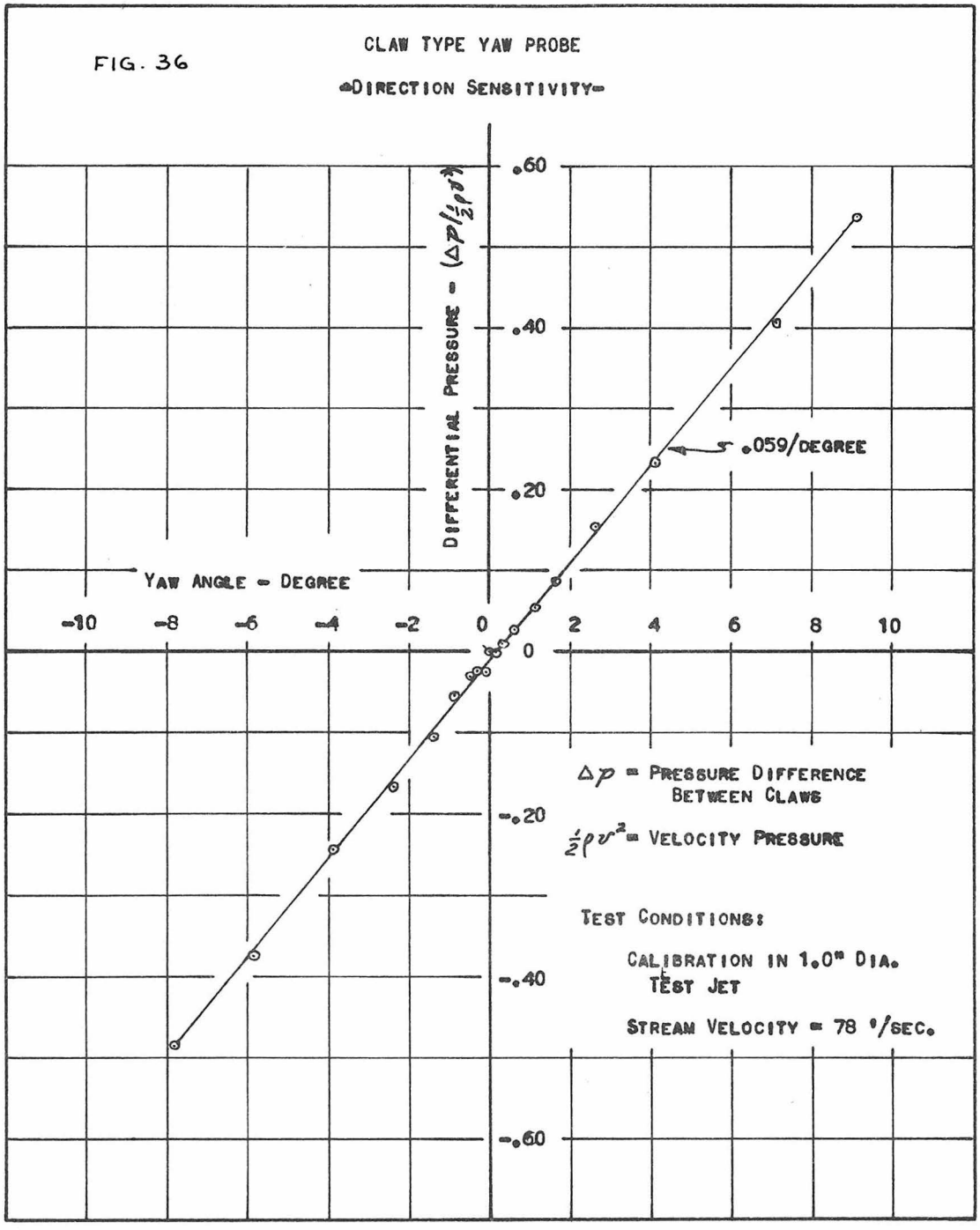

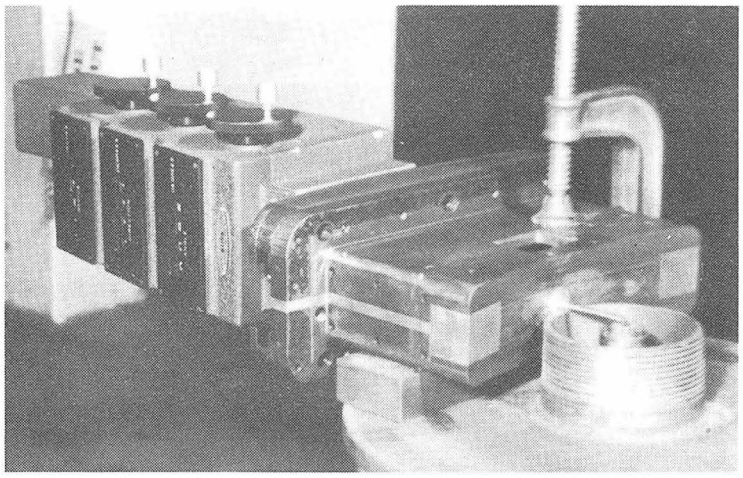

FIG. 37 INSTRUMENT CARRIAGE ON CALIBRATION STAND

THE SHOWN INSTRUMENT CARRIAGE IS SHOWN AS INSTALLED FOR CALIBRATING THE DIRECTION FINDING CLAW PROBE. THE CARRIAGE IS MOUNTED IN A PERFECTLY HORIZONTAL POSITION AND THE DIRECTION OF THE JET IS THEN DETERMINED. THE CARRIAGE IS THEN MOUNTED IN A SIMILAR POSITION BUT DISPLACED BY 180° AND THE DIRECTION READING IS REPEATED. THE MEAN OF THE TWO READINGS GIVEN THE ZERO DIRECTION OF THE PROBE.

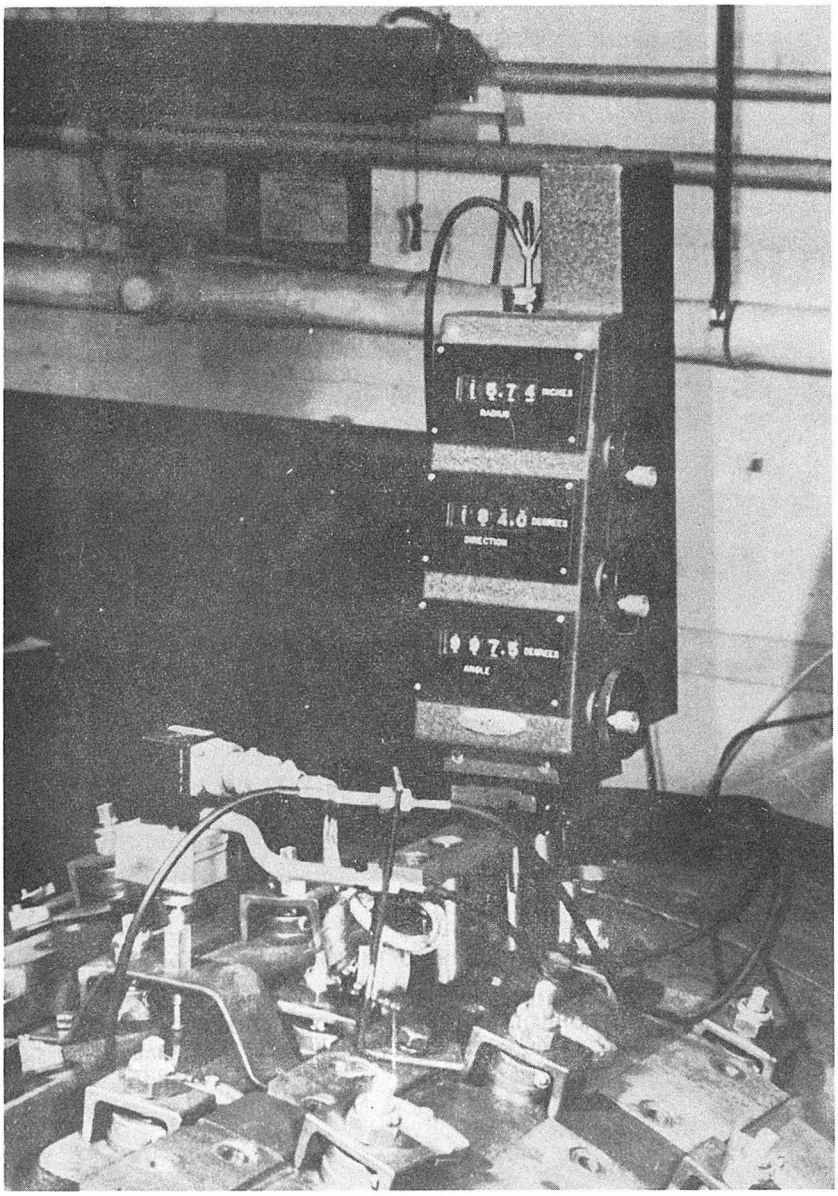

FIG. 38

THE INSTRUMENT CARRIAGE IS SHOWN IN THE SPECIAL MOUNTING FOR RADIAL SURVEYS. IN THE LOWER LEFT CORNER THE ELECTRICAL PRESSURE PICKUP IS SEEN IN ITS USUAL MOUNTING.

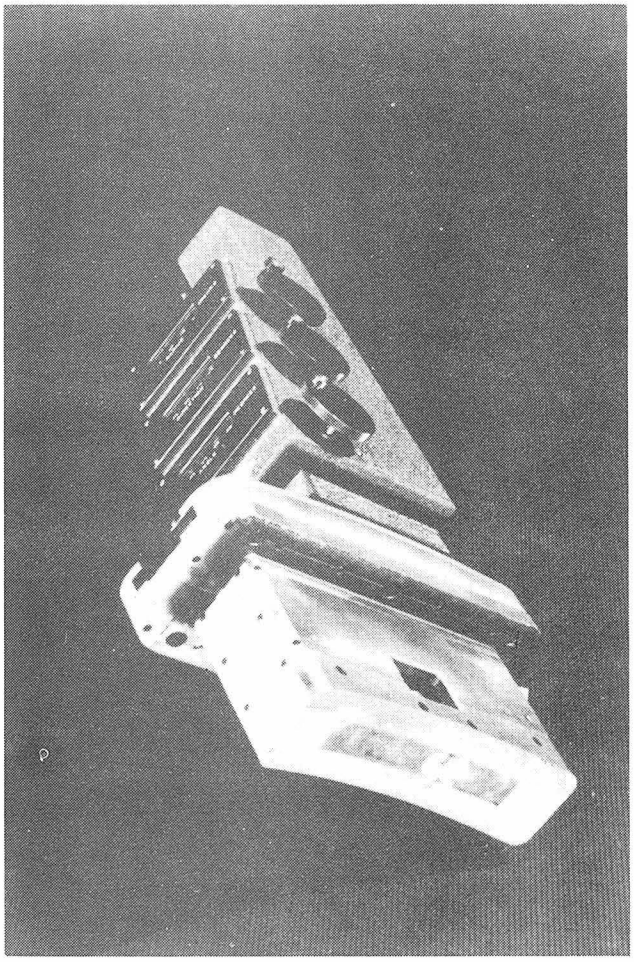

FIG. 39 INSTRUMENT CARRIAGE – BOTTOM VIEW

THE PHOTOGRAPH SHOWS HOW THE SLIDING TAPE FITS SMOOTHLY TO THE CURVED CONTOUR OF THE BASE. A TOTAL HEAD TUBE IS PROTUDING THROUGH THE TAPE.

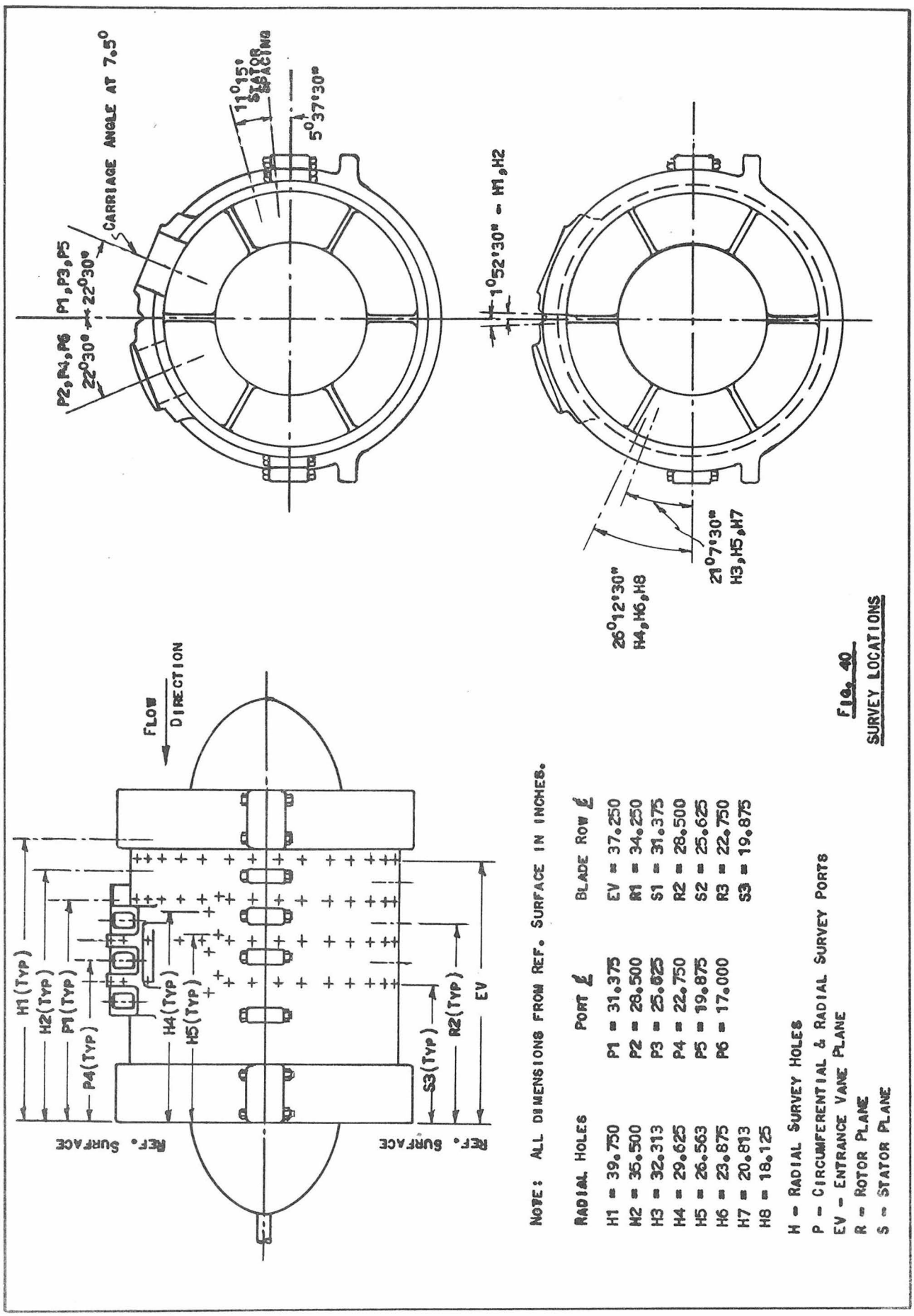

NOTE: ALL DIMENSIONS FROM REF. SURFACE IN INCHES.

RADIAL HOLES	PORT ℄	BLADE ROW ℄
H1 = 39.750	P1 = 31.375	EV = 37.250
H2 = 35.500	P2 = 28.500	R1 = 34.250
H3 = 32.313	P3 = 25.625	S1 = 31.375
H4 = 29.625	P4 = 22.750	R2 = 28.500
H5 = 26.563	P5 = 19.875	S2 = 25.625
H6 = 23.875	P6 = 17.000	R3 = 22.750
H7 = 20.813		S3 = 19.875
H8 = 18.125		

H - RADIAL SURVEY HOLES
P - CIRCUMFERENTIAL & RADIAL SURVEY PORTS
EV - ENTRANCE VANE PLANE
R - ROTOR PLANE
S - STATOR PLANE

FIG. 40
SURVEY LOCATIONS

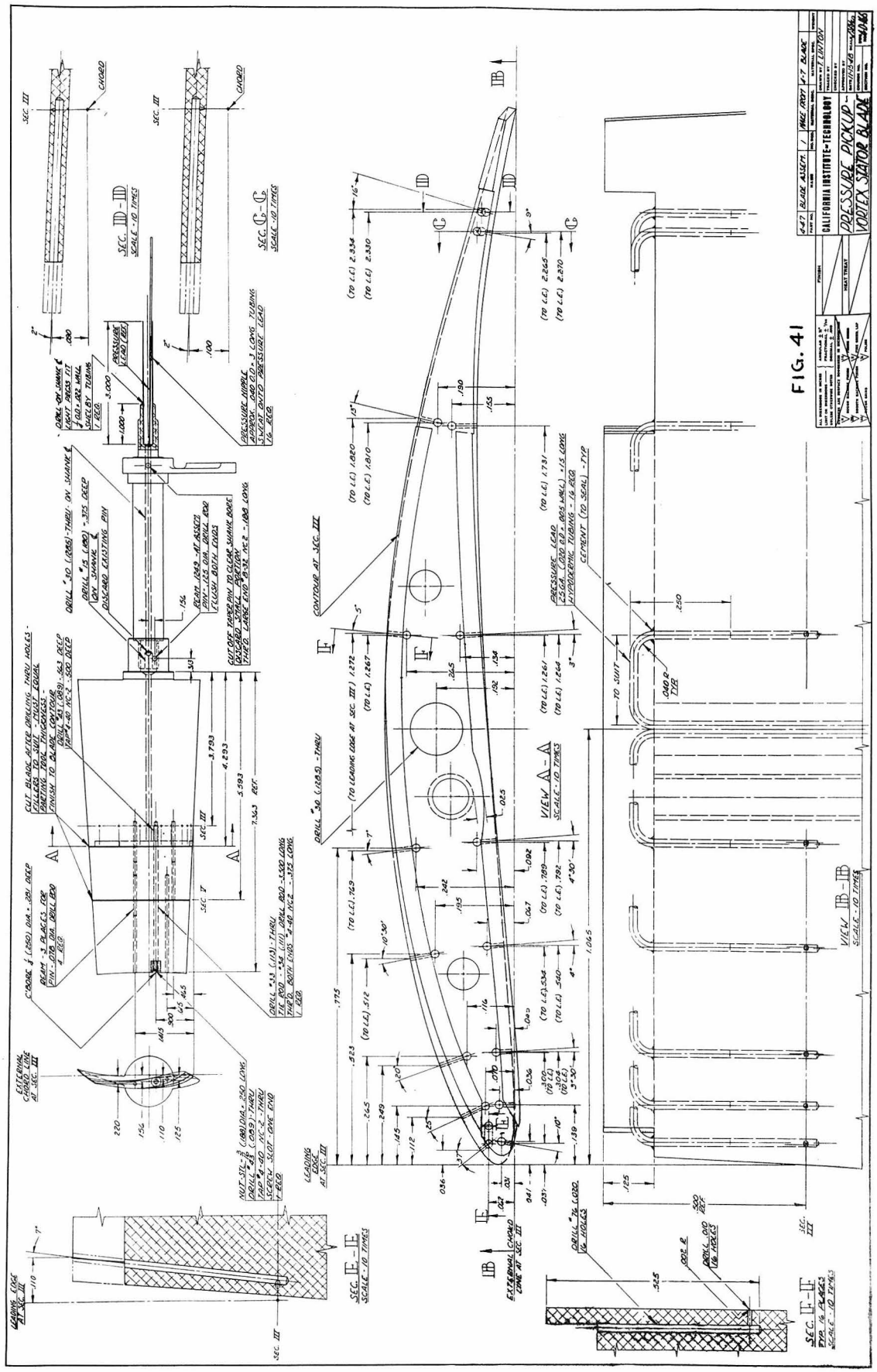
CALIFORNIA INSTITUTE of TECHNOLOGY
PRESSURE PICKUP - VORTEX STATOR BLADE
SECT. III
SECT. IF
SECT. IB
SECT. IE
SECT. ID
SECT. IC
VIEW A-A
VIEW IB-IB
SEC. ID-ID
SEC. IC-IC
SEC. IE-IE
SEC. IF-IF
CHORD
LEADING EDGE AT SEC. III
TRAILING EDGE AT SEC. III
CONTOUR AT SEC. III
CEMENT (TO SEAL)
TO SUIT

FIG. 41

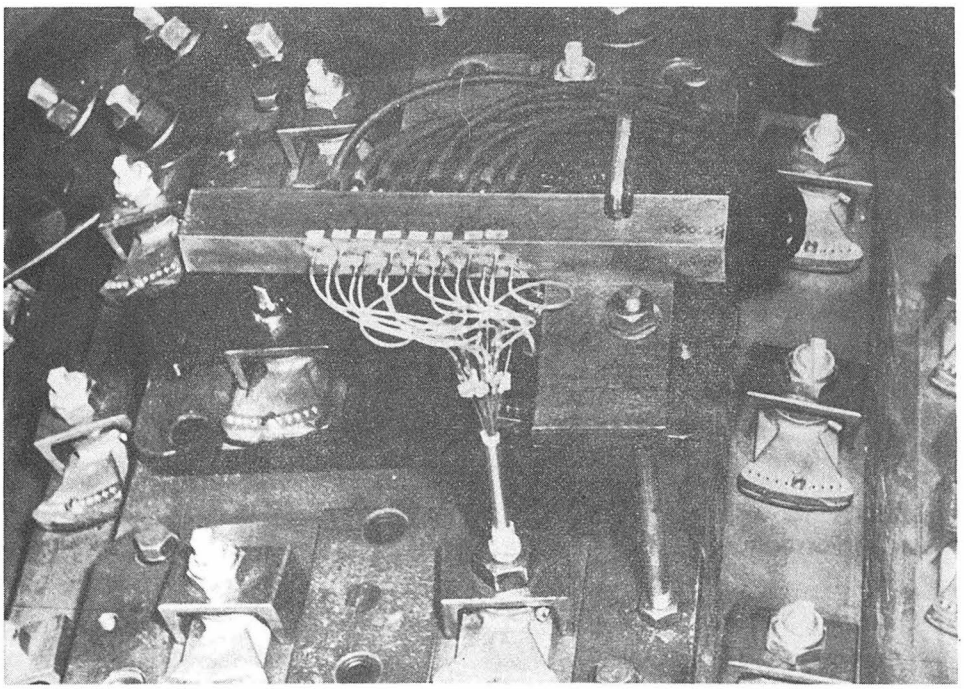

FIG.42: THE STATIC PRESSURE BLADE
- SHOWING SELECTOR BAR

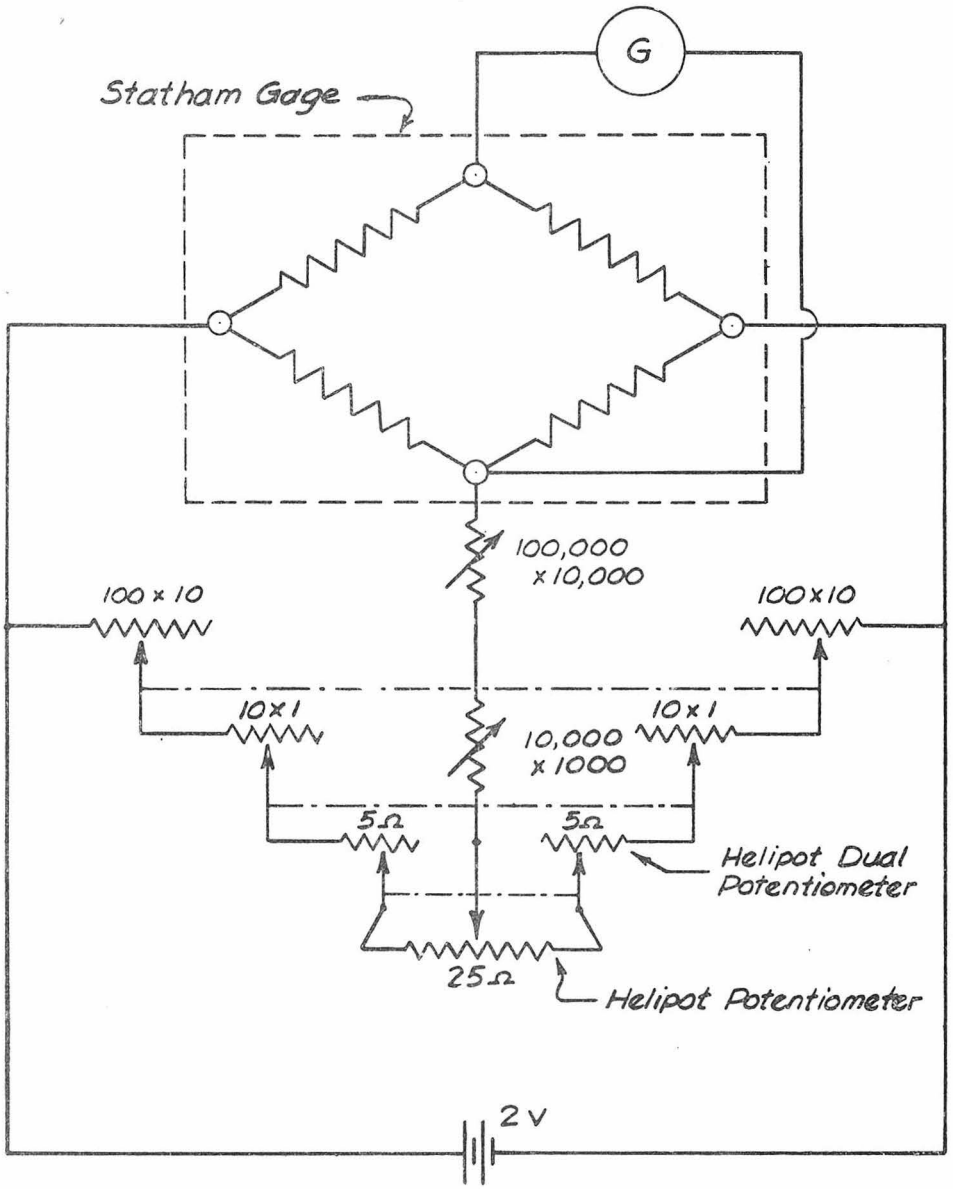

FIG. 43

BRIDGE FOR USE WITH STATHAM PRESSURE GAGE

– CIRCUIT DIAGRAM –

(DESIGN BY C. THIELE)

NOTES

– – – – – – MECHANICAL CONNECTION

100 x 10 = 100 OHM RHEOSTAT ADJUSTABLE IN 10 OHM STEPS. ALL DECADE RESISTORS WERE PROCURED FROM GENERAL RADIO CO.

FIG. 44

STATHAM GAGE CALIBRATION CURVE

FOR STATHAM GAGE PRESSURE TRANSMITTER

SERIAL No. 95 MODEL P5-0.20 - 250

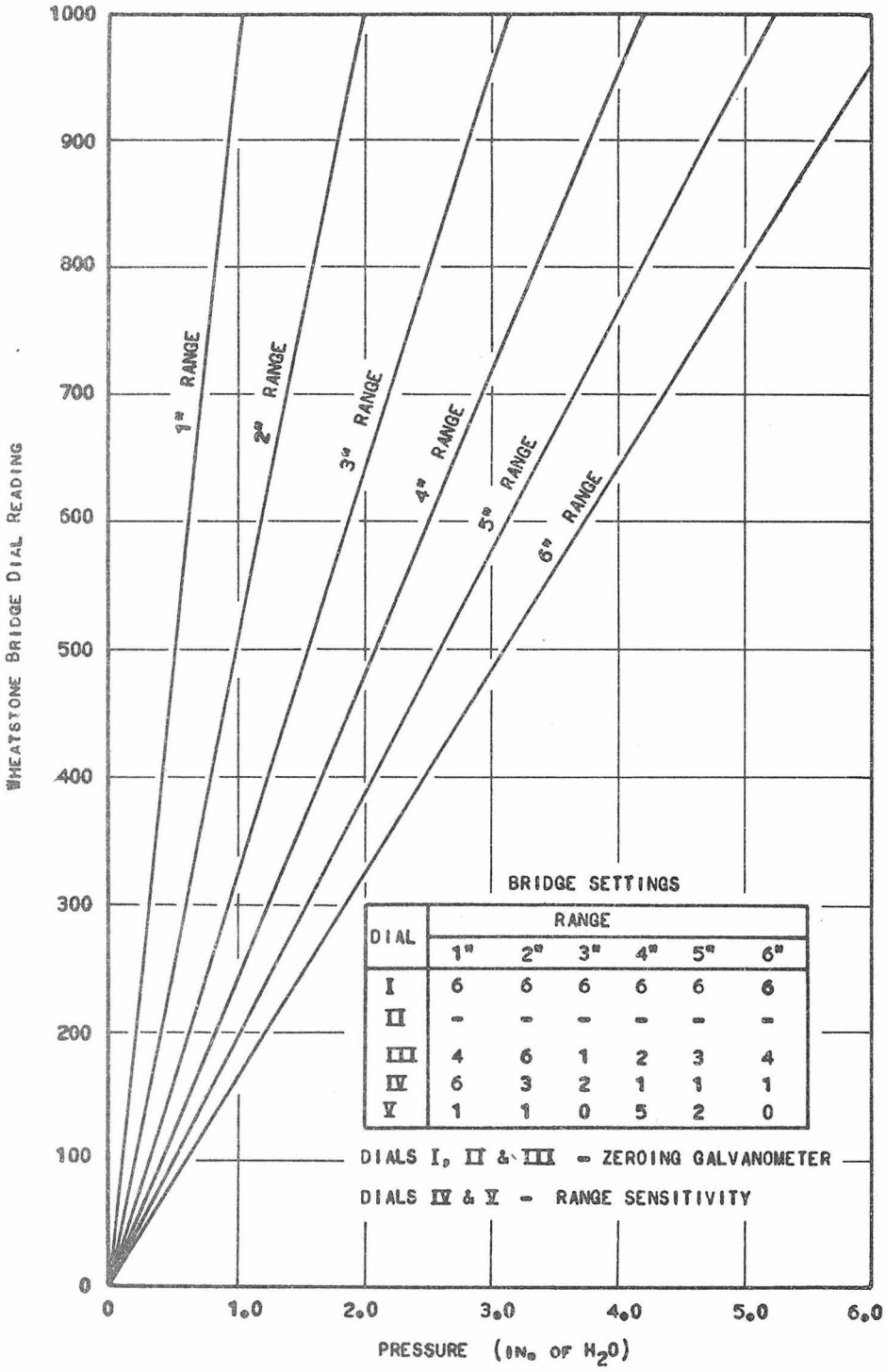

BRIDGE SETTINGS

DIAL	RANGE					
	1"	2"	3"	4"	5"	6"
I	6	6	6	6	6	6
II	-	-	-	-	-	-
III	4	6	1	2	3	4
IV	6	3	2	1	1	1
V	1	1	0	5	2	0

DIALS I, II & III - ZEROING GALVANOMETER

DIALS IV & V - RANGE SENSITIVITY

FIG. 45

COMPRESSOR CASCADE NOTATION

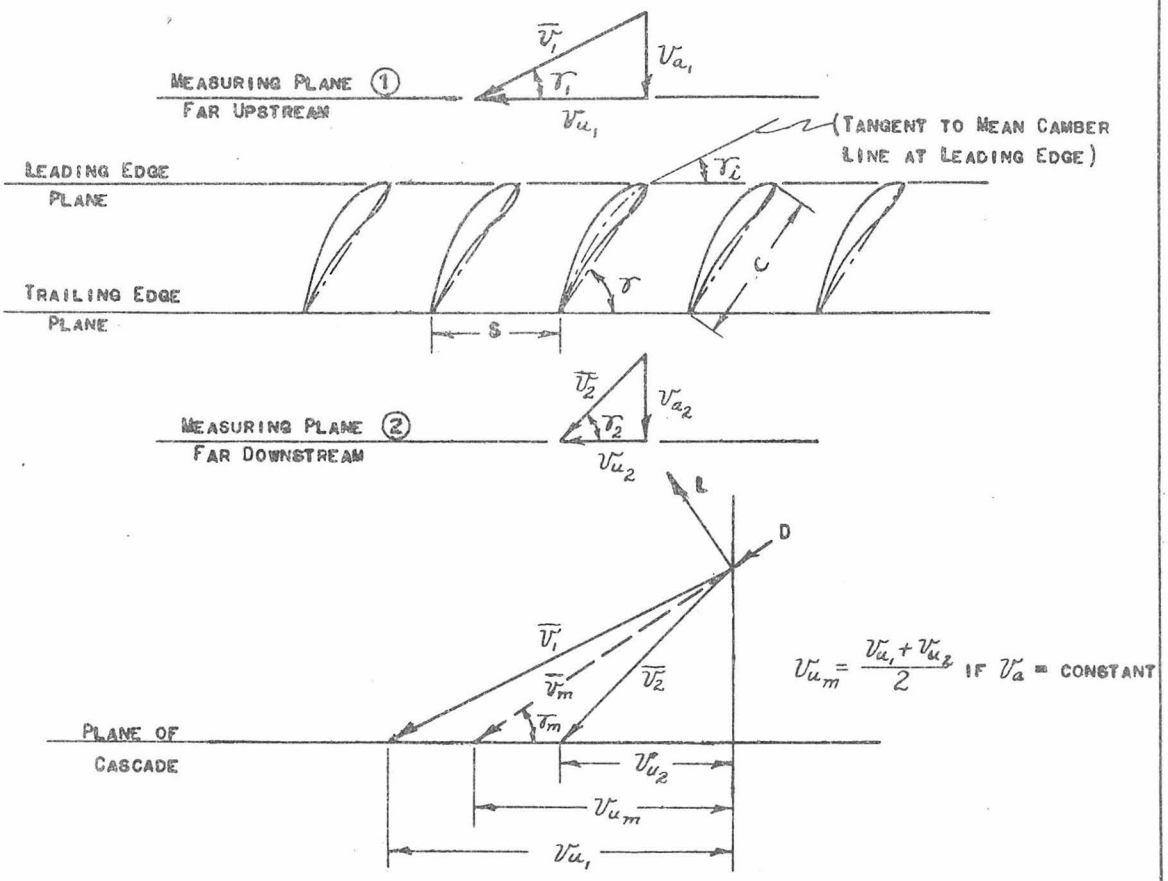

$$V_{u_m} = \frac{V_{u_1} + V_{u_2}}{2} \text{ IF } V_a = \text{CONSTANT}$$

DEFINITIONS:

- $\bar{V}_1$ = CASCADE ENTRANCE VELOCITY MEASURED IN PLANE ① = FT./SEC.
- $\bar{V}_2$ = CASCADE EXIT VELOCITY MEASURED IN PLANE ② = FT./SEC.
- V_m = VECTOR MEAN VELOCITY = FT./SEC.
- γ_1 = ENTERING FLOW DIRECTION = MEASURED AS SHOWN
- γ_2 = EXIT FLOW DIRECTION = " i^* "
- γ_m = MEAN VELOCITY DIRECTION = " " "
- γ_ℓ = DIRECTION OF TANGENT TO LEADING EDGE CAMBER LINE
- θ^* = AIR TURNING ANGLE = $\gamma_2 - \gamma_1$
- S = CASCADE SPACING = INCHES
- C = CASCADE AIRFOIL CHORDAL DISTANCE = INCHES
- γ = CASCADE STAGGER ANGLE
- L = AIRFOIL LIFT FORCE = LBS$_\perp$/IN.
- D = AIRFOIL DRAG FORCE = LBS.$_\parallel$/IN.
- $i^* = (\gamma_\ell - \gamma_1)$ = FLOW INCIDENCE ANGLE

(SUBSCRIPTS a, u DENOTE VECTOR COMPONENTS PERPENDICULAR AND PARALLEL RESPECTIVELY TO THE CASCADE PLANE)

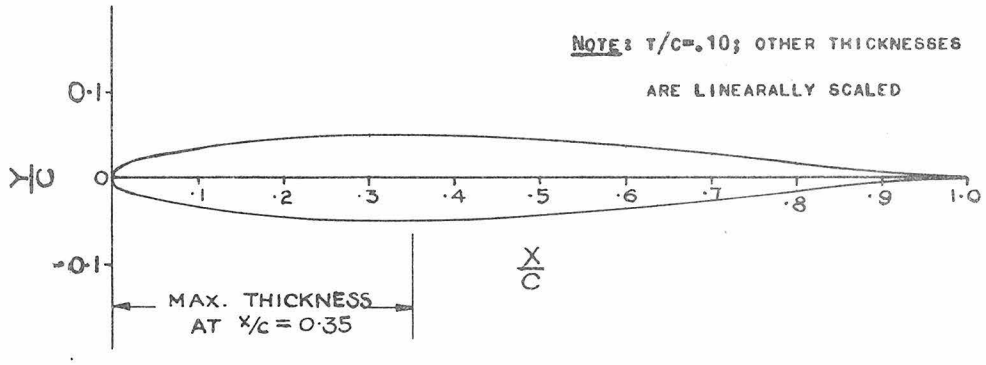

FIG. 46

BASIC AIRFOIL THICKNESS FOR COMPRESSOR BLADE DESIGN

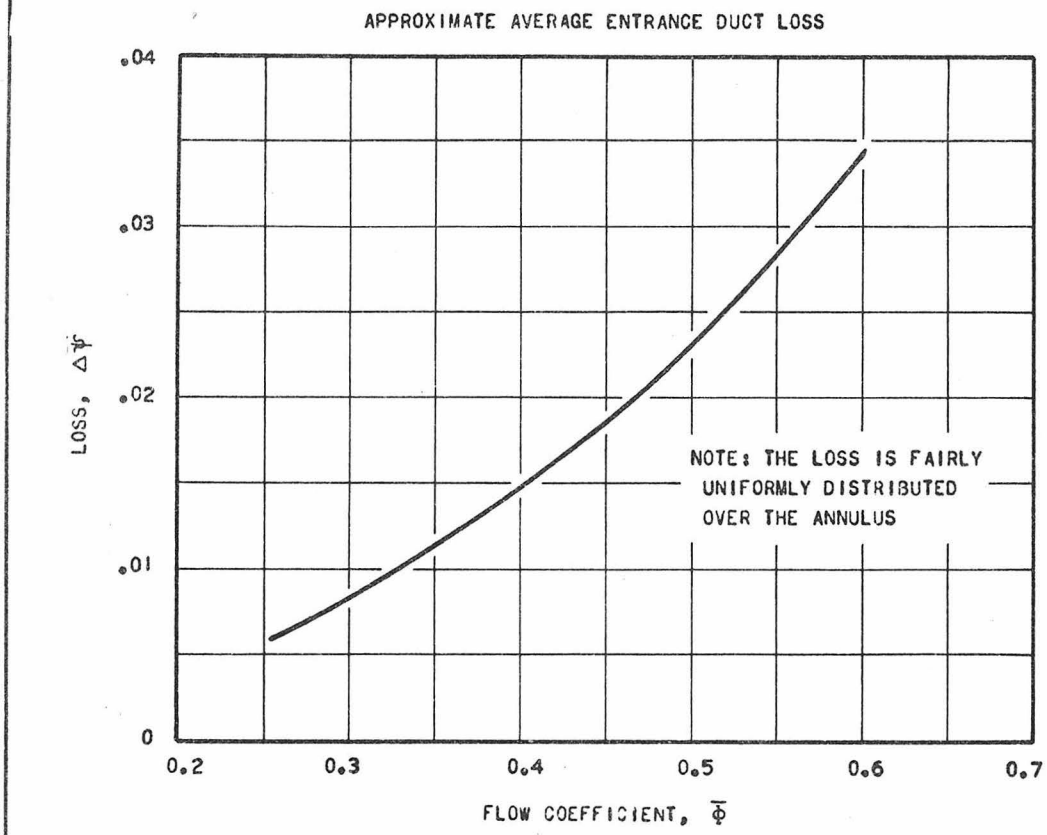

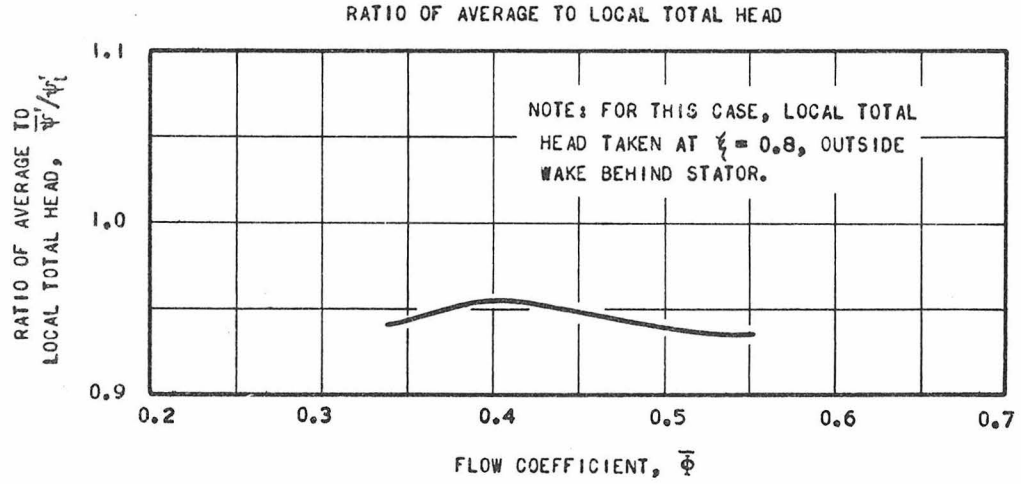

FIG. 47

COMPRESSOR TOTAL PRESSURE CORRECTIONS

FIG. 48

FREE VORTEX BLADING ◆ OVERALL PERFORMANCE

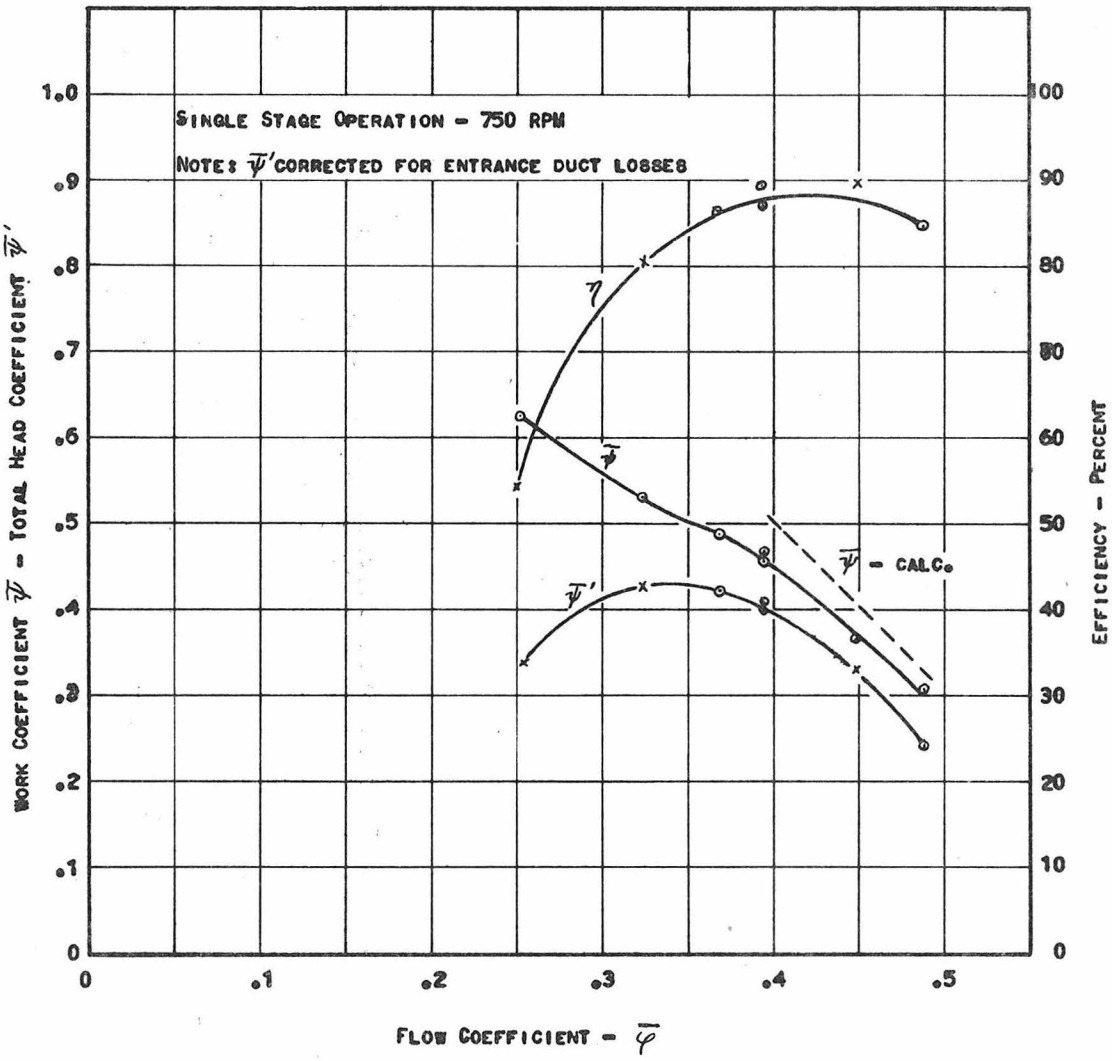

Fig. 49

MAXIMUM COMPRESSOR EFFICIENCY vs. REYNOLDS NUMBER

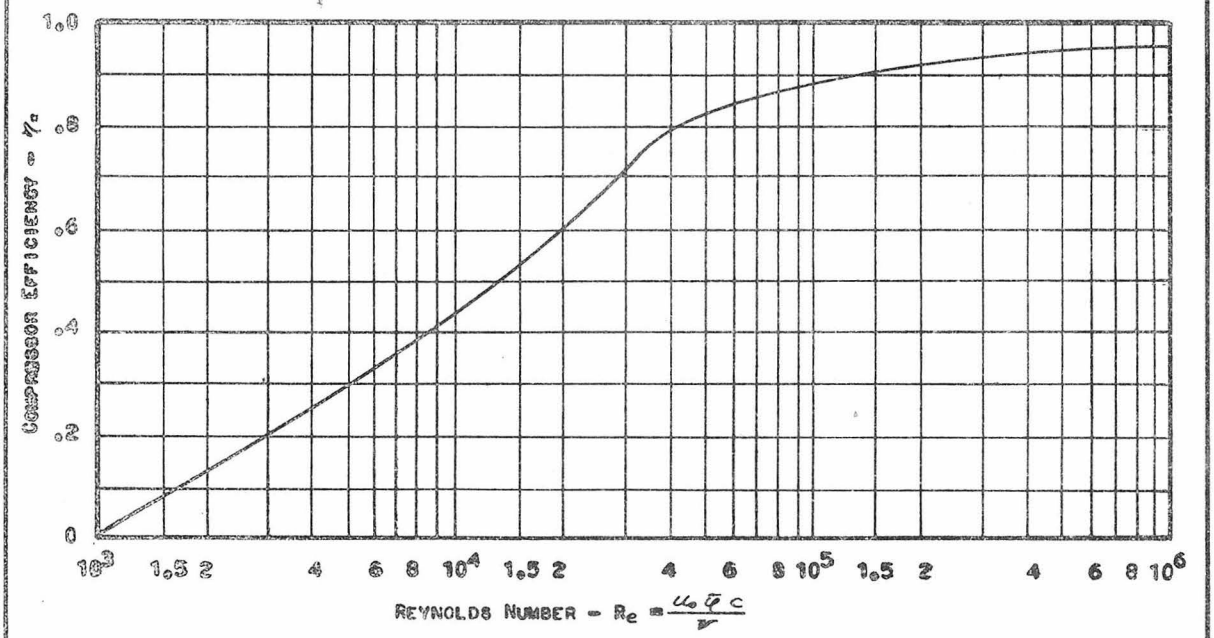

NOTE: CURVE SHOWN IS ENVELOPE OF A NUMBER OF EFFICIENCY CURVES.
REPRODUCED FROM ECKERT'S REPORT (REF. 32)

Fig. 50

FREE VORTEX BLADING - OVERALL PERFORMANCE

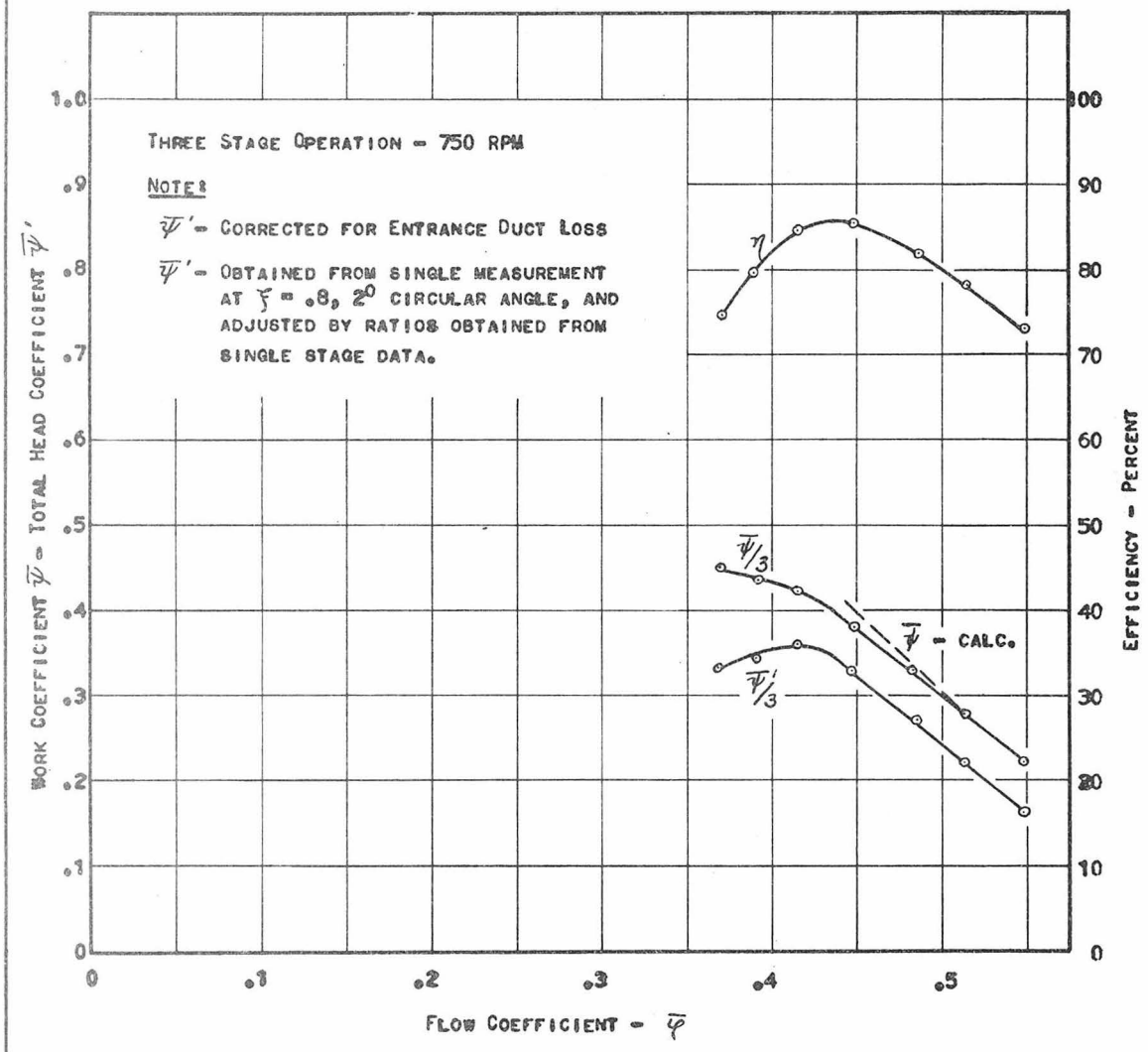

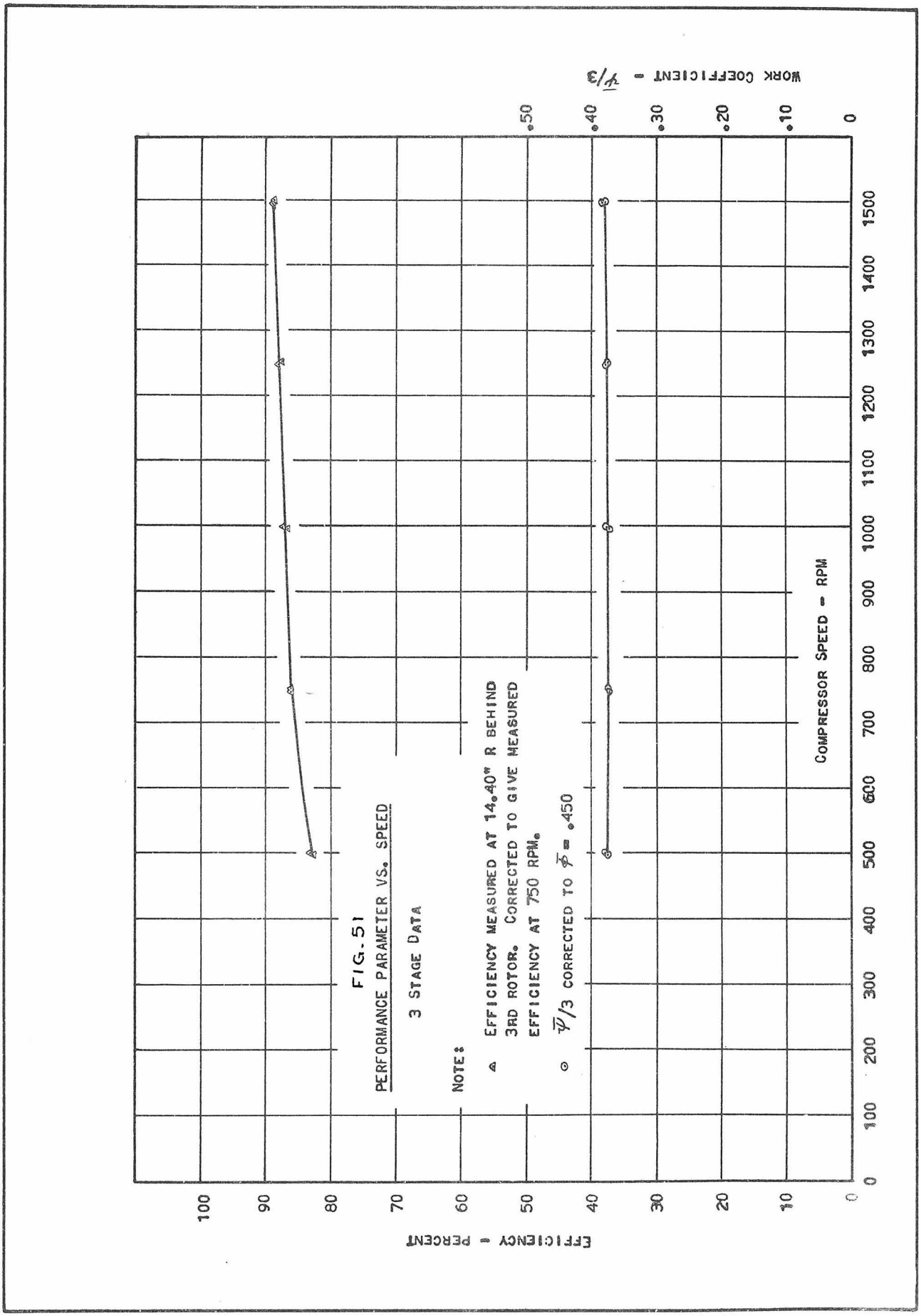

FIG. 51

PERFORMANCE PARAMETER VS. SPEED

3 STAGE DATA

NOTE:

△ EFFICIENCY MEASURED AT 14.40" R BEHIND 3RD ROTOR. CORRECTED TO GIVE MEASURED EFFICIENCY AT 750 RPM.

○ $\bar{\psi}/3$ CORRECTED TO $\bar{\phi} = .450$

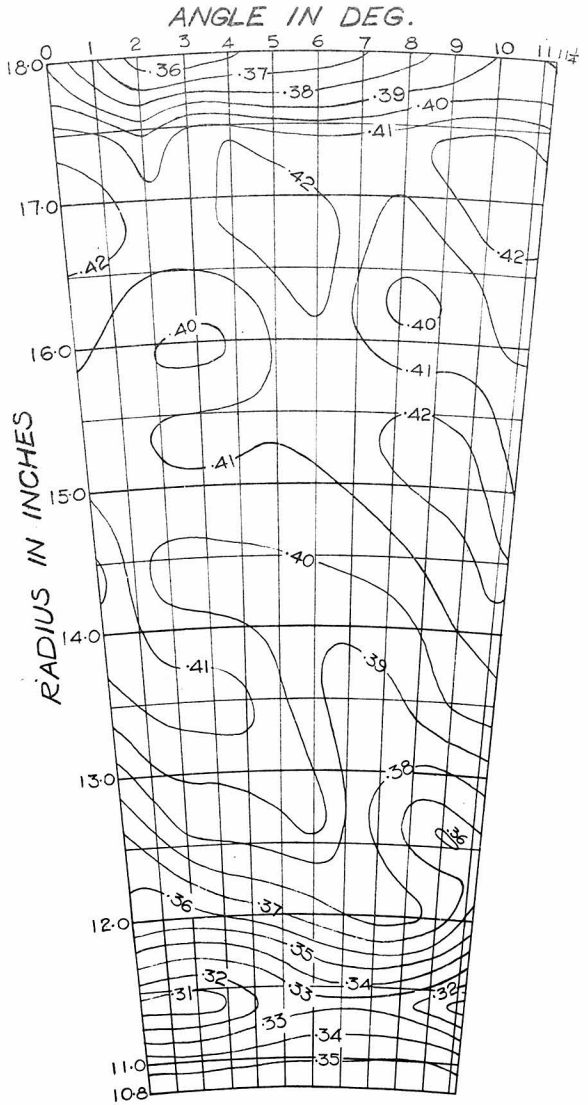

A) DOWNSTREAM OF 1ST ROTOR

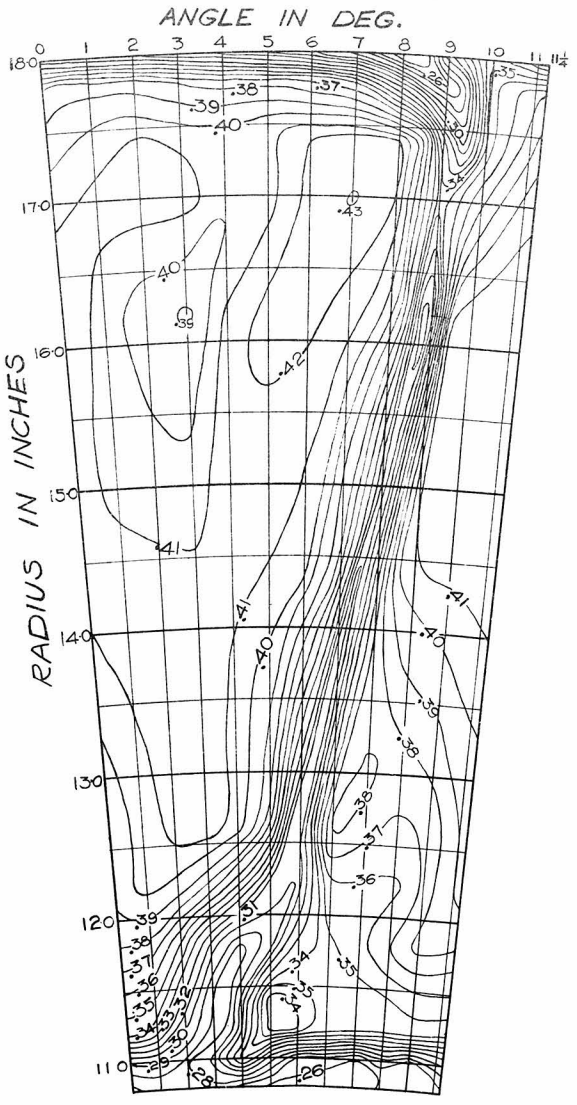

B) DOWNSTREAM OF 1ST STATOR

NOTE:

A) CONTOURS ARE LINES OF $\psi' = const.$ where

$$\psi' = \frac{P_t - P_s}{\frac{1}{2}\rho u_o^2}$$

B) THE ANGLE $11\frac{1}{4}^\circ$ IS EQUIVALENT TO ONE STATOR BLADE PITCH (32 BLADES). PATTERNS REPEAT AROUND COMPLETE ANNULUS.

FIG. 52 TOTAL PRESSURE CONTOUR PLOTS

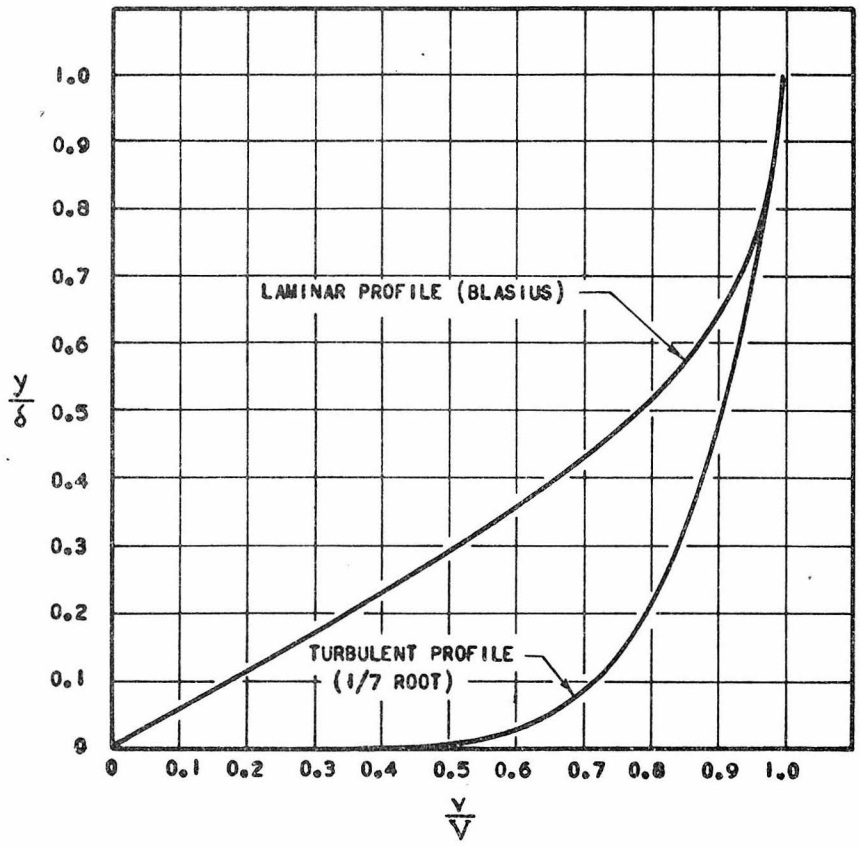

Fig. 53

BOUNDARY LAYER VELOCITY PROFILES

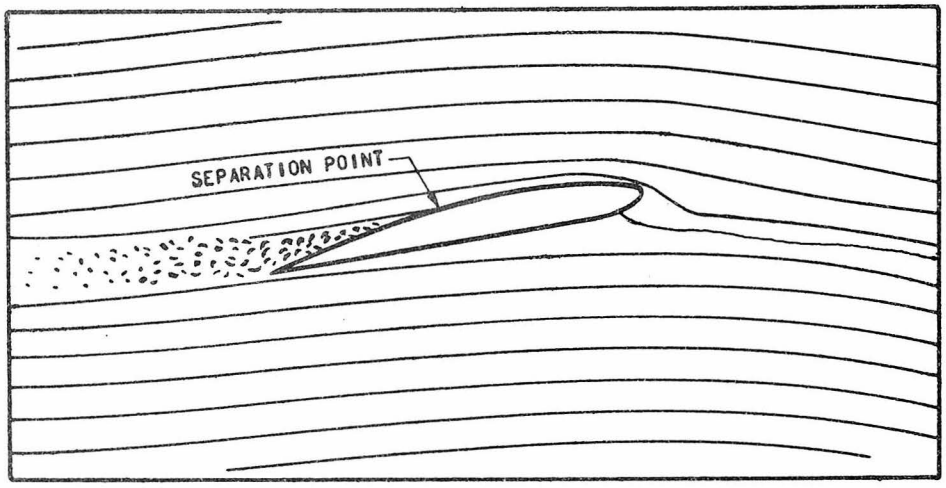

Fig. 54

FLOW SEPARATION ON AN AIRFOIL

Fig. 55

CASE BOUNDARY/ FLOW PROFILE BEHIND 1st ROTOR

750 RPM HYPO PROBE $\bar{\varphi}$ = .392

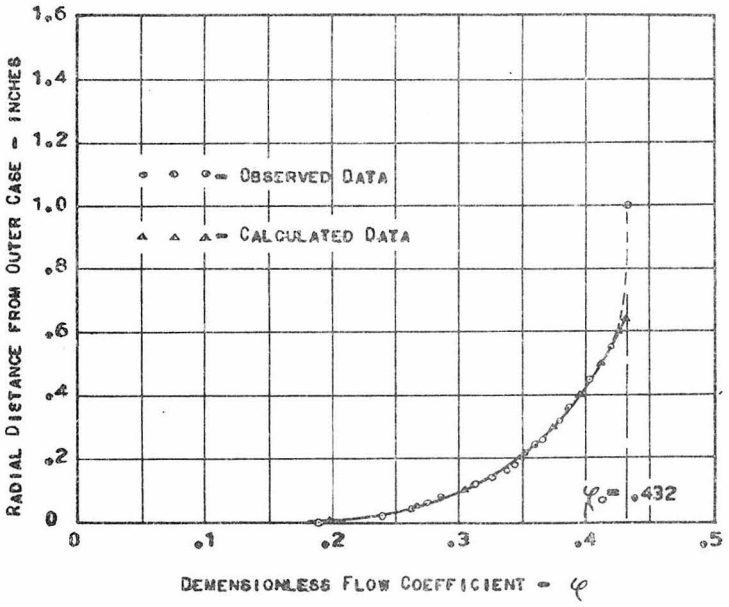

Fig. 56

WAKE PROFILES BEHIND STATOR

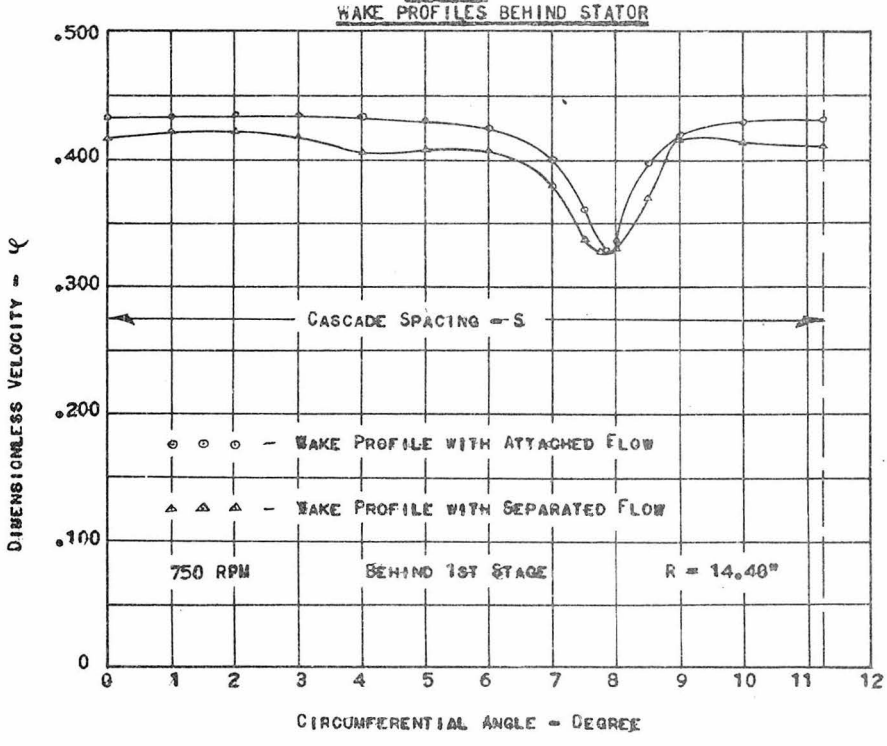

VORTEX STATOR CASCADE
FIG. 57

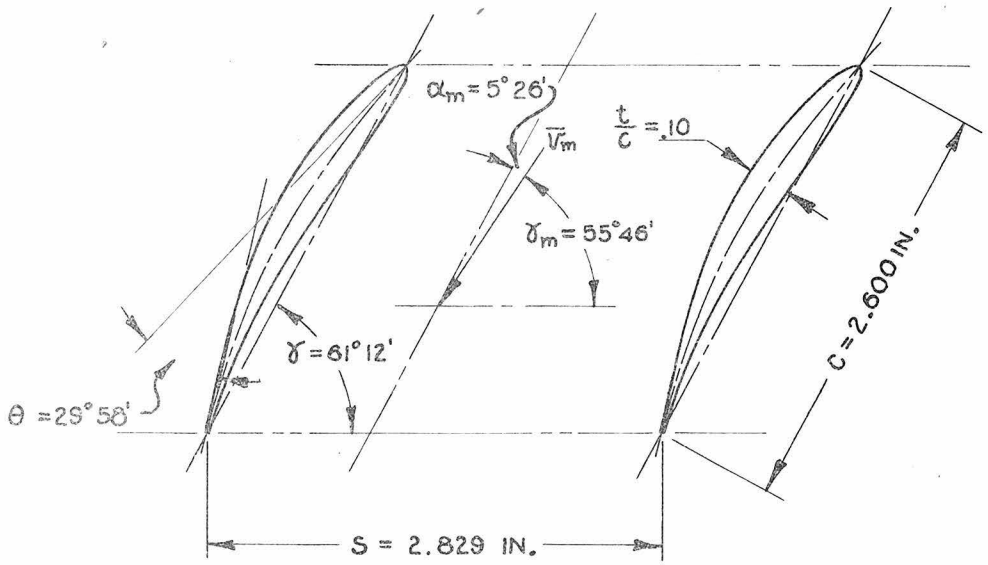

R = 14.40 IN.
(SEE TABLE 5)

FIG. 58

CALCULATION POINTS ON THIN AIRFOIL

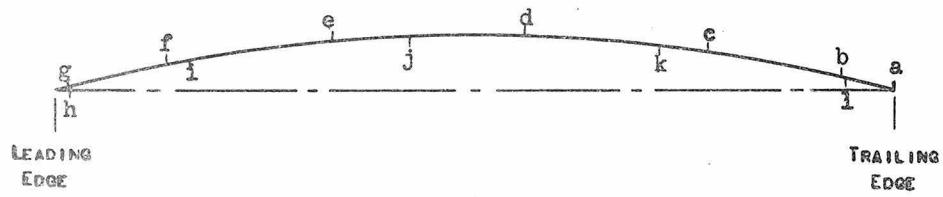

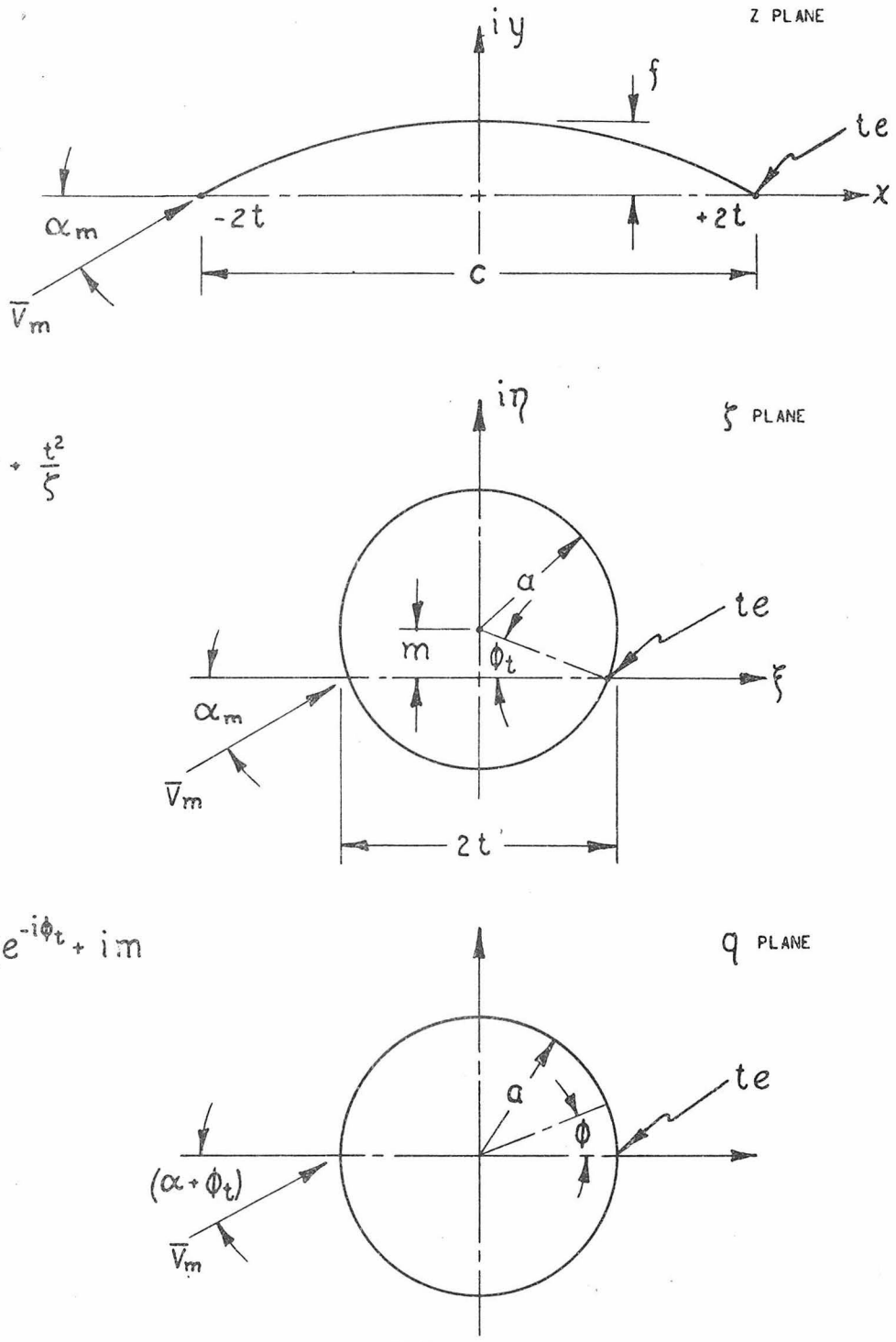

FIG. 59

TRANSFORMATIONS FOR CIRCULAR ARC AIRFOIL

Fig. 60

CALCULATED SURFACE POTENTIALS

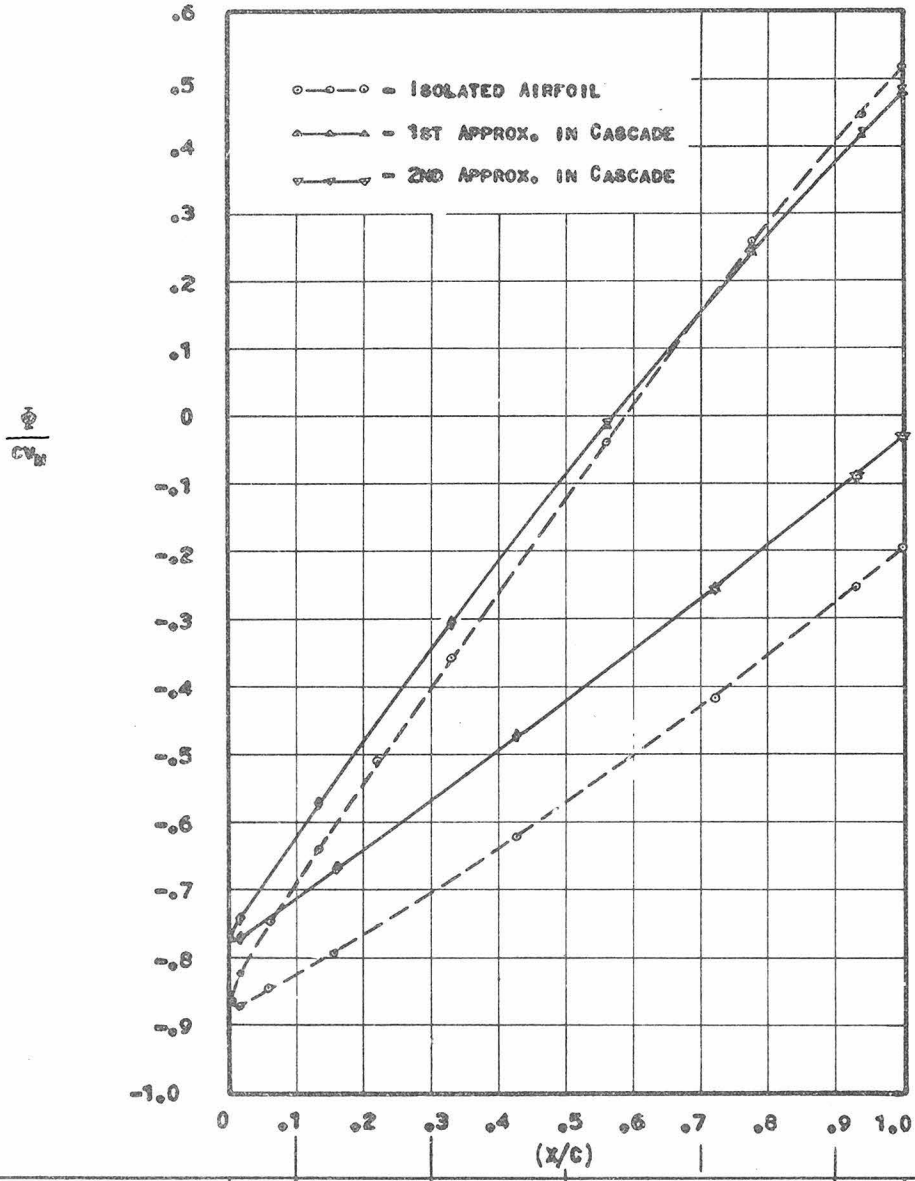

DISTRIBUTED VORTICITY	α ↻ ↓	β ↻ ↓	γ ↻ ↓	δ ↻ ↓	ε ↻ ↓	TOTAL CIRCULATION $-\Gamma/CV_M$	C_L
ISOLATED AIRFOIL	.225	.160	.142	.118	.067	.712	1.424
1ST APPROXIMATION	.159	.117	.098	.083	.053	.510	1.020
2ND APPROXIMATION	(ESSENTIALLY IDENTICAL)					.513	1.026

Fig. 61

CALCULATED SURFACE VELOCITIES

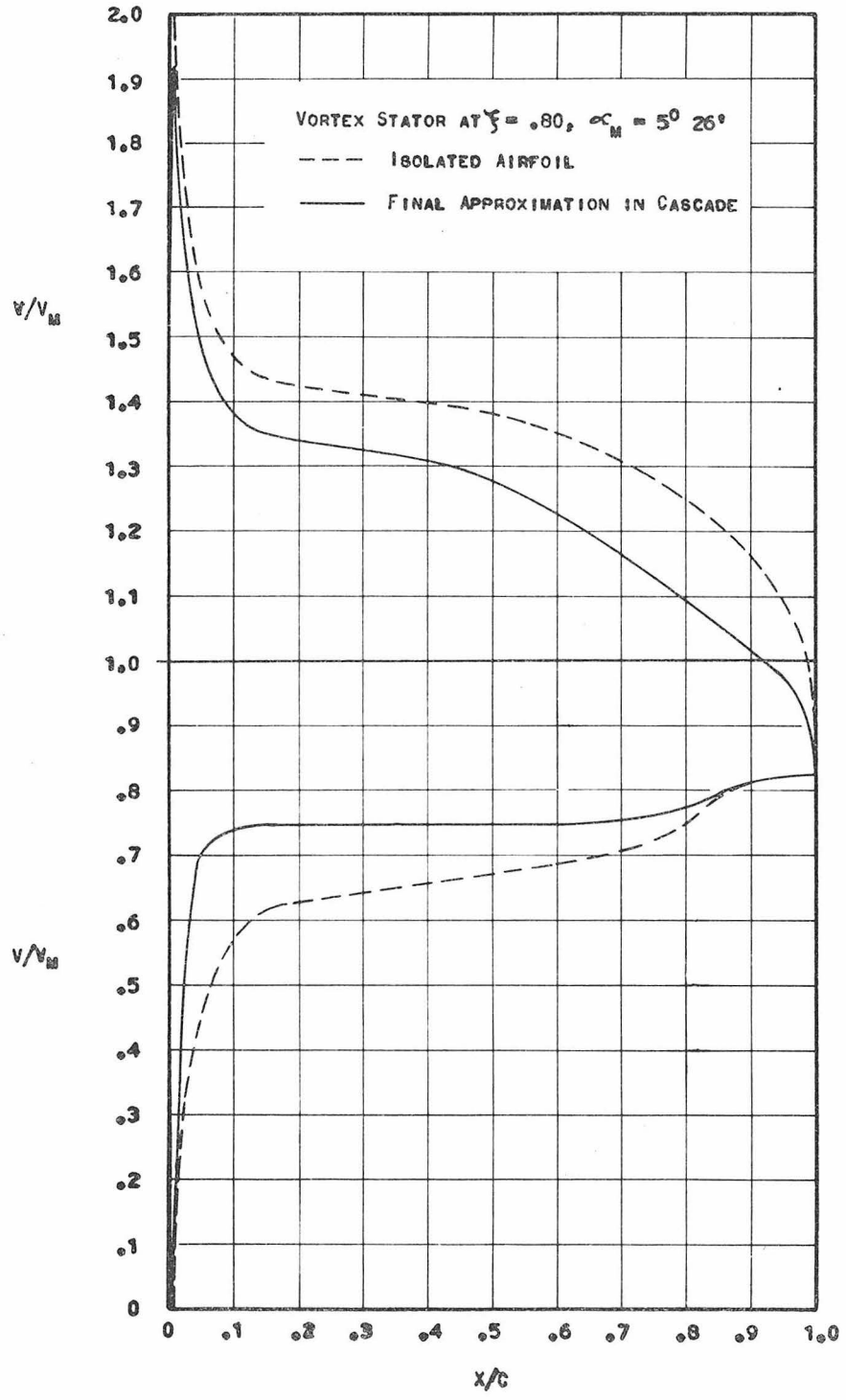

FIG. 62

CASCADE AIRFOIL SURFACE PRESSURE

VORTEX STATOR R = 14.40"

ϕ = .392 C_L = .89

$\gamma_s = \frac{P - P_2}{\frac{1}{2}\rho U_2^2}$ = STATIC PRESSURE COEFFICIENT

⊙ - MEASURED POINT - CONVEX SURFACE

σ - MEASURED POINT - CONCAVE SURFACE

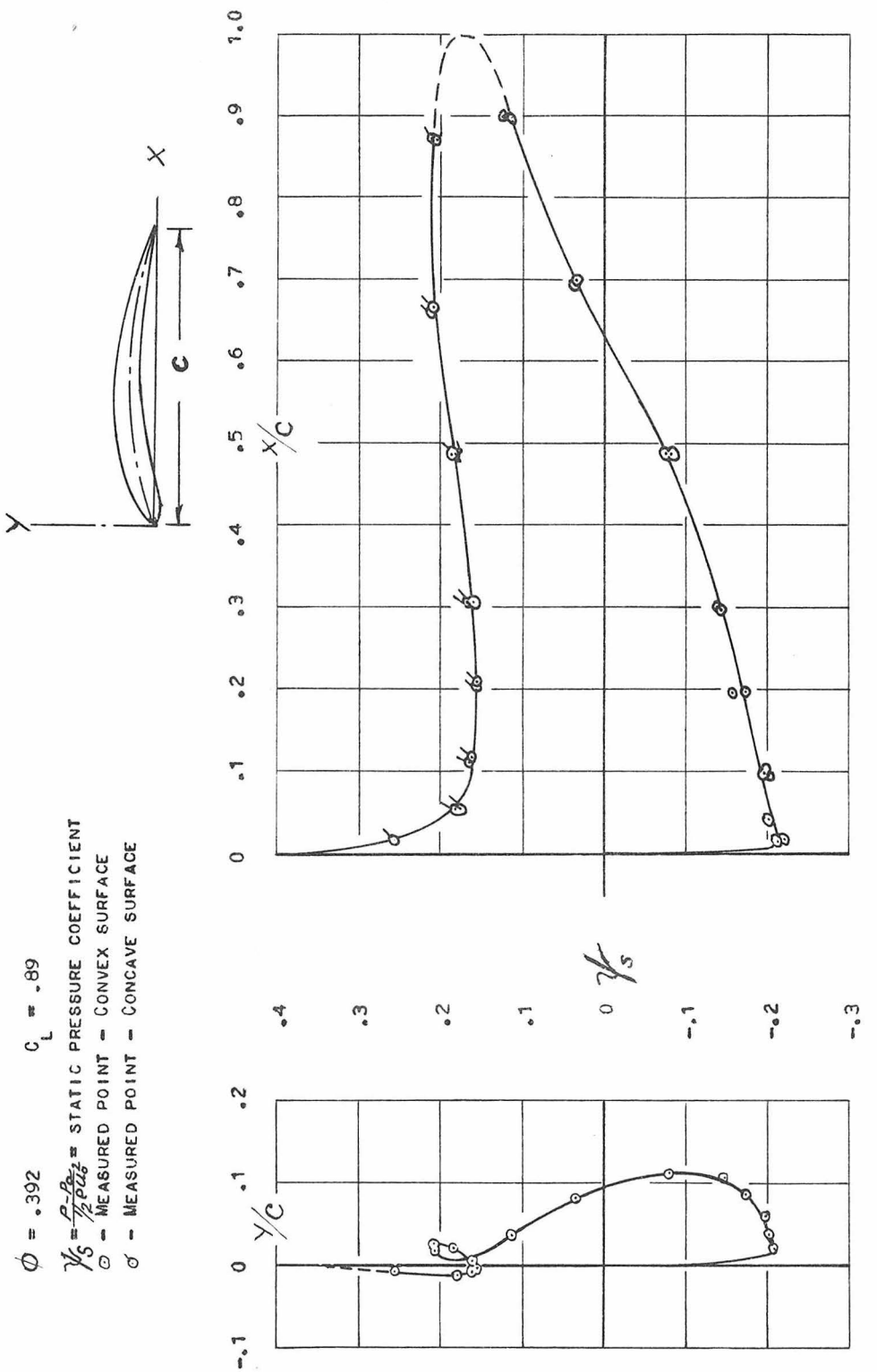

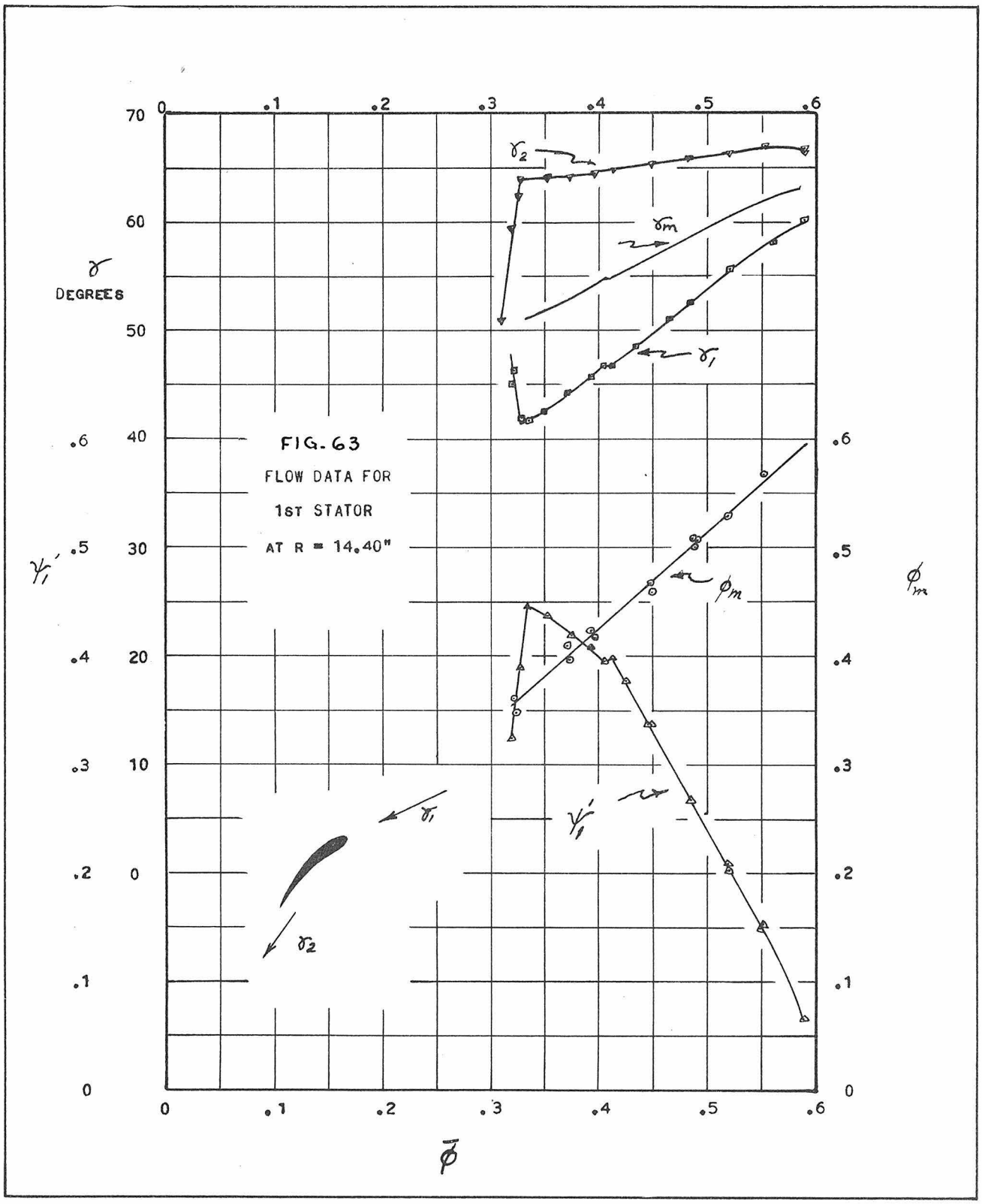
FIG. 63
FLOW DATA FOR
1ST STATOR
AT R = 14.40"
γ DEGREES
ψ'1
φm
φ̄
γ2
γm
γ1
0 .1 .2 .3 .4 .5 .6
70 60 50 40 30 20 10 0

FIG. 64

SURFACE VELOCITY DISTRIBUTION

FOR VORTEX STATOR CASCADE AT R = 14.40 IN.

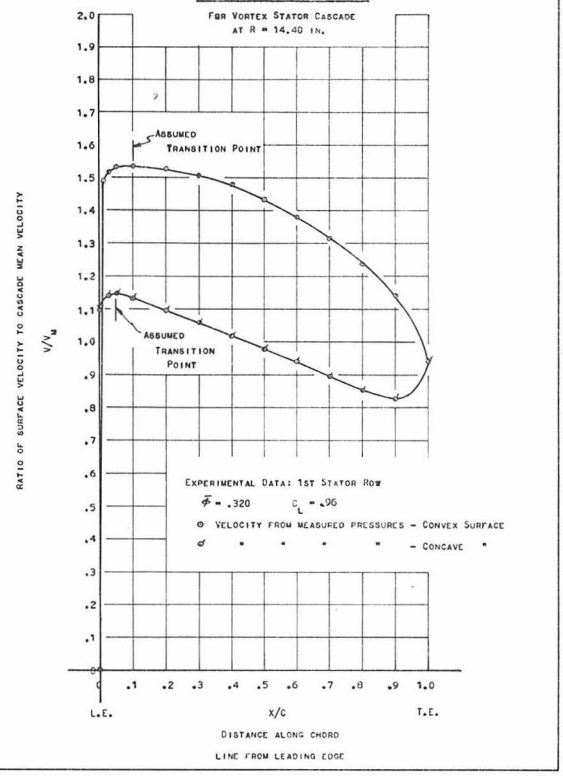

FIG. 65

SURFACE VELOCITY DISTRIBUTION

FOR VORTEX STATOR CASCADE AT R= 14.40 IN.

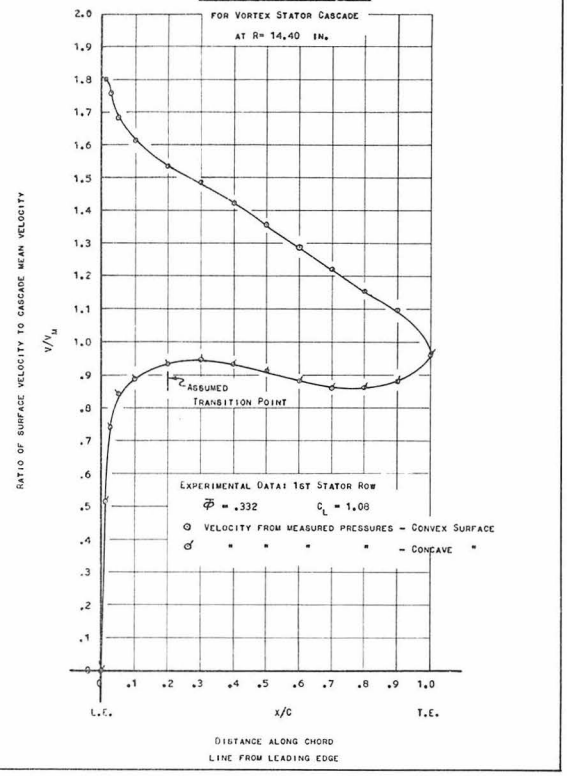

FIG. 66

SURFACE VELOCITY DISTRIBUTION

FOR VORTEX STATOR CASCADE AT R = 14.40 IN.

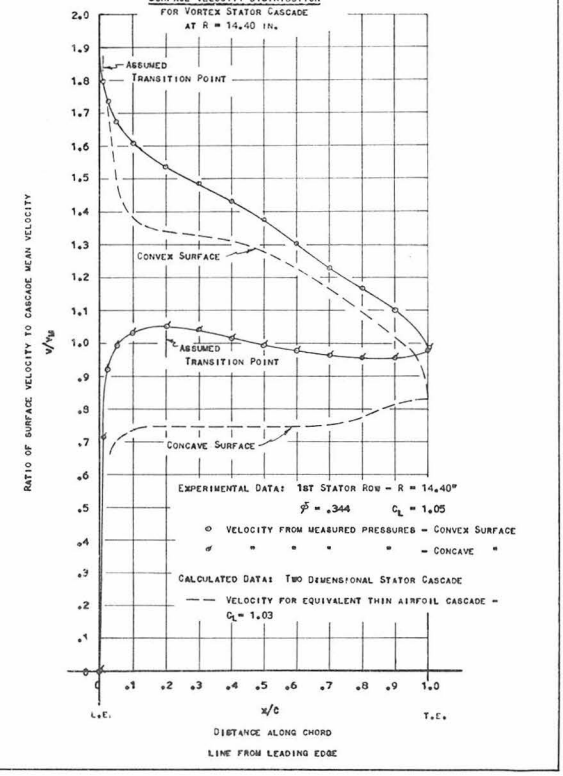

FIG. 67

SURFACE VELOCITY DISTRIBUTION

FOR VORTEX STATOR CASCADE AT R = 14.40 IN.

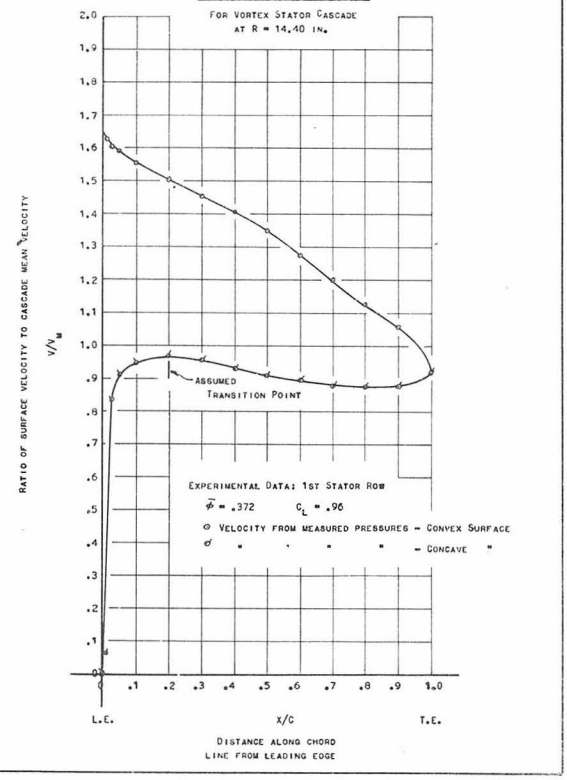

FIG. 68

SURFACE VELOCITY DISTRIBUTION
FOR VORTEX STATOR CASCADE
AT R = 14.40

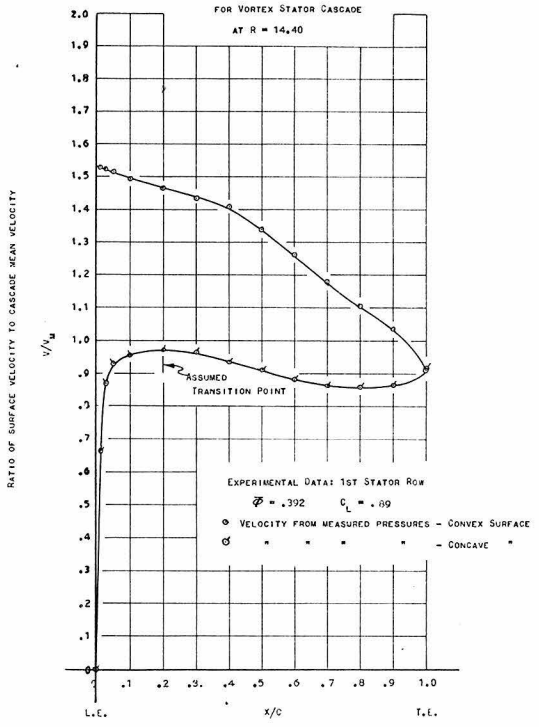

FIG. 69

SURFACE VELOCITY DISTRIBUTION
FOR VORTEX STATOR CASCADE
AT R = 14.40 IN.

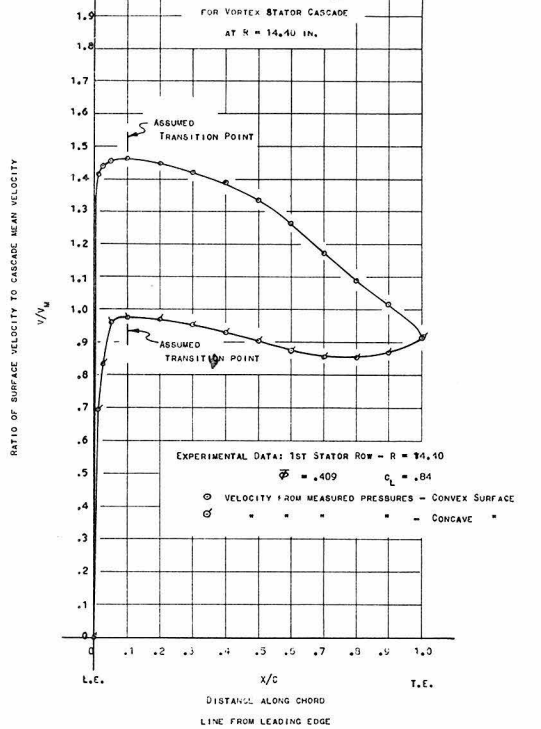

FIG. 70

SURFACE VELOCITY DISTRIBUTION
FOR VORTEX STATOR CASCADE
AT R = 14.40 IN.

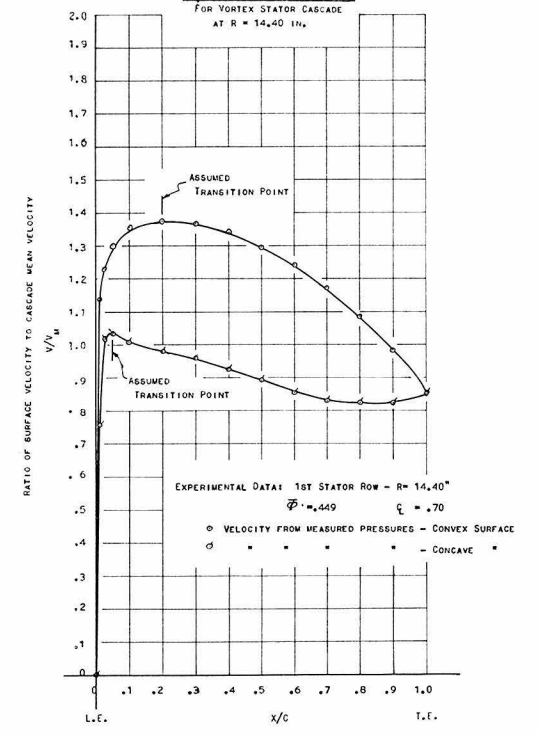

FIG. 71

SURFACE VELOCITY DISTRIBUTION
FOR VORTEX STATOR CASCADE
AT R = 14.40 IN.

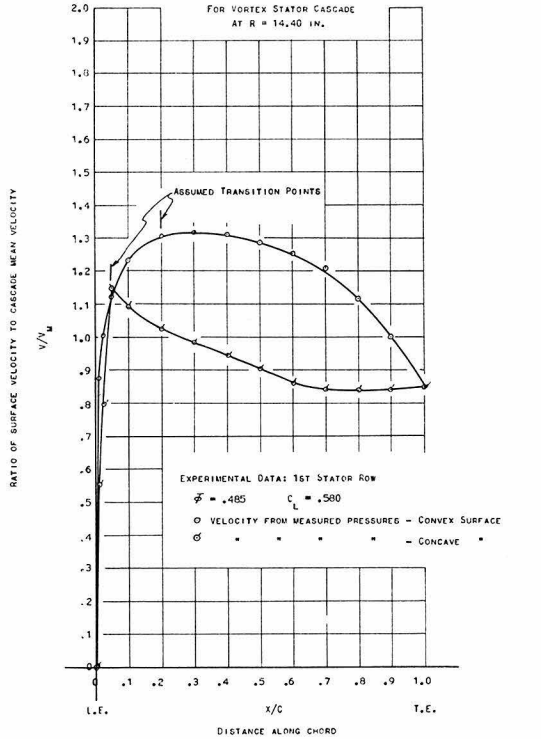

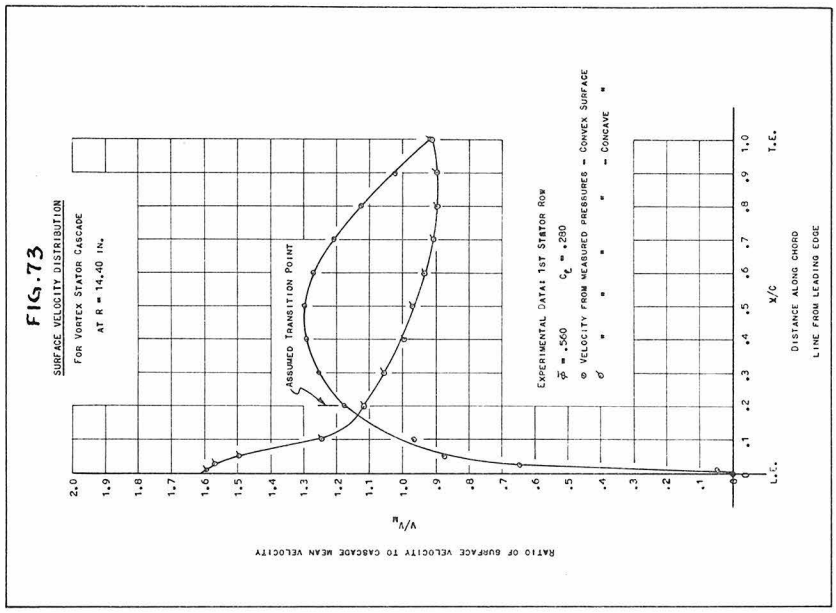
FIG. 73
SURFACE VELOCITY DISTRIBUTION
FOR VORTEX STATOR CASCADE
AT R = 14.40 IN.
ASSUMED TRANSITION POINT
EXPERIMENTAL DATA: 1ST STATOR ROW
$\bar{\sigma}$ = .560 C_L = .280
⊙ VELOCITY FROM MEASURED PRESSURES - CONVEX SURFACE
σ " " " " - CONCAVE "
RATIO OF SURFACE VELOCITY TO CASCADE MEAN VELOCITY
V/V_m
L.E.
T.E.
X/C
DISTANCE ALONG CHORD
LINE FROM LEADING EDGE

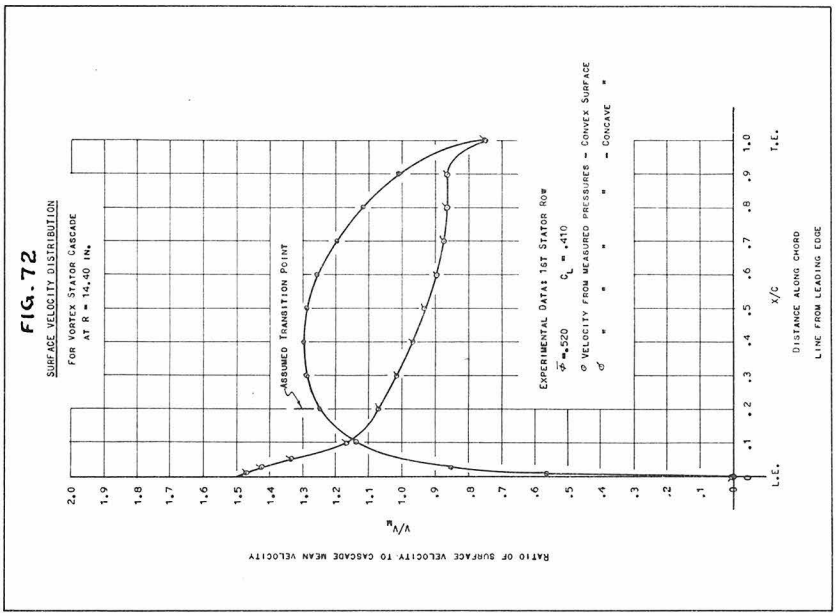
FIG. 72
SURFACE VELOCITY DISTRIBUTION
FOR VORTEX STATOR CASCADE
AT R = 14.40 IN.
ASSUMED TRANSITION POINT
EXPERIMENTAL DATA: 1ST STATOR ROW
$\bar{\sigma}$ = .520 C_L = .410
⊙ VELOCITY FROM MEASURED PRESSURES - CONVEX SURFACE
σ " " " " - CONCAVE "
RATIO OF SURFACE VELOCITY TO CASCADE MEAN VELOCITY
V/V_m
L.E.
T.E.
X/C
DISTANCE ALONG CHORD
LINE FROM LEADING EDGE

FIG. 74

CALCULATED BOUNDARY LAYERS

FOR STATOR CASCADE (R=14.40) AT C_L =1.026

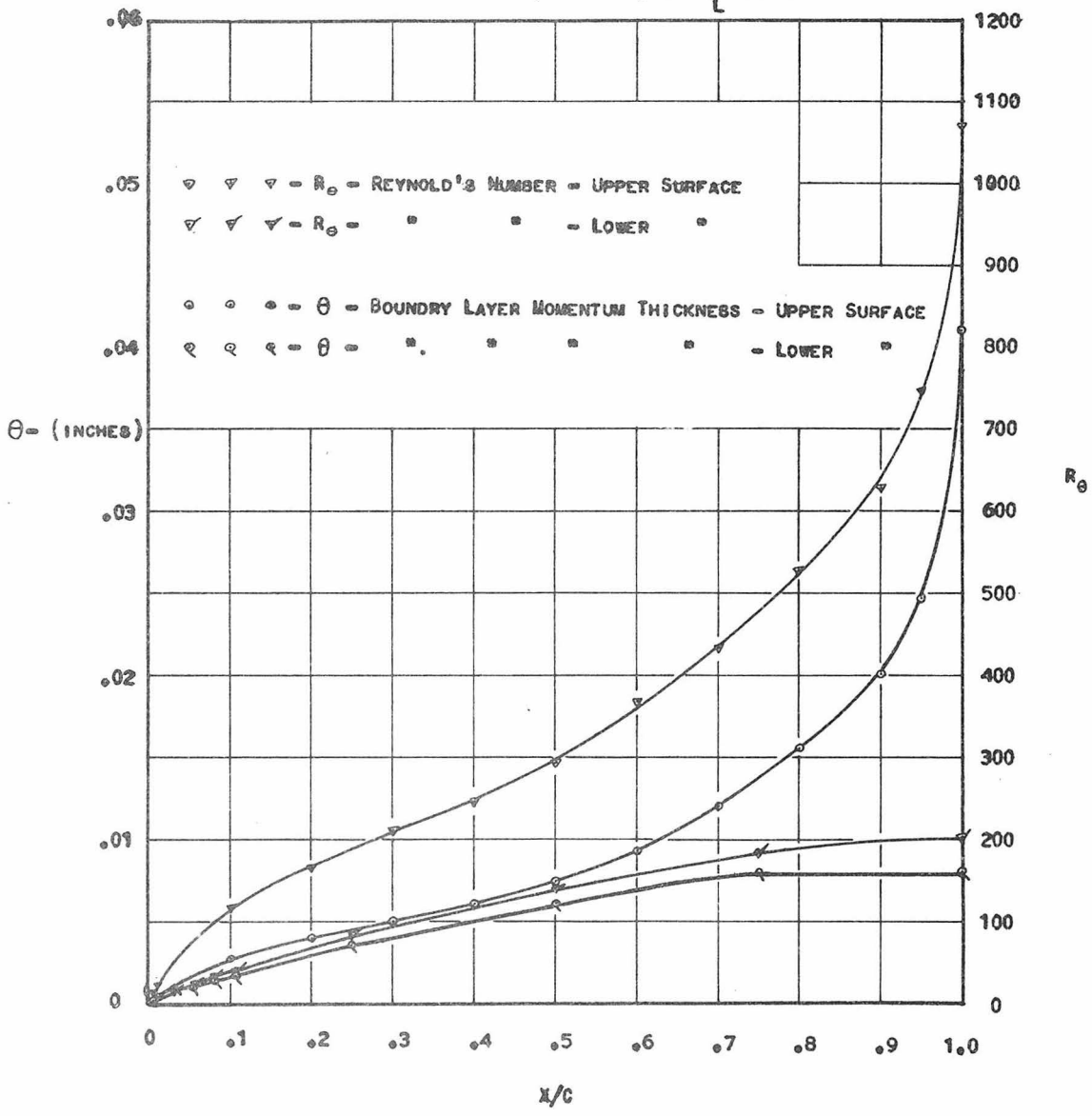

FIG. 75 - CASCADE BOUNDARY LAYER REGIONS

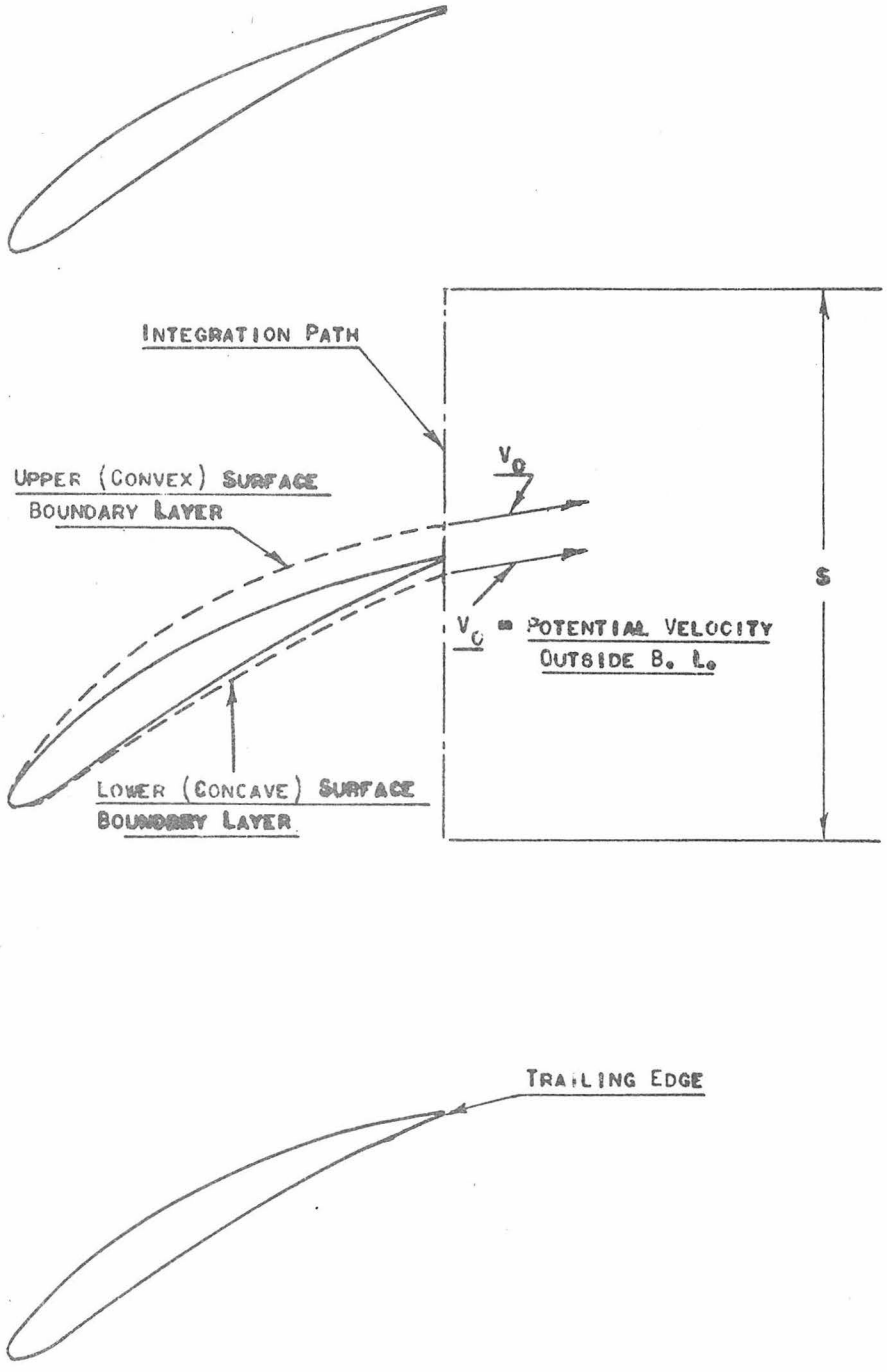

FIG. 76

LOSS AND TURNING ANGLE DATA

FOR VORTEX STATOR CASCADE R=14.40 IN.

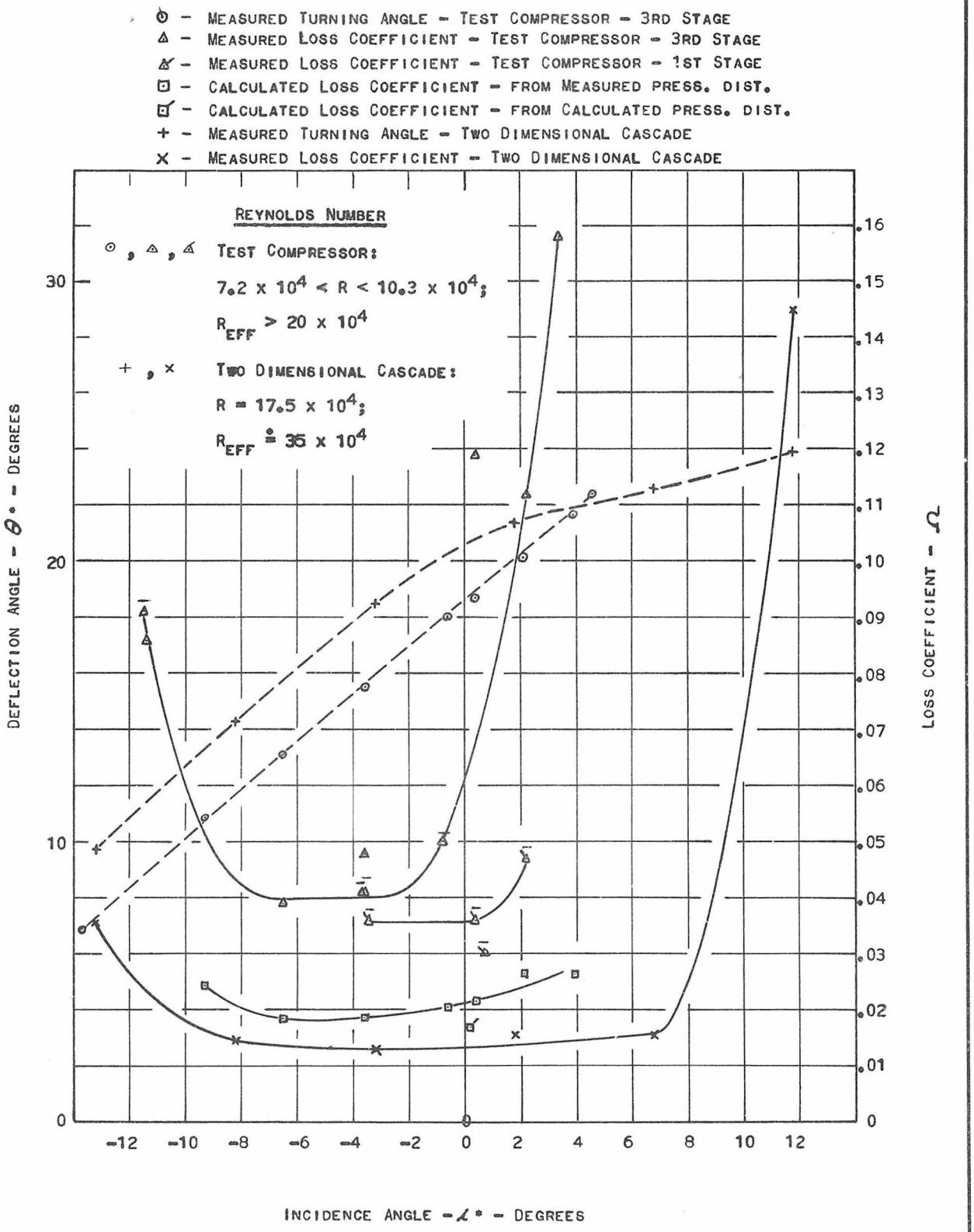

FIG. 77
WAKE SURVEY DATA

⊙ – TOTAL PRESSURE COEFFICIENT $-\psi'_2$
Δ – AXIAL VELOCITY " $-\phi_2$
LOCATION: DOWNSTREAM OF 3RD STATOR
R = 14.40" , .05 IN. FROM T.E. PLANE
CONDITIONS: $\bar{\phi}$ = .324, $i^* = 2.0°$, $\theta^* = 17.8$
SPEED= 750 R.P.M. , 3 STAGES

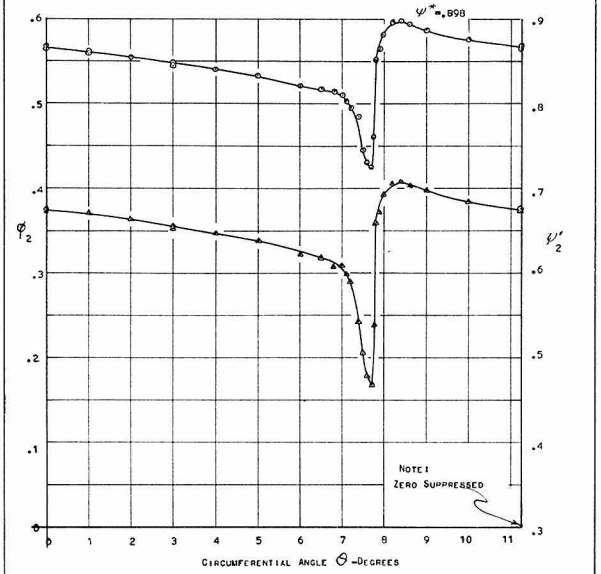

FIG. 78
WAKE SURVEY DATA

⊙ – TOTAL PRESSURE COEFFICIENT $-\psi'_2$
Δ – AXIAL VELOCITY " $-\phi_2$
LOCATION: DOWNSTREAM OF 3RD STATOR
R= 14.40", .05 IN. FROM T.E. PLANE
CONDITIONS: $\bar{\phi}$ = .352 , $i^* = 3.4$, $\theta^* = 21.3$
SPEED: 750 R.P.M., 3 STAGES

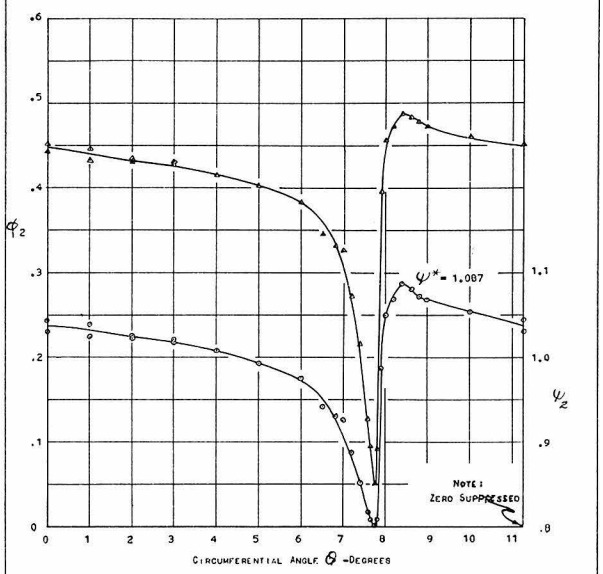

FIG. 79
WAKE SURVEY DATA

⊙ – TOTAL PRESSURE COEFFICIENT $-\psi'_2$
Δ – AXIAL VELOCITY " $-\phi_2$
LOCATION: DOWNSTREAM OF 3RD STATOR
R = 14.40", .05 IN. FROM T.E. PLANE
CONDITIONS: $\bar{\phi}$ = .370, $i^* = 2.2$, $\theta^* = 20.2$
SPEED= 750 R.P.M., 3 STAGES

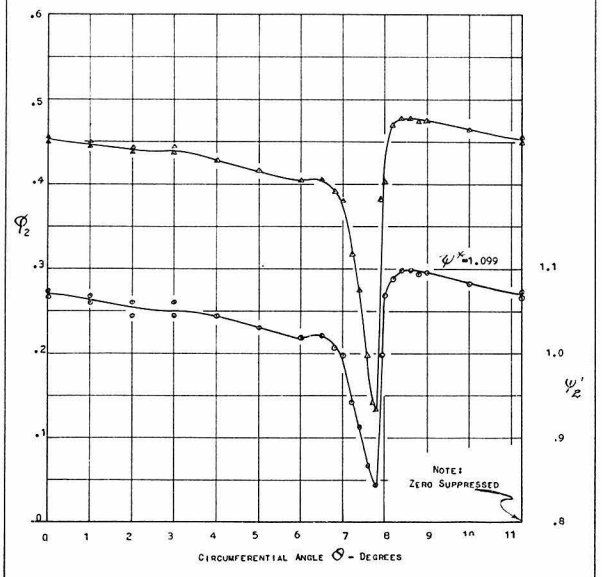

FIG. 80
WAKE SURVEY DATA

⊙ – TOTAL PRESSURE COEFFICIENT $-\psi_2$
Δ – AXIAL VELOCITY " $-\phi_2$
LOCATION: DOWNSTREAM OF 3RD STATOR
R = 14.40" , .05 IN. FROM T.E. PLANE
CONDITIONS: $\bar{\phi}$= .392, $i^* = 4°$, $\theta^* = 18.7°$
SPEED= 750 R.P.M., 3 STAGES

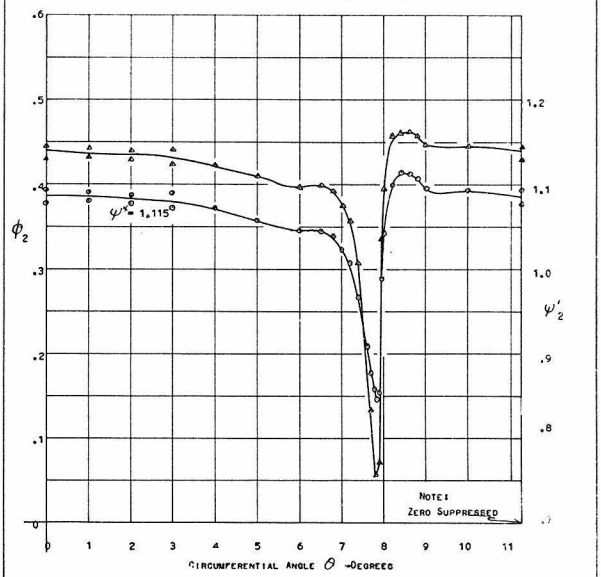

FIG. 81
WAKE SURVEY DATA

⊙-TOTAL PRESSURE COEFFICIENT $-\psi'_2$
△-AXIAL VELOCITY " $-\phi_2$
LOCATION: DOWNSTREAM OF 3RD STATOR
R=14.40" , .05 IN. FROM T.E. PLANE
CONDITIONS: $\bar{\phi}$= .448, i^* = -3.6° , θ^* = 15.4°
SPEED = 750 R.P.M., 3 STAGES

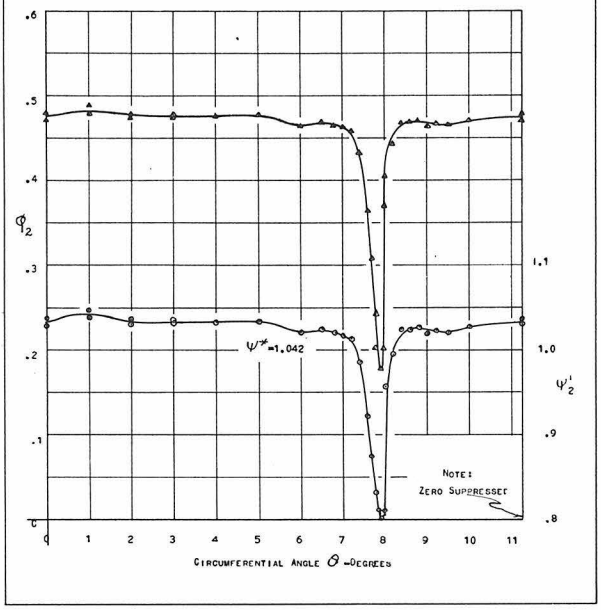

FIG. 82
WAKE SURVEY DATA

⊙ - TOTAL PRESSURE COEFFICIENT $-\psi'_2$
△ - AXIAL VELOCITY " $-\phi_2$
LOCATION: DOWNSTREAM OF 3RD STATOR
R = 14.40", .05 IN. FROM T.E. PLANE
CONDITIONS: $\bar{\phi}$= .485 , i^* = -6.5° , θ^* = 13.1°
SPEED= 750 R.P.M. , 3 STAGES

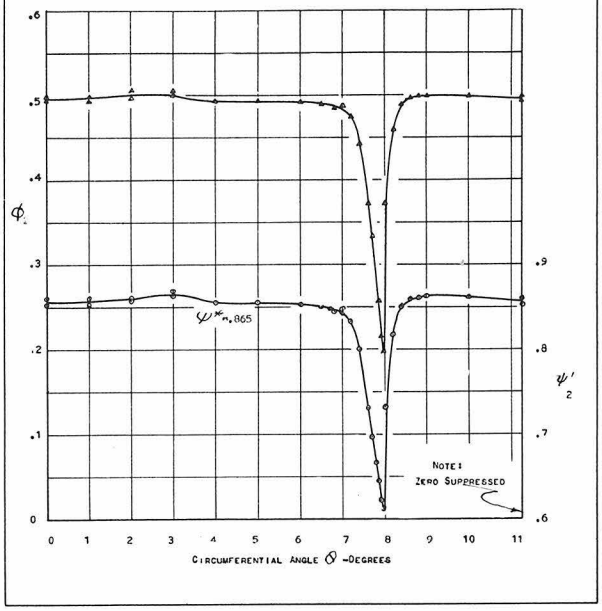

FIG. 83
WAKE SURVEY DATA

⊙ - TOTAL PRESSURE COEFFICIENT $-\psi'_2$
△ = AXIAL VELOCITY " $-\phi_2$
LOCATION: DOWNSTREAM OF 3RD STATOR
R= 14.40" , .05 IN. FROM T.E. PLANE
CONDITIONS: $\bar{\phi}$ =.552, i^* = -11.4° , θ^* = 9.3°
SPEED = 750 R.P.M., 3 STAGES

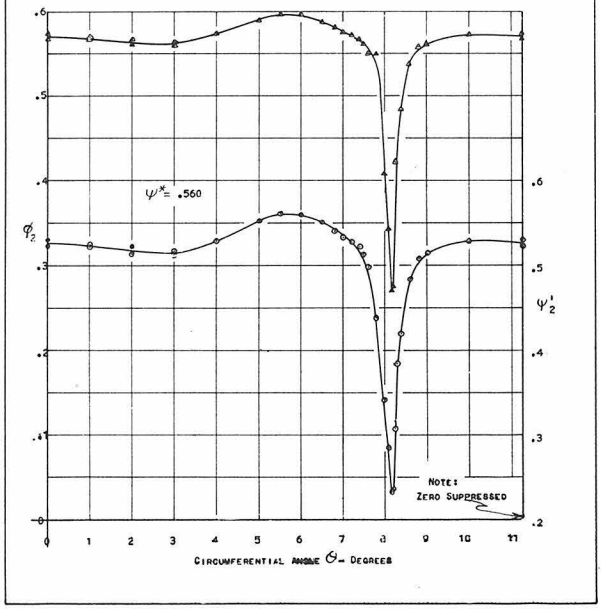

FIG. 84
WAKE SURVEY DATA

⊙ - TOTAL PRESSURE COEFFICIENT $-\psi'_2$
△ - AXIAL VELOCITY " $-\phi_2$
LOCATION: DOWNSTREAM OF 3RD STATOR
R= 14.40" , -1.07 IN. FROM T.E. PLANE
CONDITIONS: $\bar{\phi}$ = .320 , i^* = -.8° , 12.5°
SPEED = 750 R.P.M., 3 STAGES

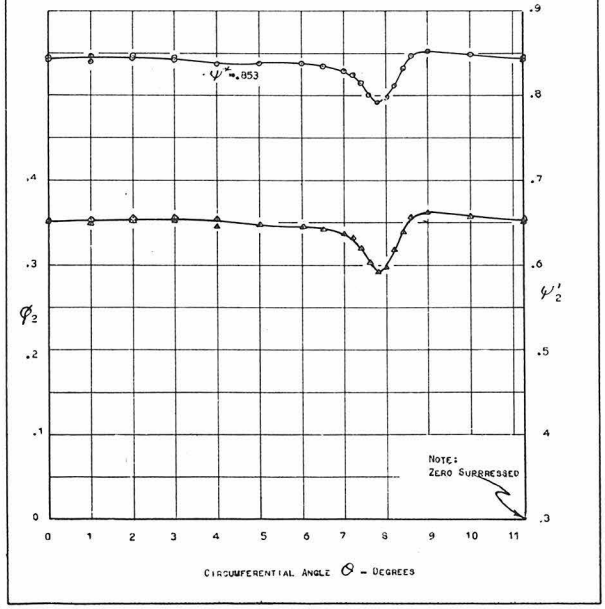

FIG. 85

WAKE SURVEY DATA

○ – TOTAL PRESSURE COEFFICIENT – ψ'_2

△ – AXIAL VELOCITY " – ϕ_2

LOCATION: DOWNSTREAM OF 3RD STATOR

R=14.40", 1.07 IN. FROM T.E. PLANE

CONDITIONS: $\bar{\phi}$=.449, $i^* = -3.7°$, $\theta^* = 15.4°$

SPEED = 750 R.P.M., 3 STAGES

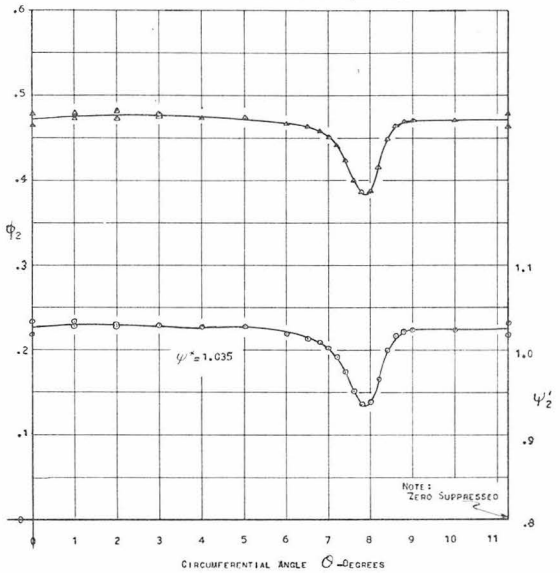

FIG. 86

WAKE SURVEY DATA

○ – TOTAL PRESSURE COEFFICIENT – ψ'_2

△ – AXIAL VELOCITY " – ϕ_2

LOCATION: DOWNSTREAM OF 3RD STATOR

R = 14.40", 1.07 IN. FROM T.E. PLANE

CONDITIONS: $\bar{\phi}$ = .553, $i^* = -11.5°$, $\theta^* = 9.2°$

SPEED = 750 R.P.M., 3 STAGES

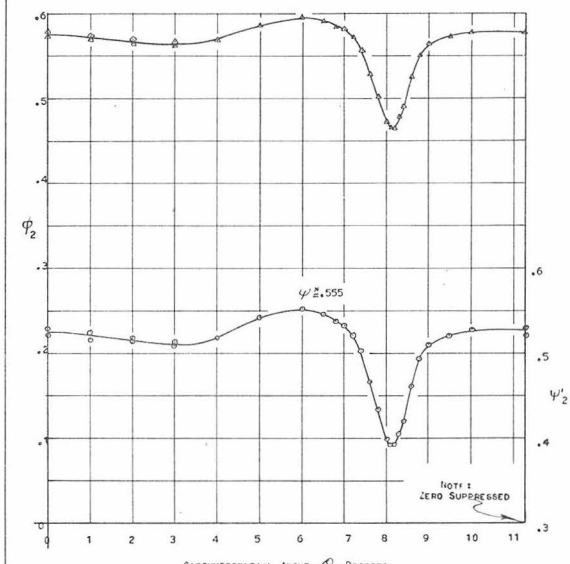

FIG. 87

WAKE SURVEY DATA

○ – TOTAL PRESSURE COEFFICIENT – ψ'_2

△ – AXIAL VELOCITY " – ϕ_2

LOCATION: DOWNSTREAM OF 3RD STATOR

R= 14.40", .250 IN. FROM T.E. PLANE

CONDITIONS: $\bar{\phi}$ = .448, $i^* = -3.6$, $\theta^* = 15.4$

SPEED: 750 R.P.M., 3 STAGES

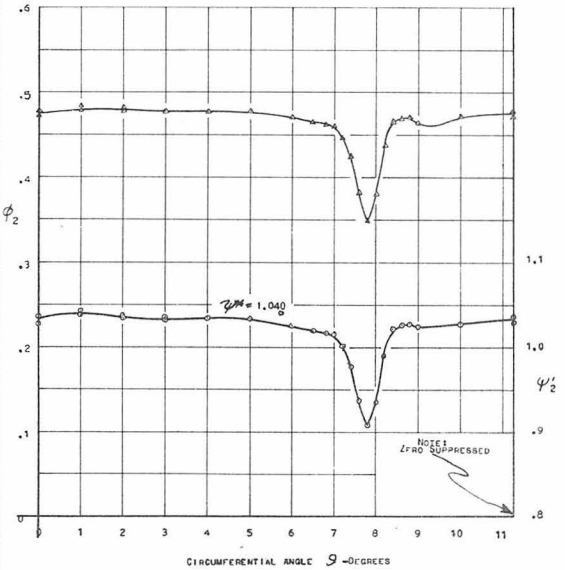

FIG. 88

WAKE SURVEY DATA

○ – TOTAL PRESSURE COEFFICIENT – ψ'_2

△ – AXIAL VELOCITY " – ϕ_2

LOCATION: DOWNSTREAM OF 1ST STATOR

R = 14.40", 1.07 IN. FROM T.E. PLANE

CONDITIONS: $\bar{\phi}$ = .370, $i^* = 2.2°$, $\theta^* = 20.2$

SPEED = 750 R.P.M., 1 STAGE

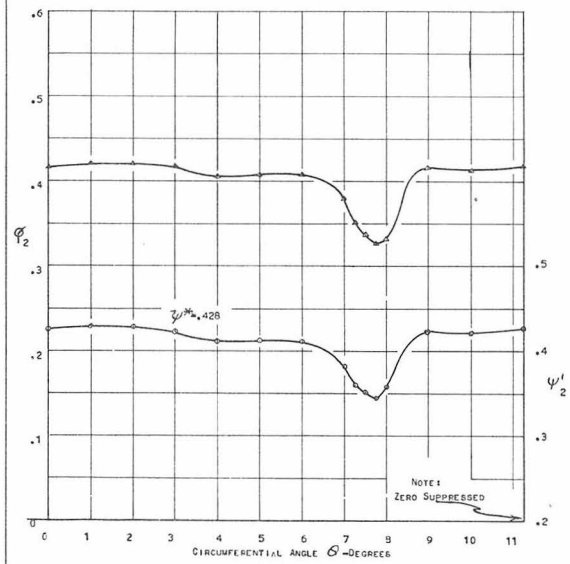

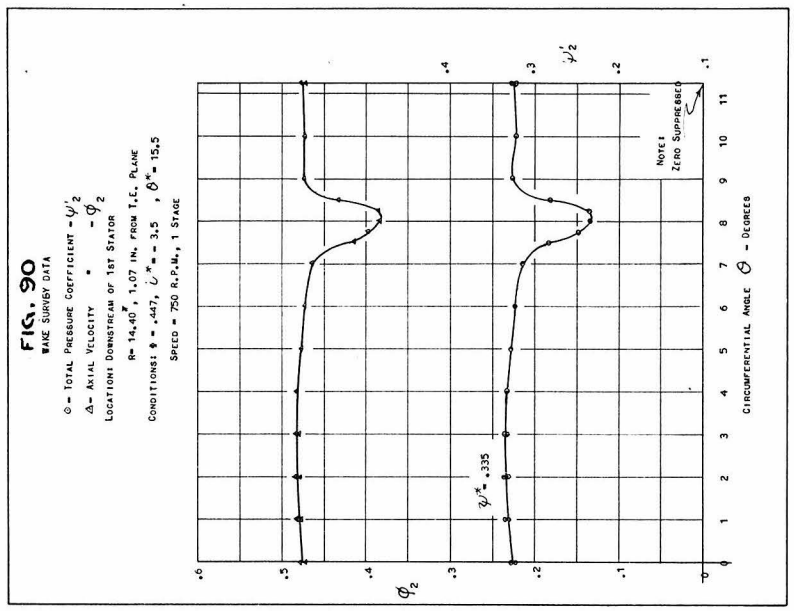
FIG. 90
WAKE SURVEY DATA
○ - TOTAL PRESSURE COEFFICIENT - ψ'_2
Δ - AXIAL VELOCITY " - ϕ_2
LOCATION: DOWNSTREAM OF 1ST STATOR
R= 14.40", 1.07 IN. FROM T.E. PLANE
CONDITIONS: $\bar{\phi}$ = .447, i^* = 3.5 , δ^* = 15.5
SPEED = 750 R.P.M., 1 STAGE
ψ'^* = .335
NOTE: ZERO SUPPRESSED
CIRCUMFERENTIAL ANGLE θ - DEGREES

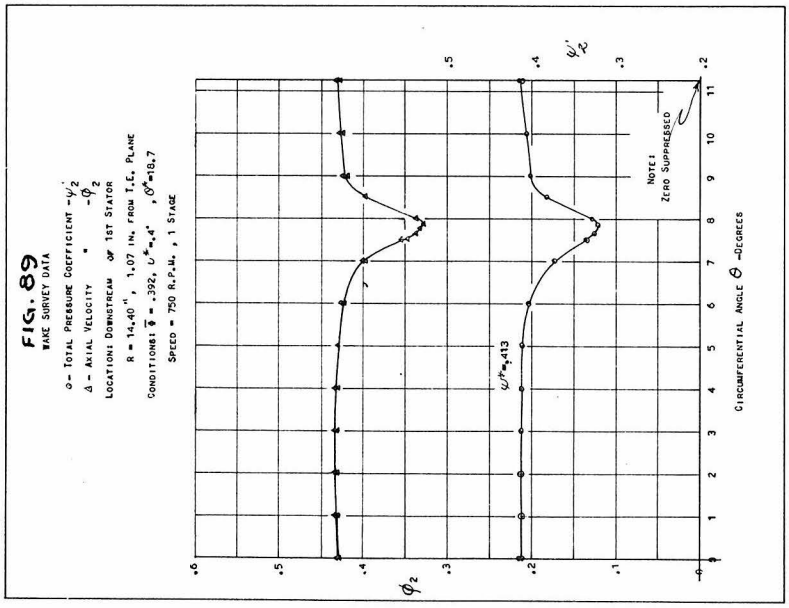
FIG. 89
WAKE SURVEY DATA
○ - TOTAL PRESSURE COEFFICIENT - ψ'_2
Δ - AXIAL VELOCITY " - ϕ_2
LOCATION: DOWNSTREAM OF 1ST STATOR
R = 14.40", 1.07 IN. FROM T.E. PLANE
CONDITIONS: $\bar{\phi}$ = .392, i^*=.4° , δ^*=18.7
SPEED = 750 R.P.M., 1 STAGE
ψ'^*=.413
NOTE: ZERO SUPPRESSED
CIRCUMFERENTIAL ANGLE θ -DEGREES

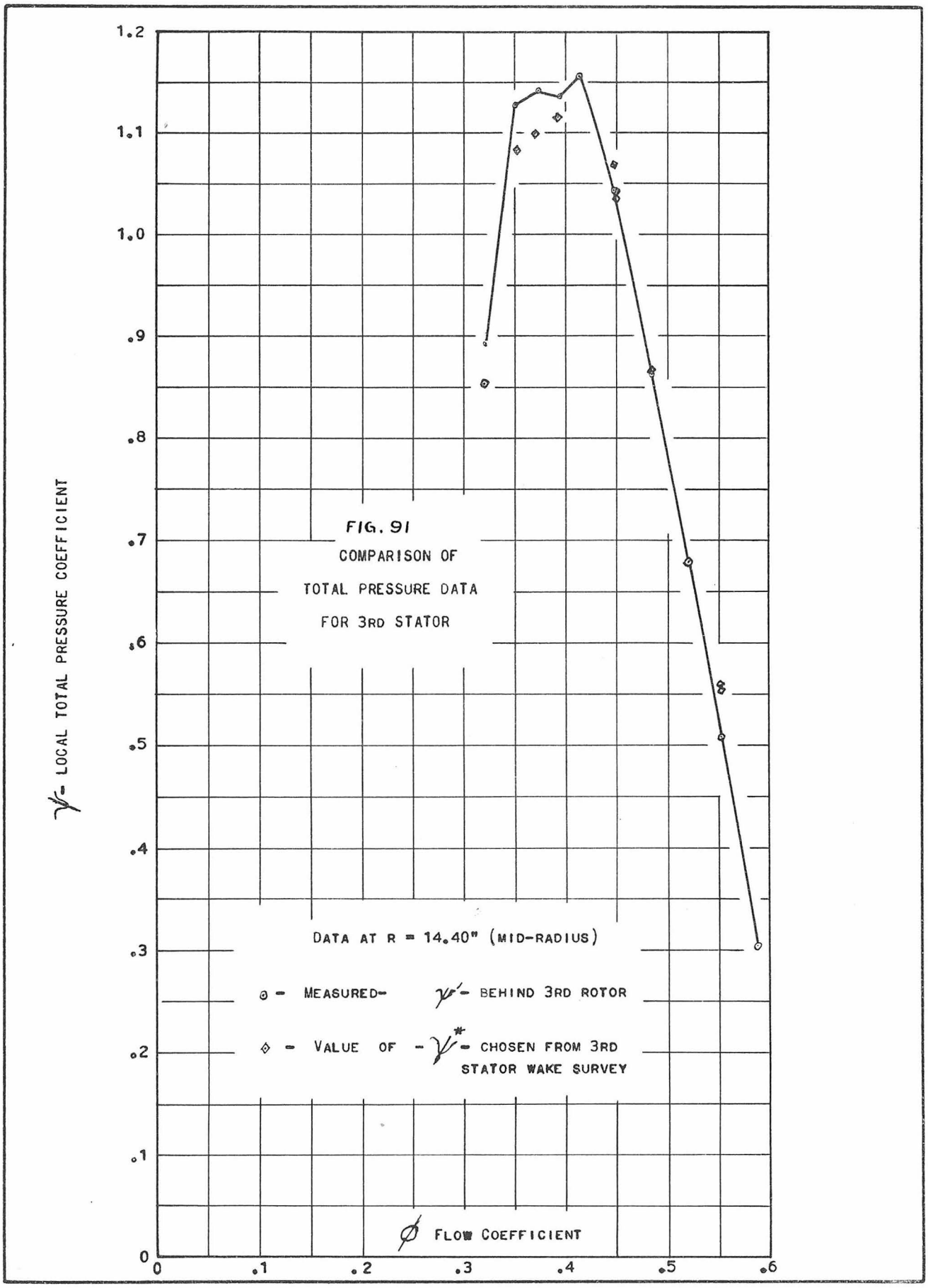
1.2
1.1
1.0
.9
.8
.7
.6
.5
.4
.3
.2
.1
0
0
.1
.2
.3
.4
.5
.6
ψ - LOCAL TOTAL PRESSURE COEFFICIENT
FIG. 91
COMPARISON OF
TOTAL PRESSURE DATA
FOR 3RD STATOR
DATA AT R = 14.40" (MID-RADIUS)
⊙ - MEASURED- ψ' - BEHIND 3RD ROTOR
◇ - VALUE OF - ψ* - CHOSEN FROM 3RD STATOR WAKE SURVEY
φ FLOW COEFFICIENT

FIG. 92

LOSS AND ANGLE DATA

* 1ST VORTEX STATOR *

OPERATING CONDITIONS: SINGLE STAGE

750 R.P.M. $\bar{\phi}$ = .392

⊙ – LOSS FROM WAKE SURVEY

——— – TURNING ANGLE FROM FAIRED CURVE

– – – – – – INCIDENCE ANGLE FROM FAIRED CURVE

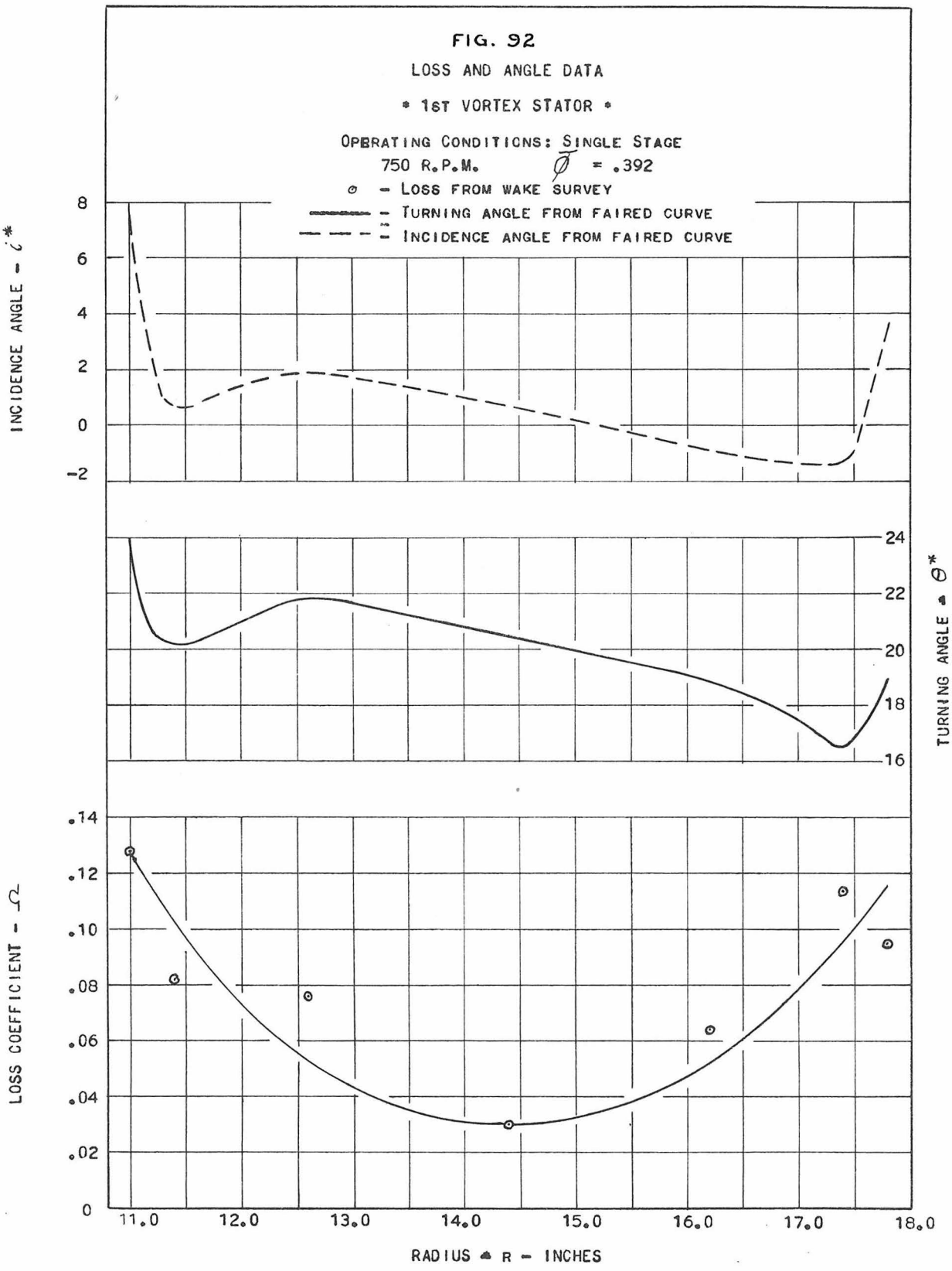

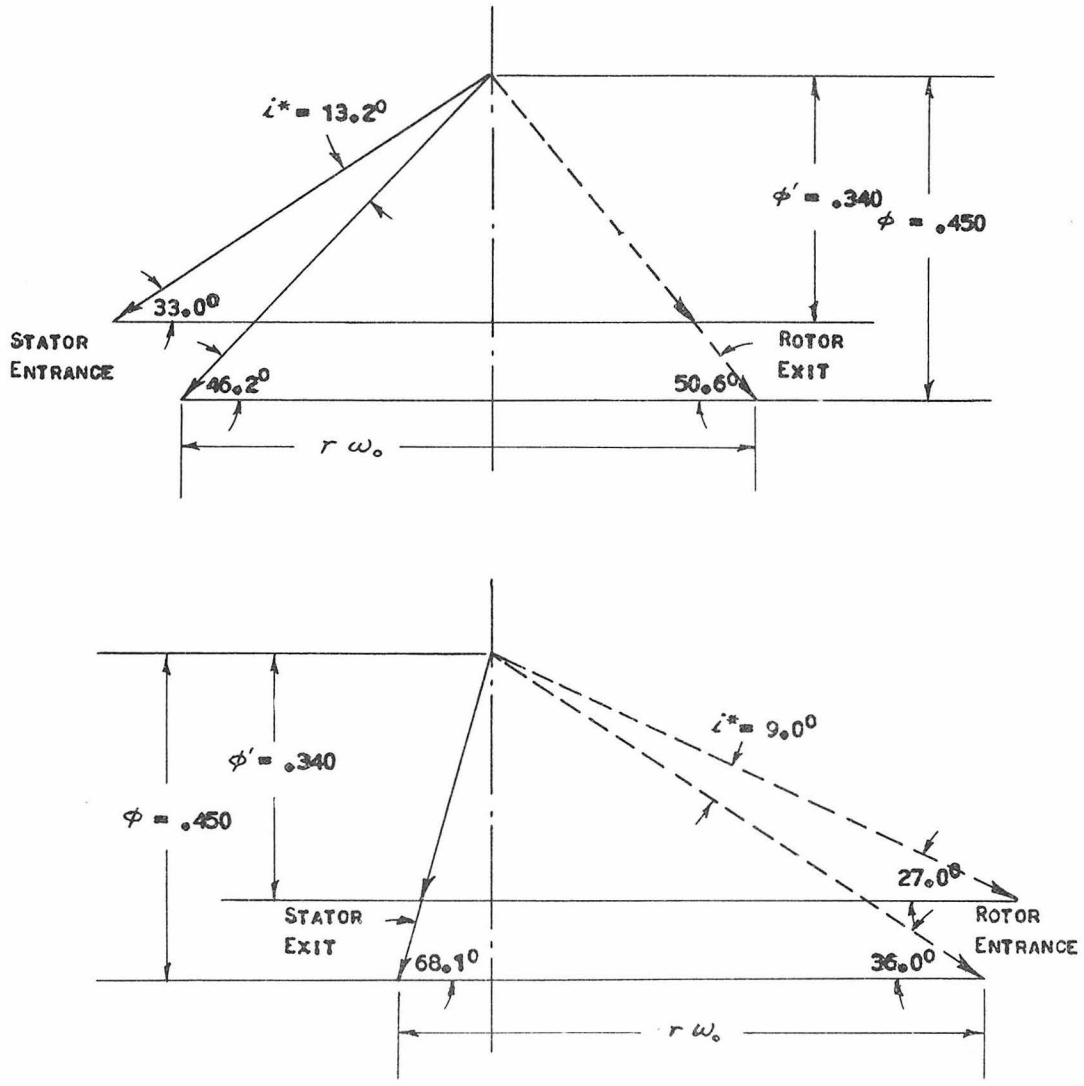

FIG. 93

EFFECT OF CASCADE WAKES ON VELOCITY DIAGRAMS

(R = 14.40")

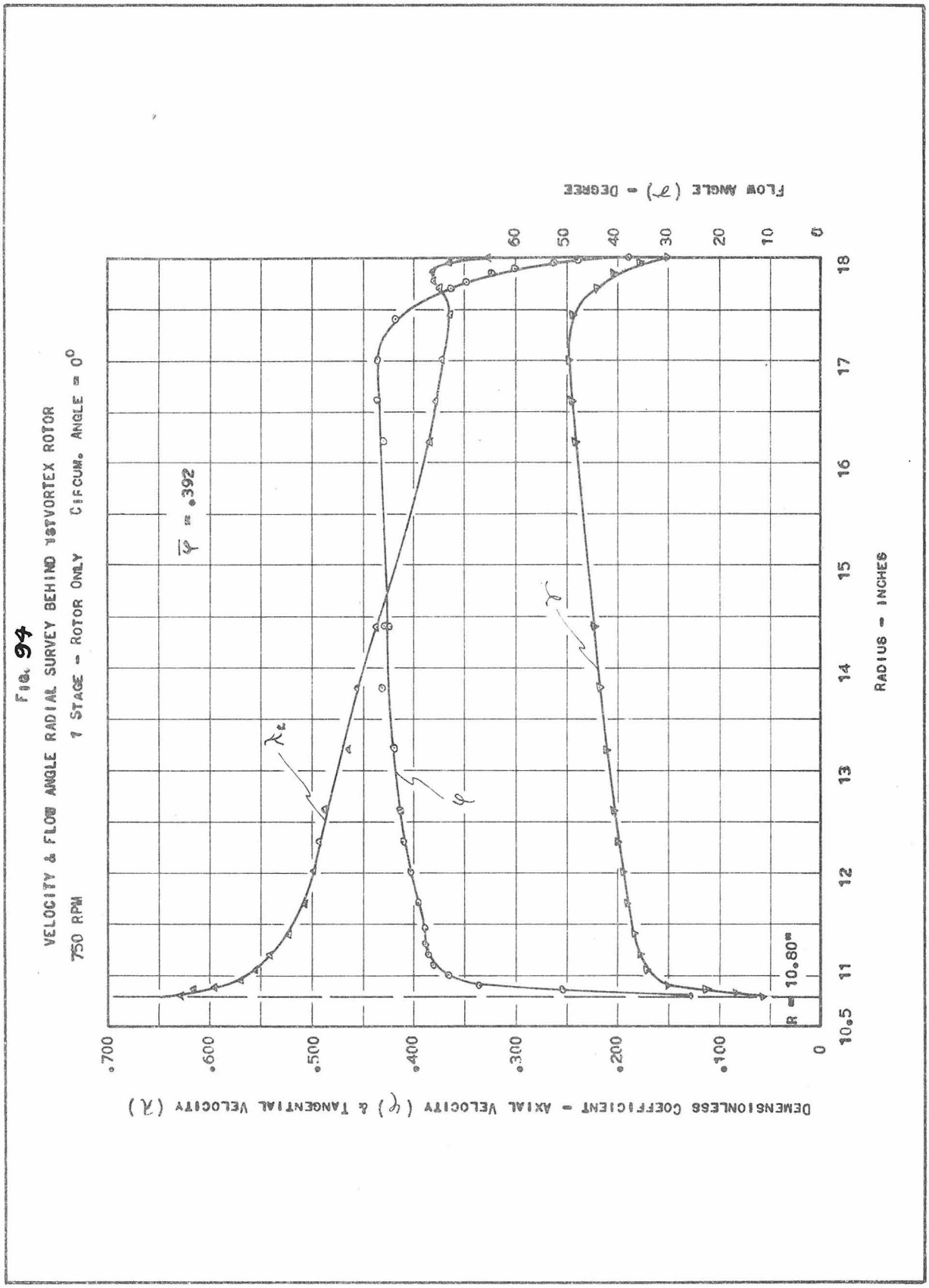
Fig. 94
VELOCITY & FLOW ANGLE RADIAL SURVEY BEHIND VSTVORTEX ROTOR
750 RPM 1 STAGE - ROTOR ONLY CIRCUM. ANGLE = 0°
$\bar{\varphi}$ = .392
R = 10.80"
DEMENSIONLESS COEFFICIENT - AXIAL VELOCITY (φ) & TANGENTIAL VELOCITY (λ)
FLOW ANGLE (γ) - DEGREE
RADIUS - INCHES
.700
.600
.500
.400
.300
.200
.100
0
60
50
40
30
20
10
0
10.5
11
12
13
14
15
16
17
18

FIG. 95A - AXIAL VELOCITY CONTOURS* BEHIND 1ST FREE VORTEX STATOR

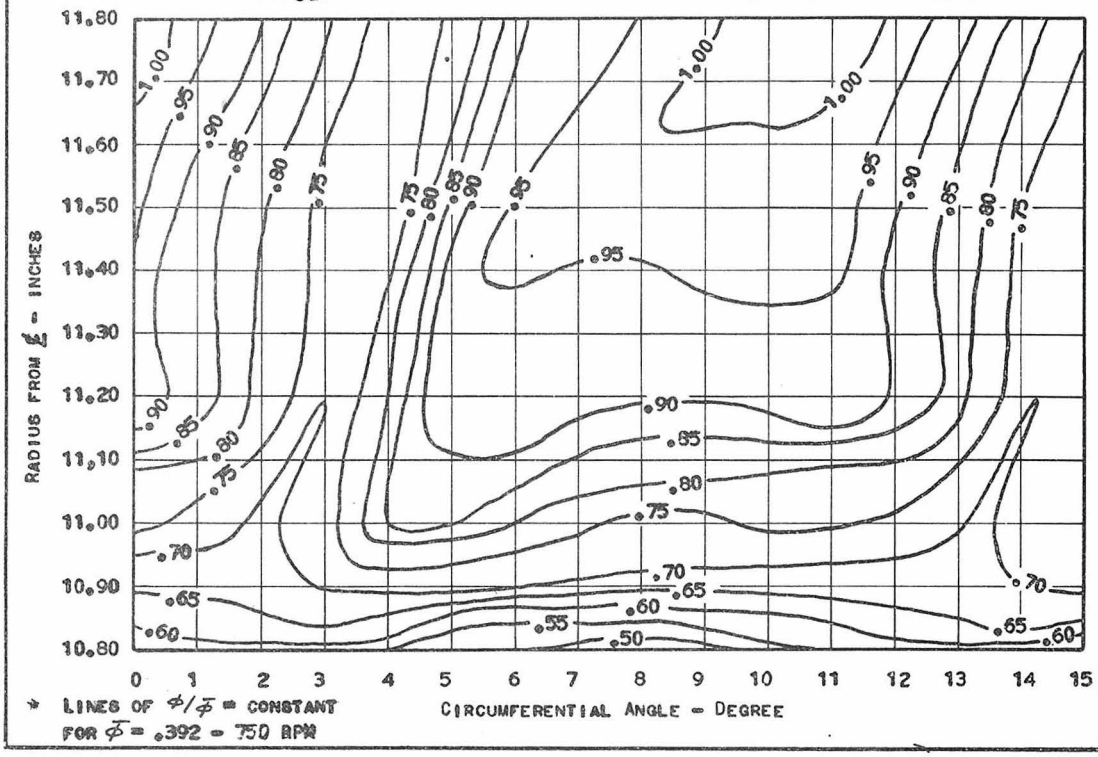

FIG. 95B - AXIAL VELOCITY CONTOURS* BEHIND 1ST FREE VORTEX STATOR

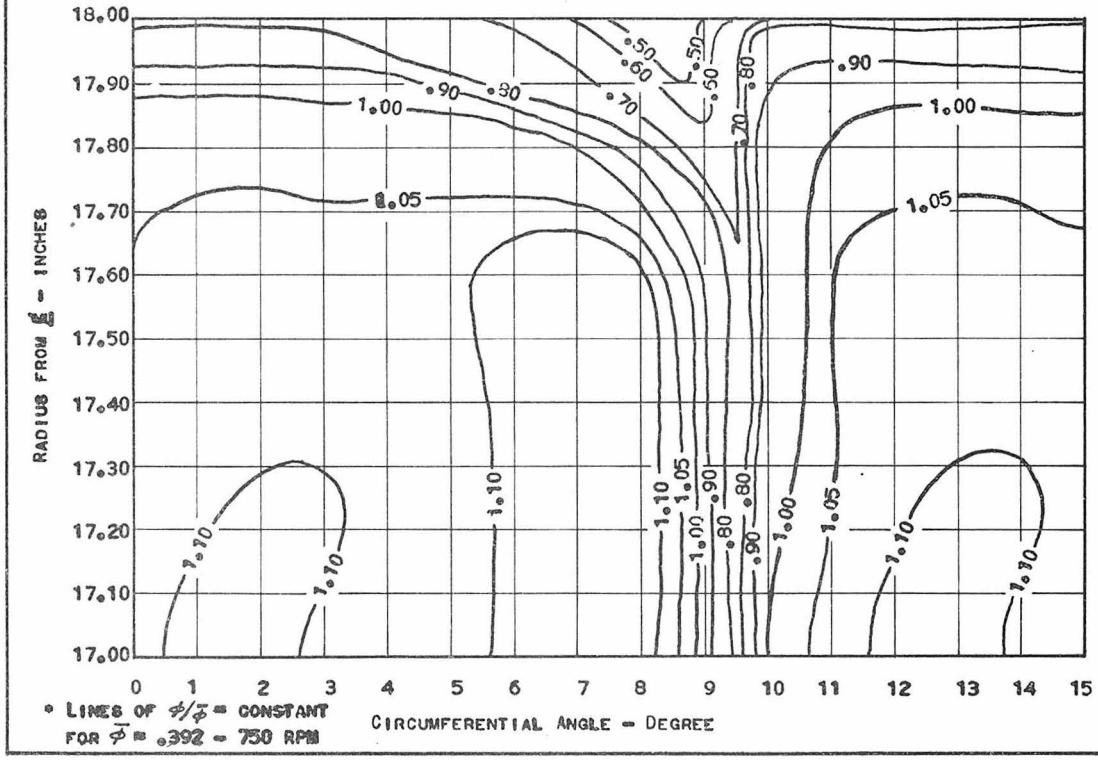

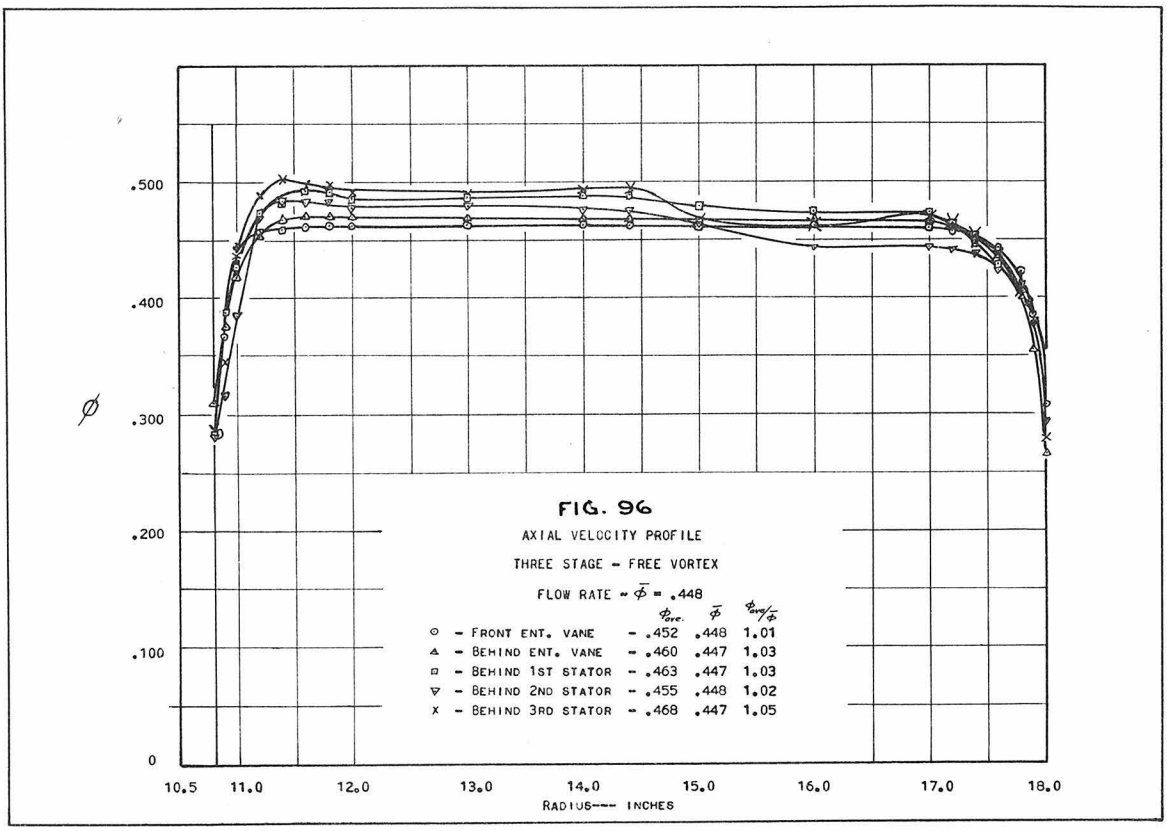
.500
.400
.300
.200
.100
0
Φ
10.5
11.0
12.0
13.0
14.0
15.0
16.0
17.0
18.0
RADIUS--- INCHES
FIG. 96
AXIAL VELOCITY PROFILE
THREE STAGE - FREE VORTEX
FLOW RATE ~ Φ̄ = .448
Φ_ave. Φ̄ Φ_ave/Φ̄
○ - FRONT ENT. VANE - .452 .448 1.01
△ - BEHIND ENT. VANE - .460 .447 1.03
□ - BEHIND 1ST STATOR - .463 .447 1.03
▽ - BEHIND 2ND STATOR - .455 .448 1.02
X - BEHIND 3RD STATOR - .468 .447 1.05

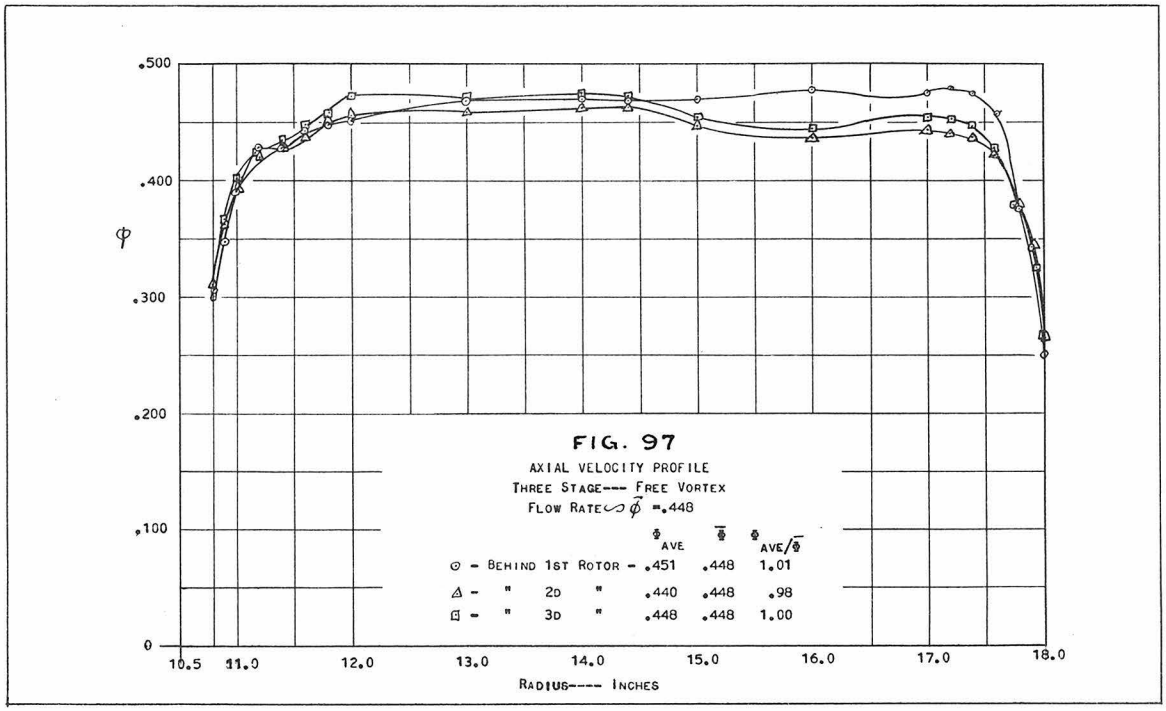
.500
.400
.300
.200
.100
0
Φ
10.5
11.0
12.0
13.0
14.0
15.0
16.0
17.0
18.0
RADIUS---- INCHES
FIG. 97
AXIAL VELOCITY PROFILE
THREE STAGE--- FREE VORTEX
FLOW RATE ~ Φ̄ =.448
Φ_AVE Φ̄ Φ_AVE/Φ̄
⊙ - BEHIND 1ST ROTOR - .451 .448 1.01
△ - " 2D " .440 .448 .98
□ - " 3D " .448 .448 1.00

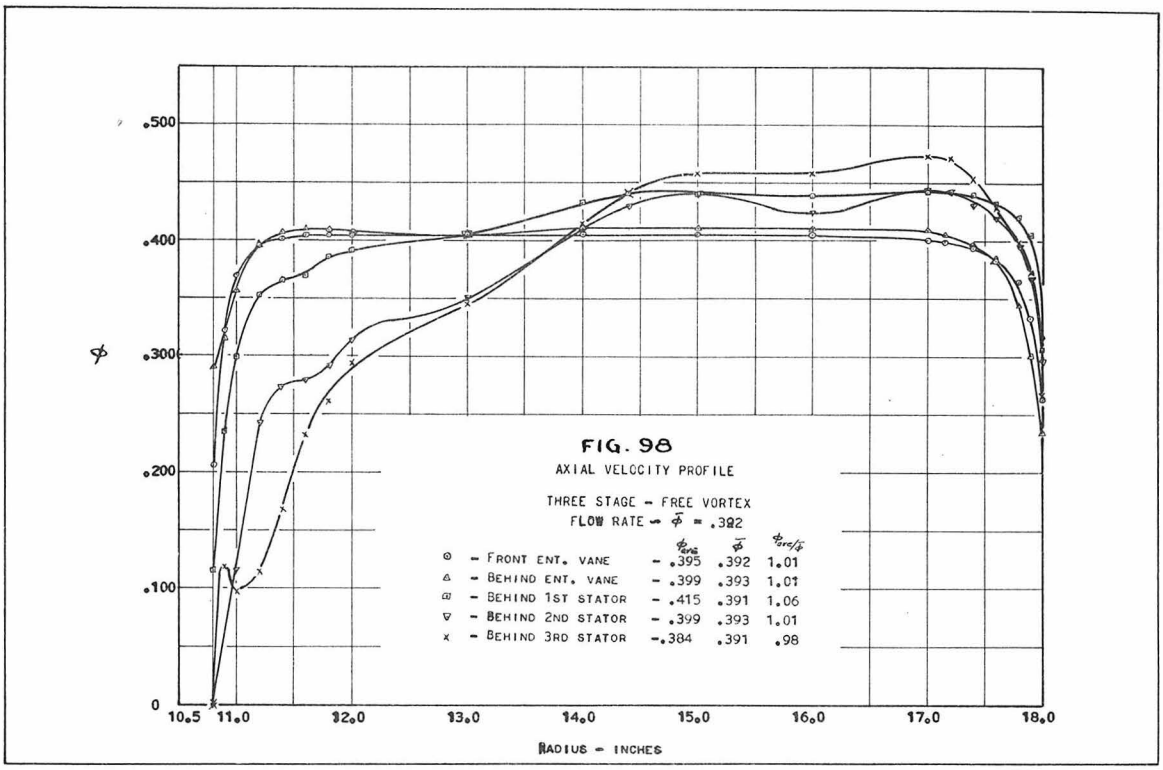
.500
.400
.300
.200
.100
0
Φ
10.5
11.0
12.0
13.0
14.0
15.0
16.0
17.0
18.0
RADIUS - INCHES
FIG. 98
AXIAL VELOCITY PROFILE
THREE STAGE - FREE VORTEX
FLOW RATE ∽ Φ̄ = .392
Φ_ave Φ̄ Φ_ave/Φ̄
⊙ - FRONT ENT. VANE - .395 .392 1.01
△ - BEHIND ENT. VANE - .399 .393 1.01
⊡ - BEHIND 1ST STATOR - .415 .391 1.06
▽ - BEHIND 2ND STATOR - .399 .393 1.01
x - BEHIND 3RD STATOR - .384 .391 .98

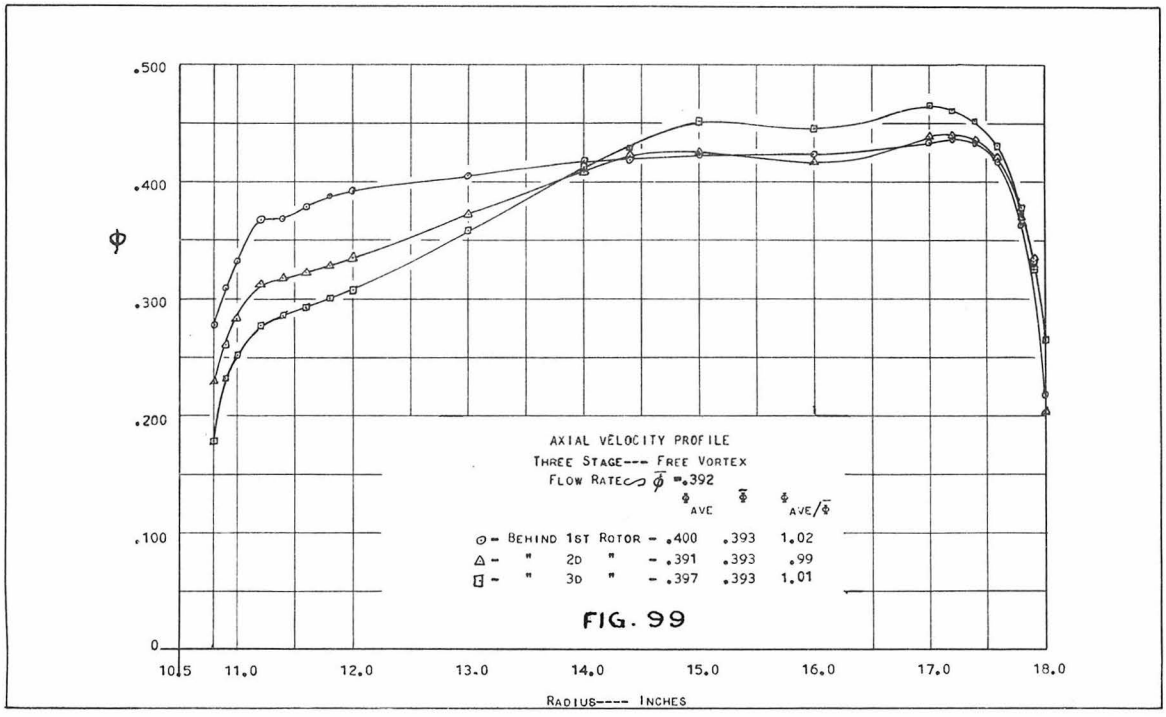
.500
.400
.300
.200
.100
0
Φ
10.5
11.0
12.0
13.0
14.0
15.0
16.0
17.0
18.0
RADIUS---- INCHES
AXIAL VELOCITY PROFILE
THREE STAGE--- FREE VORTEX
FLOW RATE∽ Φ̄ =.392
Φ_AVE Φ̄ Φ_AVE/Φ̄
⊙ - BEHIND 1ST ROTOR - .400 .393 1.02
△ - " 2D " - .391 .393 .99
⊡ - " 3D " - .397 .393 1.01
FIG. 99

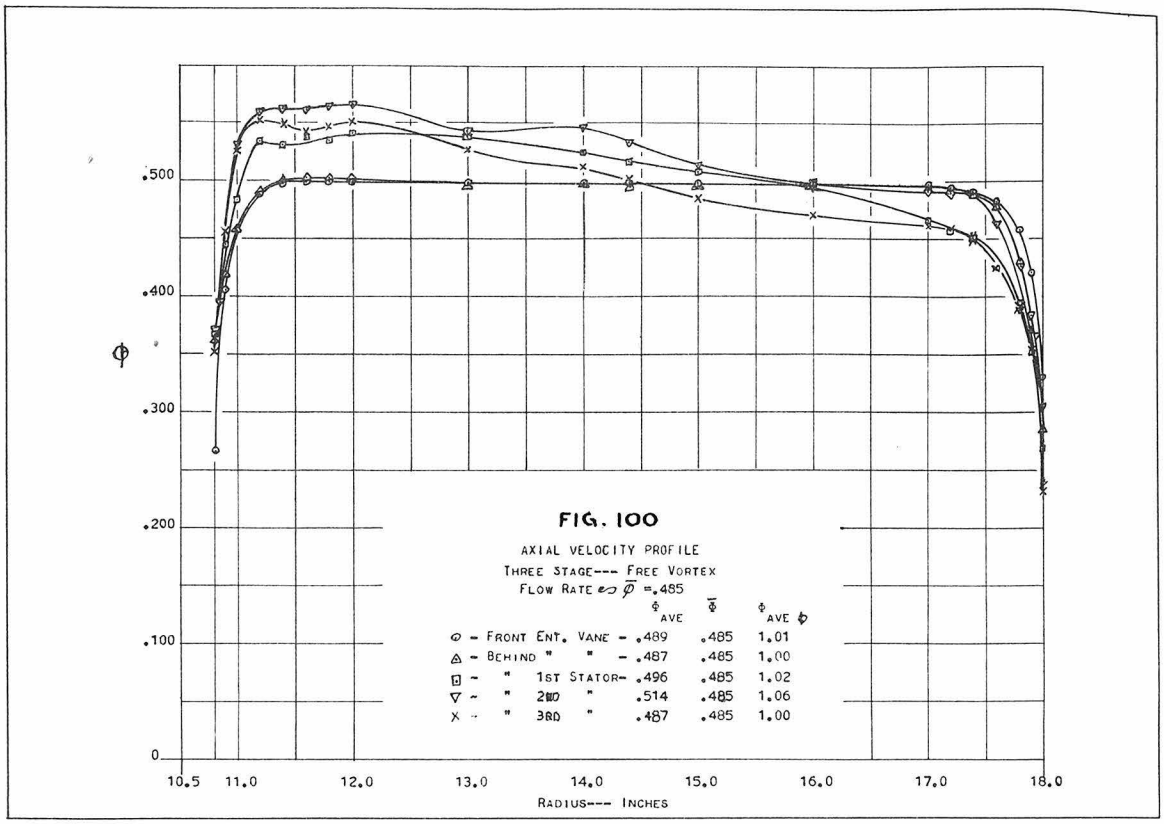

FIG. 100

AXIAL VELOCITY PROFILE
THREE STAGE--- FREE VORTEX
FLOW RATE $\overline{\phi}$ =.485

	Φ_{AVE}	$\overline{\Phi}$	$\Phi_{AVE}/\overline{\Phi}$
○ - FRONT ENT. VANE -	.489	.485	1.01
△ - BEHIND " " -	.487	.485	1.00
□ - " 1ST STATOR-	.496	.485	1.02
▽ - " 2ND "	.514	.485	1.06
X - " 3RD "	.487	.485	1.00

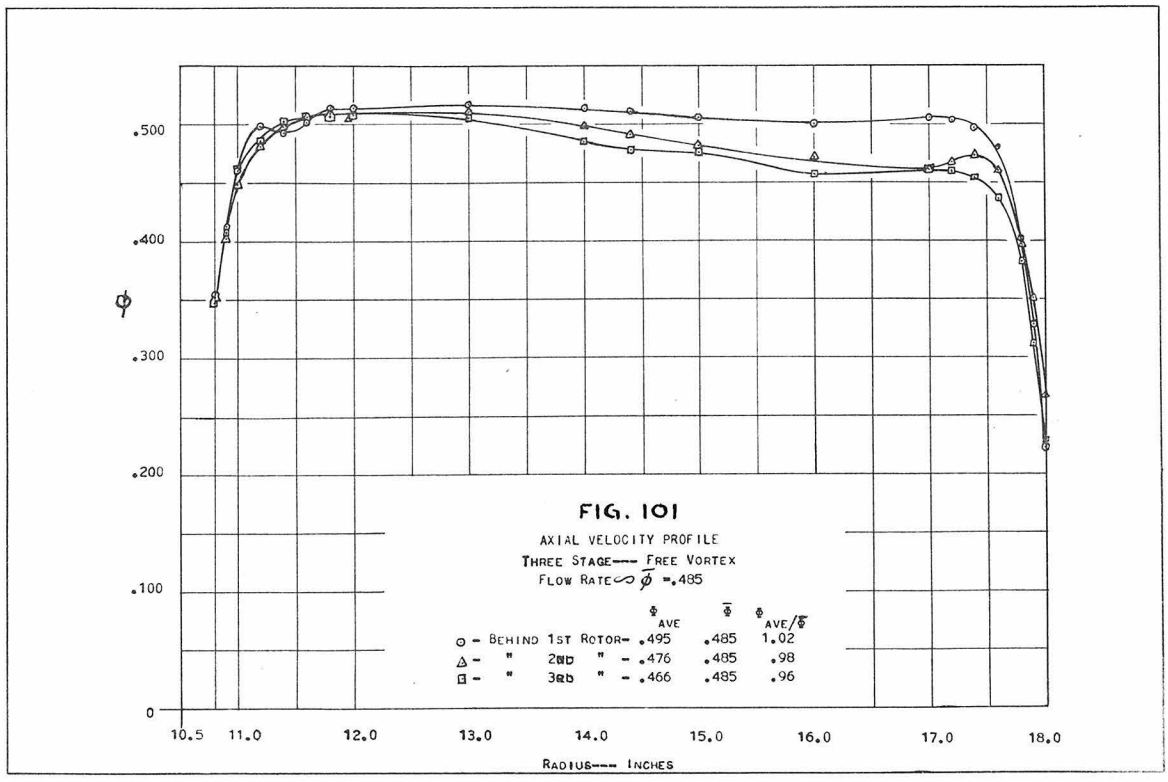

FIG. 101

AXIAL VELOCITY PROFILE
THREE STAGE--- FREE VORTEX
FLOW RATE $\overline{\phi}$ =.485

	Φ_{AVE}	$\overline{\Phi}$	$\Phi_{AVE}/\overline{\Phi}$
○ - BEHIND 1ST ROTOR-	.495	.485	1.02
△ - " 2ND " -	.476	.485	.98
□ - " 3RD " -	.466	.485	.96

FIG. 102

BOUNDARY LAYER MEASUREMENTS NEAR COMPRESSOR OUTER BOUNDARY

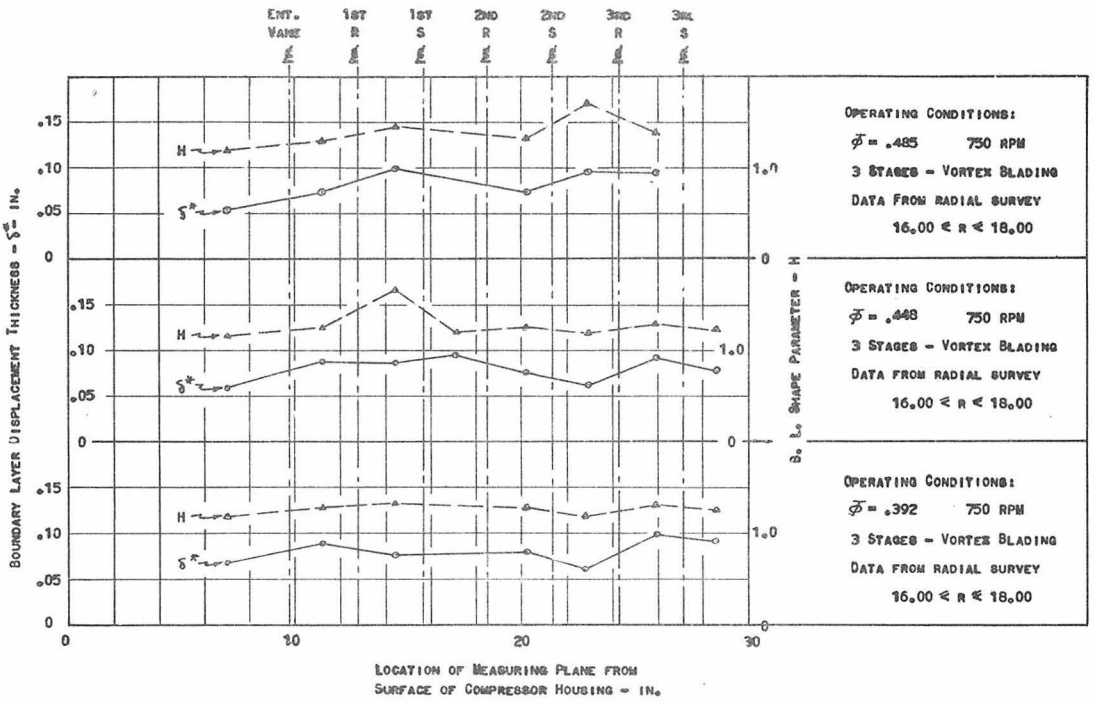

FIG. 103

BOUNDARY LAYER MEASUREMENTS NEAR COMPRESSOR INNER BOUNDARY

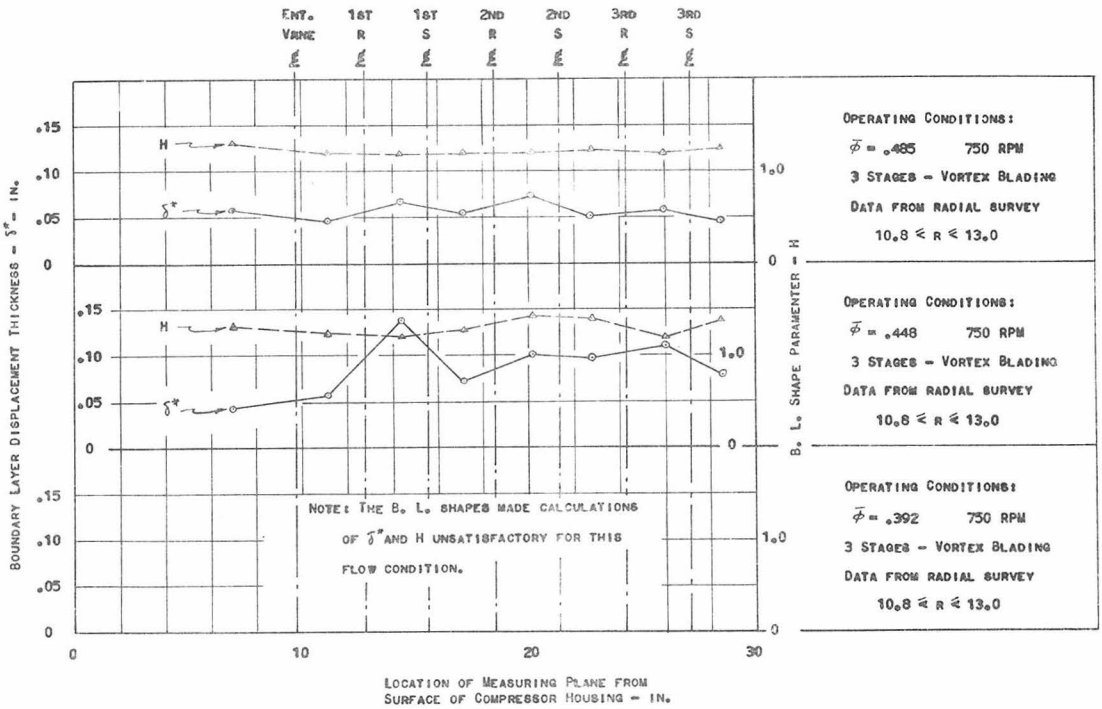

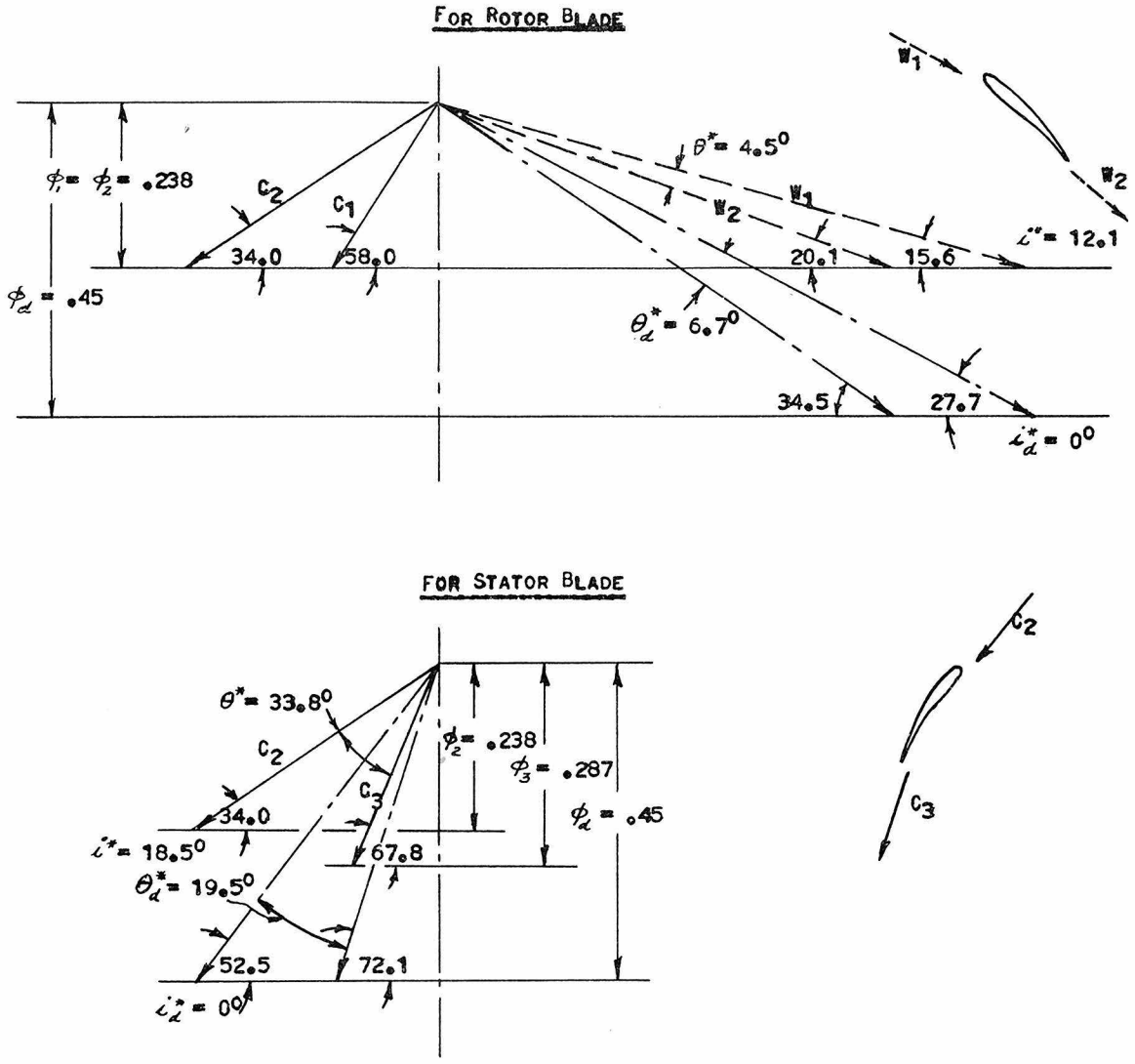

← — — — VELOCITY RELATIVE TO ROTOR - MEASURED

← ——— " " " STATOR - "

← - - - BLADE DESIGN VELOCITY

FIG. 104

MEASURED FLOW DIAGRAMS AT R = 17.98"

-SINGLE STAGE OPERATION-

$\bar{\phi} = .392$

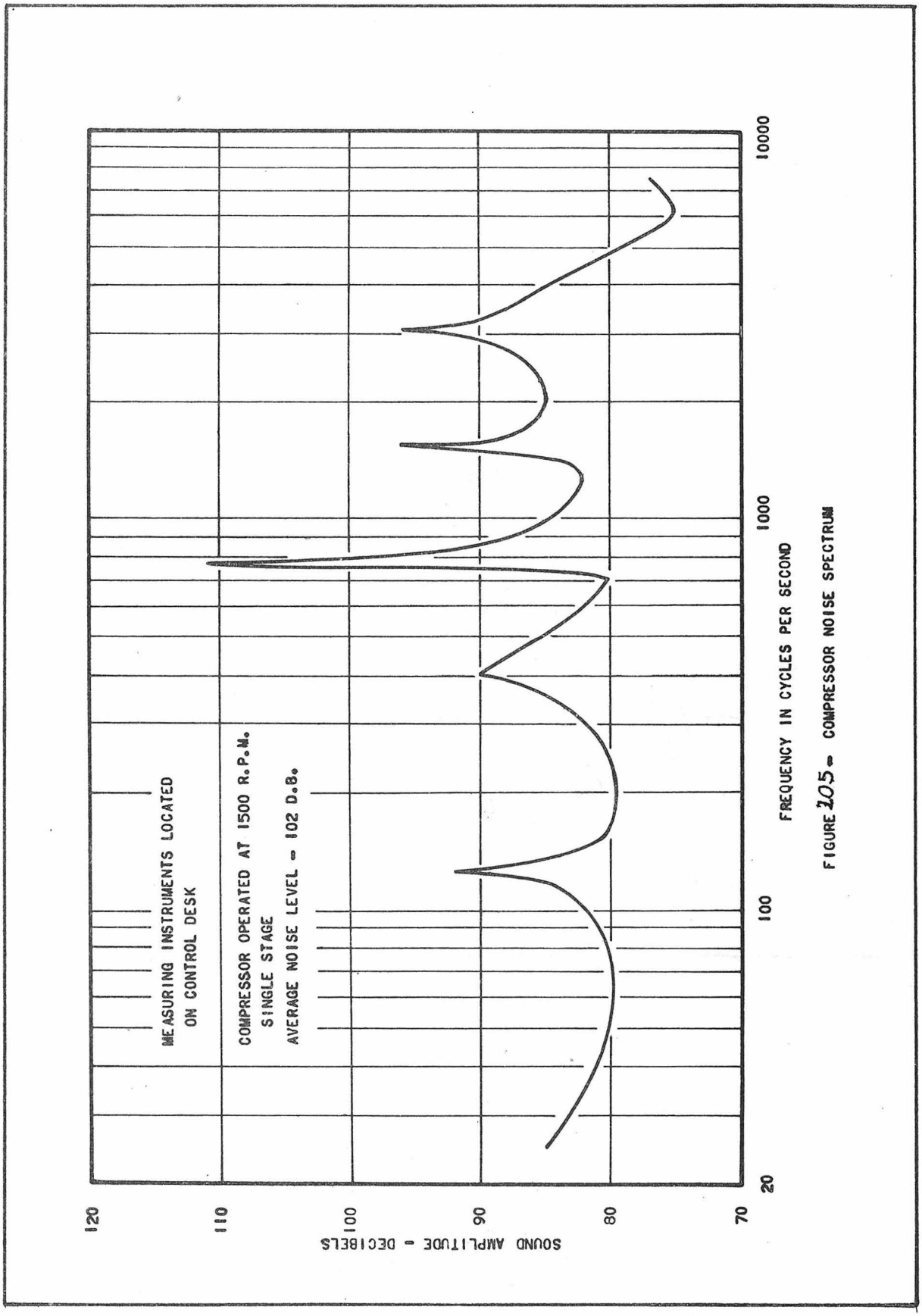

FIGURE 105 - COMPRESSOR NOISE SPECTRUM

Fig. 106

BOUNDRY LAYER NOTATION

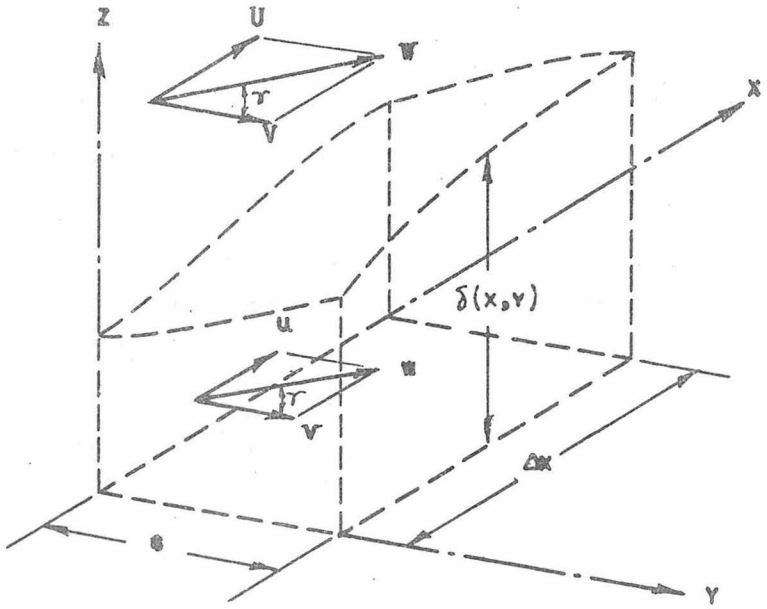

TABLE 1

AIRFOIL CALCULATIONS:

STATOR BLADE SECTION III
($\bar{\sigma}$ = .80)

PARABOLIC CAMBER LINE:
$\frac{\theta}{2}$ = 14 59'
TAN $\frac{\theta}{2}$ = .26764
MAX. THICKNESS = 10% C
C = 2.600 INCHES
TAN $\phi = \frac{dy_c}{dx_c}$

$\frac{x}{c}$	$1 - \frac{2x}{c}$	TAN ϕ	SIN ϕ	COS ϕ	$\frac{y_T}{c}$	$\frac{y_T}{c}$ SIN ϕ (3)	$\frac{y_T}{c}$ COS ϕ (4)	$1 - \frac{x}{c}$	$\frac{x}{c}\left(1 - \frac{x}{c}\right)$	$\frac{y_c}{c}$ (2)
0	1	.26764	.25854	.96600	0	0	0	1	0	0
.0050	.9900	.26496	.25601	.96667	.00850	.00218	.00822	.9950	.00498	.00133
.0100	.9800	.26229	.25376	.96727	.01222	.00310	.01182	.9900	.00990	.00265
.0200	.9600	.25693	.24897	.96851	.01667	.00415	.01615	.9800	.01960	.00524
.0300	.9400	.25158	.24390	.96980	.02084	.00508	.02021	.9700	.02910	.00779
.0400	.9200	.24623	.23910	.97100	.02317	.00554	.02250	.9600	.03400	.00910
.0500	.9000	.24088	.23429	.97217	.02542	.00596	.02471	.9500	.04750	.01271
.0600	.8800	.23552	.22920	.97338	.02772	.00635	.02698	.9400	.05640	.01509
.0700	.8600	.23017	.22438	.97450	.02970	.00666	.02894	.9300	.06510	.01742
.0800	.8400	.22482	.21928	.97566	.03147	.00690	.03070	.9200	.07360	.01970
.0900	.8200	.21946	.21445	.97673	.03311	.00710	.03234	.9100	.08190	.02192
.1000	.8000	.21411	.20933	.97784	.03463	.00725	.03386	.9000	.09000	.02409
.1500	.7000	.18735	.18424	.98288	.04044	.00745	.03975	.8500	.12750	.03412
.2000	.6000	.16058	.15845	.98737	.04460	.00707	.04404	.8000	.16000	.04282
.2500	.5000	.13382	.13354	.99118	.04744	.00634	.04702	.7500	.18750	.05018
.3000	.4000	.10706	.10655	.99431	.04938	.00526	.04910	.7000	.21000	.05620
.3500	.3000	.08029	.07991	.99680	.05000	.00400	.04984	.6500	.22750	.06089
.4000	.2000	.05353	.05346	.99857	.04937	.00264	.04930	.6000	.24000	.06423
.4500	.1000	.02676	.02675	.99964	.04784	.00128	.04782	.5500	.24750	.06624
.5000	0	0	0	1.00000	.04516	0	.04516	.5000	.25000	.06691
.5500	- .1000	-.02676	-.02675	.99964	.04148	-.00111	.04147	.4500	.24750	.06624
.6000	- .2000	-.05353	-.05346	.99857	.03712	-.00198	.03707	.4000	.24000	.06423
.6500	- .3000	-.08029	-.07991	.99680	.03222	-.00251	.03212	.3500	.22750	.06089
.7000	- .4000	-.10706	-.10655	.99431	.02687	-.00286	.02672	.3000	.21000	.05620
.7500	- .5000	-.13382	-.13354	.99118	.02109	-.00282	.02090	.2500	.18750	.05018
.8000	- .6000	-.16058	-.15845	.98737	.01600	-.00254	.01580	.2000	.16000	.04280
.8500	- .7000	-.18735	-.18424	.98288	.01140	-.00210	.01120	.1500	.12750	.03412
.9000	- .8000	-.21411	-.20933	.97784	.00719	-.00151	.00703	.1000	.09000	.02409
.9500	- .9000	-.24088	-.23429	.97217	.00372	-.00087	.00362	.0500	.04750	.01271
1.0000	-1.0000	-.26764	-.25854	.96600	.00111	-.00029	.00107	0	0	0

TABLE 1 (CONT)

(1)		(1)-(3)	(2)+(4)	(1)+(3)	(2)-(4)					
$\frac{X}{C}$	Yc INCHES	$\frac{X_U}{C}$	$\frac{Y_U}{C}$	$\frac{X_\ell}{C}$	$\frac{Y_\ell}{C}$	X_U INCHES	Y_U INCHES	X_ℓ INCHES	Y_ℓ INCHES	X INCHES
0	0	0	0	0	0	0	0	0	0	0
.0050	.00346	.00282	.00955	.00718	-.00689	.00733	.02483	.01867	-.01791	.01300
.0100	.00689	.00690	.01447	.01310	-.00917	.01794	.03762	.03406	-.02384	.02600
.0200	.01362	.01585	.02139	.02415	-.01091	.04121	.05561	.06279	-.02837	.05200
.0300	.02025	.02492	.02800	.03508	-.01242	.06479	.07280	.09121	-.03229	.07800
.0400	.02366	.03446	.03160	.04554	-.01340	.08960	.08216	.11840	-.03484	.10400
.0500	.03305	.04404	.03742	.05596	-.01200	.11450	.09729	.14550	-.03120	.13000
.0600	.03923	.05365	.04159	.06635	-.01189	.13949	.10813	.17251	-.03091	.15600
.0700	.04529	.06334	.04636	.07666	-.01152	.16468	.12054	.19932	-.02995	.18200
.0800	.05122	.07310	.05040	.08690	-.01100	.19006	.13104	.22594	-.02860	.20800
.0900	.05699	.08290	.05426	.09710	-.01042	.21554	.14108	.25246	-.02709	.23400
.1000	.06263	.09275	.05795	.10725	-.00977	.24115	.15067	.27885	-.02540	.26000
.1500	.08871	.14255	.07387	.15745	-.00563	.37063	.19206	.40937	-.01464	.39000
.2000	.11133	.19293	.08686	.20707	-.00122	.50162	.22584	.53838	-.00317	.52000
.2500	.13047	.24366	.09720	.25634	.00316	.63352	.25272	.66648	.00822	.65000
.3000	.14612	.29474	.10530	.30526	.00710	.76632	.27378	.79368	.01846	.78000
.3500	.15831	.34600	.11073	.35400	.01105	.89960	.28790	.92040	.02873	.91000
.4000	.16700	.39736	.11353	.40264	.01493	1.03314	.29518	1.04686	.03882	1.04000
.4500	.17222	.44872	.11406	.45128	.01842	1.16667	.29656	1.17333	.04789	1.17000
.5000	.17397	.50000	.11207	.50000	.02175	1.30000	.29138	1.30000	.05655	1.30000
.5500	.17222	.55111	.10771	.54889	.02477	1.43289	.28005	1.42711	.06440	1.43000
.6000	.16700	.60198	.10130	.59802	.02716	1.56515	.26338	1.55485	.07062	1.56000
.6500	.15831	.65257	.09301	.64743	.02877	1.69668	.24183	1.68332	.07480	1.69000
.7000	.14612	.70286	.08292	.69714	.02948	1.82744	.21559	1.81256	.07665	1.82000
.7500	.13047	.75282	.07108	.74718	.02928	1.95733	.18481	1.94267	.07613	1.95000
.8000	.11133	.80254	.05860	.79746	.02700	2.08660	.15236	2.07340	.07020	2.08000
.8500	.08871	.85210	.04532	.84790	.02292	2.21546	.11783	2.20454	.05959	2.21000
.9000	.06263	.90151	.03112	.89849	.01706	2.34393	.08091	2.33607	.04436	2.34000
.9500	.03305	.95087	.01633	.94913	.00909	2.47226	.04246	2.46774	.02363	2.47000
1.0000	0	1.00029	.00107	.99971	-.00107	2.60075	.00278	2.59925	-.00278	2.60000

TABLE 2

ELECTRICAL SPECIFICATIONS

DYNAMOMETER

ELECTRIC PRODUCTS CO., D.C. MOTOR (REBUILT), TYPE 1-7264, STABILIZED SHUNT WOUND, 250 VOLTS, 450 AMPS., MAX. SPEED 2000 R.P.M.

MOTOR GENERATOR SET

DRIVING MOTOR: ELECTRIC MACHINERY MFG. CO., SYNCHRONOUS MOTOR, SERIAL NO. 83382, THREE PHASE, 60 CYCLES, 125 H.P., 2400 VOLTS, 32 AMPS., SPEED 1200 R.P.M.

GENERATORS (2): TROY ENGINE AND MACHINE CO., DIRECT CURRENT GENERATOR (REBUILT), COMPOUND WOUND, 60 K.W., 120 VOLTS, 500 AMPS., SPEED 1200 R.P.M.

TABLE 3

VORTEX ROTOR BLADE ANGLE CALCULATIONS

ASSUMPTIONS: $\xi_{HUB} = 0.60000$, $\bar{\psi}_a = 0.40000$, $\bar{\phi}_a = 0.45000$, $\xi_1 = 0.70000$, $C_o = 0.98000$, $\frac{1}{\bar{\phi}_a} = 2.2222$, $\frac{C_o - \bar{\psi}_a}{4} = 0.14500$, $\frac{C_o + \bar{\psi}_a}{4} = 0.34500$, $\frac{\pi D}{N} = \frac{\pi \times 36}{30} = 3.7700$

SECTION	VIII	VII	VI	V	IV	III	II	I
ξ	0.60000	0.62000	0.65000	0.70000	0.75000	0.80000	0.90000	1.00000
$1/\xi$	1.6666	1.6129	1.5385	1.4286	1.3333	1.2500	1.1111	1.00000
λ_1	0.24167	0.23387	0.22380	0.20715	0.19333	0.18125	0.16111	0.14500
λ_2	0.57498	0.55645	0.53078	0.49287	0.45999	0.43125	0.38333	0.34500
$\xi - \lambda_1$	0.35833	0.38613	0.42720	0.49285	0.55667	0.61875	0.73889	0.85500
$\xi - \lambda_2$	0.02502	0.06355	0.11922	0.20713	0.29001	0.36875	0.51667	0.65500
$\cot \beta_1$	0.79628	0.85806	0.94932	1.09521	1.23703	1.37497	1.64196	1.89998
$\cot \beta_2$	0.05559	0.14122	0.26493	0.46028	0.64446	0.81944	1.14814	1.45554
c	2.60000	2.60000	2.60000	2.60000	2.60000	2.60000	2.60000	2.60000
s	2.26194	2.33734	2.45044	2.63893	2.82743	3.01592	3.39291	3.7699
s/c	0.86998	0.89898	0.94248	1.01497	1.08747	1.15997	1.30497	1.4500
$\sqrt{s/c}$	0.933	0.949	0.971	1.007	1.043	1.077	1.142	1.204
$0.26\sqrt{s/c}$	0.24258	0.24674	0.25246	0.26182	0.27118	0.28002	0.29692	0.31304
(EXIT) β_2	86° 49'	81° 58'	75° 10'	65° 17'	57° 12'	50° 40'	41° 3'	34° 29'
(ENTRANCE) β_1	51° 21'	49° 22'	46° 29'	42° 24'	38° 57'	36° 2'	31° 21'	27° 45'
$\theta°$	35° 28'	32° 36'	28° 41'	22° 53'	18° 15'	14° 38'	9° 42'	6° 44'
$1 - 0.26\sqrt{s/c}$	0.75742	0.75326	0.74754	0.73818	0.72882	0.71998	0.70308	0.68696
θ	46° 40'	43° 17'	38° 22'	31° 0'	25° 2'	20° 19'	13° 47'	9° 48'
β_e	98° 8'	92° 39'	84° 51'	73° 24'	63° 59'	56° 21'	45° 8'	37° 33'
$\theta/2$	23° 20'	21° 39'	19° 11'	15° 30'	12° 31'	10° 10'	6° 54'	4° 54'
β'	74° 48'	71° 1'	65° 40'	57° 54'	51° 28'	46° 12'	38° 15'	32° 36'
t_m/c	0.12	0.118	0.115	0.11	0.105	0.10	0.09	0.08

TABLE 4

VORTEX STATOR BLADE ANGLE CALCULATIONS

ASSUMPTIONS: ξ HUB = 0.60000, $\bar{\psi}_d$ = 0.40000, $\bar{\phi}_d$ = 0.45000, ξ_1 = 0.70000, C_o = 0.98000, $\frac{1}{\bar{\phi}_d}$ = 2.2222, $\frac{C_o - \bar{\psi}_d}{4}$ = 0.14500, $\frac{C + \bar{\psi}_d}{4}$ = 0.34500, $\frac{\pi \times D}{N} = \frac{\pi \times 36}{32}$ = 3.53572

SECTION	VIII	V	III	II	I
ξ	0.60000	0.70000	0.80000	0.90000	1.0000
$1/\xi$	1.6666	1.4286	1.2500	1.1111	1.0000
λ_1	0.24167	0.20715	0.18125	0.16111	0.14500
λ_2	0.57498	0.49287	0.43125	0.38333	0.34500
$\xi - \lambda_1$	0.25833	0.49285	0.61875	0.73889	0.85500
$\xi - \lambda_2$	0.02502	0.20713	0.36875	0.51667	0.65500
$\cot \gamma_1$	0.53704	0.46033	0.40277	0.35802	0.32222
$\cot \gamma_2$	1.27772	1.09526	0.95832	0.85184	0.76666
c	2.20000	2.4000	2.6000	2.8000	3.0000
s	2.12432	2.47500	2.82858	3.18215	3.53572
s/c	0.965600	1.031250	1.087915	1.136482	1.178573
$0.26\sqrt{s/c}$	0.25558	0.26416	0.27118	0.27716	0.28236
γ_1 (EXIT)	61° 46'	65° 17'	68° 4'	70° 18'	72° 8'
γ_2 (ENTRANCE)	38° 3'	42° 24'	46° 13'	49° 34'	52° 31'
$\theta°$	23° 43'	22° 53'	21° 51'	20° 44'	19° 37'
$1 - 0.26\sqrt{s/c}$	0.74442	0.73584	0.72882	0.72284	0.71764
$\sqrt{s/c}$	0.983	1.016	1.043	1.066	1.086
θ	31° 53'	31° 6'	29° 59'	28° 41'	27° 20'
γ_e	69° 56'	73° 30'	76° 12'	78° 15'	79° 51'
$\theta/2$	15° 57'	15° 33'	14° 59'	14° 21'	13° 40'
γ	54° 0'	57° 57'	61° 12'	63° 55'	66° 11'
t_m/c	.10	.10	.10	.10	.10

TABLE 5

COMPARISON OF FLOW RATE MEASUREMENTS

THE FOLLOWING DATA GIVE A COMPARISON BETWEEN THE FLOW COEFFICIENT DETERMINED FROM ENTRANCE DUCT MEASUREMENTS, AND FROM COMPLETE SURVEYS BEHIND THE BLADE ROWS. THE CLOSE AGREEMENT AND THE RANDOM SCATTER GIVE A CHECK ON THE ACCURACY OF THE SURVEY MEASUREMENTS AND INDICATE THAT THERE IS NO SYSTEMATIC ERROR DUE TO WAKE FLUCTUATIONS.

STATION	$\bar{\phi}_w$ FLOW COEFF. FROM ENTR. DUCT	$\bar{\phi}_s$ FLOW COEFF. FROM SURVEYS	$\frac{\bar{\phi}_w}{\bar{\phi}_s}$
BEHIND 1ST STATOR	.393	.392	1.003
BEHIND 1ST STATOR	.366	.382	.958
BEHIND 1ST STATOR	.487	.492	.990
BEHIND 1ST ROTOR	.394	.399	.987
BEHIND 1ST ROTOR	.392	.387	1.013

TABLE 6

COMPUTATION OF CASCADE LIFT AND DRAG

C_L = LIFT COEFFICIENT FROM PRESSURE MEASUREMENTS

C_D = DRAG " " " "

C_L' = LIFT " " ANGLE "

$\bar{\phi}$	γ_1	γ_2	γ_m	C_L'	f_x	f_y	ϕ_m	C_L	C_D
.320	47.0	59.5	52.7	.59	-.0155	.191	.355	.96	.07
.332	41.6	64.0	51.1	1.08	-.0315	.236	.365	1.08	.05
.344	42.3	64.0	51.6	1.04	-.0313	.239	.376	1.05	.04
.372	44.1	64.2	52.8	.95	-.0295	.240	.401	.96	.02
.392	45.8	64.5	54.1	.87	-.0270	.237	.419	.89	.01
.409	46.8	64.8	54.8	.83	-.0245	.237	.435	.84	.01
.449	49.8	65.3	56.9	.70	-.0150	.220	.470	.70	.00
.485	52.7	65.8	58.8	.58	.0000	.202	.503	.58	.03
.520	55.5	66.4	60.7	.47	+.0006	.155	.534	.41	.01
.560	58.1	67.0	62.4	.38	+.0155	.114	.569	.28	.03
.590	59.9	66.8	63.2	.29	-	-	-	-	-

COMPUTED FROM:

$$\cot \gamma_m = \frac{\cot \gamma_1 + \cot \gamma_2}{2}$$

$$C_L' = 2\left(\frac{s}{c}\right)(\cot \gamma_1 - \cot \gamma_2) \sin \gamma_m \qquad \text{WHERE} \quad \frac{s}{c} = 1.088$$

$$C_L = \frac{\sin^2 \gamma_m}{\phi_m^2}\left\{f_y \cos(\gamma - \gamma_m) - f_x \sin(\gamma - \gamma_m)\right\}$$

WHERE $\gamma = 61.2°$

$$C_D = \frac{\sin^2 \gamma_m}{\phi_m^2}\left\{f_y \sin(\gamma - \gamma_m) + f_x \cos(\gamma - \gamma_m)\right\}$$

TABLE 7 COMPUTATION OF CASCADE BOUNDARY LAYER GROWTH

θ_2 = T.E. B.L. MOMENTUM THICKNESS

SURFACE	$\bar{\phi}$	ϕ_m	γ_m	R_c	$(\frac{x}{c})_1$	$(\frac{V_1}{V_m})$	$\int_0^{(\frac{x}{c})_1} (\frac{V_1}{V_m})^{2.17} d(\frac{x}{c})$	$(\frac{\theta_1}{c})$	$(\frac{V_2}{V_m})$	$\int_{(\frac{x}{c})_1}^{(\frac{x}{c})_2} (\frac{V}{V_m})^{4.25} d(\frac{x}{c})$	θ_2 in.	$\theta_u + \theta_L$ in.
U	.320	.355	52.7	7.15×10^4	.10	1.538	2.925	$.60\times10^{-3}$	.940	3.77	.042	.054
L	"	"	"	"	.05	1.148	.143	.16	"	.87	.012	
U	.332	.365	51.1	7.51	0	-	0	0	.960	4.11	.038	.045
L	"	"	"	"	.20	.935	.069	.86	"	.39	.007	
U	.344	.376	51.6	7.66	0	-	0	0	.979	4.30	.036	.048
L	"	"	"	"	.20	1.050	.235	.93	"	.80	.012	
U	.372	.401	52.8	8.04	0	-	0	0	.919	3.76	.040	.050
L	"	"	"	"	.20	.970	.109	.89	"	.54	.010	
U	.392	.419	54.1	8.30	0	-	0	0	.908	3.46	.039	.049
L	"	"	"	"	.20	.970	.121	.92	"	.52	.010	
U	.409	.435	54.8	8.51	.10	1.462	1.997	.56	.920	2.67	.034	.044
L	"	"	"	"	.10	.979	.054	.59	"	.61	.010	
U	.449	.470	56.9	8.99	.20	1.376	2.456	.80	.855	1.97	.036	.050
L	"	"	"	"	.05	1.033	.100	.61	"	.63	.014	
U	.485	.503	58.8	9.40	.20	1.303	1.026	.65	.850	1.84	.033	.049
L	"	"	"	"	.05	1.151	.035	.21	"	.81	.016	
U	.520	.534	60.7	9.91	.20	1.248	.567	.58	.749	1.79	.048	.077
L	"	"	"	"	0	-	0	0	"	1.06	.029	
U	.560	.569	62.4	10.25	.20	1.178	.261	.50	.912	1.76	.023	.041
L	"	"	"	"	0	-	0	0	"	1.42	.018	
U	THIN	-		8.0×10^4	0	-	0	0	.830	2.95	.047	.055
L	AIRFOIL			"	.20	.748	14.5	1.05×10^{-3}	"	.26	.008	

LAMINAR B. L.

$$\left(\frac{\theta_1}{c}\right)^2 = \frac{.442}{R_c}\left(\frac{V_m}{V_1}\right)^{9.17}\int_0^{(\frac{x}{c})_1}\left(\frac{V}{V_m}\right)^{8.17} d\left(\frac{x}{c}\right)$$

TURBULENT B. L.

$$\left(\frac{\theta_2}{c}\right) = \left(\frac{V_m}{V_2}\right)^{3.5}\left\{\frac{.0234}{R_c^{.30}}\int_{(\frac{x}{c})_1}^{1.0}\left(\frac{V}{V_m}\right)^{4.25} d\left(\frac{x}{c}\right) + \left(\frac{\theta_1}{c}\right)^{1.3}\left(\frac{V}{V_m}\right)^{4.55}\right\}^{.769}$$

WHERE $R_c = \frac{u_\infty c}{\nu}\frac{\phi_m}{\sin\gamma_m} = 16.0\times10^4\frac{\phi_m}{\sin\gamma_m}$

TABLE 8

COMPUTATION OF CASCADE LOSS

(FROM BOUNDARY LAYER DATA)

$\bar{\phi}$	$\frac{v_0}{v_m}$	γ_1	γ_m	$\frac{\theta_u + \theta_l}{c}$	Ω	i^*
.320	.940	47.0	52.7	.0208	.030	- .8
.332	.960	41.6	51.1	.0173	.023	+ 4.6
.344	.979	42.3	51.6	.0182	.026	+ 3.9
.372	.919	44.1	52.8	.0193	.027	+ 2.1
.392	.908	45.8	54.1	.0189	.022	+ .4
.409	.920	46.8	54.8	.0170	.020	- .6
.449	.855	49.8	56.9	.0193	.019	- 3.6
.485	.850	52.7	58.8	.0189	.019	- 6.5
.520	.749	55.5	60.7	.0298	.020	- 9.3
.560	.912	58.1	62.4	.0159	.020	-11.9
THIN AIRFOIL	.830	46.0	55.5	.0214	.0179	+ .2

COMPUTED FROM:

$$\Omega = 1.578 \left(\frac{v_0}{v_m}\right)^3 \frac{\sin^3 \gamma_1}{\sin^2 \gamma_m} \left(\frac{\theta_u}{c} + \frac{\theta_l}{c}\right)$$

$$i^* = 46.2 - \gamma_1$$

TABLE 9

COMPUTATION OF CASCADE LOSS

(FROM WAKE DATA)

SOURCE	$\bar{\phi}$	ψ^*	$\Delta\overline{\psi}'$	ϕ_m	γ_1	Ω	i^*	REMARKS
FIG. 77	.324	.898	.0378	.358	44.2	.144	2.0	Ω PROBABLY IN ERROR
" 78	.352	1.087	.0692	.451†	42.8	.158	3.4	
" 79	.370	1.099	.0453	.443†	44.0	.112	2.2	
" 80	.392	1.115	.0441	.419	45.8	.129	.4	
" 81	.448	1.042	.0180	.469	49.8	.048	-3.6	
" 82	.485	.865	.0156	.502	52.7	.039	-6.5	
" 83	.552	.560	.0382	.562	57.6	.086	-11.4	
" 84	.320	.853	.0117	.355	47.0	.050	- .8	i^* PROBABLY IN ERROR
" 85	.449	1.035	.0160	.470	49.9	.042	- 3.7	
" 86	.553	.555	.0405	.563	57.7	.091	-11.5	
" 87	.448	1.040	.0159	.469	49.8	.042	- 3.6	
" 88	.370	.428	.0155	.399	44.0	.047	2.2	
" 89	.392	.413	.0123	.419	45.8	.036	.4	
" 90	.447	.335	.0134	.468	49.7	.036	-3.5	
	.392	.412	.0103	.414†	45.5	.030	+ .7	

† ϕ_m OBTAINED FROM WAKE INTEGRATION

COMPUTED FROM

$$\Delta\overline{\psi}' = \frac{\int_0^{\phi_s} \phi_2 (\psi^* - \psi_2')\, d\theta}{\int_0^{\phi_s} \phi_2\, d\theta}$$

$$\Omega = \Delta\overline{\psi}' \frac{\sin^2\gamma}{\phi_m^2}$$

$$i^* = 46.2 - \gamma_1$$